HAL
open science

Study of magnetic heterostructures with perpendicular anisotropy by resonant magnetic reflectivity of soft X-rays

Vartika Bansal

To cite this version:

Vartika Bansal. Study of magnetic heterostructures with perpendicular anisotropy by resonant magnetic reflectivity of soft X-rays. Condensed Matter [cond-mat]. Université Grenoble Alpes [2020-..], 2023. English. NNT : 2023GRALY008 . tel-04152695

HAL Id: tel-04152695

https://theses.hal.science/tel-04152695v1

Submitted on 5 Jul 2023

HAL is a multi-disciplinary open access archive for the deposit and dissemination of scientific research documents, whether they are published or not. The documents may come from teaching and research institutions in France or abroad, or from public or private research centers.

L'archive ouverte pluridisciplinaire **HAL**, est destinée au dépôt et à la diffusion de documents scientifiques de niveau recherche, publiés ou non, émanant des établissements d'enseignement et de recherche français ou étrangers, des laboratoires publics ou privés.

THÈSE

Pour obtenir le grade de

DOCTEUR DE L'UNIVERSITÉ GRENOBLE ALPES

École doctorale : PHYS - Physique
Spécialité : Physique de la Matière Condensée et du Rayonnement
Unité de recherche : Institut Néel

Etude d'hétérostructures magnétiques à anisotropie perpendiculaire par réflectivité magnétique résonante des rayons X mous

Study of magnetic heterostructures with perpendicular anisotropy by resonant magnetic reflectivity of soft X-rays

Présentée par :

Vartika BANSAL

Direction de thèse :

Jean-Marc TONNERRE — Directeur de thèse
DIRECTEUR DE RECHERCHE, Université Grenoble Alpes

Rapporteurs :

BORIS VODUNGBO
Maître de conférences HDR, SORBONNE UNIVERSITE
THOMAS HAUET
Maître de conférences HDR, UNIVERSITE DE LORRAINE

Thèse soutenue publiquement le **3 février 2023**, devant le jury composé de :

BORIS VODUNGBO — Rapporteur
Maître de conférences HDR, SORBONNE UNIVERSITE

THOMAS HAUET — Rapporteur
Maître de conférences HDR, UNIVERSITE DE LORRAINE

ARISTIDE LEMAITRE — Examinateur
Directeur de recherche, CNRS DELEGATION ILE-DE-FRANCE SUD

MASSIMILIANO MARANGOLO — Examinateur
Professeur des Universités, SORBONNE UNIVERSITE

MAIRBEK CHSHIEV — Président
Professeur des Universités, UNIVERSITE GRENOBLE ALPES

Thank you first and foremost my parents for always being by my side,

My brother Shravan for his kind words when I needed them,

My thesis supervisor Jean-Marc, for his help throughout the process, I am really grateful,

To colleagues I go to know and worked with at Institut Neel and synchrotron soleil,

To all the people I got to know in Grenoble and who supported me always, Camille and her cats – Toxo and Medor, her mom Marie Aline, my dearest friend Julio, Kylia, my flatmate Laureen, Lucile, Sanchayan, Swati and Phani.

And my boyfriend Jack for his immense support, even through the most difficult times.

Phd journey isn't an easy one and it certainly wasn't for me. It was full of struggles, both self-inflicted and circumstantial. There were times when I didn't know if I would even make it. However, it is said that growth happens only through difficulties and challenges. It happens by making mistakes, tons of them, getting up and then falling but then getting up again.

It is when we learn.

So, thank you also to all good and bad times that helped me grow.

RESUME (EN FRANCAIS)

Le comportement magnétique dans les structures en couches minces a suscité un intérêt considérable pour ses applications technologiques très variées. Au fur et à mesure que la dimension des films magnétiques diminue, ils sont capables de présenter diverses propriétés magnétiques n'ayant pas d'équivalent dans le matériau en vrac à mesure que le magnétisme interfacial devient plus important. Cependant, sonder les interfaces magnétiques enterrées dans de telles hétérostructures peut être un défi majeur. L'anisotropie magnétique perpendiculaire (PMA) est une telle quantité induite par l'interface qui se produit à l'interface entre différents types de matériaux. Cette thèse porte sur la détermination du profil d'aimantation hors plan à travers des films ferromagnétiques ultrafins enterrés avec divers matériaux adjacents par réflectivité magnétique des rayons X doux (SXRMR), fournissant ainsi une description directe du magnétisme aux interfaces inférieure et supérieure. Cette technique combine les informations résolues en profondeur de la réflectivité des rayons X avec la sélectivité des espèces du dichroïsme circulaire magnétique des rayons X pour sonder le profil de magnétisation dans le plan (ip) et hors du plan (oop) avec une résolution inférieure au nanomètre dans les couches minces.

Les systèmes à base de métal lourd/ferromagnétique/oxyde sont bien connus pour leur capacité à fournir un-PMA élevé se produisant principalement par l'hybridation à l'interface FM/oxyde par recuit à des températures plus élevées. Nous avons étudié le profil d'aimantation dans des séries d'échantillons de MgO/CoFeB/(W)/Ta avant et après recuit à différentes températures par des mesures au bord Fe L3. Une transition de l'axe magnétique facile de ip à oop pour les couches de couverture Ta et W a été observée, accompagnée de changements dans la distribution magnétique de Fe sur l'épaisseur de CoFeB. L'échantillon en couches de ta coiffe a montré un profil d'aimantation amélioré et plus homogène après recuit à un recuit à 340°C par rapport à une distribution de gradient avant recuit. Cette distribution s'est encore modifiée après un recuit à 400°C où l'axe magnétique facile est revenu à ip. Pour la couche de protection W, nous avons observé un profil de gradient avant ainsi qu'après le recuit à 400°C, mais accompagné d'une amélioration de l'aimantation aux deux interfaces.

Nous avons également étudié un autre système de Gd en couches minces Pt/Co/Gd qui s'est avéré être un empilement prometteur dans le contexte des études de déplacement de paroi de domaine chiral en raison du couplage antiferromagnétique sur des sites atomiques individuels de l'interface Co/Gd. Avec SXRMR, nous avons obtenu la distribution de l'aimantation hors du plan à travers les couches Co à partir de mesures au bord Co L3 ainsi que les couches Gd à partir de mesures au bord Gd M5 à différentes températures de 300K à 40K. Pour la couche de Co, dont la température de Curie est supérieure à la température ambiante, l'analyse montre un profil homogène sur l'évolution de la température. En revanche, pour la couche de Gd, dont la température de Curie est connue pour être proche de la température ambiante, nous avons observé un profil magnétique inhomogène sur la plage de température de 43K à 300K. Bien que pour 300K, un profil de magnétisation oop pur a été résolu à l'interface immédiate avec Co. À des températures plus basses, nous avons observé un changement dans le profil oop et la manifestation de la composante ip plus loin de l'interface d'interface immédiate Co/Gd où Gd est fortement mélangé avec le bouchon Al couche

RESUME (IN ENGLISH)

Magnetic behavior in thin-film structures has attracted considerable interest for its wide-ranging technological applications. As the dimension of magnetic films reduce, they are able to exhibit various magnetic properties having no equivalent in bulk material as interfacial magnetism become more important. However, probing buried magnetic interfaces in such heterostructures can be a major challenge. Perpendicular magnetic anisotropy (PMA) is one such interface induced quantity that occurs at the interface between different types of materials. This thesis focuses on determination of the out-of-plane magnetization profile through buried ultrathin ferromagnetic films with various adjacent materials by soft X ray magnetic reflectivity (SXRMR), thus providing a direct description of the magnetism at the bottom and top interfaces. This technique combines the depth-resolved information of X-ray reflectivity with the species selectivity of X-ray magnetic circular dichroism for probing in-plane (*ip*) and out-of-plane (*oop*) magnetization profile with sub nanometer resolution in thin films.

Heavy metal/ferromagnet/oxide-based systems are well known for their capability to provide high PMA mainly occurring through the hybridization at FM/oxide interface through annealing at higher temperatures. We investigated the magnetization profile in series of samples of MgO/CoFeB/(W)/Ta before and after annealing at different temperatures by measurements at Fe L3 edge. A transition in easy magnetic axis from ip to oop for both Ta and W cap layers was observed which was accompanied by changes in Fe magnetic distribution over CoFeB thickness. Ta cap layered sample showed an enhanced and more homogeneous magnetization profile after annealing at annealing at 340°C compared to from a gradient distribution before annealing. This distribution further modified after annealing at 400°C where easy magnetic axis turned back to ip. For W cap layer, we observed a gradient profile before as well as after annealing at 400°C however accompanied by an enhancement of magnetization at both interfaces.

We also studied another system of Pt/Co/Gd thin film Gd which has proven to be a promising stack in the context of chiral domain wall displacement studies due to the antiferromagnetic coupling at individual atomic sites of the Co/Gd interface. With SXRMR we obtained the distribution of the out-of-plane magnetization across the Co layers from measurements at the Co L3 edge as well as Gd layers from measurements at the Gd M5 edge over various temperature from 300K to 40K. For the Co layer, whose Curie temperature is higher than the ambient temperature analysis shows a homogeneous profile over temperature evolution. On the other hand, for Gd layer, whose the Curie temperature is known to be close to room temperature, we observed an inhomogeneous magnetic profile over temperature range of 43K to 300K. Although for 300K, a pure oop magnetization profile was resolved at the immediate interface with Co. At lower temperatures we observed change in oop profile and manifestation of *ip* component further away from immediate Co/Gd interface interface where Gd is strongly intermixed with the Al cap layer.

TABLE OF CONTENTS

RESUME (EN FRANCAIS) 2

RESUME (IN ENGLISH) 4

TABLE OF CONTENTS 6

1 INTRODUCTION 1

1.1 GENERAL OVERVIEW 1
1.2 ESSENTIAL DEFINITIONS: MAGNETISM 4
1.3 PERPENDICULAR MAGNETIC ANISOTROPY 6
1.4 INTERFACIAL MAGNETISM 8
1.5 MOTIVATION FOR PROBING THE DEPTH DEPENDENCE OF MAGNETIZATION 10

2 RESONANT X RAY MAGNETIC SCATTERING 11

2.1 CHARACTERISTICS OF X RAYS 12
2.2 INTERACTION OF X - RAYS WITH MATTER 14
2.3 INTERACTION OF X-RAYS WITH *MAGNETIC* MATTER 18
2.4 ANALYTICAL EXPRESSIONS OF XRMS: KINEMATICAL APPROACH 26
2.5 X RAY RESONANT MAGNETIC REFLECTIVITY 32
2.6 DYNAMICAL APPROACH: OPTICAL POINT OF VIEW 36
2.7 OTHER TECHNIQUES FOR INVESTIGATING MAGNETIC PROFILOMETRY 39
2.8 CONCLUSION 41

3 EXPERIMENTAL TECHNIQUES AND DATA COLLECTION 42

3.1 SYNCHROTRON RADIATION CENTER: 42
3.2 SEXTANTS 44
3.3 RESOX AND ITS PROPERTIES 45
3.4 DATA COLLECTION AT RESOXS 49
3.5 ANALYSIS OF EXPERIMENTAL DATA 57
3.6 IN LAB EXPERIMENTS (CONDUCTED OUTSIDE OF SYNCHROTRON RADIATION): 65
3.7 CONCLUSION 67

4 DEPTH RESOLVED MAGNETIZATION PROFILE OF COFEB/MGO/COFEB/(W)TA PERPENDICULAR HALF MAGNETIC TUNNEL JUNCTIONS 68

4.1 CONTEXT 68

4.2 SAMPLE GROWTH 72
4.3 MACROSCOPIC MAGNETIC PROPERTIES 73
4.4 INVESTIGATION BY SOFT X RAY RESONANT MAGNETIC REFLECTIVITY 75
4.5 DISCUSSION 120
4.6 CONCLUSIONS 125

5 DEPTH RESOLVED MAGNETIZATION PROFILE OF CO AND GD IN TA/PT/CO/GD/ALOX 126

5.1 CONTEXT 126
5.2 MOTIVATION 128
5.3 SAMPLE GROWTH 130
5.4 HARD X RAY REFLECTIVITY MEASUREMENTS 131
5.5 SOFT X-RAY MAGNETIC REFLECTIVITY (SXRMR) 132
5.6 DISCUSSION AND CONCLUSION 159

6 CONCLUSION AND PERSPECTIVE 160

7 ANNEX 165

7.1 COMPARISON BETWEEN REVPOL AND FLIPHLON MODES OF MEASUREMENT 165
7.2 EFFECT OF A SMALL *IN-PLANE* APPLIED MAGNETIC FIELD 166
7.3 CHANGING APPLIED *IP* MAGNETIC FIELD 169
7.4 ELIMINATING APPLIED LONGITUDINAL FIELD, HLON = 0 171

8 BIBLIOGRAPHY 173

1 INTRODUCTION

In this thesis, we are interested in investigation of depth resolved magnetic profiles in ultra-thin film sample with perpendicular magnetic anisotropy (PMA) by resonant magnetic scattering. It is essential to understand why we are motivated by PMA, its origin and the systems that give rise to this phenomenon. This will be followed by importance of studying interfacial effects, magnetism, and why we are motivated by it.

1.1 General overview

Since properties of magnetic thin films and multilayers first triggered interest more than 60 years ago [1], various new physical phenomenon such as interfacial perpendicular magnetic anisotropy in thin films [2,3], Giant Magnetoresistance (GMR) [4,5], Tunnel magnetoresistance (TMR) at room temperature [6,7], oscillatory character of RKKY exchange coupling [8] and others have been discovered. These phenomena all consider spin of the electron in addition to its charge thus associating magnetism and electronic transport with new term – ***spintronics*** [9].

It was the discovery of giant magneto resistance (GMR) in a sample of Fe/Cr multilayer by Fert and Gruenberg, which won them a noble prize in 2007 that had the strongest impact on both fundamental and applied physics. The Fe electrodes were separated by Cr layers and their magnetic state was changed into parallel or anti-parallel through manipulation by an external magnetic field. The orientation of the external magnetic field when changed gave two different resistance states (low and high) for electron transport measurements. It is the large resistance variation between parallel and anti-parallel magnetization giving rise to the name GMR. A schematic diagram represented in Figure 1.1, shows a case of two ferromagnetic layers (F1 and F2 in blue color) that are separated by nonmagnetic (NM) layer (in yellow color).

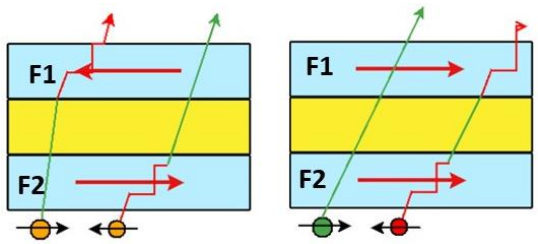

Figure 1.1 Schematic explanation of the GMR effect.

From application point of view, discovery of GMR offered a new concept for magnetic sensor device: *spin valve* [10] which were then rapidly integrated into read/write heads by hard disk drive (HDD) industry after showing improved sensitivity. Development of such HDDs has been a strong driving force in micro magnetism, nano magnetism and spintronics. This has allowed increase in areal density of information

stored in HDD at an average rate of 60% per year, representing more than 8 orders of magnitude over 50 years.

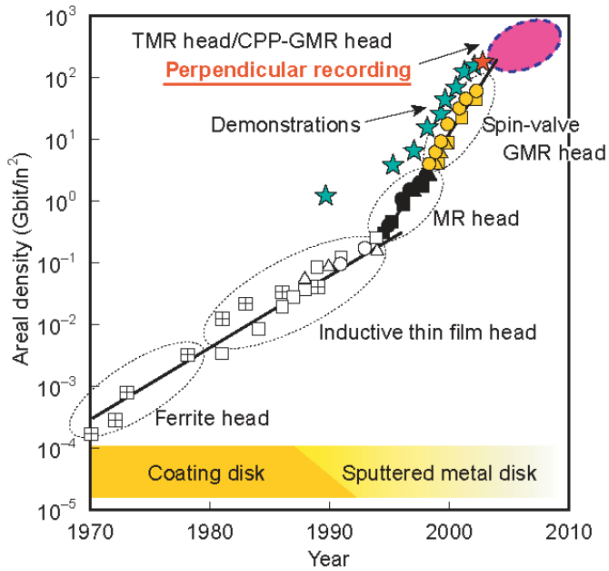

Figure 1.2 Read/Write heads technologies which contributed to areal density increase in HDD [11]

In these devices, digital data is stored as magnetization direction of a tiny nanometer sized magnetic domains. Each of these domains with a specified magnetization direction defines a bit. The orientation of small magnetic domains (bits) where storage magnetic media is designed to have two stable states at remanence. This is achieved by the uniaxial axis of anisotropy that provides a specific orientation of magnetism. Thus, magnetisation has two possible directions along anisotropy axis. The uniaxial anisotropy is characterized by an anisotropy energy per unit volume K_u and thus anisotropy energy is given by:

$$E = -K_u(\boldsymbol{M} \cdot \hat{n})^2 \qquad (1.1.1)$$

Where $\boldsymbol{M}$ is the orientation of magnetization with respect to the easy axis of magnetization.

Since in HDDs, we want to increase the areal density, the aim has been to decrease size and increase storage density. Writing information requires switching magnetisation of the grains of the magnetic material from one stable state to other overcoming an energy barrier ΔE that separates the 2 stable states. The required energy is given by [12]:

$$\Delta E = K_u V \qquad (1.1.2)$$

Where K_u is the anisotropy per unit volume of the storage layer and V is volume of the storage layer, i.e., the grain size. It is ΔE that determines the stability of written information. If the barrier is not high enough, magnetization, of a grain can switch to opposite direction due to thermal fluctuations ($k_B T$). This will result in degradation of stored information. Typical switching time to overcome energy barrier given by

$$\tau = \tau_0 exp\left(\frac{\Delta E}{k_B T}\right) \qquad (1.1.3)$$

Where τ_0 is the characteristic attempt time of 1 ns. In order for the information to remain stable through retention time $t_{retention\ time}$ energy barrier must be:

$$\Delta E > k_B T log\left(\frac{t_{retention\ time}}{\tau_0}\right) \quad (1.1.4)$$

Thus, for a 10-year retention period,

$$\Delta E = K_u V > 45 k_B T \quad (1.1.5)$$

At room temperature, to fulfil this condition, anisotropy needs to be increased too. This was initially achieved in hcp-CoCr based alloys which were doped with Pt in order to switch in plane to out of plane anisotropy [13]. This was done to reduce negative impact demagnetizing energy has effective anisotropy with decreasing bit size**.**

MRAM devices (magneto resistive random-access memory), are universal memory devices introduced by spintronics based on **MTJ** (magnetic tunnel junction) technology. MTJ is a spintronic device derived from spin valves, consisting of two magnetic layers separated by an insulting tunnel barrier. From the spin valves the metallic spacer is replaced by a very thin insulator (oxide) layer so that electrons can pass from one ferromagnetic layer to the other by tunnelling. Spin filtering effect is dominant in such case leading to a very high relative resistance variation called tunnel magnetoresistance (TMR) [14]. The resistance of this barrier depends on the relative orientation of the magnetization of the two layers which may be further imagined for binary coding in new recording applications.

After the first device demonstration in 1993, it was seen that MRAMs provided reduced noise, no volatility and a lower power consumption with a high density in the smallest chip [15], [16]. This also proved to be attractive for industrial applications [17]. Like in HDDs, in case of MRAMS too, retention can be directly linked to barrier height $K_u V$. If the memory cell size is reduced to increase storage capacity, anisotropy has to be increased in order to meet criterion for thermal stability. However, we cannot increase anisotropy too much, otherwise energy to write information will be too large and the system will be useless. These considerations show us that the anisotropy of a magnetic material plays an important role in applications of magnetism particularly those related to memory and storage.

Although initially, in the studies of spintronic devices, the magnetization of FM layer was kept *in plane*, it has been shown that PMA of a magnetic material can be of great importance in applications of magnetism specially those related to memory and storage.

A solid-state memory, which is a device that reads and writes data with high speeds, used electronic state of capacitors and transistors to store data. Although these devices enabled high performance, such static and dynamic random-access memory (SRAM and DRAM) where data constantly needs to be refreshed also don't seem as an ideal solution. Another device called flash memory was developed, which although nonvolatile, relied on moving parts, imposing size and speed limitations [18].

Materials with ***out of plane anisotropy*** has come out as a solution in order to keep the magnetization along a defined axis in MTJ and thus enhance robustness against thermal fluctuations [19–21]. Thus, in this thesis, we are motivated to study specifically ultra-thin film systems with PMA.

1.2 Essential definitions: Magnetism

In order to further our study, we will take some time to understand some basic terms that will be used throughout the thesis, sometimes in repetition.

1.2.1 Magnetic moment order

Electrons revolve around a nucleus giving us orbital magnetic moment m_L. However, it does not suffice to explain the total magnetic moment which is experimentally higher. Thus, we introduce the notion of m_S, which is intrinsic angular momentum of electron taking the value S = ±1/2. Therefore, the total magnetic moment is given by:

$$m = m_L + m_S \tag{1.2.1}$$

These two magnetic moments can interact with each other giving rise to **spin orbit coupling** (explained further in details).

For magnetic moments within a volume density is defined by net magnetisation, ***M*** (in Am^{-1}). M_s is the saturation magnetisation, which is the maximum magnetisation available in the system when all the magnetic moments are collinear. It must be noted here that, this definition of magnetisation and magnetic moment is for general systems. It can be different at interfaces due to effect of neighbouring atoms which we will discuss in more detail in further sections.

A ferromagnet (FM) is a material that exhibits magnetisation due to all the magnetising moments pointing in the same direction below a certain ordering temperature defined as curie temperature (T_c). As we go above T_c, the thermal fluctuations lead to cancellation of magnetisation as they outweigh the interaction between magnetic moments resulting in a paramagnetic state. Antiferromagnetic (AF) material exhibits net 0 magnetization due to antiparallel alignment of neighbouring magnetic moments. It is temperature dependent and exists below T_N called the Neel temperature. Lastly, if the magnetisation of a system with AF order is not fully compensated, system is known to have ferrimagnetism due to different magnitudes of AF coupled magnetic moments.

1.2.2 Spin – orbit coupling

Spin orbit coupling (SOC) is a relativistic interaction that occurs between the electron spin and orbital angular momenta [22] thus, we can say that SOC describes the effect of the electron orbital motion on its spin. The consequence of spin orbit interaction makes the angular momentum tend to align to spin of

electron with preferential crystal axes and creates **magneto crystalline anisotropy** (discussed in detail further).
SOC is a source of multitude of phenomenon such as perpendicular magnetic anisotropy (PMA), spin hall effect, Rashba effect [23] and also Dyaloshinkii – Moriya interaction [24], [25], [26].

In transition metals, valence electrons in the 3d band, electric field is formed by ions of the crystal called **crystalline field**. This is so strong that it blocks the orbital moment, making it insensitive to the spin moment. This is called **quenching** [27], [28]. In many transition metals, the net magnetic moment has contributions from orbital moments ≈ 5% to 10% of the spin moments [29]. In absence of SOC, magnetic moment of 3d ions would in fact be pure spin moment.

In rare earth materials (unfilled f band) SOC is larger than crystal field energy, resulting in large moments and large orbital momentum contribution and lower T_C due to weaker indirect exchange interactions of more shielded f electrons.

1.2.3 Magnetic domains

Magnetic domains was introduced by Pierre Weiss in 1907 [30], when he was explaining why a ferromagnetic material can exist in demagnetised state, which was later confirmed in 1931 by Bitter through a visualization technique. It can simply be described as a region where atomic magnetic moments are approximately oriented in the same direction which arise from the need to balance contribution of different energy terms such as magnetostatic energy, exchange energy and magneto crystalline energy**.** On increase of number of domains, magnetostatic energy term reduces followed by increase of the other energy terms.

1.2.4 Domain wall internal structure

The region at the interface in between two magnetic domains is called a domain wall (DW). This region brings an increase in exchange and anisotropy energy. A DW has finite width that results from the competition between exchange and anisotropic energies. For thin films with PMA, mainly two types of DW can be found, which can be distinguished from one another in the way atomic magnetic moments turn in a wall which are called as Bloch and Neel walls as shown in Figure *1.3*. In a Bloch DW, magnetisation rotates in a plane parallel to the plane of domain wall while in a Neel DW, it rotates in a plane perpendicular to the plane of the DW. The Bloch walls are found to be most stable in thin films with PMA.

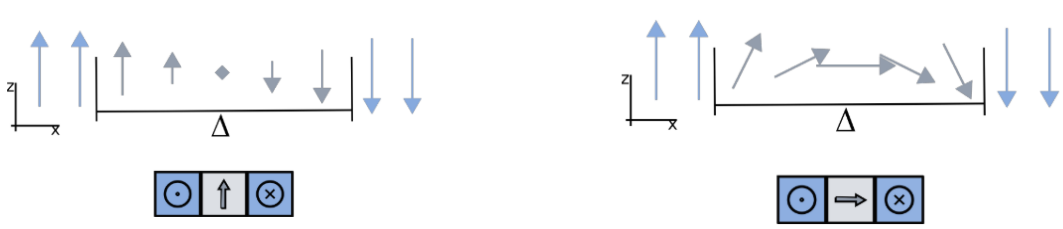

Figure 1.3 (a) Bloch domain wall; (b) Neel domain wall; Δ is the DW width parameter.

1.3 Perpendicular magnetic anisotropy

In magnetic media, spontaneous magnetization can lie in some preferred directions with respect to crystallographic axis. **This property is called magnetic anisotropy**. The energy involved in rotating the magnetization from the low energy direction (easy axis) to a higher energy direction (hard axis) is called anisotropy energy *E*. There are several kinds of anisotropy:

1. Magneto crystalline anisotropy
2. Shape anisotropy
3. Stress anisotropy
4. Exchange anisotropy

Out of all these, only magneto crystalline anisotropy is intrinsic, while the others are extrinsic or induced.

1.3.1 Magneto crystalline anisotropy

Due to SOC, spins prefer to align along the certain crystallographic directions in order to minimize SOC energy. This contribution is known as **magneto-crystalline anisotropy**. It can be observed by measuring magnetization curves in different directions. For cubic close packed structures in case of Fe or Ni, the magneto crystalline energy is given by series of expansion in terms of angles between different directions of easy and cubic axes. It is sufficient to represent the anisotropy in an arbitrary direction by first two terms in series of expansion - K_0 and K_1 since the rest of the terms are really small. In hexagonal, tetragonal and rhombohedral structures - K_u.

1.3.2 Interface induced magnetic anisotropy

First predicted by Néel in 1953, in multi layered thin film heterostructures, broken symmetry at interfaces generates an anisotropy [1] which can also be described by the uniaxial anisotropy energy [31]:

$$\varepsilon_S = \frac{K_S}{t}\sin^2\theta \qquad (1.3.1)$$

Where K_S is the surface anisotropy constant, t is the magnetic film thickness and θ is the angle between the magnetization and the film normal. This tends to bring the magnetisation in the *out of the plane* direction. The term K_s has two contributions from 2 interfaces and introduces an easy axis perpendicular to the film and adds to MCA as well as shape anisotropy that arises from the dipole-dipole interaction [22]. The effective anisotropy energy K_{eff} can be written as:

$$K_{eff} = K_1 + \frac{K_s}{t} - \frac{\mu_0 M_S^2}{2} \qquad (1.3.2)$$

Where, shape anisotropy is given by the last term in the eq.(1.3.2). **In ultra-thin film heterostructures, volume anisotropy is mostly dominated by shape anisotropy** since MCA contribution (K_1) is much smaller, and where the effective anisotropy is then given by:

$$K_{eff} = \frac{K_s}{t} - \frac{\mu_0 M_S^2}{2} \quad (1.3.3)$$

Here, $K_u = K_s/t$ (Jm^{-3}) and $K_{eff} = K_u - K_d$, (K_d representing the shape anisotropy). $\boldsymbol{K_{eff}}$ **> 0 which implies that interface anisotropy outweighs shape anisotropy giving rise to PMA.** We can see from this empirical expression that interfacial contribution of anisotropy increases when the magnetic layer thickness (t) decreases. Thus, we can define a critical FM thickness t_c where for thickness greater than t_c magnetization will lie in plane. For systems such as Co/Pt, this thickness ≈ 1nm as illustrated in Figure 1.4.

For thicker films, shape anisotropy dominates and favors *ip* magnetization. However, for thinner films, the interfacial contribution dominates leading to perpendicular magnetic anisotropy (PMA).

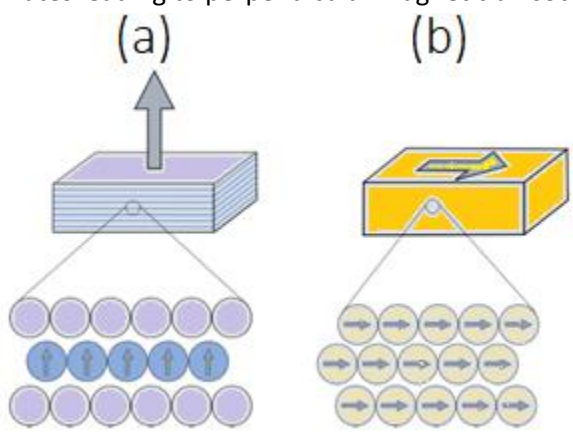

Figure 1.4 Illustration of magnetic anisotropies in two often found cases. a) Out of plane magnetisation b) In plane magnetisation (Figure adapted from [32])

1.3.2.1 Systems with PMA

Out of plane (*oop*) elements are promising for industrial applications [33]. PMA occurring in thin film systems can have different origins, of materials where the phenomenon of PMA appears such as ferromagnetic/heavy metal systems such as in Co/Pt, Co/Pd multilayers [34] or with rare earth metal such as Gd [35]**.** According to observation, it was believed that to obtain PMA, it is essential to have heavy metal present at the magnetic metal interface (that could be linked to the strongest SOC in heavy metal).

In the recent years, interfacial perpendicular magnetic anisotropy (*iPMA*) discovered at interfaces between magnetic transition metals and oxides [36] despite the weak spin orbit coupling. This phenomenon can be observed with a variety of amorphous and crystalline oxides along with various transition metals such as Co, Fe, CoFe or CoFeB alloys that can be formed either from natural oxidation of metallic element or plasma oxidation. This is a remarkable phenomenon considering that the measured anisotropy amplitude between CoFeB/MgO is comparable or in some cases even larger to that found in thin film systems with Co/Pt interfaces (1.4 erg/cm^2) despite the weak spin orbit coupling since the elements involved are light (Co, Fe, O, Mg etc.)
Detailed characterization techniques such as XAS (X ray absorption spectroscopy) and XPS (X ray photoemission) have revealed that oxygen plays an essential role in occurrence of interfacial

perpendicular anisotropy (iPMA) at magnetic metal/oxide interfaces produced by formation of Fe(Co) – oxygen bonds [37], [38]. *Ab initio* calculations later showed that hybridization between the *sp* oxygen orbitals and dz^2 orbitals in 3d metals along with the decrease in degeneracy in *d* orbitals causes such an anisotropy [39]. Thus, the origin of large PMA is ascribed to the following factors:

- Degeneracy lift of *oop* 3d orbitals as a cause of weak spin orbit coupling.
- This leading to Hybridizations between dz^2, dxz and dyz 3d orbitals.

Level of oxidation can also be an important factor to consider according to a study by Yang et al., [39], where three structures have been shown (a) "pure" (O-terminated) interface, (b) an over oxidized interface (with O inserted at the interfacial magnetic layer), and (c) an under oxidized (Mg-terminated) interface. Infact largest values for PMA have been obtained for ideal interfaces while it is reduced for the case of over- or under oxidized interfaces [40].

1.4 Interfacial magnetism

In this thesis our focus is on nanomagnetic behaviour at thin film interfaces, it is important to understand how magnetic behaviour originates at and near interfaces, especially those between thin films. This behaviour is due to breaking of inversion symmetry interfaces and surfaces that can produce a variety of effects. Magnetism is known to arise from the strong short-range correlations occurring due to electronic spin and orbital degrees of freedom which are inherently altered at interfaces, particularly in the presence of strong spin-orbit coupling and during responses to stimuli. Therefore, interfaces not only modify bulk magnetic properties, but can also create magnetism from nonmagnetic layers, alter the nature of a magnetic state, or can impact its dynamic evolution following an electrical, optical, thermal, or magnetic pulse as shown in Figure *1.5* where the circles with arrows in purple colour indicates interfacial atoms. These indicate interfacial mixing of structure, chemical, magnetic, and electronic states which can modify spin as well as orbital properties on each side to create new magnetic properties [41]. Here, time-dependent stimuli such as charge currents, optical pulses, heat, and electric and magnetic fields (shown in different incoming directions) can produce spin currents, which can in turn modify the electronic and magnetic states. When we talk about *interfacial magnetism*, all such effects and changes in magnetism occurring at interfaces are incorporated in that term.

One such effect that we studied is, PMA which creates a unique axis perpendicular to the interface. Thus, it is intriguing to study how interfaces in heterostructures with PMA can affect the magnetization distribution across a layer.

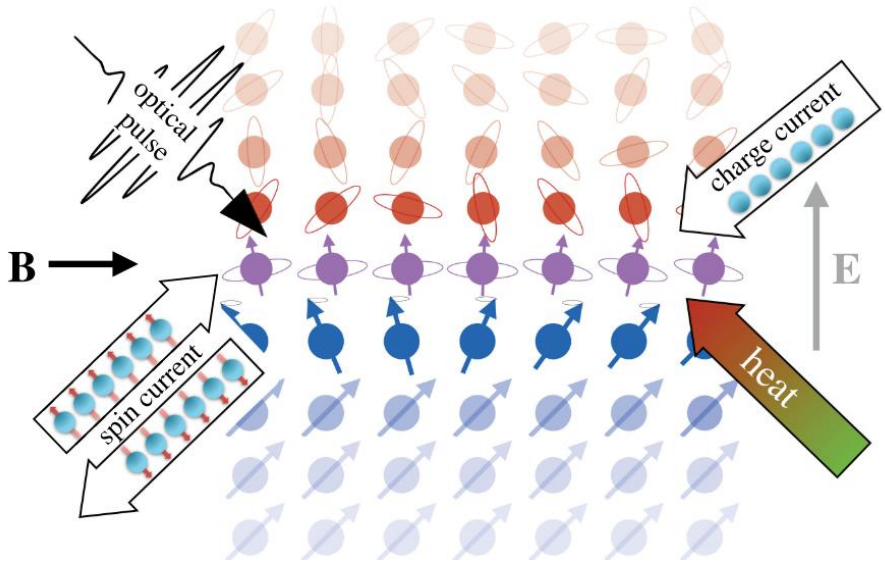

Figure 1.5 Interface between a ferromagnet (blue atoms with arrows) and a heavy metal with strong spin-orbit coupling (red atoms with circles). Interface atoms are shown in purple with circles and arrows. The different directions around the heterostructure are time-dependent charge currents, optical pulses, heat, and electric and magnetic fields (taken from [41])

1.4.1 Thin films surface and interface surface effects

In general, for ideal systems, the interfaces are perfect and thus we expect very less effects from extrinsic factors related to structures of thin films and their interfaces. However, in real systems, the interfaces are far from ideal and consist of disorder effects such as interdiffusion, roughness, strain and defects etc. Some examples include interfacial roughness effects on GMR of spin valve structures [42–45], spin transport across interfaces [46–48] and a phenomenon called exchange biasing [49] occurring at the interface between an antiferromagnets and a ferromagnet which may give rise to an enhancement of magnetic ordering temperature due to proximity effect [50]. Also, TMR effect is sensitive to the interfacial region at the FM electrode/tunnelling barrier. It is known that extrinsic factors such as magnetic impurities or structural dislocations formed at the barrier interface can largely degrade TMR [51–53]. For example, a strong interface sensitivity of TMR has also been indicated by enhancement or reduction after insertion of 4-monolayer bcc Co and 1-monolayer Cr at the barrier interface have been observed previously [54].

Efficiency of spin injection determined by the magnetic properties in the immediate interface region (a few monolayers from the interface) in a heterostructure with a ferromagnet (FM) [55]. Therefore, in order to improve the spin-injection efficiency, we need to be able to separate out the magnetic properties at the interfaces from those at the centre of the thins films [55].

On magnetic systems, effects of surface such as critical behaviour near the transition temperature have been studied extensively [56–58]. It is also common to see a shift in the T_C (Curie temperature) or T_N (Neel temperature) for ultra-thin films due to reduction of thickness [59–61]. This can be due to extrinsic effects or even intrinsic finite size objects. These due to lesser neighbours atoms at interfaces, spin orbit

coupling [62] or correlation effects (due to reduced coordination) that can modify the underlying electronic band structure [63]. In the case of antiferromagnets, it has been seen that the consequences of surface exchange modifications can prove to be particularly dramatic since the net spontaneous moment of the material is dominated by surfaces and defects [64–66].

1.5 Motivation for probing the depth dependence of magnetization

Thin film magnetic heterostructures with PMA which play an essential role in current recording media industry and technologies [67] are the core study of this thesis. Since PMA is an interfacial property, and interfaces are known to play a fundamental role to create new methods of rapid manipulation [68] in the field of spintronics. We want to go beyond the layer-averaged description of magnetism in heterostructures and see the effects at a more local scale, and how far the effects extend from the interface.

The progress of techniques with elemental specifies and monolayer sensitivity by using the non-destructive depth profiling technique of X rays (XMCD at scattering condition) open up opportunities to understand the magnetism of the buried interfaces. The high flux available at the third-generation synchrotron source permits magnetization density profiles to be obtained with higher spatial resolution than possible with polarized neutrons [14]. This is the technique we performed in this thesis and will be discussed in depth in the next chapter

2 RESONANT X RAY MAGNETIC SCATTERING

Scattering experiments have been one of the most powerful ways to obtain information about structure of matter. Through conventional scattering methods of electrons and neutrons we have been able to study precise spacing as well as location of atoms in various solids. Experimental techniques which use X rays such as X ray diffraction and reflectivity have been known as standard methods to study the structure in solids. X ray diffraction is a method that uses hard X rays which are close to energy range of 10 KeV in order to accurately determine crystal structure determination [69]. Due to high interface sensitivity, X ray reflectivity technique in specular condition has been one of the work horses to determine structural properties such as layer thickness and interface roughness in thin film heterostructures. Also, since penetration depth of X rays is of the order of micrometers in 10KeV, they have also allowed one to probe real bulk properties. Thus, easy availability and cheapness of these X ray sources have aided in widespread use of these techniques.

However, along with determination of lattice structures, determination of magnetic structures has been another challenge in solid state physics. To probe bulk magnetic properties, we have techniques such as magneto optical Kerr effect (MOKE) and superconducting quantum interference device (SQUID), however in these methods we are only limited to average value of magnetisation over the whole sample. We are not sensitive to information in a certain thickness, or the effect of interfaces, within the thin film samples. We have studied in the previous chapter; how interfacial affects play a significant role in improving thin film heterostructures for magnetic recording applications.

Thanks to the tunability of the synchrotron radiation in the mid-1980s providing possibility to change the polarization of incoming light has opened gates to many magnetic scattering experiments. Synchrotron radiation is an intense as well as versatile source of X rays providing increased brightness and flux with X rays that more brilliant compared to lab sources by a factor of 10^{12}. This has allowed one to work at energies where electronic transitions occur for specific elements, thus enabling research at elemental resonances. This has been used to carry out absorption experiments to study local magnetic properties of magnetic materials such as X ray magnetic dichroism (XMCD) effect , introduced in the year 1987 by Gisela Schutz, et al. [70,71].

When reflectivity measurements are made at energy is tuned at absorption edges: $L_{2,3}$ edges for transition metals and $M_{4,5}$ edges for rare earth metals, dramatic changes occur in atomic scattering factor as a function of the magnetization of the sample [72–74]. Thus, in general, by using circular polarized light tuned in resonant edge energy, any technique can be turned into its magnetic counterpart through effect of XMCD.

In this thesis, our main focus will be on a specific scattering technique called **soft X ray resonant magnetic reflectivity (SXRMR)**, better known as a combination of XRR and XMCD as it involves measuring intensity of specular reflectivity at resonant energies by changing the angle of circular polarised light. This method enables us to measure magnetic moment depth profile of a chosen element along the growth axis with high accuracy [75] [76],[77]. Kao at NSLS Dragon beamline measured one of the first reported results on SXRMR on Co [78,79]. A strong asymmetry was measured at Co L2,3 edge indicating strong sensitivity and a relation to XMCD effect. This technique is popularly known to determine interfacial magnetism in heterostructures which can be important for applications into spin injection, TMR and GMR where high spin polarisation through interface is an essential issue.

2.1 Characteristics of X rays

Since being discovered in 1895 by Wilhelm Conrad Rontgen, X rays have been an invaluable probe to study structure of matter for a range of materials. They are electromagnetic waves with a wavelength in the region of an Angstrom (10^{-10}m). Here, we will discuss some the important characteristics of X rays.

2.1.1 Propagating electromagnetic wave

Electromagnetic radiation such as X rays can be thought of as superposition of electromagnetic waves. They have both electric field $\boldsymbol{E}^*$ and magnetic field $\boldsymbol{B}$ as shown in the Figure 2.1 which are perpendicular to each other and the wave propagates in a direction perpendicular to them (we can say transverse direction). Both electric field $\boldsymbol{E}^*$ and magnetic field $\boldsymbol{B}$ can be written as:

$$\boldsymbol{E}^{*1} = \boldsymbol{E}_{\boldsymbol{0}}^{*} exp^{-i(\omega t - \boldsymbol{k}.\boldsymbol{r})} \qquad \boldsymbol{B} = \boldsymbol{B} exp^{-i(\omega t - \boldsymbol{k}.\boldsymbol{r})} \tag{2.1.1}$$

The term $(\omega t - \boldsymbol{k}.\boldsymbol{r})$ is the phase of the wave, $\boldsymbol{r}$ is the position vector, t is the time and $\omega = 2\pi\nu$ is the pulsation.

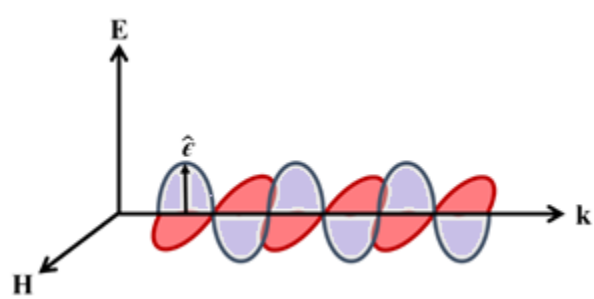

Figure 2.1 An X-ray is an electromagnetic wave where the electric field $\boldsymbol{E}^*$ and magnetic field $\boldsymbol{B}$ are perpendicular to each other and to the propagation vector $\boldsymbol{k}$.

[1] Here we have used **E*** to represent electric field to not confuse with E for energy.

2.1.2 Polarization

As the electromagnetic waves are described vectorially, we can introduce the notion of polarization. It describes the orientation of oscillations of the electric field $\boldsymbol{E}^*$and magnetic field $\boldsymbol{B}$. Figure 2.1 shows an electromagnetic wave that is linearly polarized since with time the two planes of polarization do not change their orientation. Thus, electromagnetic wave can be said to be polarized when all waves that compose it have electric planes parallel to each other and it is represented by vector $\boldsymbol{\epsilon}$.

We can also write the equation (*2.1.1*) taking polarization into account as since direction of $\boldsymbol{\epsilon}$ is same as that of $\boldsymbol{E}^*$

$$\boldsymbol{E}^* = \boldsymbol{\epsilon} E_0^* exp^{-i(\omega t - \boldsymbol{k}.\boldsymbol{r})} \qquad (2.1.2)$$

In the third-generation synchrotrons, we can have X ray beams with almost all photons having the same polarization. Radiation from a bending magnetic is linearly polarized whereas that from insertion device can be also circularly polarized.

a) Linear $\boldsymbol{\sigma}$ and $\boldsymbol{\pi}$ polarizations

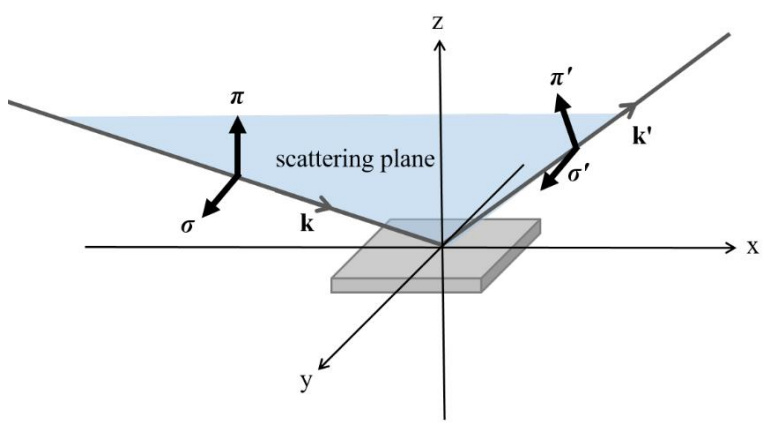

Figure 2.2 Geometry of scattering experiment with polarized light showing the directions of the σ and π vectors with respect to the scattering plane

In scattering, polarized X rays are defined to have one component perpendicular to the scattering plane $\boldsymbol{\sigma}$ and the other component parallel to the scattering plane is $\boldsymbol{\pi}$. Figure 2.2 shows the orientation of both $\boldsymbol{\sigma}$ and $\boldsymbol{\pi}$ with respect to the scattering plane. A plane wave that has only $\boldsymbol{\sigma}$ components (or alternatively only $\boldsymbol{\pi}$ component) is said to be linearly polarized. Linear polarization states have 0 angular momentum that is projected along the propagation direction. We can represent electric field as a matrix

$$\boldsymbol{E}_{\boldsymbol{\sigma}}^* = \begin{pmatrix} 1 \\ 0 \end{pmatrix}, \boldsymbol{E}_{\boldsymbol{\pi}}^* = \begin{pmatrix} 0 \\ 1 \end{pmatrix} \qquad (2.1.3)$$

Where $\boldsymbol{E}_{\boldsymbol{\sigma}}^*$ and $\boldsymbol{E}_{\boldsymbol{\pi}}^*$ denote waves polarized in σ and π directions.

b) **Circularly polarized light**

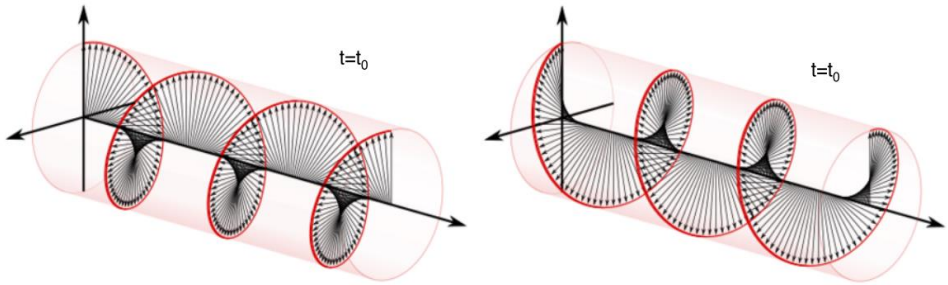

Figure 2.3 Shows the circular polarized waves at a given time (a) Left-handed circular polarized light C^-(b) Right-handed circular polarized light C^+

An electromagnetic beam is called *circularly polarized* when the electric field rotates around the propagation vector $\boldsymbol{k}$. With propagation vector along z direction and phase along y is shifted by π/2 with respect to x, amplitude for circular polarized light is:

$$C^{\pm} = \mp \frac{1}{\sqrt{2}} \begin{pmatrix} 1 \\ \pm i \\ 0 \end{pmatrix} \tag{2.1.4}$$

Here, $C^+$and C^- are the right and left polarization and $\mp$ sign ensures that angular momentum is $\pm$ along the direction of propagation.

2.1.3 Photon wavelength and energy

A useful relation between wavelength and energy of X rays is given as follows:

$$\lambda(\text{Å}) = \frac{12.398[KeV \cdot \text{Å}]}{E[KeV]} \tag{2.1.5}$$

Where E is the energy of X rays and λ is the wavelength also where $\frac{hc}{e} = 12.398[KeV \cdot A]$. When we talk about *hard X rays*, the wavelength is in range of 0.1 to 1nm, which is comparable to the interatomic distances. For *soft X rays*, the wavelength is between 1 and 10nm which is comparable to distances in nanometers for solids, and is usually used to study magnetic ordering.

2.2 Interaction of X - rays with matter

X ray photon interacts with matter in form of scattering and absorption. In this section, we will present the fundamental aspects of interaction of X rays with matter in order to further develop the theory of magnetic scattering.

2.2.1 Absorption

Absorption is described as an energy dependent process occurring when incoming X ray photons are absorbed by an atom. It is known to be very useful process to study electronic properties of the outer shell of atom such as a valence state or local atomic displacements with methods like Extended X-ray Absorption Fine Structure [80], X-ray Anomalous Near-Edge Structure (XANES) [81].

When the energy of the photon is large enough to overcome the binding energy between the electron and the nucleus, electron is expelled from the atom leaving it ionized. This is called the **photoelectric effect**; it has been shown in *Figure 2.4* X ray absorption is given by linear *absorption coefficient* μ where μdz is the attenuation of the X ray beam, after travelling thickness dz distance at a depth of z from the surface.

The intensity $I(z)$ changes from z to $z + dz$ is:

$$I(z + dz) - I(z) = -I(z)\mu dz \qquad (2.2.1)$$

Which gives,

$$I = I(0)e^{-\mu z} \qquad (2.2.2)$$

When an X ray photon expels an electron from an inner atomic shell, it creates a hole in that shell which can be subsequently filled by an electron from the outer shell. This results in emission of the photon with energy equal to the difference of the binding energy of the 2 shells. Emitted radiation is also called **fluorescence**. This emitted photon may result in emission of a secondary electron from an outer shell. This secondary emitted electron is called **Auger electron**. All 3 of these processes are shown in Figure 2.4.

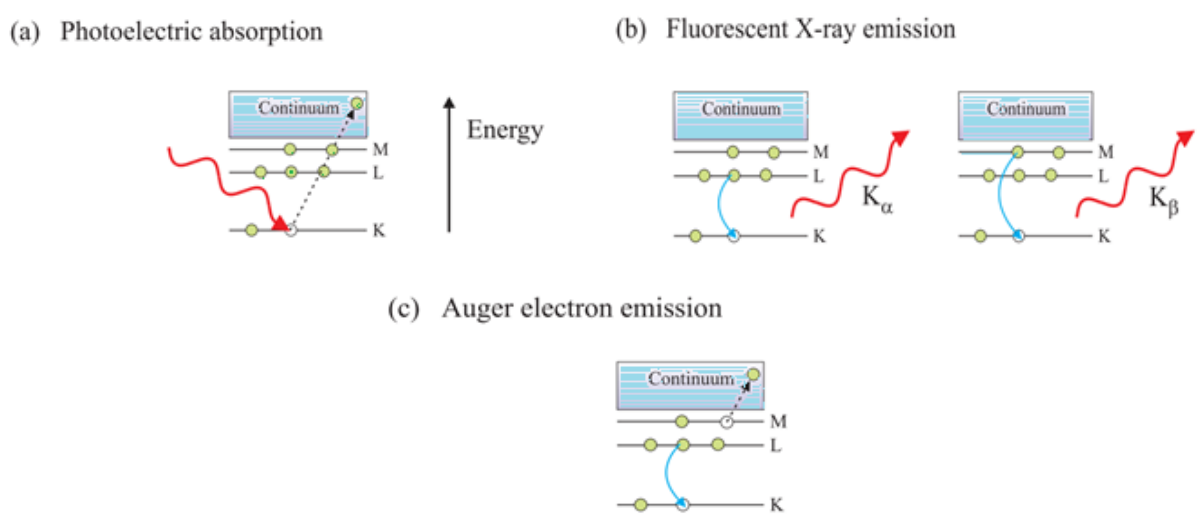

Figure 2.4 Schematic energy level diagram of an atom (a) The photoelectric absorption process (b) Fluorescent X-ray emission (c) Auger electron emission

The absorption coefficient is related to the atomic absorption cross section σ_{abs}:

$$\mu[m^{-1}] = \rho\sigma_{abs}[m^{-3}m^{2}] \qquad (2.2.3)$$

Where ρ is the atomic density. While the process of absorption is distinct from scattering, it should be borne in mind that the two are actually related which will be discussed in the following sections.

2.2.2 Scattering

Now, we come to the other form of interaction of X rays with matter – scattering. It has been one of the most important physical phenomena to enable the study of microscopic structure of matter such as photons, electrons and neutrons. One method to study structure as introduced before is XRD that has been used as a great tool to structurally characterize crystalline systems, relying on Thomson scattering mechanism related to the interaction between the photos and the charge density of the electrons. This method uses hard X rays with photon energies near $\hbar\omega = 10\,KeV$ for crystal structure determination [82]. Since, X ray wavelength is comparable to the interatomic distances in solids, enabling us to solve the lattice structure.

In the classical description of the scattering event electric field of the incident X ray exerts force on the electronic charge which then accelerates and radiates the scattered wave. Scattering event can be classified as elastic or inelastic. Elastic scattering is *a photon in-photon out* process where there is no loss of energy whereas in inelastic scattering, a change of energy takes place. Sometimes in quantum mechanics we may observe that the scattered photon has lower energy relative to the energy of incident photon. This inelastic process is called Compton scattering.
In this section, we will outline some key concepts such as scattering vector and differential cross section.

2.2.2.1 Scattering from one electron

We begin by considering electron as the most basic scattering object. Thus, the ability of an electron to scatter an X-ray is defined as the *scattering length*. In order to make any progress, we will begin with a fundamental quantity the *differential cross section* written as:

$$\frac{d\sigma}{d\Omega} = \frac{R}{\phi\Delta\Omega} \qquad (2.2.4)$$

Here, the strength of the incident beam is given by the flux, ϕ which is simply the number of photons passing through unit area per second. The incident beam interacts after interaction with the scattering object. The number of scattered photons recorded per second in a detector is I_{sc} subtends a solid angle $\Delta\Omega$. The differential cross- section is thus a measure of the efficiency of the scattering process where details of the experiment.

2.2.2.2 Scattering from an atom

Here we describe the elastic scattering from a single atom with Z electrons. It is important to mention here that in an atom, protons and neutrons are not known to participate in the scattering since they are too heavy and neutrons are not charged.

Since, we take the interaction of X rays with electrons, we start by considering a distribution of electronic charge by a number density, $\rho(\boldsymbol{r})$. Thus, the scattered radiation from the atom is a superposition of contributions from different volume parts of this charge distribution. From Figure 2.5, the phase difference between the volume element at origin and at position $\boldsymbol{r}$ is $-\boldsymbol{k}' \cdot \boldsymbol{r}$, where incident wave is of wave vector $\boldsymbol{k}$ is written as,

$$\Delta\boldsymbol{\varphi}(\boldsymbol{r}) = (\boldsymbol{k} - \boldsymbol{k}') \cdot \boldsymbol{r} = \boldsymbol{Q} \cdot \boldsymbol{r} \tag{2.2.5}$$

Where, $\boldsymbol{Q}$ is the scattering vector as defined before and $\boldsymbol{Q} = 2|\boldsymbol{k}| \sin\theta = \left(\frac{4\pi}{\lambda}\right) \sin\theta$

A volume element $d\boldsymbol{r}$ at $\boldsymbol{r}$ will contribute an amount $-r_0\rho(\boldsymbol{r})d\boldsymbol{r}$ to the scattered field with a phase factor of $e^{i\boldsymbol{Q}\cdot\boldsymbol{r}}$. The total scattering length of an atom is given as,

$$-r_0 f^0(\boldsymbol{Q}) = -r_0 \int \rho\,(\boldsymbol{r}) e^{i\boldsymbol{Q}\cdot\boldsymbol{r}} dr \tag{2.2.6}$$

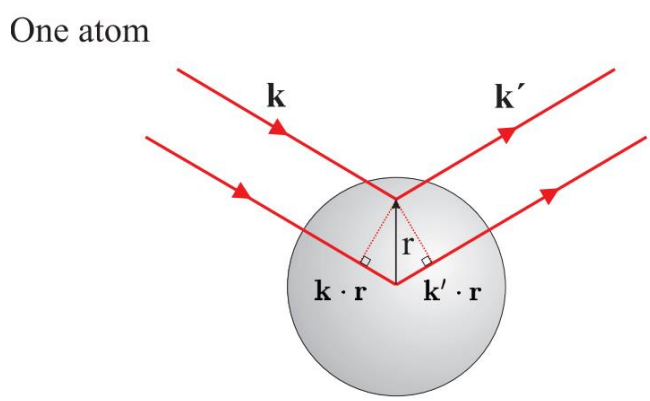

Figure 2.5 Scattering from an atom. An X-ray with a wave vector **k** scatter from an atom to the direction specified by **k'**

Where $f^0(\boldsymbol{Q})$ is called the *atomic form factor*. Thus, we can define the atomic form factor as a response of atoms to the electromagnetic X rays depending on the interaction between photons and electrons.

For $Q \to 0$ all the volume elements scatter in phase thus $f^0(\boldsymbol{Q} = 0) = Z$ which is the number of electrons in the atom. The right-hand side of equation above is a Fourier transform.

2.2.3 Resonant elastic scattering

In the classical picture of the X ray scattering from an atom, the electric field of the incident wave exerts force on the electronic charge causing the electrons to oscillate and radiate the scattered wave. The oscillating electron thus becomes the source of re- radiating the X ray. This scattering of an X ray is characterized by change in its momentum $\Delta\mathbf{P}$ and energy E. An incident particle with wave vector $\boldsymbol{k_i}$ scatters and resulting in the final wave vector $\boldsymbol{k_f}$. The momentum transfers during this process

$$\Delta\mathbf{P} = \hbar\boldsymbol{k_i} - \hbar\boldsymbol{k_f} = \hbar\mathbf{Q} \qquad (2.2.7)$$

Where $\hbar = h/2\pi$, h is the planks constant and $\mathbf{Q} = \boldsymbol{k_i} - \boldsymbol{k_f}$ is defined as the scattering vector.

The difference in the incident and scattered wave vectors then provide with information on momentum transfer scattering vector $\mathbf{Q}$ and energy transfer

$$\Delta E = E_i - E_f = \hbar(\omega_i - \omega_f) \qquad (2.2.8)$$

In our study, we will only deal with the case of elastic scattering where $\Delta E = 0$ and only $\mathbf{Q}$ is modified.

In order to understand resonant scattering, it is important to understand what this term means in our study. An excitation process is simply described as resonant or non-resonant depending on whether the energy of the incident photon $\hbar\omega$ corresponds to the excitation energy ΔE.

At resonance, however we define atomic form factor as,

$$f(\boldsymbol{Q}, E) = f^0(\boldsymbol{Q}) + f'(E) + if''(E) \qquad (2.2.9)$$

Where f' and f'' are **dispersion corrections** to f^0 which is an isotropic non resonant term. The dispersion corrections assume their values when the X ray energy is equal to one of the absorption edge energies of the atom. In order to derive these terms, we solve an equation of motion of bound electrons in an alternating electromagnetic field. These dispersion corrections are also known as anomalous dispersion corrections even though there isn't anything anomalous about them.

It must be noted here that in case where energy of the X rays is different compared to the energies of occupation of electrons, we can consider that there is no absorption and only f^0 is taken into account.

2.3 Interaction of X-rays with *magnetic* matter

Till now we have learnt about charge scattering, interpreted through Thomson scattering however, we also want to obtain information on the microscopic magnetic properties in magnetic samples. This sensitivity to magnetism arises from the spin component of the electromagnetic wave. A well-known probe that is sensitive to such information is related to the use of visible or near visible light, where the angle of polarization of light is modified with the magnetization of the sample [83], [84]. This can happen

in reflection (Kerr rotation) or in transmission (Faraday rotation). As these techniques are based on the application of light, they are non-destructive and contactless. Since then, these magneto-optical effects are widely employed, and use laser radiation. These effects are related to inter- or intra-band transitions, accessible by dipole allowed transitions utilizing photon energies in the eV range. However, they are not element selective and these methods do not provide a way to separate between spin and angular momenta, and they are only quantitative after comparison with other magnetometry results.

The advent of synchrotron radiation will increase access to increasingly fine effects [85]. This gave ability to perform a magneto optical experiment conducted by X rays, such as XMCD.

2.3.1 Basics behind magnetic X ray investigations: XMCD

Magnetic circular dichroism is based on the difference occurring in **absorption of left and right circular polarized light due to change in magnetization in presence of an applied magnetic field.** The direction of this applied field is parallel to the direction of propagation of X ray vector.

Before a sample experience a magnetic field, the electrons are equally distributed over the orbitals. On applying a magnetic field is applied, electrons with different spins are energetically separated. Due to the spin-orbit interaction all the orbitals, except the s orbital ($l=0$), will be separated further into more energy levels. **To be able to detect magnetic circular dichroism, the measured sample must both have spin-orbit interaction and spin polarization.**

As we put the X ray radiation beam on the sample, it results in **absorption of the photons by the electrons** which in turn becomes photo electrons. Thus, the X ray absorption signal is recorded by measuring the current on the surface of the sample by exciting electrons into conduction band. Initially, the photo electron is spin polarized through absorption of right circularly polarised (RCP) and left circularly polarised (LCP) photons which carry angular momentum. This process has been shown in left hand side of Figure 2.6.

The *2p* electrons are resonantly excited from deep bound Fe 2p level. SOI causes the Fe 2p level to split into a less bound $2p_{3/2}$ and a more bound $2p_{1/2}$ state excitation, with 13 eV energy difference which ae also known as the L3 and L2 edges. (Left side of Figure 2.6) Then, magnetic properties enter when the spin polarized photoelectron is excited into an unoccupied valence state.

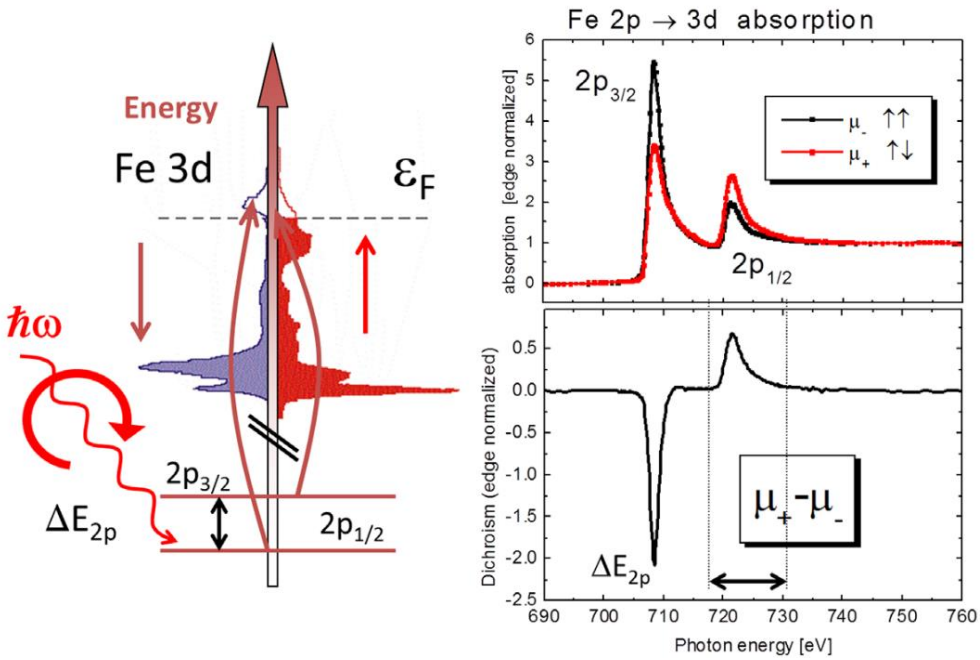

Figure 2.6 2p to 3d transition on incidence of circular polarized X rays (on the left). Energy dependent edge absorption of Fe for parallel and anti-parallel magnetization and corresponding XMCD signal. (Figure taken from [86])

The excited photoelectron present in the final or intermediate state acquires a spin polarization through the spin-orbit coupling interaction. Thus, it becomes sensitive to the spin imbalance in the unoccupied density of states near the Fermi energy.

By measuring the difference in absorption or scattering of X rays with opposite helicities, a measurement of this spin imbalance is obtained, which is proportional to the absorbing or scattering atom's net magnetic moment. This difference is shown in right hand side of Figure 2.6.

2.3.1.1 Sum rules:

Thus, a direct relation of XMCD amplitude and the magnetic moment implies a general quantitative character to this method. This technique is successful not only because of its element and site specificity but also the fact that we can separate spin and orbit contributions to the total magnetic moment by so called sum rules which have been introduced by Thole and Carra. With the help of a single ion approximation, they were able to derive a sum rule for projection of the orbital moment $\langle L_z \rangle$ [87] and also for the spin moment $\langle S_z \rangle$ [88].

2.3.2 X-ray resonant magnetic scattering – the basics

In this section, we aim to understand both effects of polarization as well as working at resonant energy along with sensitivity to magnetism in this section and develop the expression for resonant magnetic

scattering, and we will derive the atomic scattering factor containing magnetic related terms arising from X ray magnetic circular dichroism.

In order to obtain the scattering amplitude, **time dependent perturbation theory has to be used** and resonant processes requires a full quantum mechanical treatment. In the quantum mechanical picture of resonant scattering as shown in Figure *2.7*, an incoming incident photon excites an electron to a higher lying level. Electron then decays back into the initial state by emitting a photon having same energy as the incident one via an intermediate state. Scattering cross section in such process is derived by considering the time dependent perturbation of the sample by the incident photon where resonance is considered an intermediate state.

Figure 2.7 Diagram of resonant x-ray absorption showing each energy level with the electronic quantum states.

In order to further develop the theory, we introduce scattered intensity I into a solid angle $d\Omega$ is given as the square of scattering amplitude $f(\boldsymbol{q}, E)$.

$$\left(\frac{d\sigma}{d\Omega}\right) = |f(Q, E)|^2 \tag{2.3.1}$$

The charge and magnetic dipole scattering without anomalous dispersion are described by M. Blume's approach [89], thus we can express eq. (2.3.1) as:

$$\left(\frac{d\sigma}{d\Omega}\right)^{scat} = |f(\boldsymbol{Q}, E)|^2 = \left(\frac{1}{I_0}\right) P_{i\to f} \cdot \rho(E_f) \tag{2.3.2}$$

which relates scattered intensity to *transition probability* $P_{i\to f}$ which is then multiplied by density of intermediate state $\rho(E_f)$ and normalized by intensity of the incident light I_0. Transition probability $P_{i\to f}$ per unit time for second order perturbation theory can be written as:

$$P_{i\to f} = \frac{2\pi}{\hbar}\left|\langle f|H|i\rangle + \sum_n \frac{\langle f|H|n\rangle\langle n|H|i\rangle}{E_i - E_n}\right|^2 \times \delta(E_i - E_f) \tag{2.3.3}$$

Here, eigenstates $|i\rangle$ describes the initial state where electron is excited and then decays back into the final state $|f\rangle$ where $|n\rangle$ is the eigenstate for intermediate state of the excitation. The first order term which includes transitions directly from $|i\rangle$ to $|f\rangle$ without intermediary states is called the *Fermi's golden rule*.

The material in initial state $|i\rangle$ is characterized by an electronic ground state $|a\rangle$ with incident photon with wave vector $\boldsymbol{k}$ and polarisation vector $\boldsymbol{\epsilon}$, giving $|i\rangle = |a;\boldsymbol{k};\boldsymbol{\epsilon}\rangle$. Then, the Hamiltonian H might induce a new transition of the system to a new eigenstate $|f\rangle = |b;\boldsymbol{k}';\boldsymbol{\epsilon}'\rangle$.

The *interaction Hamiltonian* in equation (2.3.3) for quantised electromagnetic wave is then given as,

$$H = -\frac{e^2}{2mc^2}\sum_n \boldsymbol{A}^2(\boldsymbol{r_j}) - \frac{e^2}{mc}\sum_n \boldsymbol{A}(\boldsymbol{r_j})\cdot\boldsymbol{p_j} - \frac{e\hbar}{mc}\sum_n \boldsymbol{s_j}\cdot[\nabla\times\boldsymbol{A}(\boldsymbol{r_j})] - \frac{e^3\hbar}{2mc^4}\sum_n \boldsymbol{s_j}\cdot[\dot{\boldsymbol{A}}(\boldsymbol{r_j})\times\boldsymbol{A}(\boldsymbol{r_j})] \quad (2.3.4)$$

where, $\boldsymbol{A}(\boldsymbol{r_j})$ is the vector potential of the electromagnetic wave linked to electric and magnetic field $\boldsymbol{E}(\boldsymbol{r})$ and $\boldsymbol{M}(\boldsymbol{r})$ vectors through Maxwell's equations [90]. The j electron states are described by $\boldsymbol{p}_j$, $\boldsymbol{r}_j$ and $\boldsymbol{s}_j$ (impulse, position and spin respectively).

In equation (2.3.4) first term describes radiation field itself while 2nd term introduces the interaction of electron this field corresponding to a charge dipole term. 3rd term represents interaction of electromagnetic field with spin and the last term accounts for the spin orbit coupling. Splitting the Hamiltonian, we can write the full elastic scattering amplitude as:

$$f_{full} = \frac{e^2}{mc^2}\left[\langle b|e^{i\boldsymbol{Q}\boldsymbol{r_j}}|a\rangle(\boldsymbol{\epsilon}'\cdot\boldsymbol{\epsilon}) - i\frac{\hbar\omega}{mc^2}\langle b|\textstyle\sum_j e^{i\boldsymbol{Q}\boldsymbol{r_j}}s_j|a\rangle(\boldsymbol{\epsilon}'\times\boldsymbol{\epsilon}) + \frac{\hbar^2}{m}\sum_c \frac{\langle b|\boldsymbol{M_i}(\boldsymbol{k}',\boldsymbol{\epsilon}'''')|c\rangle\langle c|\boldsymbol{M_j}(\boldsymbol{k},\boldsymbol{\epsilon}|a\rangle}{(E_a-E_c)+\hbar\omega-\frac{i\Gamma_c}{2}} + \frac{\hbar^2}{m}\sum_c \frac{\langle b|\boldsymbol{M_j}(\boldsymbol{k},\epsilon|c\rangle\langle c|\boldsymbol{M_j}(\boldsymbol{k}',\boldsymbol{\epsilon}''|a\rangle}{(E_a-E_c)-\hbar\omega'}\right]\times(E_a-E_b+\hbar\omega-\hbar\omega') \quad (2.3.5)$$

The first 2 terms account for charge and spin distributions related to scattering while third and fourth are related to the resonant excitation. This equation contains most of the X ray scattering phenomenon such as dichroism and polarization.

Finite width of the energy distribution of the intermediate state $|c\rangle$ introduces a modification of the denominator in the form of inverse lifetime τ_C. It must be noted that the intermediate state is expressed now by eigenstate $|c\rangle$. The transition matrices $\boldsymbol{M_{i,j}}(\boldsymbol{k},\boldsymbol{\varepsilon})$ can be written as,

$$\boldsymbol{M_{i,j}}(\boldsymbol{k},\boldsymbol{\varepsilon}) = \sum_h\left(\frac{\boldsymbol{\epsilon}\cdot\boldsymbol{P_{i,j}}}{\hbar} + i(\boldsymbol{k}\times\boldsymbol{\epsilon})\cdot\boldsymbol{s_{i,j}}\right)e^{-i\boldsymbol{k}\cdot\boldsymbol{r_{i,j}}} \quad (2.3.6)$$

It is important to differentiate the pure magnetic scattering which is a direct interaction between the magnetic moment and the electromagnetic wave from the resonant magnetic scattering which deal with an additional **magnetization-sensitive component** in the atomic structure factor in the vicinity of an edge.

First let's investigate the case where we look at magnetic scattering far away from resonance as derived by M. Blume [91]. After simplifying the second order terms in equation (2.3.5). The scattering amplitude for non-resonant charge and magnetic scattering is given as:

$$f^{non-res} = \frac{e^2}{mc^2}\langle b|e^{i\boldsymbol{Q}\boldsymbol{r}_j}|a\rangle(\boldsymbol{\epsilon}'\cdot\boldsymbol{\epsilon}) - i\frac{\hbar\omega e^2}{m^2c^4}\left\langle b\left|\sum_j\left(i\frac{\mathbf{Q}\times\mathbf{P_j}}{\hbar k^2}\cdot\mathbf{A}+s_j\cdot\mathbf{B}\right)\right|a\right\rangle(\boldsymbol{\epsilon}'\cdot\boldsymbol{\epsilon}) \quad (2.3.7)$$

With the substitution vectors for the polarization,

$$\boldsymbol{A} = 2(1-\boldsymbol{k}\cdot\boldsymbol{k}')(\boldsymbol{\epsilon}'\times\boldsymbol{\epsilon}) - (\boldsymbol{k}\times\boldsymbol{\epsilon})(\boldsymbol{k}\cdot\boldsymbol{\epsilon}') + (\boldsymbol{k}'\times\boldsymbol{\epsilon})(\boldsymbol{k}'\cdot\boldsymbol{\epsilon}') \quad (2.3.8)$$

$$\boldsymbol{B} = (\boldsymbol{\epsilon}'\times\boldsymbol{\epsilon}) + (\boldsymbol{k}'\times\boldsymbol{\epsilon}')(\boldsymbol{k}'\cdot\boldsymbol{\epsilon}) - (\boldsymbol{k}\times\boldsymbol{\epsilon})(\boldsymbol{k}\cdot\boldsymbol{\epsilon}') - (\boldsymbol{k}'\times\boldsymbol{\epsilon}')(\boldsymbol{k}\cdot\boldsymbol{\epsilon}) \quad (2.3.9)$$

It is worth to realise that $\boldsymbol{A}$ and $\boldsymbol{B}$ are formally different which means that spin and orbital momentum contribute differently. Using the charge density $\boldsymbol{n}(\boldsymbol{Q})$ Fourier transform, spin density $\boldsymbol{S}(\boldsymbol{Q})$ and orbital momentum $\boldsymbol{L}(\boldsymbol{Q})$ equation (2.3.10) can be written as,

$$f^{res}_{non-mag} = \boldsymbol{n}(\boldsymbol{Q})(\boldsymbol{\epsilon}'\cdot\boldsymbol{\epsilon}) - i\left(\frac{\hbar\omega}{mc^2}\right)f_D\left[\frac{1}{2}\boldsymbol{L}(\boldsymbol{Q})\cdot\boldsymbol{A} + \boldsymbol{S}(\boldsymbol{Q})\cdot\boldsymbol{B}\right] \quad (2.3.11)$$

This equation has 2 terms where the first term describes scattering from charge distribution and second term describes the magnetization densities. f_D is the *Debye – Waller factor.* Although both electric and magnetic transitions contribute, electric multipole transitions that are dominant. Magnetic contributions are smaller by a factor by a factor $\hbar\omega/mc^2$,

$$\frac{\sigma_{mag}}{\sigma_{charge}} \approx \left(\frac{\hbar\omega}{mc^2}\right)^2\frac{N^2_{Mag}}{N}\langle\boldsymbol{S}\rangle^2\frac{f^2_{mag}}{f^2} \quad (2.3.12)$$

In conclusion, **the non-resonant magnetic contribution is negligible** in comparison to the resonant contribution further described in the next section. A more detailed description on this can be found in [92].

2.3.2.1 Magnetic moment dependence of the atomic scattering factor

To calculate the resonant magnetic scattering, we consider the case when incident photon has an energy of $\hbar\omega$ corresponding to the transition energy of a bound electron state in the atom $(E_a - E_c)$. The scattering amplitude is then dominated by the third term of the equation(2.3.3). The transition matrix $\boldsymbol{M_i}(\boldsymbol{k},\boldsymbol{\varepsilon})$ is determined for the respective electric 2^l-pole transition E_l. Lifetime of τ_C of intermediate

excited state directly influences scattering amplitude. In other words, transition is directly proportional to density of unoccupied states in the conduction band above the Fermi energy E_F.
In this discussion, we will only focus on electric dipole $(E1, l = 1)$ transition in the following discussion. Corresponding quadruple resonant $(E2)$ transition can be found in the literature [93].

Within the dipole approximation the transition matrix element reduces to:

$$\boldsymbol{M}(\boldsymbol{k}, \boldsymbol{\varepsilon}) = \sum_N \sum_n \boldsymbol{p_n} \cdot \boldsymbol{\epsilon} e^{i\boldsymbol{k}\cdot\boldsymbol{r}_N} \tag{2.3.13}$$

In 3d transition metal magnetism strongly affects the 2p → 3d excitation and that the electric dipole transition E1 is the dominant transition in these systems. The magnetic resonant scattering factor is then given as [94]:
Where,

$$f_{E1}^{res} = \left[(\boldsymbol{\epsilon}' \cdot \boldsymbol{\epsilon})F^{(0)} - i(\boldsymbol{\epsilon}' \times \boldsymbol{\epsilon}) \cdot \boldsymbol{M}F^{(1)} + (\boldsymbol{\epsilon}' \cdot \boldsymbol{M})(\boldsymbol{\epsilon} \cdot \boldsymbol{M})F^{(2)}\right] \tag{2.3.14}$$

$$F^{(0)} = \left(\frac{3}{4k}\right)[F_{11} + F_{1-1}] \tag{2.3.15}$$

$$F^{(1)} = \left(\frac{3}{4k}\right)[F_{11} - F_{1-1}] \tag{2.3.16}$$

$$F^{(2)} = \left(\frac{3}{4k}\right)[2F_{10} - F_{11} - F_{1-1}] \tag{2.3.17}$$

This equation fully describes the anomalous scattering from charge as well as magnetism within dipole corrections. $F^{(0)}$ is independent of magnetic moment $\boldsymbol{M}$ and is the pure charge scattering not sensitive to the sample magnetization related to resonant enhancement at absorption edge. $F^{(1)}$ is dependent on the difference $[F_{11} - F_{1-1}]$ of the transition matrix elements for left and right polarised light and scalar product of the incident X ray polarisation and magnetisation $\boldsymbol{M}$. The third term is quadratic in $\boldsymbol{M}$ is the origin of the so called X ray magnetic linear dichroism [95]. **This term is usually omitted since its very small in comparison to circular dichroism.**

For simplicity in differentiating charge and magnetic terms, we can rewrite equation(2.3.18) as

$$f^{res} = (\boldsymbol{\epsilon}' \cdot \boldsymbol{\epsilon})F_c - i(\boldsymbol{\epsilon}' \times \boldsymbol{\epsilon}) \cdot \boldsymbol{M}F_m \tag{2.3.19}$$

Where,

$$F_c = -f_0 - f' + if'' \tag{2.3.20}$$

$$F_m = m' + im'' \tag{2.3.21}$$

This expression of the magnetic resonant atomic scattering factor is only valid for an isotropic crystallographic system where the spherical or cubic symmetry is broken only by the magnetic moment.

The isotropic part is described by the triplet (f_0, f', f'') which doesn't change the polarisation of the scattered beam. We have already described term $f_0(q)$ related to Thomson charge scattering and f' and $f''$are the anomalous charge scattering given by $[F_{11} + F_{1-1}]$ and can be separated into two separate processes. First process is related to the excitation of the bound states to unbound continuum states which lead to the step like structure in XAS absorption (absorption edges). This kind of scattering is usually independent of the chemical environment of the atoms and whose tabulated values can be found in []. The second type of process is the dipole selected, bound- bound excitation of the core electrons to the unoccupied states. These are responsible for the characteristic resonances (*white lines*) at resonant edge of an atom. Since it involves excitations from the valence shell, the resonance shape depends on the local environment.

Finally magnetic scattering with terms m', m'' describe the magnetic contribution (XMCD) at resonant edges and are given by $[F_{11} - F_{1-1}]$. It is a part of the bound – bound excitation process with a different polarization dependence.

We omit the third term in equation here since it is considerably smaller than circular dichroism in the second term. In general expression, we also omit $f_{mag}^{non-res}$ since its several order magnitudes smaller than $2p \rightarrow 3d$ circular dichroism.

Thus, f', f'', m', m'' are called the resonant parameters that need to be determined in order to quantify a magnetisation profile. The determination of these parameters will be described in chapter 3 of this thesis.

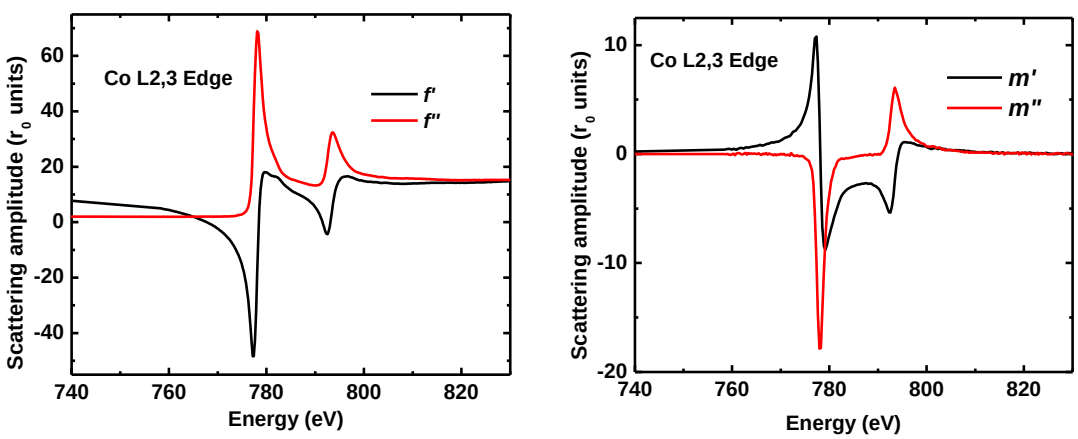

Figure 2.8 Resonant parameters *f', f'', m'* and *m''* near Co absorption threshold deduced from the measurement of absorption by the sum's rules for *m''* and by the transformation of Kramers Kronig for *m'*

2.3.2.2 Asymmetry ratio

Thus, till now we have learnt the expression for atomic scattering factor at resonance whose expression contains both charge and magnetic sensitive parameters. The magnetisation-sensitive effects occur in ferro(ferri)magnets because the intensity contains a product of a magnetic and a nonmagnetic amplitude. This term is obtained by measuring **the asymmetry ratio which is defined as R**,

$$R = \frac{I^+ - I^-}{I^+ + I^-} \qquad (2.3.22)$$

Where I^+ and I^- are reflected intensities are the reflected intensities for positive and negative helicities respectively.

To achieve such results, one measures twice the intensity reflected once with a definite direction of the magnetic moment or, of the photon's polarization, and a second time with one of these moments reversed. There are therefore two ways to calculate the ratio. One is to fix a given polarization and to measure the intensity twice applying a field in two opposite directions and the other one is with a fixed applied field to change the polarization of the incoming photons between the two reflectivity measurements.

2.4 Analytical expressions of XRMS: Kinematical approach

Kinematical approach to XRMS introduces us to a formalism which doesn't take into account several layers' multiple reflections and transmissions that can be as well as the roughness of the interfaces. It is based on the reflected intensity from one layer thus in principle, it doesn't allow derivation of a magnetic profile as a function of depth, although it enables the sensitivity to orientation of magnetisation as well as the experimental configurations. Thus, through this formalism, we are able to express the reflected intensity in terms of magnetisation components of m_{pol}, m_{tran} and m_{lon} (Figure 2.9) that correspond to the transverse, longitudinal and polar components from the polarisation and the angle θ.
We have understood by now that resonant atomic scattering factor depends on polarization of incident and reflected beam. Thus, one way to express reflected intensity as a function of polarisation is to express atomic scattering factor in a linear and circular basis. Following the work of Brunnel and De Bergevin [96] Hill and McMorrow in their paper formulated scattering factor in linear basis $(\boldsymbol{\sigma}, \boldsymbol{\pi})$ [97].

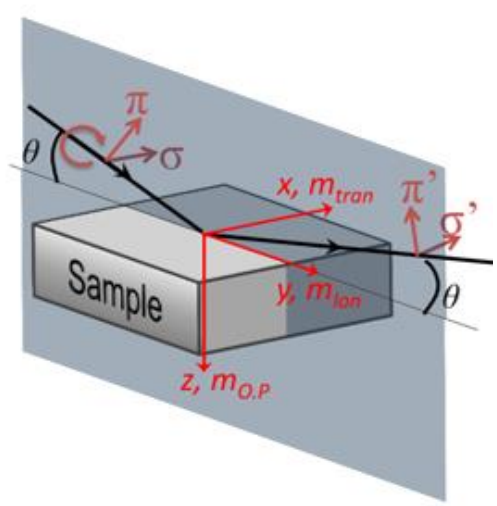

Figure 2.9 Sensitivity to components of magnetisation

$$\hat{f}^{res} = F_c \begin{pmatrix} 1 & 0 \\ 0 & \cos(2\theta) \end{pmatrix} - i\varepsilon F_m \begin{pmatrix} 0 & m_{lon}\cos\theta + m_{pol}\sin\theta \\ -m_{lon}\cos\theta + m_{pol}\sin\theta & -m_{trans}\sin 2\theta \end{pmatrix} \quad (2.4.1)$$

This is the matrix form for resonant scattering amplitude. As defined before, **here $\boldsymbol{\varepsilon} = \pm\mathbf{1}$ is the sign for reversing magnetisation**. From this expression we can express reflected intensity as a function of polarization of the incident beam, $\boldsymbol{\epsilon}$.

$$\begin{aligned} I &= I_{\sigma'} + I_{\pi'} \\ &\approx \left|\sum_n e^{i\boldsymbol{Q}\boldsymbol{r}_n}\right|^2 \left(\left[f_{\sigma'}^{res}\right]^2 + \left[f_{\pi'}^{res}\right]^2\right) \\ &= \left[f_{\sigma'}^{res}\right]^2 + \left[f_{\pi'}^{res}\right]^2 \end{aligned} \quad (2.4.2)$$

We can express the incident polarization as a combination of linear polarizations π and σ as e_σ and e_π. We take into account the phase shift by a complex part, thus the incident polarization vector can be written as

$$\boldsymbol{\epsilon} = \begin{pmatrix} e_\sigma \\ i\delta e_\pi \end{pmatrix} \quad (2.4.3)$$

Here, δ = ±1 which allows to consider + or – phase. We can develop expression for intensity I, as a function of components of magnetization, its sign (ε), angle θ, and polarization of incident beam,

$$I = \left[f_{\sigma'}^{res}\right]^2 + \left[f_{\pi'}^{res}\right]^2 \quad (2.4.4)$$

$$I = \left[\epsilon_\sigma f_{\sigma,\sigma'} + i\delta\epsilon_\pi f_{\pi,\sigma'}\right]^2 + \left[\epsilon_\sigma f_{\sigma,\pi'} + i\delta\epsilon_\pi f_{\pi,\pi'}\right]^2 \quad (2.4.5)$$

Putting,

$$\boldsymbol{F_c} = \boldsymbol{f_1} + \boldsymbol{f_2} \quad (2.4.6)$$

$$\boldsymbol{F_m} = \boldsymbol{m_1} + \boldsymbol{m_2} \quad (2.4.7)$$

Where f_1, f_2, m_1 and f_2 are the resonant parameters (used in experimental chapters), we arrive at the expression for I

$$
\begin{aligned}
I = \left(e_\sigma + e_\pi cos^2(2\theta)\right)|F_c|^2 \\
&+ \left[(e_\sigma + e_\pi)\left({m_{lon}}^2 cos^2(\theta) + {m_{pol}}^2 sin^2(\theta)\right) + (e_\sigma - e_\pi) m_{lon} m_{pol}\, sin(2\theta)\right. \\
&\left. + {m_{tran}}^2\, sin^2(2\theta) e_\pi\right] |F_m|^2 \\
&+ \delta 4\sqrt{e_\sigma e_\pi}\left(-m_{lon} cos^3(\theta) + m_{pol} sin^3(\theta)\right)(f_1 m_1 + f_2 m_2) \\
&+ \varepsilon e_\pi m_{tran} sin(4\theta)\,(f_2 m_1 - f_1 m_2)
\end{aligned}
\tag{2.4.8}
$$

This is the expression for intensity taking into account the incident linear polarized light and the interaction with components of magnetization. Here if we replace ε, δ, e_σ and e_π, we can calculate this expression to calculate different asymmetries.

2.4.1 Calculating the asymmetry for different components of magnetism

In order to be sensitive only to the magnetic components, we calculate R, given as

$$R = \frac{Ip - Im}{Ip + Im} \tag{2.4.9}$$

Here, *Ip* and *Im* are the intensities collected by either flipping the field ($\boldsymbol{\varepsilon = \pm 1}$) or by reversing the polarization (δ = ±1). A finite value for R will indicate sensitivity to magnetism.

Using) we can calculate I by putting values values for e_π, e_σ, ε and δ for each configuration and thus calculate R for incident beam linearly (σ , π) or circularly polarized to check the sensitivity to each component of magnetization - m_{lon}, m_{pol} and m_{tran}.

2.4.1.1 *Through, linear σ polarized light* where $e_\sigma = 1, e_\pi = 0, \varepsilon = \pm 1, \delta = 1$

- **Sensitivity to $\boldsymbol{m_{lon}}$** $\rightarrow m_{tran} = 0, m_{pol} = 0,$

$$I = |F_C|^2 \tag{2.4.10}$$
$$\boldsymbol{R = 0}$$

- **Sensitivity to $\boldsymbol{m_{tran}}$** $\rightarrow m_{lon} = 0, m_{pol} = 0$

$$I = |F_C|^2 + cos^2(\theta)|F_M|^2 \tag{2.4.11}$$
$$\boldsymbol{R = 0}$$

- **Sensitivity to $\boldsymbol{m_{pol}}$** $\rightarrow m_{lon} = 0, m_{tran} = 0$

$$I = |F_C|^2 + sin^2(\theta)|F_M|^2 \qquad (2.4.12)$$
$$\boldsymbol{R = 0}$$

This shows us that we don't obtain sensitivity to either of the 3 components with the linear σ polarized light. Thus, no asymmetry ratio means that we can use σ polarized light to calculate structure but not magnetism in the sample.

2.4.1.2 Through Linear π polarized light where $\epsilon_\pi = 1, \epsilon_\sigma = 0, \varepsilon = \pm 1, \delta = 1$

- **Sensitivity to $\boldsymbol{m_{lon}}$** $\rightarrow m_{tran} = 0, m_{pol} = 0$

$$I = cos^2(2\theta)|F_C|^2 + cos^2(\theta)|F_M|^2 \qquad (2.4.13)$$
$$\boldsymbol{R = 0}$$

- **Sensitivity to $\boldsymbol{m_{tran}}$** $\rightarrow m_{lon} = 0, m_{pol} = 0$

$$I = cos^2(2\theta)|F_C|^2 + sin^2(\theta)|F_M|^2 + \varepsilon sin(4\theta)(f_2 m_1 - f_1 m_2) \qquad (2.4.14)$$
$$\boldsymbol{R = \frac{2tan(2\theta)(f_2 m_1 - f_1 m_2)}{|F|^2 + tan^2(2\theta)|M|^2}} \qquad (2.4.15)$$

- **Sensitivity to $\boldsymbol{m_{pol}}$** $\rightarrow m_{lon} = 0, m_{tran} = 0$

$$I = cos^2(2\theta)|F_C|^2 + sin^2(\theta)|M|^2 \qquad (2.4.16)$$
$$\boldsymbol{R = 0}$$

This shows that, we are only sensitive to m_{tran} through the use of linear π polarized light.

Now, we turn to circularly polarized light. **It must be noted that all experiments in this thesis were conducted using circular polarization.**

2.4.1.3 Through the use of Circular polarized light $\rightarrow \epsilon_\pi = 1, \epsilon_\sigma = 1, \varepsilon = 1, \delta = \pm 1$

- **Sensitivity to $\boldsymbol{m_{lon}}$** $\rightarrow m_{tran} = 0, m_{pol} = 0$

$$I = \left(1 + cos^2(2\theta)\right)|F_C|^2 + 2cos^2(\theta)|M|^2 - \varepsilon\delta 4cos^3(\theta)(f_1 m_1 + f_2 m_2) \qquad (2.4.17)$$
$$\boldsymbol{R = \frac{-4cos^3(\theta)\,(f_1 m_1 + f_2 m_2)}{\left(1 + cos^2(2\theta)\right)|F_C|^2 + 2cos^2\theta|M|^2}} \qquad (2.4.18)$$

- Sensitivity to $\boldsymbol{m_{tran}} \rightarrow m_{lon} = 0, m_{pol} = 0$

$$I = \left(1 + cos^2(2\theta)\right)|F_C|^2 + sin^2(2\theta)|M|^2 + \varepsilon sin(4\theta)(f_2 m_1 - f_1 m_2) \quad (2.4.19)$$

$$\boldsymbol{R} = \frac{\mathbf{sin}(\boldsymbol{4\theta})\,(f_2 m_1 - f_1 m_2)}{\left(\mathbf{1} + \boldsymbol{cos^2}(\mathbf{2}\boldsymbol{\theta})\right)|F_C|^{\mathbf{2}} + \boldsymbol{sin^2}(\mathbf{2}\boldsymbol{\theta})|\boldsymbol{M}|^{\mathbf{2}}} \quad (2.4.20)$$

- **Sensitivity to $\boldsymbol{m_{pol}} \rightarrow m_{lon} = 0, m_{tran} = 0$**

$$I = \left(1 + cos^2(2\theta)\right)|F_C|^2 + 2sin^2(\theta)|F_m|^2 - \varepsilon\delta 4sin^3(\theta)(f_1 m_1 + f_2 m_2) \quad (2.4.21)$$

$$\boldsymbol{R} = \frac{-\mathbf{4sin^3}(\boldsymbol{\theta})\,(f_1 m_1 + f_2 m_2)}{\left(\mathbf{1} + \boldsymbol{cos^2}(\mathbf{2}\boldsymbol{\theta})\right)|F_C|^{\mathbf{2}} + \mathbf{2}\boldsymbol{sin^2\theta}|F_m|^{\mathbf{2}}} \quad (2.4.22)$$

Thus, if we apply circular polarized light, we arrive at an expression of asymmetry ratio for all 3 components of magnetism. However, this only makes it possible to be sensitive only to the components ***longitudinal*** *(m_{lon})* and ***out-of-plane magnetization*** *(m_{pol})* since if the magnetism of transverse component cannot be probed by circular polarization.

If we observe asymmetry signal is located rather at small angles then the magnetization is longitudinal due to dependence on $\mathbf{cos^3}(\boldsymbol{\theta})$ from the expression of ml_{on}.

If we get while if the asymmetry signal is strong at large angles, the magnetization has an *out-of-plane* component due to dependence on $\mathbf{sin^3}(\boldsymbol{\theta})$ from the expression of asymmetry.

If the asymmetry is zero, it does not mean that the sample is not magnetic, only that there is no magnetic component in the diffraction plane.

All the configurations with linear σ, linear π and circular light have been summarized below in the table below.

Table 1 Summary of sensitivity to 3 components of magnetization with linear or circular polarized light

	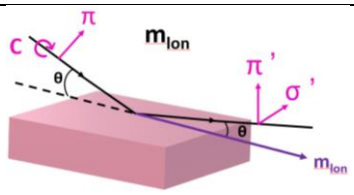 $m_{pol} = 0, m_{tran} = 0$	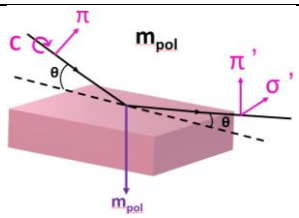 $m_{lon} = 0, m_{tran} = 0$	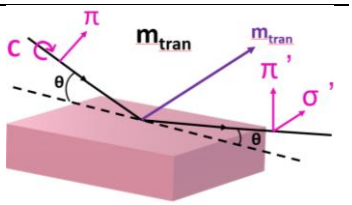 $m_{lon} = 0, m_{pol} = 0$
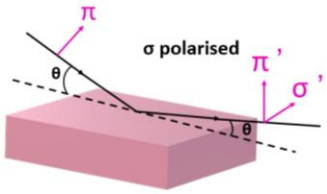 $\epsilon_\pi = 0$, $\epsilon_\sigma = 1$, $\varepsilon = \pm 1$ and $\delta = 1$			
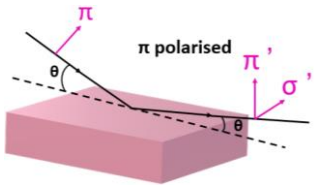 $\epsilon_\pi = 1$, $\epsilon_\sigma = 1$, $\varepsilon = 1$ and $\delta = \pm 1$			
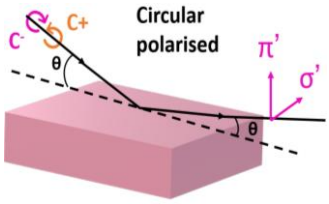 $\epsilon_\pi = 1$, $\epsilon_\sigma = 1$, $\varepsilon = 1$ and $\delta = \pm 1$			

Till now, we have discussed how sensitivity to each component of magnetization arises by the use of different polarizations. However, the magnetization component can also rotate in a plane, in which they maybe be described by resolving the magnetization vector in 2 components.

A. <u>Rotation in M_{yz} *plane*</u>

When the magnetization also has a tendency to rotate in yz plane we will see, by using which configuration of polarization we can be sensitive to the magnetization vector. Since it is tedious to calculate it, we will just summarize them below.

Using **Linear σ polarization** or **Linear π polarization,** we are not able to achieve any sensitivity to such rotation however with **circular polarized light** we obtain the expression **for R** as,

$$= \frac{4\left(-m_{lon}cos^3(\theta) + m_{pol}sin^3(\theta)\right)(f_1m_1 + f_2m_2)}{(1 + cos^2(2\theta)|F_C|^2 + \left[2\left({m_{lon}}^2cos^2(\theta) + {m_{pol}}^2sin^2(\theta)\right)\right]|F_m|^2} \quad (2.4.23)$$

Where, we can collect intensity to calculate ratio either by changing field or by changing helicity. They are equivalent. Such a rotation of magnetization in yz plane was investigated in our thesis (given in Annex).

B. Rotation in $\mathbf{M}_{xy}$ *plane*

In this case, we do not obtain any sensitivity using linear σ polarized light, however both π polarized and circular polarized make us sensitive to this magnetization vector with different ratios for flipping field or flipping helicity.

Conclusion: These expressions of the energy dependence of magnetic asymmetry at different angular position are not suitable to calculate the full angular dependence of the X-ray reflectivity and hence the angular dependence of the magnetic asymmetry since they do not take into account multiple reflections phenomenon in a stratified media nor the roughness of the interfaces. For a complete analysis of the XRMR data it is necessary to use 4x4 matrix formalism briefly presented in the next section.

Thus, these expressions using kinematic approach will enable us to be able to comment from the shape of the magnetic asymmetries **if the sample presents a net magnetization and what are the components of the magnetization: longitudinal, transverse, or polar (OP).** This way of being able to understand data, is also sometimes called ***qualitative analysis*** which have used in this thesis.

2.5 X ray resonant magnetic Reflectivity

Thus, X ray resonant magnetic reflectivity can be expressed as a technique that combines nondestructive depth profiling potential of X ray reflectometry with excellent sensitivity for magnetic phenomenon using the1 XMCD. Momentum transfer and scattering provide structural information while XMCD provides magnetic information of the chosen element with high accuracy [75–77,98,99].

Within the framework of this thesis, we are interested in studying thin film stacks which can be considered as a succession of continuous media having different densities and therefore interfaces. In order to study thickness of layers as well as quality of interface, we wish to study the oscillations that are generated by constructive interference of X rays that is reflected by each layer where the dimensions are greater than interatomic distances.

2.5.1 Refractive index

Since X rays are electromagnetic waves, it is essential that we consider some sort of refraction phenomenon that can occur at interfaces between media. In order to understand such phenomenon, each

media is given its own refractive index, n. Macroscopic optical properties of a material are described in terms of n. Refractive index of vacuum is 1, by definition. For visible light in glass, refractive index is known to lie between 1.5 to 1.8. However, for X rays, the refractive index is known to be very small, usually close to 1. In general, X rays the refractive index can be expressed as:

$$n = 1 - \delta + i\beta \tag{2.5.1}$$

Where δ and β are called optical constants. δ is related to the dispersion within the medium and β is related to the absorption and in conventional X ray regime they lie in the range of 10^{-5} - 10^{-8}.

In the soft X ray range, they can reach up to 10^{-12} values at resonance. In case of hard X ray regime energy of incoming photons lies mostly above resonant edges, δ is seen to be positive that causes n to become smaller than 1. However, in optical regime n is larger than 1 since incoming photon energy is less than any resonant edge.

We understand from the description of atomic form factor that it describes the response of atom to the electromagnetic field. For a material that consists of only 1 kind of homogeneously distributed nonmagnetic atoms, refractive index n with form factor f can be written as [100] :

$$n(\omega) \equiv 1 - \frac{2\pi\rho_a}{k^2} r_0 f(\omega)_{Q=0} = 1 - \frac{2\pi\rho_a}{k^2} r_0 \{f^0_{q=0} + f'(\omega) + if''(\omega)\} \tag{2.5.2}$$

Where scattering amplitude is in the forward scattering direction $\boldsymbol{Q} = 0$. Here $\rho_a = \rho N_A/M$ which is the atomic mass density, N_A is the Avogadro constant, r_0 is the Thomson scattering length and $k = 2\pi/\lambda$. Like the scattering amplitude, refractive index is strongly dependent on energy at resonance. In a non-isotropic system where, optical properties are polarization dependent, δ corresponds to the real part of the scattering amplitude, written as:

$$\delta(\omega) \equiv \frac{2\pi\rho_a}{k^2} r_0 (f^0_{q=0} + f'(\omega)) \tag{2.5.3}$$

And β relates to its imaginary part given as,

$$\beta(\omega) \equiv -\frac{2\pi\rho_a}{k^2} r_0 f''(\omega) \tag{2.5.4}$$

For conventional X rays not at resonance, we can write,

$$n \approx 1 - \delta \approx 1 - \frac{2\pi\rho_a}{k^2} \cdot r_0 f^0 \tag{2.5.5}$$

Since in this case, f' and f'' are negligible. The propagation direction of the X-ray beam in the material is shallower than in vacuum, since n is smaller than unity (the medium is optically less dense than vacuum). This leads to the occurrence of total external reflection for angles smaller than the critical angle. **In this case electromagnetic wave cannot penetrate the second medium and the entire intensity is reflected**. This effect occurs also for soft X-rays, if δ > 0.

Optical theorem connects linear absorption coefficient μ to β as follows:

$$-r_0 \cdot f''(\omega) = \frac{k}{4\pi} \cdot \sigma_a(\omega) \qquad (2.5.6)$$

It states that absorption cross section $\sigma_a(\omega)$ of a scattering process is proportional to imaginary part of scattering length.

2.5.2 Reflectivity

X ray reflectivity is a well-established tool is used find structural compositions of ultra-thin film and multi-layer systems on a nanometer scale specially in hard X ray region. When partial beams reflected in thin films interfere with each other, it gives rise to constructive and destructive interference. This is geometry dependent as we get constructive interference only for wavelength that can fit into the geometry related effective phase difference. This makes reflection measurements as a depth profiling technique.

In simple words, reflectivity is described by the *interference of X-rays* which are reflected at different interfaces. In X ray range, even a small change in n will introduce an interface and thus travelling x ray will be reflected.

In the **specular reflectivity, incident angle is equal to the reflected angle and the scattering vector $\boldsymbol{Q}$** is perpendicular to the surface. Thus, XRMR provides magnetic spatial distribution with a precision down to angstrom scale, sub-monolayer sensitivity and can possibly separate the spin and orbital magnetic moments by changing the angle of circularly polarized incoming light at resonance energies and then measuring the intensity of the specular reflection.

2.5.2.1 Scattering geometry in reflectivity experiments

From above, we understand how reflectivity occurs. **Now, we are motivated to understand the scattering geometry that is used to obtain scans for specular reflectivity.** A beam is incident on the sample at an angle θ and the reflected beam intensity can be measured as a function of θ. z component of the scattering vector Q_z is parallel to the z axis which is perpendicular to the surface is the component of the reciprocal space. This illustrated in Figure 2.10.

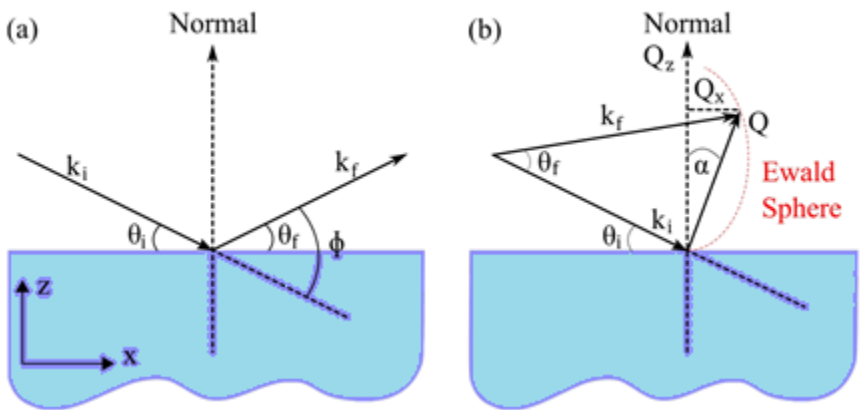

Figure 2.10 scattering geometry used in reflectivity experiments.

k_i is the incident wave vector at an angle θ_i to the sample surface and k_f is the reflected beam after scattering through an angle θ_f. Thus, scattering vector can be written as:

$$\boldsymbol{Q} = \boldsymbol{k_f} - \boldsymbol{k_i} = \frac{4\pi}{\lambda}\sin\theta \qquad (2.5.7)$$

Where λ is the wavelength of the incident beam. For elastic scattering, where there is no change in energy of incident and reflected beam, the magnitudes of these wave vectors remain the same.

$$|k_i| = |k_f| = |k| = \frac{1}{\lambda} \qquad (2.5.8)$$

The out of plane and in plane components Q_Z and Q_X respectively can be expressed in terms of k_i and k_f. Thus, the transformations are:

$$Q_Z = \frac{2\pi}{\lambda}[\sin(\phi - \theta) + \sin\theta] \qquad (2.5.9)$$

And,

$$Q_X = \frac{2\pi}{\lambda}[\cos(\phi - \theta) - \cos\theta] \qquad (2.5.10)$$

Here $\phi = \theta_f + \theta_i$ and we take $\theta = \theta_i$ and are respectively known as detector and sample angles. $\alpha = \theta - \left(\frac{\phi}{2}\right)$, using this we can write equations (2.5.9) and (2.5.10) in terms of α and ϕ as,

$$Q_Z = \frac{4\pi}{\lambda}[\sin\left(\frac{\phi}{2}\right)\cos\alpha] \qquad (2.5.11)$$

$$Q_X = \frac{4\pi}{\lambda}[\sin\left(\frac{\phi}{2}\right)\sin\alpha] \qquad (2.5.12)$$

These equations have a common factor $\frac{2}{\lambda}[\sin\left(\frac{\phi}{2}\right)$ which only depends on the detector angle and the difference between Q_Z and Q_X depends upon α.

Through these equations, determination of different types of grazing scans specular, **off specular (diffuse)** and **rocking scan (transverse)** are possible.

In the case of specular condition angle of incidence is equal to angle of reflection, which means $\boldsymbol{\theta_i = \theta_f}$ and thus $\alpha = 0$. As a result, Q_X disappears and scattering is only sensitive to the out of plane component.

2.6 Dynamical approach: optical point of view

We have seen that among other techniques to understand structure of layered systems, reflectivity is a technique to characterize properties along the growth axis. Through this technique, we are able to determine properties such as atomic density, thickness and roughness of thin films and multilayers. When we do not take magnetism inside the thin films into consideration, Parratt formalism is applied in order to understand propagation of light of from one medium to another such as from vacuum to inside a material. Reflectivity can be solved by using classical physics considering interaction of X ray with matter as dynamical.

If we include magnetism, in order to study magnetic profile, we tune the energy of the X rays at the resonant edge of the element we are studying. To determine such a profile, based on a classical Maxwell approach that solves the propagation of waves in the media along with a quantum mechanical description for the atomic interactions.

In our technique XRMR, the origin of sensitivity to magnetism based on magneto-optic Kerr effect [101], [84] which is based on rotation of polarization of the optical photon due to the magnetization in transmission as well as reflectivity geometries. Various theories introduced by Mansuripur et al., [102] and Zak et al [103] have been introduced in the past to be able to study propagation of waves in magnetic media originally written for optics (Kerr, Faraday effects) but used just as well in the X-ray range.

Some of the previous PhD students Marta Elzo, Emmanuelle Jal etc., developed a formalism for resonant magnetic reflectivity applied to a stratified magnetic media [104]. This was done by Eigen-waves propagation in the media along with a quantum mechanical description of atomic interaction with a photon. Eigen waves are known as the waves with indices of refraction which do not undergo a change in polarization state while propagating. In our case we will show that eigenvectors are the circular polarization vectors. For this boundary propagation matrices method was used [105]. The theory that has been coded in DYNA in a MATLAB environment.

In order to have a proper understanding, we will briefly explain the developed theory for a general system with the help of Marta [105] and Emmanuelle's [106] thesis following it very fast.

We do this with the steps of boundary propagation method (BPM) by using Eigen waves as propagating waves.

2.6.1 Formalism

For electric field the medium has a linear, tensorial and dispersive response and for magnetizing field the medium has linear and scalar response, the constitutive relations of beam propagation are given by:

$$\boldsymbol{D_i} = \in_{ij} \boldsymbol{E_j} \qquad (2.6.1)$$

$$\boldsymbol{B} = \mu \boldsymbol{H} \tag{2.6.2}$$

Where $\boldsymbol{D}$ is the electric displacement, $\in_{ij}$ is a tensorial dielectric permittivity with $i, j = x, y, z$, which takes into account the process of magnetic resonant X-ray scattering, $\boldsymbol{B}$ the magnetic induction and $\boldsymbol{H}$ the magnetic field. The relation between $\in$ and the scattering factor is:

$$\hat{\chi} = \frac{4\pi}{k_0^2} \sum_a n_a \hat{f}_a \tag{2.6.3}$$

$$\hat{\in} = 1 + \chi \tag{2.6.4}$$

Where n_a is the number of the atom a per unit volume, χ is the dielectric susceptibility and $\hat{f}_a$ is the scattering length. As the wave propagates, the change in the direction and amplitude of the wave vector $k_0 = \frac{2\pi}{\lambda}$ in the vacuum which on propagating through a medium is changed to $\mathbf{k} = (n_x k_{0x}, n_y k_{0y}, n_z k_{0z})$. Here we also define refractive index $\boldsymbol{n}$, which will be given by taking into consideration the Maxwell's equations with constitutive equations developed before for a monochromatic plane wave with $\mathbf{k} = \frac{2\pi}{\lambda}\boldsymbol{n}$, leading to:

$$\nabla \times \mathbf{E} = -\frac{\partial \mathbf{B}}{\partial t} \tag{2.6.5}$$

$$\nabla \times \mathbf{B} = \hat{\epsilon}\mu \frac{\partial \mathbf{E}}{\partial t} \tag{2.6.6}$$

$$\mathbf{n} \times (\mathbf{n} \times \mathbf{E}) + \hat{\in}\, \mathbf{E} = 0 \tag{2.6.7}$$

The solution of equation will lead to 2 indices of refraction corresponding to two Eigen waves with with p_1 and p_1 polarizations. This can be rewritten as,

$$\mathbf{D} = \mathbf{n} \times (\mathbf{E} \times \mathbf{n}) \tag{2.6.8}$$

Which gives an expression of $\mathbf{D}$ equivalent to photon polarization of the propagating wave in the medium. We apply boundary conditions using the conservation of planar fields electric field $\mathbf{E}$ and magnetizing field $\mathbf{H}$ at interfaces once we know $\mathbf{D}_{p1}$ and $\mathbf{D}_{p2}$ as eigen waves, giving us:

$$\mathbf{E} = \hat{\in}^{-1}\mathbf{D} \tag{2.6.9}$$

$$\mathbf{H} = \mathbf{n} \times \mathbf{E} = \mathbf{n} \times (\hat{\in}^{-1}\, \boldsymbol{D}) \tag{2.6.10}$$

We introduce a matrix called $\hat{A}_m$ whose job is mathematical. It projects $\mathbf{D}_m$ of the eigenwaves amplitudes into x and y planar components

$$A_m D_m = \begin{pmatrix} (\hat{\epsilon}_m^{-1})_x \\ (\hat{\epsilon}_m^{-1})_y \\ (n \times \hat{\epsilon}_m^{-1})_x \\ (n \times \hat{\epsilon}_m^{-1})_y \end{pmatrix} = \begin{pmatrix} E_{x,m} \\ E_{y,m} \\ H_{x,m} \\ H_{y,m} \end{pmatrix} \tag{2.6.11}$$

$\hat{A}_m$ is a 4x4 matrix and there is one for each media. The benefit of using this matrix is one can now use matrix algebra. The condition of continuity at the interface between the media m and $m+1$ is then written:

$$A_m \boldsymbol{D_m} = A_{m+1} \boldsymbol{D_{m+1}} \tag{2.6.12}$$

This permits us to calculate change of polarization of the wave between media m and $m+1$:

$$D_{m+1} = {A_{m+1}}^{-1} A_m D_m \tag{2.6.13}$$

We have just modeled the passage of an electromagnetic wave from one medium to another for a perfect interface.

Now, we consider the propagation of the waves within the medium. When an electromagnetic wave propagates through the medium, it is attenuated and its phase ϕ is modified. This modification depends on refractive index of the medium $n_m^{\pm}$, angle of incidence θ along with the depth at which wave is found, z. Thus, we need to apply the pseudo vector Dm by following propagation matrix to know the amplitudes of electromagnetic waves when they are at a thickness z within the medium.

$$P_m(z) = \begin{pmatrix} e^{\frac{2\pi}{\lambda} n^{+\downarrow} \sin\theta_z} & 0 & 0 & 0 \\ 0 & e^{\frac{2\pi}{\lambda} n^{-\downarrow} \sin\theta_z} & 0 & 0 \\ 0 & 0 & e^{\frac{2\pi}{\lambda} n^{+\uparrow} \sin\theta_z} & 0 \\ 0 & 0 & 0 & e^{\frac{2\pi}{\lambda} n^{-\uparrow} \sin\theta_z} \end{pmatrix} \tag{2.6.14}$$

Finally, in case of a multilayer, one multiplies the matrices corresponding to the boundary conditions at each interface with the matrices corresponding to the propagation in each layer (Figure 2.11). **The polarization state in the final layer is:**

$$D_f = A_f^{-1} \left(\prod_m A_m P_m A_m^{-1} \right) A_0 D_i = M D_i \tag{2.6.15}$$

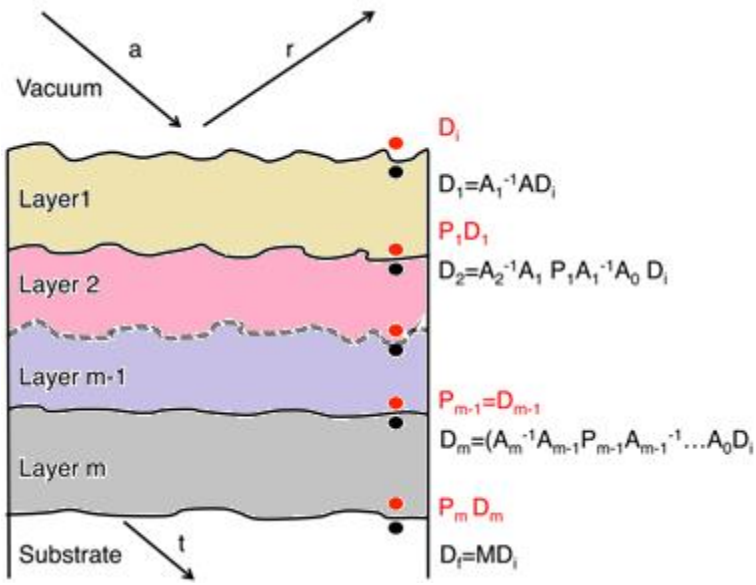

Figure 2.11 Schematic diagram indicating the reflectivity process. Here, $D_i = E_i$ is polarization state of the electromagnetic field in the vacuum, $A_m^{-1}A_{m-1}$ relates the polarization states on both sides of an interface. Pm propagates the wave between the two interfaces of the *m*th layer

The matrix M is a 4x4 matrix relating incoming and outgoing waves with the polarization states in the vacuum. We solve the system by conditions that the two amplitudes of the incident eigenwave states are known, and the two amplitudes of the states coming upward from the last layer are zero:

$$D_i = M^{-1}D_f \qquad (2.6.16)$$

Roughness, is taken into account with a Debye-Waller treatment where the assumption is that the roughness is stationary, the roughness σ is not dependent of the point under consideration. At the interface of *m - 1* layer with m layer, the matrix element $A_m^{-1}A_{m-1}$ must be multiplied by $e^{\pm} = e^{-(k_m \pm k_{m+1})^{2\sigma^2/2}}$, where ± stands for the matrix element that relies waves with the same or different direction of propagation.

Thus, the formalism that has been presented can be used for whatever orientation of the magnetism with respect to the polarisation of the incident beam, but only samples with different media are homogeneous and where the spin-orbit coupling electrons 3d can be neglected because of a very great symmetry (spherical or cubic) or the phenomenon of "quenching". In this thesis, the refinement carried out by using this formalism will be discussed as ***quantitative analysis.***

2.7 Other techniques for investigating magnetic profilometry

Apart from the technique of X ray resonant magnetic scattering, synchrotron radiation has given birth to various other techniques in order to study the magnetic properties.

2.7.1 Depth dependent XMCD

XMCD is a technique that we described extensively in the previous section, where total electron yield is often used to investigate surface/interface magnetic moments. It is capable to detect escape depth of secondary and auger electrons ranging between 2–5 nm from the surface and along with the elemental sensitivity makes it very attractive for study of magnetic properties. However, it lacks sensitivity to investigate magnetic moments in a real surface/interface region surface/interface.
An alternative technique known as depth resolved XMCD has been developed where, unlike the conventional setups electrons are collected by the use of detection angle dependence of their effective escape depth thus electrons emitted at different angles are collected separately. Since electrons have finite elastic mean free path λ_e in solids, probability of inelastic electrons at depth z escaping into the volume is proportional to $\exp\left[-z/\lambda_e \sin\theta_d\right]$ where θ_d is the angle between emission direction and surface of the sample. Thus, detection of electrons as a function of detection angle yields depth dependent XAS and XMCD spectra. It has proved to be a powerful tool to investigate magnetism in surface and inner layers separately in a FM film [55,107].

2.7.2 Polarized neutron reflectivity

Polarised neutron reflectivity has the ability to directly probe atomic magnetic moments and provide information about the *in plane* magnetic moment in absolute units. However, this technique is not element specific and also has limited spatial resolution due to low incoming neutron beam flux. In the case of magnetic heterostructures, PNR can detect local variations in magnetic moment and PNR spectra can be described by model magnetisation profiles [108].
Ultra-thin films can pose situations with broken symmetry at interfaces, finite size effects as well as asymmetric termination of the layer stacks having different layers at top and bottom which can play an important role in these structures. In comparison to SXRMR, one of the major differences is we have higher resolution in case of SXRMR (0.5-1nm in SXRMR and 2-3 nm for PNR). Also, in SXRMR we have sensitivity in all directions but not the same can be said for PNR where, we are limited to direction in the plane of the surface of the sample.

2.7.3 Nuclear resonant scattering

It is an atomistic spectroscopy technique based on Mossbauer effect making it possible to probe the direction of the magnetization within the sample in a vertically resolved manner with the use of inserting isotopes at different positions within the film. The resolution of this technique, however, this technique is limited to only a few materials (mostly Fe and Co) [109].

2.8 Conclusion

In this chapter, we understood the interaction of X rays with matter and obtained the expression for atomic scattering factor at resonance, which aids us in developing the case of resonant magnetic reflectivity. Through be sensitive to the charge magnetic interference, we introduced the expression for asymmetry ratio and established if we can be sensitive different components of magnetization through different polarizations. We also introduced the dynamical approach where take into account roughness as well as multiple reflections in a thin film system. Most important we calculated the full expression of atomic scattering factor at resonance and introduced resonant parameters. In the next chapter we will discuss how to retrieve these resonant parameters and refine measured data using dynamical approach in DYNA (defined previously)

3 EXPERIMENTAL TECHNIQUES AND DATA COLLECTION

Till now we discussed why we are motivated to work on ultrathin films, especially with perpendicular magnetic anisotropy and how having a good knowledge on interfacial magnetism is essential for systems with PMA. In chapter 2, we studied that resonant soft X ray magnetic reflectivity is a technique that is based on understanding the magnetic profile of a specific element in the sample. It can be simply described as XMCD at a scattering condition. Thus, through this technique we are able to resolve the contribution of magnetic moment of a specific element throughout the thickness of layer along growth axis.

This chapter describes how the experiment was conducted at synchrotron radiation center, followed by the way data analysis was done. We then present the experimental approach of the resonant magnetic scattering of soft X-rays, from the different modes of acquisition to keys aspects of the quantitative analysis. We finally introduce other complementary methods used in the laboratory such as SQUID and the extraordinary hall effect for magnetic characterization.

3.1 Synchrotron radiation center:

Since its first observation at general electric particle accelerator, USA [110], synchrotron radiation has become a pioneer in experimental physics for its utilization in various characterization techniques due to its ability to provide unique properties such to their high brilliance, collimations, broad energy spectrum as well as coherence power. Synchrotron radiation sources produce 10^{12} times higher brilliance than laboratory-based sources with the help of insertion devices.

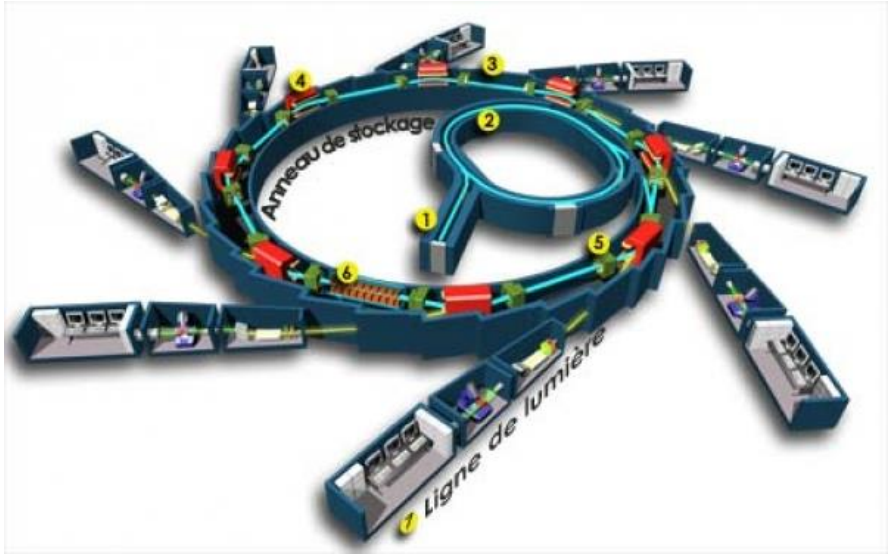

Figure 3.1 A schematic diagram of a third-generation synchrotron radiation centre. (Image taken from website of SOLEIL)

A synchrotron radiation is generated by charged particles travelling at relativistic speeds, manipulated by applied magnetic fields which force them to travel along curved paths. Figure 3.1 illustrates various elements involved in the production and use of synchrotron radiation.

(1) Electrons are produced by thermionic emission from a hot filament (electric gun) which serves as a source after which electrons are accelerated by either a microton or linear accelerator to several hundred MeV of energy. (2) Following that, electrons are transferred into booster ring which is a circular accelerator where their energy is boosted to reach main storage ring energy (2.75 GeV at SOLEIL). (3) After that, electrons are periodically injected into the storage ring. (4) In a storage ring, it is electrons and positrons that are kept circulating at constant energy where the electrons move at a relativistic speed and kinetic energies of order GeV. The ring structure consists of both bending magnets and straight sections that are composed of insertion devices such as undulators and wigglers used to produce intense **synchrotron radiation**. (5) The energy lost by the electrons in emitting the synchrotron radiation is compensated for by radiofrequency cavities. (6) The synchrotron radiation is diverted by optic systems in experimental stations called **beamlines** where (7) each beamline is a specialized laboratory, equipped to prepare and analyze samples to be studied and to process the information gathered.

Figure 3.2 shows the components of a typical experimental station, where with the help of insertion devices, the beam is directed into the beamline. Monochromator plays an important role to tune energy of radiation emitted wiggler or undulators for experiment. After, through the help of beamline optics using X ray mirrors and refractive Fresnel lenses the size of the monochromatic beam can be modified and thus can be focused on small sized samples. Thus, finally X rays are delivered to the sample on which after experiment can be performed.

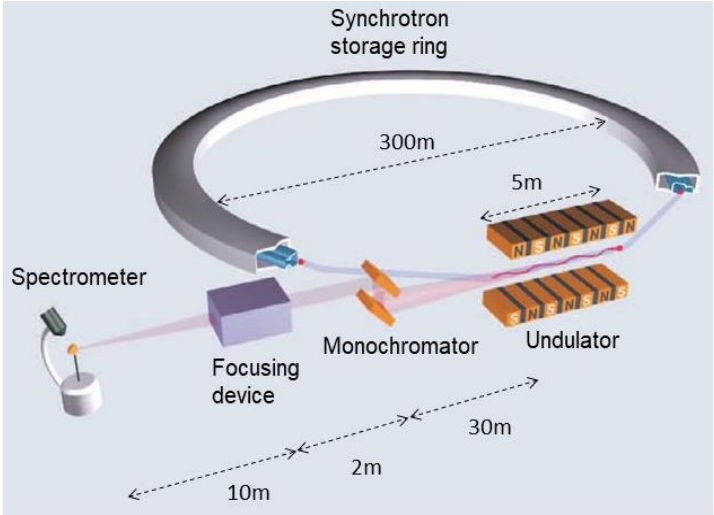

Figure 3.2 Schematic diagram of a typical X ray beamline at a third-generation light source. The distances are indicated (figure taken from [100])

In order to increase the intensity of the synchrotron beam, its energy resolution, and the control of its polarization, we use insertion elements such as **undulators**. These are periodic magnetic structures where the electrons have a forced oscillating path in the plane as shown in Figure *3.3*. The emissions of a radiation at each change of direction are coherently superimposed, which gives a very large flux of photons. The spacing and the position that are relative to each other for the 2 magnets makes it possible to not only modulate the energy but to polarize the produced X-rays [111]. Thus, thanks to these undulators it is then possible to pass from one polarization to another such as σ, π and C^+, C^-. These insertion elements are placed between two bending magnets as shown in Figure *3.3*.

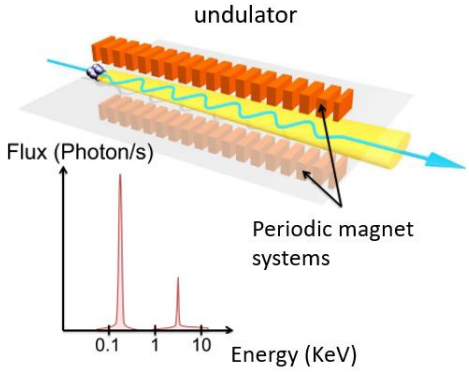

Figure 3.3 Diagram of an undulator, with its energy spectrum (Figure adapted from [106])

3.2 SEXTANTS

The measurements presented in the manuscript have been conducted at SEXTANTS beamline situated in synchrotron Soleil, Saint Aubin, France. It is a beamline dedicated to soft X ray scattering techniques covering an energy range of 50 – 1700 eV. Main scientific purpose of this beamline is investigation of

electronic and magnetic properties using elastic, inelastic, magnetic and coherent resonant X ray scattering based on element selective photon in photon out mechanism providing magnetic sensitivity.

Figure *3.4* shows a schematic diagram of the SEXTANTS beamline with the positions of working station and optical elements. The monochromator after the hutch has 5 gratings (G1-5) which enables in selection of energy of desired network according to desired power and resolution and the rotation of this network leads to the selection of energy we desire. Along with this the beamline consists of several mirrors to focus and refocus in and three main stations to perform experiments on – (A) AERHA for resonant inelastic scattering, (B) IRMA for elastic scattering and holography experiments and (C) RESOXS for elastic scattering in a reflectometer (as marked in a red circle). More details on optics of the beamline is given by M Sacchi, *et al* [112]. The beamline provides a beam with resolution of $\Delta \boldsymbol{E} > \mathbf{10^4}$, beam size sample on the sample ≈ 200 µm^{2}and polarization states **linear (vertical and horizontal),** and **circular (left and right)**.

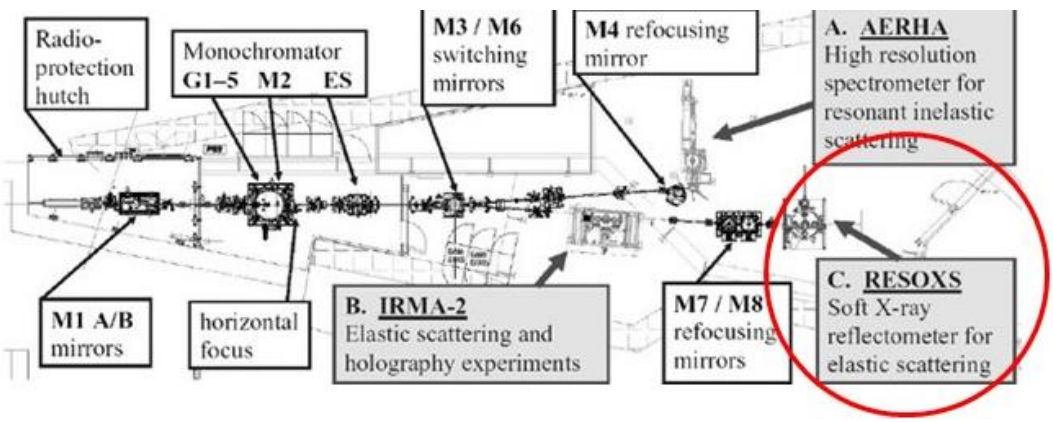

Figure 3.4 Layout of SEXTANTS beamline with main optical elements and three working stations denoted by A, B and C. RESOXS has been marked in red color where we conducted experiments in this thesis (figure taken from [112])

Although SEXTANTS beamline consists of various experimental set ups, we conducted our experiments in RESOXS chamber, which will be described in the following text.

3.3 RESOX and its properties

After one of the very first devices dedicated to soft X ray scattering experiments appeared in 1988 [113], development and improvement of their capabilities such as angular range, acquisition geometry, sample environment such as temperature, magnetic field etc. have continued to increase. In this thesis, we conducted soft X ray scattering experiments inside RESOXS shown in *Figure 3.5*, a **large volume diffractometer** designed to work **under high vacuum**, **low temperature** and **a reasonably high magnetic field** was developed by Nicholas Jaouen , Jean-Marc Tonnerre *et al*, [114].

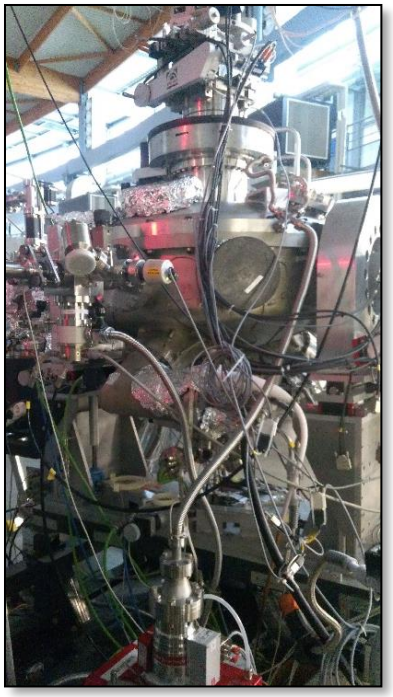

Figure 3.5 Photo of the RESOXS set up at SEXTANTS beamline.

In experiment at RESOXS, reflectivity experiments are realised by incident beam directed at a certain angle onto the sample surface followed by measurement of intensity of reflected beam. This beam is collected at the detector. The direction of the beam is fixed and it is the sample and detector which are installed on coaxial stages. The intensity is collected **for a chosen energy** and **polarisation** with the possibility of **applying a magnetic field**. Depending on the experiment requirement, it is also possible to change the temperature of the sample inside the chamber. Also, to make sure that the beam arrives at the centre of the sample, we need to align the sample with the different axes. The experiment inside the diffractometer is performed by rotating the sample on itself (relative to the perpendicular axis to the diffraction plane) and rotation of detector relative to the sample, called ϑ and 2ϑ. The schematic diagram of experimental set up is shown in Figure *3.6*.

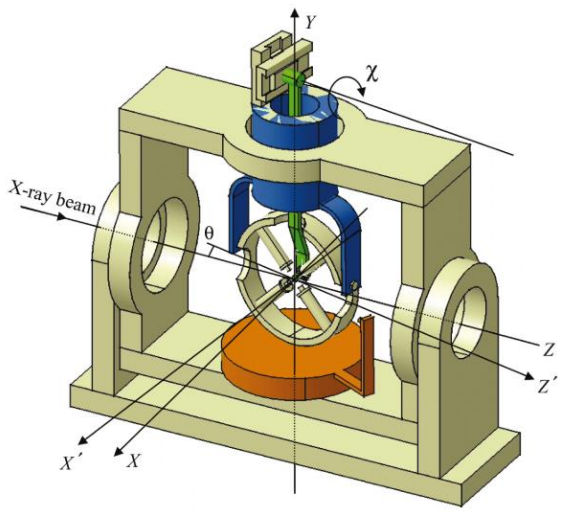

Figure 3.6 Sketch showing sample environments with incoming X ray beam and the magnetic set up on the sample. (figure taken from [114])

RESOXS set up

The RESOXS set up consists of a **chamber** with an upper and a lower flange having ϑ and 2ϑ assembly respectively where the axis of ϑ and 2ϑ are placed oppositely, on the upper and lower parts respectively. **Upper flange contains the sample manipulator, cryostat magnet system holder, all axes motion bellow, and various other parts.** This bellow allows the χ rotation and *the three translation motion axes* within a limited range as shown in Figure *3.7*. The **lower flange** is connected to the lower half of the vessel and consists of a **2θ crown and detector cables and also contains vacuum pumps, feedthroughs and main pumps**. The detector that is used in the chamber is a silicon photodiode which has a sensitive area and a silicon diode current.

When the sample is places inside the chamber, it is connected to various motors which allow rotation χ, vertical translation *ty*, horizontal translation along the beam *tz* and horizontal translation perpendicular to the beam *tx*. These motors as shown in Figure *3.7* allow movement of sample by angle θ.

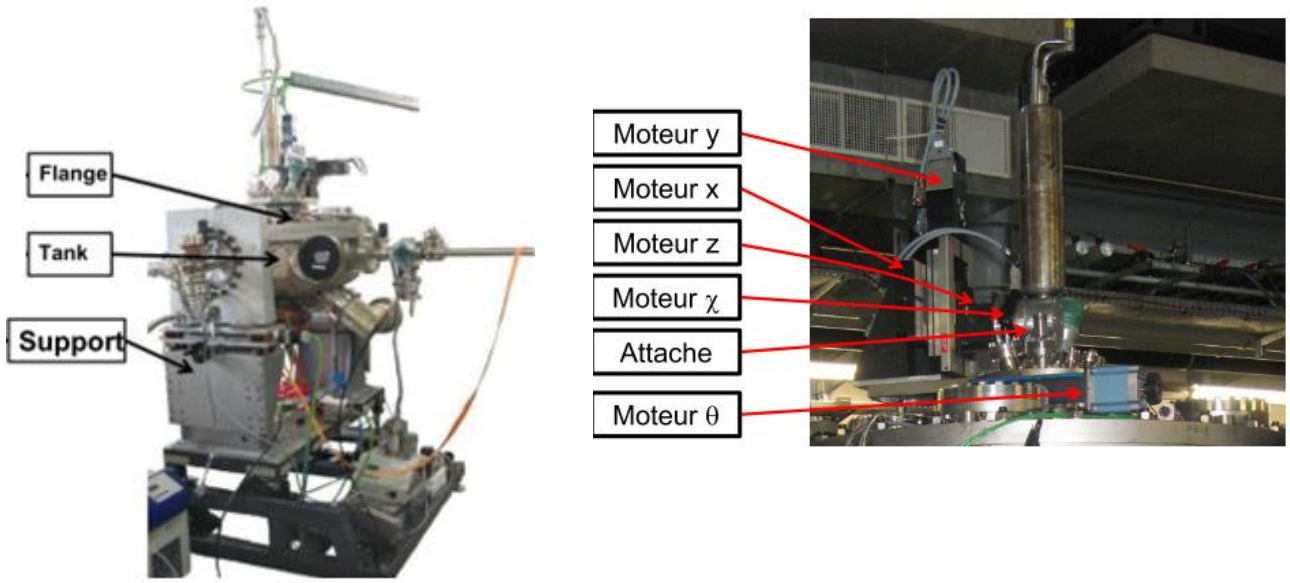

Figure 3.7 RESOXS chamber set up showing the flange, tank and support on the left hand side. View of motors that move and hold whole sample block on the right hand side.

3.3.1 Measurements at RESOX

Magnetic field – We need to apply an external magnetic field in order to orient the magnetisation of the sample with respect to the polarisation of the photons. Ideally, it would be necessary to be able to apply a field in the three directions – *transverse, longitudinal and polar*, however, at RESOXS we are limited in our options. This is due to the constraints we have concerning maintenance of ultra-high vacuum which means installing number of vacuum pumps around the beamline setup. We also want to measure up to the largest possible angular range whose benefits we will discuss in further text. These constraints make it difficult to set up a system where we can apply magnetic field along all three directions. Currently, at RESOX we are able to apply a field in transverse and longitudinal direction with respect to the sample surface, however a magnetic that can apply an external magnetic field in polar direction in the setup is under development (discussed in detail in Conclusion and perspective).

The magnetic setup at RESOXS consists of an electromagnet in the upper flange of the RESOXS chamber consisting of two pairs of cylindrical poles made of pure iron. This setting can be used to reverse magnetic field both transverse and longitudinal and also to change the amplitude of the magnetic field to obtain hysteresis curves. It is shown in right hand side of Figure *3.8*.

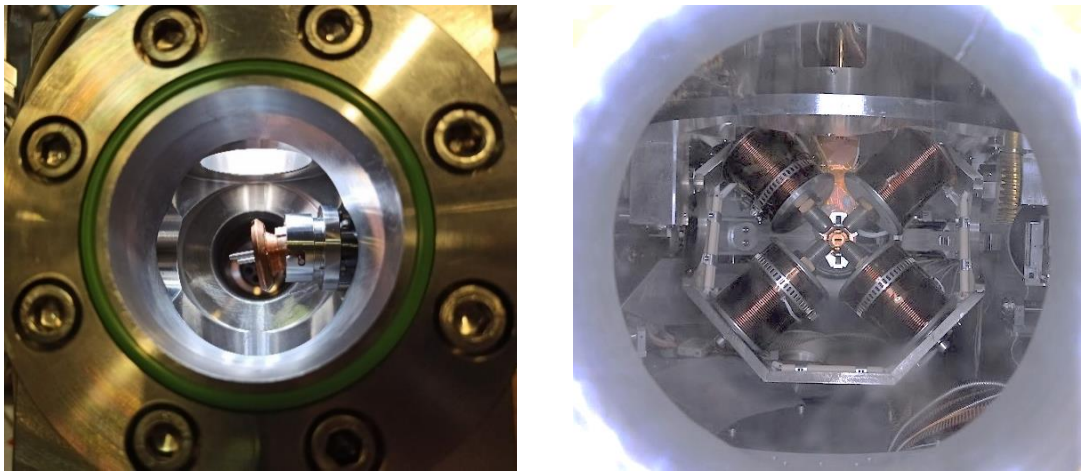

Figure 3.8 View of the sample inside put inside the transfer line in order to transfer it into the chamber using sample manipulator on the left-hand side. On the right-hand side, is a capture of sample inside the chamber from outside. The red lines are the 4 poles of magnet around the sample in order to provide longitudinal magnetic field.

For measurements, the sample is places inside the load lock as shown in Figure 3.8 on the left-hand side. Using the sample manipulator which is a long circular rod, we put the sample inside the chamber as place it as shown in Figure 3.8 on the right-hand side.

Temperature - The study of magnetic properties is also highly dependent on temperature. Magnetic behaviours have been known to change at low temperature infact, a trend of increasing magnetisation is observed as we go to the low temperature. At RESOXS we are able to go access low temperature as low as 30K, and to control the temperature which is necessary to observe magnetic properties that do not exist at ambient temperature. In this thesis too, in Chapter we will discuss results of temperature dependent magnetic profile.

3.4 Data collection at RESOXS

Data collection at RESOXS during an experiment involves several steps as discussed in this section.

3.4.1 Initial photon calibration

An experiment begins by checking the calibration of the photon energy of the beamline. This is done by measuring the absorption edge, usually in transmission through an ultra-thin foil (Figure 3.9) of a reference element (Fe, Co, ...) chosen according to the proximity of one of its absorption edges with that of interest for the element in the sample to be studied. The energy of the photons can then be chosen either at an energy close to the absorption edge or a few tens of eV below to start the alignment of the sample which has been introduced into the RESOXS chamber.

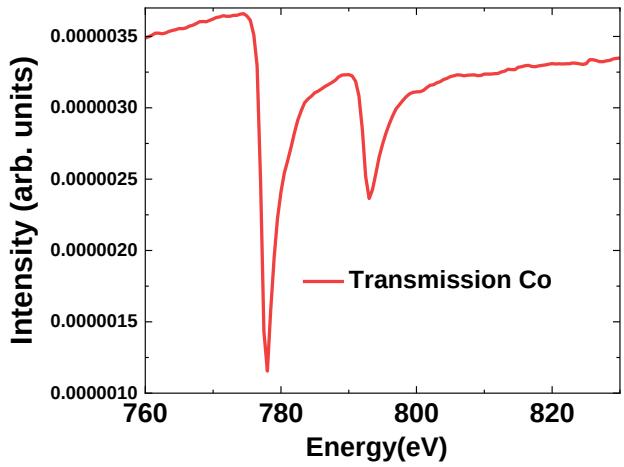

Figure 3.9 Initial scan for caliberation of energy

3.4.2 Alignment of the sample

In a typical specular X-ray reflectivity experiment, the incident beam is impinging the surface of a flat sample at an incident angle θ and the reflected beam is collected by a detector positioned at an angle corresponding to twice the value of the incident angle relative to the direct beam. The aim of the alignment is to get the surface of the flat sample as perpendicular to the diffraction plane as possible and blocking half of the direct beam at $\theta = 0°$. But it is first useful to check the zero position of the detector since the scattering vector $q_z = 4\pi\sin\theta/\lambda$ is defined from the angular position of the detector. Then, the alignment procedure generally requires 5 steps that can be repeated in a loop to optimise the first settings:

- Once positioned on the 5-axes sample manipulator of the goniometer at $\theta = 0$, the sample is translated along the surface normal (t_y) so that the intensity of the direct beam is reduced by a factor 2. The complete recording of the curve from a value close to zero to the value of the maximum intensity of the direct beam (or vice versa) makes it possible to estimate the size of the focused beam at the level of the sample.
- Then a rocking curve θ scan, for a fixed position of the detector, around an angular value corresponding to half that of the detector) is recorded with the detector set at 0°. The θ angle is positioned at the value corresponding to the maximum of intensity and set to 0. This will be the new zero position of the θ rotation (taken into account the sample) improving the parallelism of the sample surface with the direct beam. As this new angular position generally changes the intensity of the direct beam, it is useful to repeat the first step.
- A vertical translation (t_z) scan is used to centre the sample with respect to beam. From a new t_z, the two first step can be repeated.
- The shape of the rocking curve at $\theta = 0°$ gives an indication of the alignment of the sample with respect to the axis of rotation θ. An asymmetrical shape indicates that the position along the direction parallel to the beam (t_x) must be adjusted until a symmetrical rocking curve is obtained.

- The last step is to adjust the tilt of the sample (rotation relative to the x axis) to ensure that the entire beam will reach the detector throughout the angular scan from θ = 0 up to 80°.

For a reflectivity measurement over a large angular range, it is also important as a final step to check that for each pair $\theta/2\theta$ the intensity measured does indeed correspond to the maximum possible intensity. To do this, a series of rocking curves are measured for different positions of the detector between 0 and 160°. If the maximum reflected intensity occurs at a θ position which deviates from the value corresponding to half the angle of the detector, the evolution of the deviation as a function of θ is adjusted (very often by a polynomial of order 3 to correct a deviation increasing from 0 to 0.2° at very large angles) and the polynomial parameters are inserted into the control program of the goniometer to remain at the top of the rocking curve throughout the scan.

3.4.3 Types of scans

Basically, three main scan parameters determine the measurements, the angular position of sample and detector, θ and 2θ, respectively, the incident photon energy, E, and the applied magnetic field on the sample, **H**.

- In an **angular scan**, the sample and the detector are scanned and the reflected intensity is measured as a function of the incident angle which is equal to the exit angle in the specular condition.
- In an **energy scan**, the sample and the detector are positioned at a couple of values (θ,2θ) and the reflected intensity is measured as a function of E over a range covering the L2,3 edge for a 3d element and the M4,5 edge for a rare earth. For both types of scans, it is possible to flip an applied magnetic field for each data point.
- In a **magnetic field scan**, mainly dedicated to the recording of hysteresis loops for a specific magnetic element, the energy of the photons and the couple of value (θ,2θ) are chosen in order to benefit from a significant magnetic contrast.

In the following sections, we will introduce motivations for each scan with figures.
For the measurements presented in this thesis, the intensity has not been normalized by the incident intensity (I0) for the following two reasons. On the one hand, the measurement of I0 must be of very good quality so that the normalization does not affect the reflectivity signal and, in particular in the soft X-ray regime, this requires a measurement using too many photons, especially if one wishes to measure the reflectivity curves at wide angles (or over a large scattering vector domain) where the intensity could be very close to the minimum value measurable by the detection chain (2-5 10^{-13} amps in RESOXS). On the other hand, the top-up mode at the SOLEIL ensures great stability of the incident beam.

3.4.3.1 Off resonant angular scans

Once the alignment is complete, **a first angular scan is recorded at an energy of photons sufficiently below the absorption threshold (off-resonance scan as shown in** Figure *3.10*) for two reasons. First, it will allow us to select specific angular positions. Second such a scan will be useful for the **determination**

of the structural parameters since the refinement can be carry out by considering that this measurement will not be affected, or only slightly, by eventual mistakes on the corrective terms f' and f'', as well as by their magnetic counterparts m' and m'', or by a small error on the value of the photon energy used for the fit, as off-resonance means very small variations of atomic scattering factor. Thus, it is expected that the determination of the density of the layers (ρ) will more reliable. As the magnitude of the reflectivity by each layer is proportional to $\rho.f$ limiting the errors on f should lead to a more robust density determination.

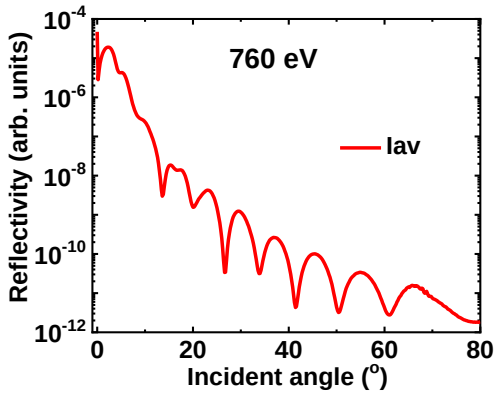

Figure 3.10 Off resonant scan at energy far below from Co L2,3 edge

3.4.3.2 Sensitivity to different components of magnetisation

Until now, the polarisation state of the beam was not important. However, in general, measurements are made with circular polarisation as this is the polarisation state of the X-ray beam most frequently used for XRMR experiments. If the studied system presents a planar and easily orientable magnetization in the diffraction plane m_{lon}, circular polarization will be used. If the system has perpendicular magnetisation m_{pol}, circular polarization will also be used. However, to be sensitive to a planar magnetization component but oriented perpendicularly with respect to the diffraction plane m_{tran}, we will prefer the linear π polarization (lying in the diffraction plane). This was described in chapter 2 for kinematical expressions. Hence, the polarisation state of the beam will be chosen with respect to the magnetization of the sample.

3.4.3.2.1 Acquisition modes

Along with this, at RESOXS chamber, we can collect data at different **acquisition modes** achieved by changing either polarisation of incoming beam or by direction of applied magnetic field. Since in the experimental chapters, we these different acquisition modes during the time of collection of data, it is necessary that they are discussed. It maybe be noted here that we will strictly discuss configurations using circular polarised light since we didn't use any linear polarised light during our experiments.

Depending on the magnetic state of the sample different acquisition mode can be used to reveal the magnetic contribution in the energy and angular scans.

- If the **magnetization is out of plane**, we currently have no possibility to reverse the magnetic configuration of the sample *in situ* during a scan thus measurements are performed at remanence. Therefore, the dichroic effect in the reflectivity curves will be highlighted by measuring a first scan **with right (or left) circular polarization** and then a second with the opposite circular polarization. In fact, to have a mean to check reliability of the observed dichroic effect we generally record four scans following the sequence CR/CL/CL/CR (or the opposite one). Figure 3.11 illustrates the method in the case of an angular scan as well the asymmetry ratio. In accordance with the analytical expressions, we derived from chapter 2, we observe asymmetry ratio at high angles when we are sensitive to *oop component.*

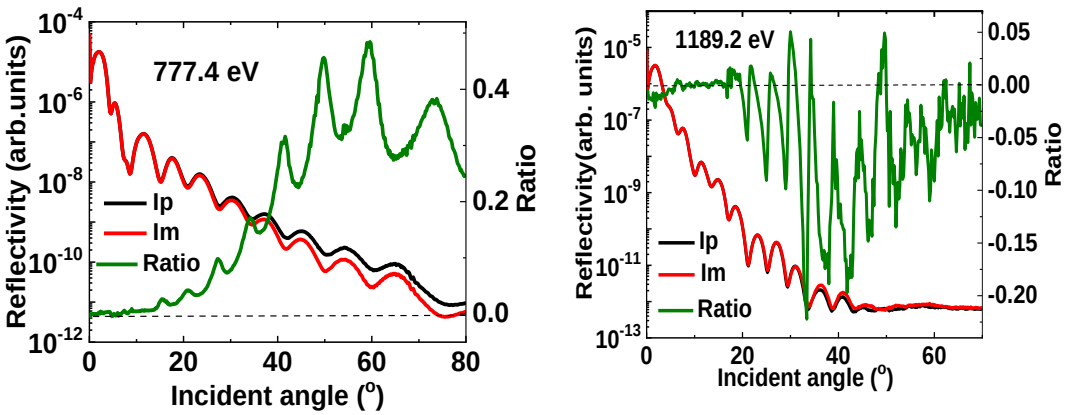

Figure 3.11 Experimental angular dependent reflectivity and their corresponding asymmetry ratio for Co and Gd edge.

To be sure to get a strong *out of plane* sensitivity and hence strong magnetic asymmetry, the magnetization of the sample can also be reversed **by approaching a 0.4T permanent magnet** (Figure 3.12) as close as possible to the surface sample. This provides the amplitude of the field strong enough and that the new magnetic configuration could maintain once the permanent magnet was removed from the RESOXS chamber.

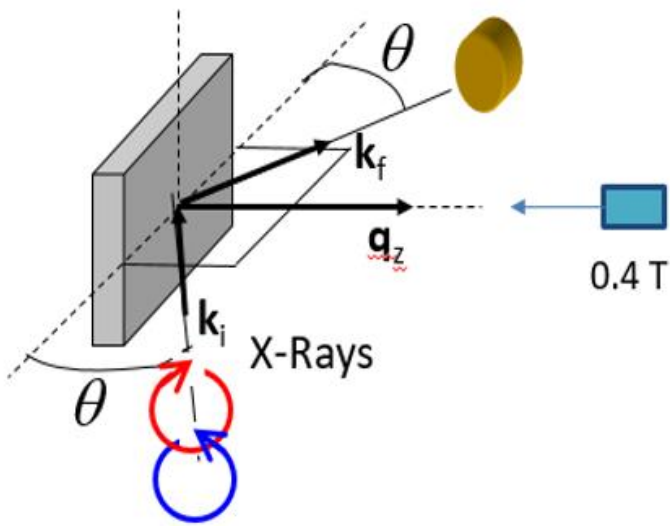

Figure 3.12 Experimental set up in order to be sensitive to polar component. A permanent magnet maybe brought close to the sample surface. The red and blue arrows represent the circular right and left polarization

This mode of acquisition will be called afterwards **RevPol** mode. In this mode of measurement, we measure the *oop* component using circular polarized light (at the present only at remanence).

- However, **if the magnetization is *in-plane***, it is possible to apply a saturating field, provided saturation or a single-domain state can be achieved with a field strength of 0.17T. The data are collected with right or left circular polarization by reversing the applied field along the longitudinal direction at each data point of the scan (referring to analytical expression from chapter 2). In the case of very small signal, it could be useful to check the dichroic nature of all the features observed in the magnetic asymmetries. The same measurements can then be for the opposite circular polarisation and the superposition of the two magnetic asymmetries indicate that the magnetic configuration established under positive and negative fields was identical to the ready sign. The experimental set up is shown in Figure 3.14. The acquisition will be named **flipHlon** mode. Figure 3.13 shows the asymmetry ratio where we see splitting of opposite intensity at lower angles which corresponds to an asymmetry ratio at lower angles as well. Thus, such a signal signifies sensitivity to *in plane* component.

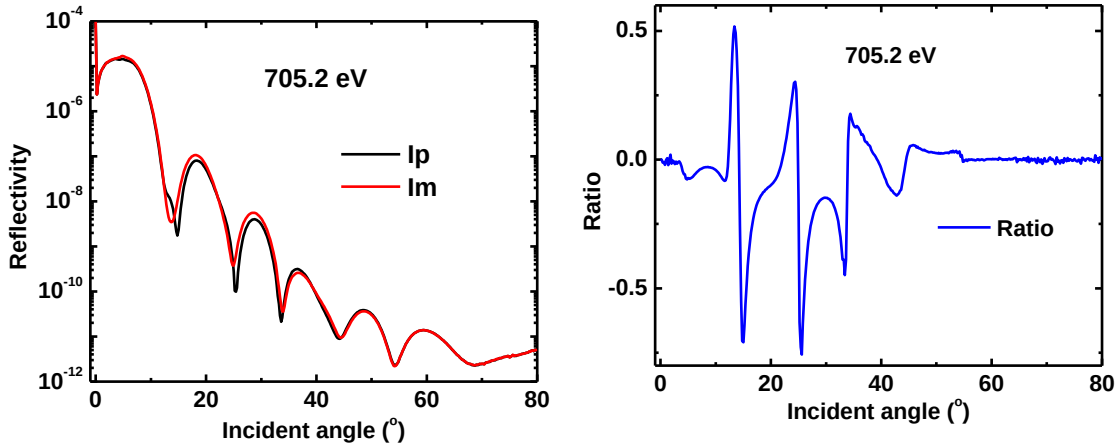

Figure 3.13 Experimental angular dependent reflectivity and their corresponding asymmetry ratio at Fe edge

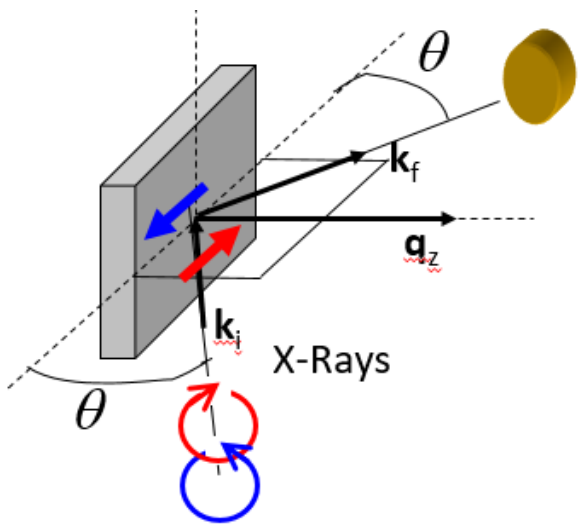

Figure 3.14 Experimental set up in order to be sensitive to longitudinal component. A permanent magnet maybe brought close to the sample surface. The red and blue arrows represent the circular right and left polarization

3.4.3.3 Motivation for Energy scans

Energy scans are collected at a few θ, 2θ positions. Based on the angular dependency of the magnetic asymmetry the angular positions is selected at low angles for *in-plane* magnetization and large angles for *out-of-plane* magnetization in order to be sensitive to the magnetic contrast.

The motivation of such scans is threefold:

- First of all, it allows the selection of a few photon energies in the vicinity of the edge to optimize charge and magnetic contrast as shown in figure Figure 3.15.
- It allows us to check the energy calibration of the beamline because it is very important to know as precisely as possible the value of the energy of the photons that we used in the quantitative

analysis of the data, carried out at from the fit of the reflectivity curves collected in the vicinity of an intense and relatively narrow absorption edge. This turns out to be easy, if the acquisition of a good drain current signal, collected simultaneously with the reflectivity measurements, is possible. Otherwise, it may be less straightforward due to the weighting of the real and imaginary parts by factors depending on the angle at which the measurement is carried out. In this case, an accurate determination of a possible difference between the energies chosen for the experiments and the energies to be used in the modelling of the data can be obtained by an adjustment of the energy scans. Sometimes, the signal is dominated by the imaginary part and looks very similar to XAS and XMCD measurements, making it easier to check the calibration.

- Moreover, in some case it could be very useful to validate the optical constant used especially when the XAS and XMCD data used as shown in figure are coming from a reference sample. If the intensities (ref and R) are nicely reproduced, this contributes to validate the optical constant derived from another (however similar) systems. All these 3 points have been illustrated in chapter 4 and 5.

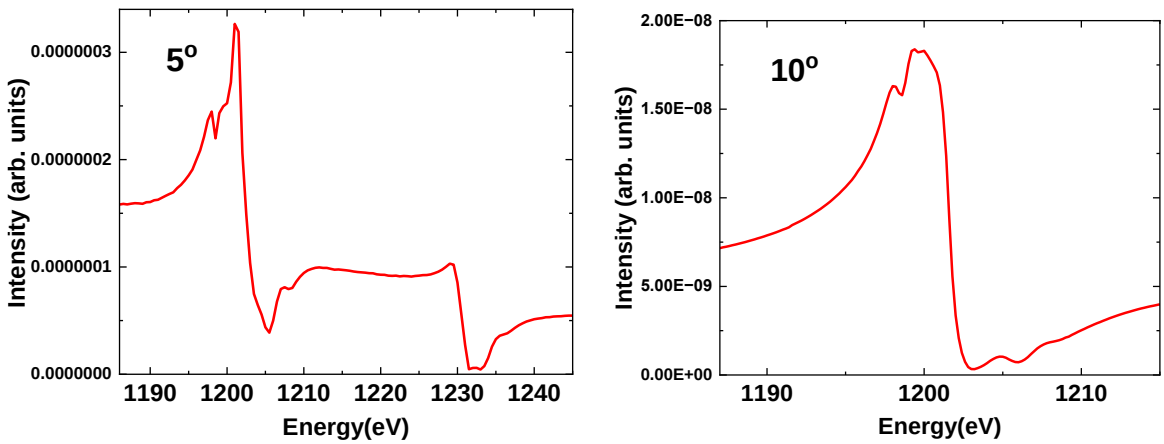

Figure 3.15 Energy dependent reflectivity scan measured at 2 specific θ in the vicinity of Gd edge.

3.4.3.4 Motivation for applied field scans

The next step is to collect hysteresis loops. Unfortunately, this is possible only for in-plane magnetisation since a magnetic device to apply variable out-of-plane magnetisation is not currently available.

First, the motivation is to compare with magnetometry data if available and, as it is a species selective hysteresis loops to provide eventually slightly different information.

Second, this allows us to check the reversal process, the shape of the loops, the coercive field and whether saturation of the magnetisation is reached or whether the magnetisation is mainly single domain. These considerations are important to establish that the field reversal leads to an identical magnetic configuration with an opposite sign.

In case of doubt concerning the single domain state, magnetic asymmetries can be measured using different methods. For example, results from the **flipHIon** acquisition mode using CR and CL can be

compared. Results obtained from **flipHlon** mode and **revPol** mode using the same amplitude for the applied field can be compared.

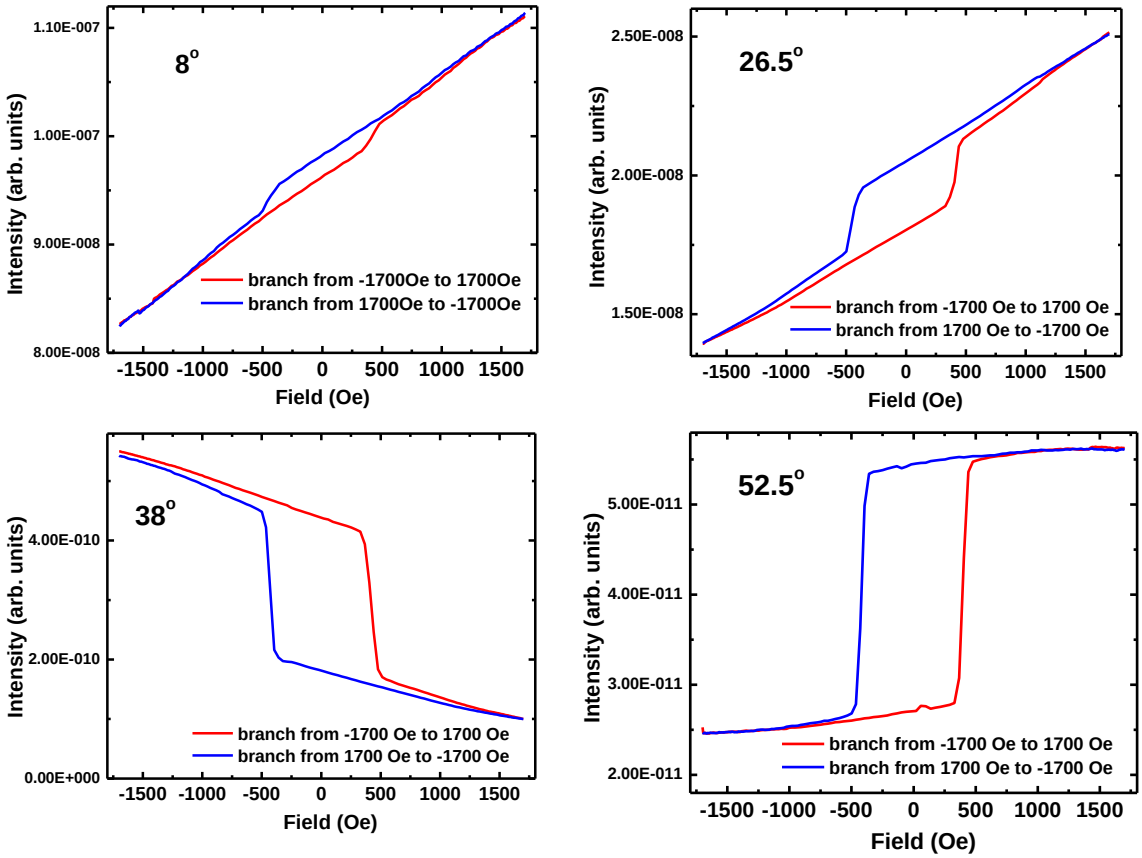

Figure 3.16 Evolution of a hysteresis loops measured at different angular positions.

3.4.3.5 Angular scans

Finally, angle dependent reflectivity curves and magnetic asymmetry can be collected at different incident energies near the edge for the quantitative analysis of the structural parameters of the heterostructure and of the magnetisation profile of the layer(s) by data refinement. The acquisition of reflectivity curves at several energies in the vicinity of an absorption edge amounts to measuring these curves with a set of four resonant parameters (f_1, f_2, m_1, m_2) of different signs and amplitudes leading to curves different in shape and amplitude and to more robustness in the model determination. These are illustrated in Figure *3.12* and Figure *3.13*.

3.5 Analysis of experimental data

In the previous chapter, we got familiar with the two theoretical approaches to understand and analyse the results of the SXRMR technique, which were – **kinematical theory**, leading to an analytical expression of magnetic asymmetry and a **dynamical approach** which took into account a matrix development to

simulate the reflectivity intensities. In this work, kinematical theory is used to discuss qualitatively the results by visualizing various geometric terms., whereas dynamical approach is used to fit the experimental data in order to determine the structure of the heterostructures as well as magnetization profiles by refining certain parameters (discussed further).

3.5.1 Dyna code interface

To obtain depth resolved magnetisation profile we perform a quantitative analysis of the experimental data which is done with the help of dynamic theory developed in chapter 2. We perform such an analysis, coded in MATLAB called **DYNA** environment [104] as shown in *Figure 3.17*.

Here, determination of the magnetisation profile of a specific atom, or the distribution of the magnetisation amplitude along the growth axis of a specific atom in a magnetic layer, is determined from the adjustment of the magnetic asymmetry by a model of flat and continuous sublayers, each of constant magnetisation whose amplitude and orientation may vary from layer to layer. As the magnetic asymmetry is strongly dependent on the structure due to the term in the denominator, a prerequisite before trying to simulate and refine the magnetic asymmetry is the determination of the structure of the multilayer stack.

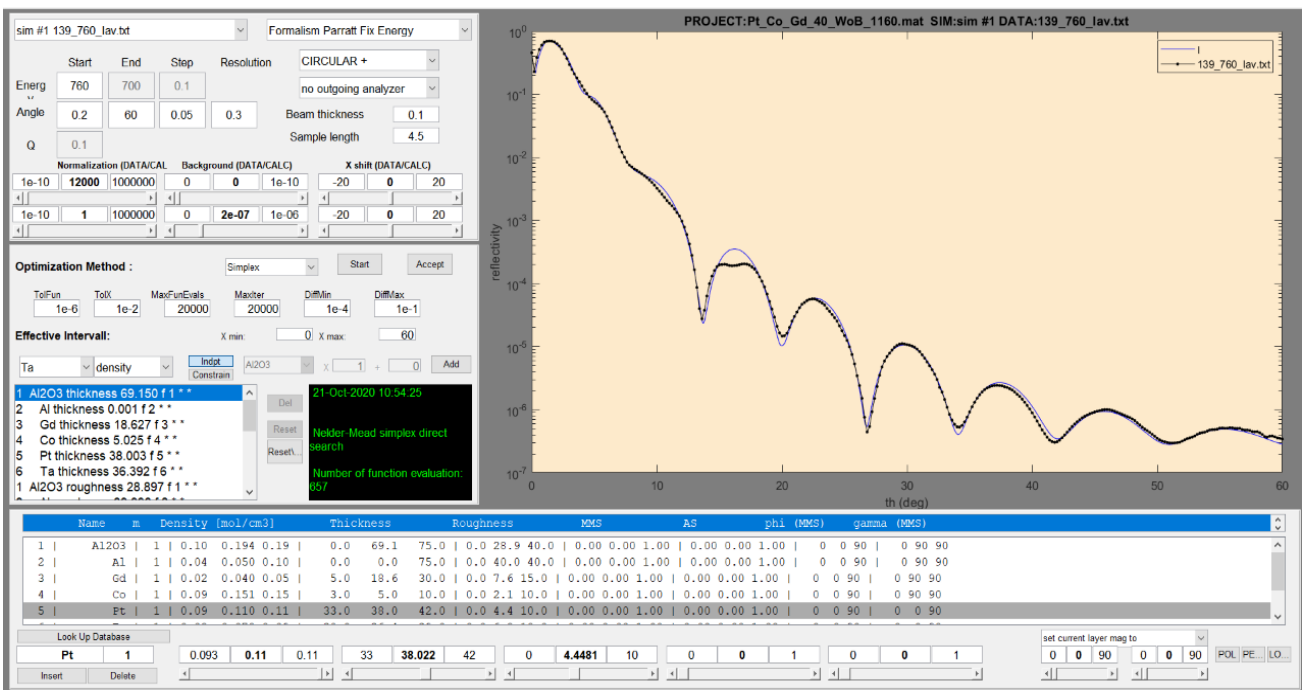

Figure 3.17 A view of software DYNA coded in Matlab

From top to bottom and left to right, the first quadrant allows us to:

- Select the formalism (Parratt or magnetic simulations) and the type of scans (energy or angle dependent scans)
- Loading of one or more experimental data for a single or multiple fit.

- Define the condition of acquisition of the data (polarization state, initial and final E or θ values, energy or angular step, angular resolution of the reflectometer
- Set the beam size and sample size in the direction of the incident beam to reproduce the intensity reduction due to the beam footprint.
- Define useful parameters for the adjustment such as the scaling factor to apply to the data or to the calculation to obtain comparable intensities, as well as a value allowing to simulate a continuous background adding to the data (stray light in RESOXS, dark current) and, in the case of energy dependent scans, an offset value to adjust for an error in the energy calibration.

The 2nd quadrant is dedicated to the parameters used for the automatic refinement and in particular to the selection of the parameters to be refined. They are listed in a window. There is also a possibility to create a link between the values of the parameters. The "start" button is used to launch a fit.

The 3rd quadrant at the bottom is used first to define the structure from the target values at the time of deposition for the thicknesses (nominal thickness) and the raw values for the densities. Obviously, the roughness values at the start are only a guess or are related to estimates from other results. The parameters *mms*, φ and γ, related the magnetization amplitude and orientation, will be defined later Here, it is also possible to set minimum and maximum values for each parameter to be used during the refinement.

The results of simulations are displayed in fourth quadrant. Experimental data can be superimposed and the automatic refinement can be started. During the refinement, it is possible to visualise the change in the simulated curves, to follow the changes of the parameters in the 2nd quadrant as well as the evolution of a few parameters such as the number of iterations and the value quantifying the quality of the fit (least square method)

The values of the four resonant parameters (f_1, f_2, m_1, m_2) do not appear in the Dyna screen. They are stored in two separated files with the name of the material constituting a layer followed by the extension .cf for E, f_1, and f_2 .mf for E, m_1, and m_2. The name of each layer and the content of .cf and .mf files must be defined by users. The code will calculate the four resonant parameters (f_1, f_2, m_1, m_2) to be used from the energy value of the simulation. In the 3rd quadrant, a button entitled "Look up database" allows access to all the resonant parameters stored in the database. In addition, the possibility of building the file for a new alloy or a new compound is given in this part of the program.

3.5.2 Determination of the resonant parameters

For simulation of the reflectivity curve using DYNA, it is an **important pre requisite to know the optical properties of all the layers of the system**. If we work at energies far away from the edge (> 100eV) the scattering factors are calculated from the first principles starting from the equation (2.3.5) which are the non-resonant scattering factors in good agreement with experimentally obtained values. These are typically used in non-resonant X ray reflectivity. Popular compilations that are used are given by Henke-Gullikson table [115] and the Chantler table [116].

XRMR and XMCD are dependent on the resonant transitions which occur from core states to the unoccupied states at the fermi level. Close to the resonant edge, optical properties on near fine edge structure of the spectrum which depends on the chemistry of the material this makes use of tabulated values (mentioned above). This makes it necessary to determine the scattering factors experimentally.

The procedure to determine the resonant parameters is described below in Figure *3.18*

Retrieving the resonant parameters

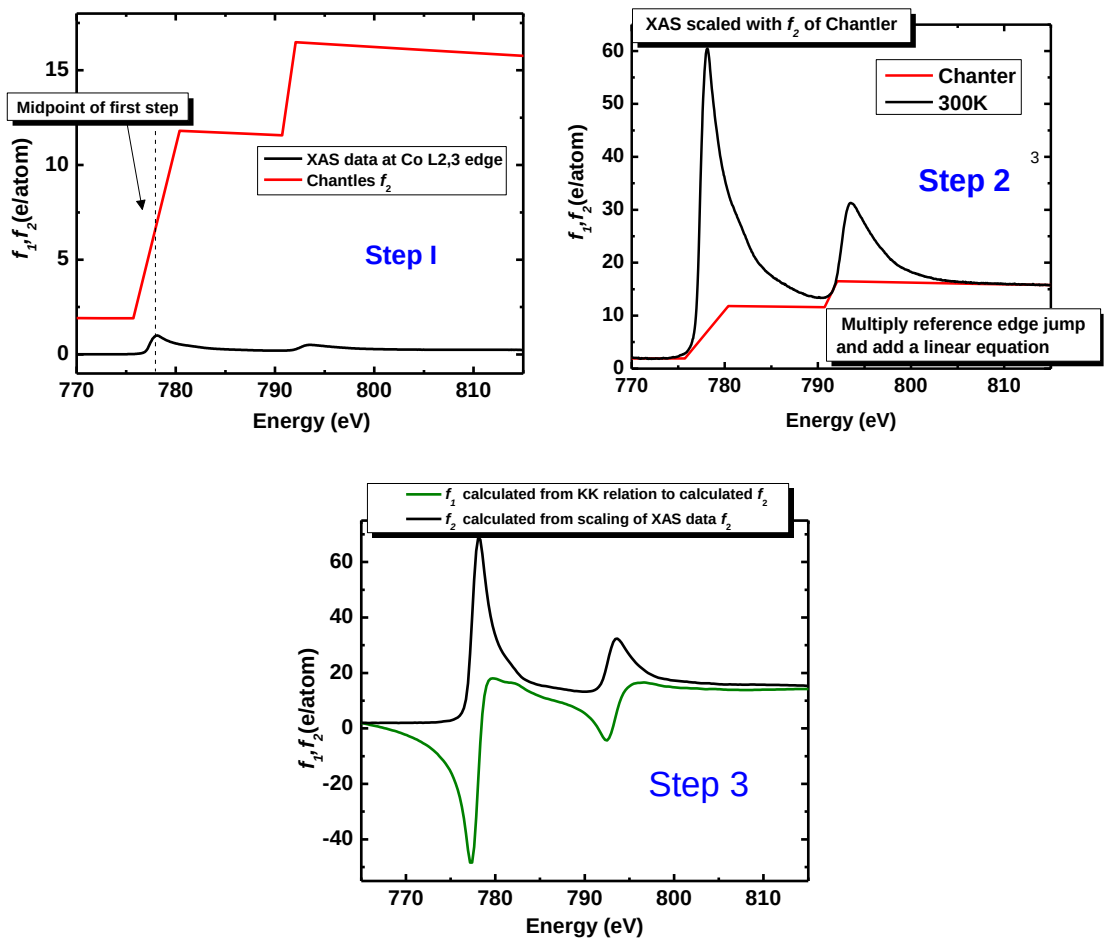

Figure 3.18 Illustrates each step to consider for retrieval of resonant parameters.

I. Before beginning the process, it is essential to check if the **energy scale of the experimental XAS data matches is similar to that of Chantlers f_2 data** which is done as shown in Step 1 of *Figure 3.18*. In most cases, we will need to modify the energy scale to equalize distance between each point since the energy scale of experimental XAS data since the peak of resonant edge will most of time be at different energy. This is done by matching the energy scale of our experimental data with the f_2 table generated from Henke or Chantler's data set. **We match the energy at L3 edge of the absorption spectra with midpoint of the first step of *generated* f_2.**

II. Next, we have to **scale the experimental absorption spectra with the f_2 values from chantlers's table for a particular element at the cloud of points far away from the edge**. For these points, away from the edge, the obtained raw data is made to superimpose with the f_2 from Chantler's table so that a comparison can be made. For f_2 values from Chantler's table, we have a step for each edge. The scaling needs to be done properly, and sometime, a linear fit need to be made for points if they stray away. Next, edge jump of the absorptive part f_2 of the table have to be determined at exactly the same energy values and ranges such as has been chosen for the data normalization. The edge jump has to be determined from the value of this linear fit compared to the tabulated value at the very same energy as it has been derived in the measured XAS spectrum. The resulting factor (edge jump) is then multiplied to the XAS data. The resulting curve should now perfectly fit into the reference Chantler curve.

III. After adjustment of the data to electron units, Kramer's Kronig relation [117] (defined below) is applied to the f_2 by entering the absorptive values in the program which applies kramers-kronig relationship to them. Thus, we get the dispersive part f_1.

$$f'(\omega) = \frac{2}{\pi} \mathrm{P} \int_0^\infty \frac{\omega' f''(\omega')}{\omega^2 - \omega'^2} d\omega' \qquad (3.5.1)$$

In terms of the magnetic part the same procedure has to be done. One measures the XMCD absorption, for example for reversed magnetization with fixed circular polarization. Both curves are adapted to tabulated values as sketched above. This provides an XMCD absorption signal, which gives the dispersive part using Kramers–Kronig relations. This procedure has been done by many groups so far.

3.5.3 Structural determination:

The first step, determination of the structural parameters (Figure 3.19) which are density (ρ), thickness (t) and roughness (σ) is essential to obtain the magnetic profile. Initially the refinement is performed for data without magnetic contribution (**off resonant scan**, as described before): this is the case of measurements far from an absorption edge (collected in the domain of soft X rays and in the laboratory with hard X rays of length 1.54 Å wavelength). This step is essential in order to get values for density as close to the real value as possible.

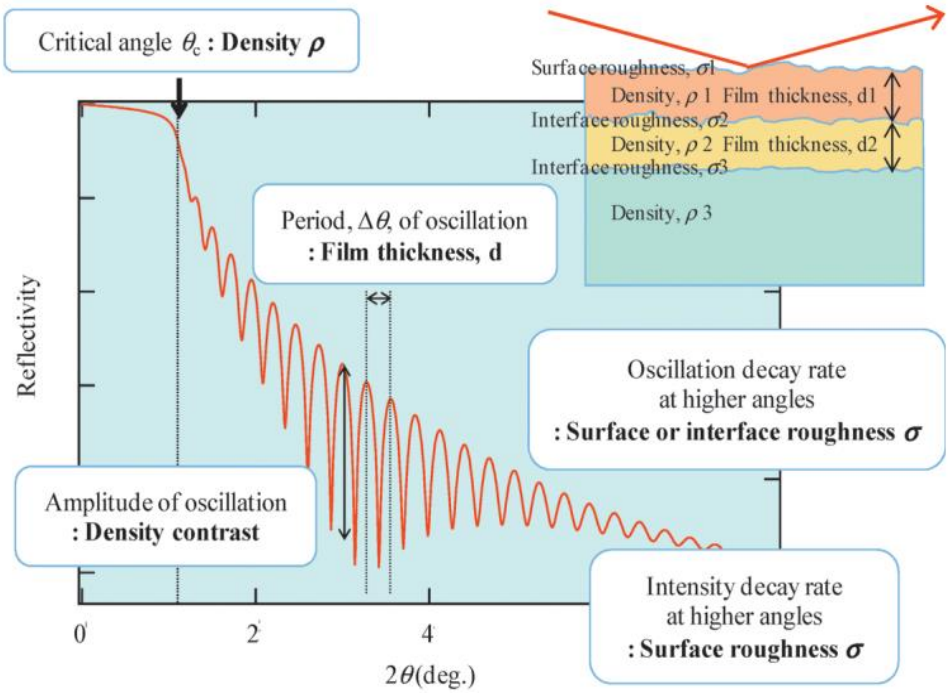

Figure 3.19 Different parameters such as thickness, density and roughness which can be derived from a reflectivity curve (figure from [118])

After, refinement for measurements at energies in the vicinity of absorption edge, by refining the average intensity I_{av} of the FlipHlon or RevPol mode. I_{av} is calculated by:

$$I_{av} = \frac{I_p + I_m}{2} \qquad (3.5.2)$$

Where *Ip* and *Im* are collected at circular right, **CR (or + applied field)** and left polarized light, **CL (or - applied field)**. The refinements will be made in the "Parratt" mode which allows a much faster simulation.

The procedure of refinement used in this thesis is described below:

1. Initially we start with refinement at energy far away from the edge. This is done to have a starting point of the structure, before going to fit data at energies in the vicinity of the edge. This done by taking into account the thickness and roughness parameters initially and working on improving the fit.
2. Since we are not working at an energy close to the edge, we may refine the densities if sometimes we need a better fit, keeping the roughness and thickness fixed and starting with the densities of the thinnest layers. The lower limits are defined 15% below the value of the densities of the crystalline phases because this could correspond to the density of an amorphous layer. The upper limits are defined as those of the crystalline phases. With the same limits, the refinement will be extended to all densities.

3. Finally, once the simulation is sufficiently close to the experiment, all the parameters are refined and certain limits made less constraining if necessary. The results of the adjustments at energies

far from the edge, where the resonance parameters have no effect and where an error in the determination of these parameters therefore has no effect, will serve as a set of starting parameters for the refinements of the measurements collected near the absorption edge.

4. For measurements at the edge, initially we start with something defined as ***multifit angular scans*** where data is uploaded at each energy and a simultaneous fit is carried out for all the data with a single model.

   However, it is rare to obtain a satisfactory fit of the data set. A significant difference can be detected for the parameters of the layer containing the resonant atom and the adjacent layers. Indeed, the significant variation in the scattering power of this atom at resonance, particularly in the soft X-ray range for the L3 and M5 edge, may be the cause of these modifications. For example, the value of the thickness can take into account the mixed resonant atoms at the interfaces. This variation of the thickness parameter can also be accompanied by a variation of the roughness. Of course, if the intermixing is reduced, this phenomenon is not important and the thickness and roughness values are very close.

5. **The new result obtained by this multifit approach serves as a starting point for the individual refinement of the angular scans at the edge**.

   With the exception of the densities, all the values of the structural parameters resulting from the best fits for each energy are used to define the average value and the standard deviation of each parameter. The different treatment of density comes from the fact that the reflected intensity is sensitive to the density of the product multiplied by the atomic structure factor. Due to potential errors on the four resonant parameters in the vicinity of the edge (scaling, energy resolution), the value of the density can be distorted, during the refinement, because it corrects these small errors. It is possible not to refine the density in resonance condition. However, in order to reduce the impact on the magnetic asymmetry of the differences between the simulated reflectivity curves and the experimental curves, it may be preferable to improve the fit of the reflectivity data with a less significant density value. All this aspect will be illustrated in chapter IV and V.

3.5.4 Determination of energy correction

Before attempting a refinement of the measured data close to the edge, we seek to determine as precisely as possible a possible difference between the energy set for the measurement and the real energy of the incident photons on the sample. This is to check the existence of a possible error in the calibration of the beamline. The amplitude of this difference will result from the refinement of the energy scans carried out at several angles of incidence. This is a tricky refinement because it is not done on a logarithmic scale but on a linear scale and is more sensitive to small errors in structural parameters. For small angles, one can try to simultaneously refine the magnetic asymmetry signal, with a constant profile (only 1 value of mms for the whole layer) because the signal is more sensitive to the average value of the magnetization than

to the magnetization profile [119].**Thus, the energy difference can be determined from the position of the edge in the reflectivity and magnetic asymmetry data.** We focus on the edge used to choose the energies of the angular scans, typically the L3 edge of 3d transition metals and M5 of rare earths. Indeed, effects of shrinking of the energy scale may appear in particular if the XAS/XMCD spectra used to determine the resonant parameters were not recorded on the same beamline at the time of the reflectivity experiments. The refinement of the energy scans carried out at small angles of incidence, where an imperfect knowledge of the structural parameters will be less penalizing, could provide information on the quality of the resonant parameters used.

We have seen that how we can begin the fit at an energy with data derived from a measurement which is far away from resonance. **When we go to resonance and work on an energy close to resonant edge, the resonant parameters play a big role as they are energy dependent**. This means we need to be very careful with which energy we choose to work on since even a small change in energy can drastically change the curve. During the experiment at the beamline, most of the time we do not work on energy same as that of the L3 edge (706.8 eV in case of Fe) since it depends on the energy calibration done at the time of experiment at the beamline. One way to solve this issue is by measuring model a theoretical curve that superimposes with the energy dependent reflectivity measured at a fixed angle. In order to perform this, we try to adjust the two peaks and bring them to superimpose with each other by shifting the energy. If there is a difference in the peaks, this number is then added to all the experimental energy values while performing refinement to reduce all possible errors that can occur from the difference in energy.

The analysis of data from an XRMR experiment aims to determine the magnetization profile of a thin film. For this, it is necessary to reproduce the angular dependence of the magnetic asymmetry revealed in reflectivity measurements carried out in the vicinity of an absorption edge presenting an effect of circular magnetic dichroism of the X-rays for a specific magnetic element. In principle, a single measurement at an incident photon energy where the magnetic dichroism signal is strongest contains all the information. However, to overcome one of the difficulties related to reflectivity experiments, namely the uniqueness of the model resulting from the refinement of the data, it is possible to adopt a ***multi-energy approach*** for which the quartet of resonant parameters is very different. In this case, it is necessary to determine the structure of the multilayer for each energy. The structure obviously does not depend on the energy of the incident photons. However, in order to reproduce as closely as possible all the characteristics of the curves of reflectivity, it is necessary to accept some differences in the value of the parameters from one energy to another, provided the differences lead to an acceptable dispersion of the results.

3.5.5 Magnetic profile determination:

The quantitative analysis of the magnetic structure is carried out **by refinement of the energy and/or the angular dependent magnetic asymmetry at several incident angles or energies near the resonance, respectively.** In order to get the most accurate magnetic profile, therefore it is essential to get a good idea about the structure. Refinement of asymmetry ratio is performed simultaneously for each energy along with the structure by including the extracted average intensity.

We start this analysis by initially considering a homogeneous distribution of magnetism in the magnetic layer however depending on the quality of the fit, we may sub divide the magnetic layer into various slices that allows deriving the depth resolved magnetic profile. Keeping the structural parameters constant that we obtained from structural refinement like it was explained in detail previously, we define a weighting factor ***mms*** which corresponds to modifying the magnetization averaged over a certain thickness across the layer is described by an amplitude called *mms* (magnetic moment scaling). It is a weighting factor whose amplitude is linked to the XMCD of the reference samples. A value equal to 1 implies an amplitude of the 3*d* magnetic moment of 2.1 μ_B for Fe and 1.7 μ_B for Co (although it can be for other magnetic atom), which result from the application of the sum rules [120].

Two angles (spherical coordinates) $\boldsymbol{\phi}$ and $\boldsymbol{\gamma}$ can be considered in case of arbitrary orientations of the magnetization vector. $\boldsymbol{\Phi}$ corresponds to the canting angle of the magnetization (rotation of the magnetization in the scattering plane) and $\boldsymbol{\gamma}$ represents the way magnetization orientation departs from the scattering plane in the sample plane. The presentation of this is displayed in Figure *3.20* These parameters will be used when we will need to define a canted magnetization profile are needed to take into account. The results were collected after measurement of R at several energies around resonance imposes a strong constraint to the analysis if magnetic profile model is fitted to whole data set [121]. The adjustment is constrained by simultaneously refining *R* and I_{ave}.

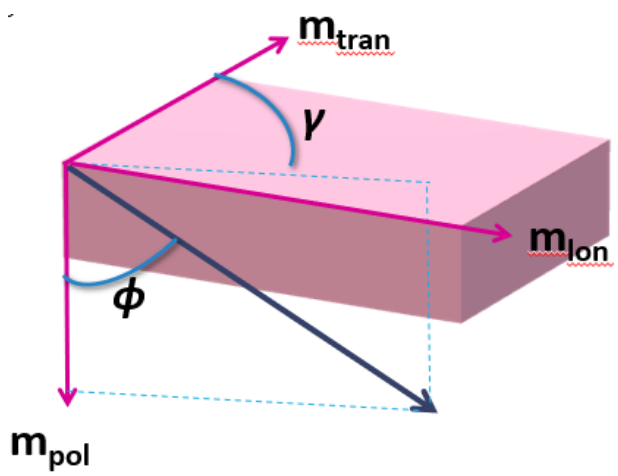

Figure 3.20 Diagram of orientation and definition of angles ϕ and v allowing to express the direction of the magnetization out of the plane and in the plane respectively

3.6 In lab experiments (conducted outside of synchrotron radiation):

There are different techniques that are sensitive to magnetism which can be utilized in order to get the variation of magnetization along the easy or the hard axis (magnetic anisotropy). During the thesis, we also performed experiments at Institute Neel, to measure average magnetization both *ip* and *oop* such as:

3.6.1 Magnetometry experiment – VSM - SQUID

SQUID is one of the most effective and sensitive ways to measure magnetic properties of ultra-thin films where changes in magnetic flux can be studied as a function of temperature and magnetic field. The magnetometer measures magnetic properties with magnetic field going up to 7 Tesla and a temperature range between 1.9K – 400K. Thus, this technique simply gives the total magnetic moment of the sample in μ_B. A schematic diagram for SQUID is shown in the Figure 3.21.

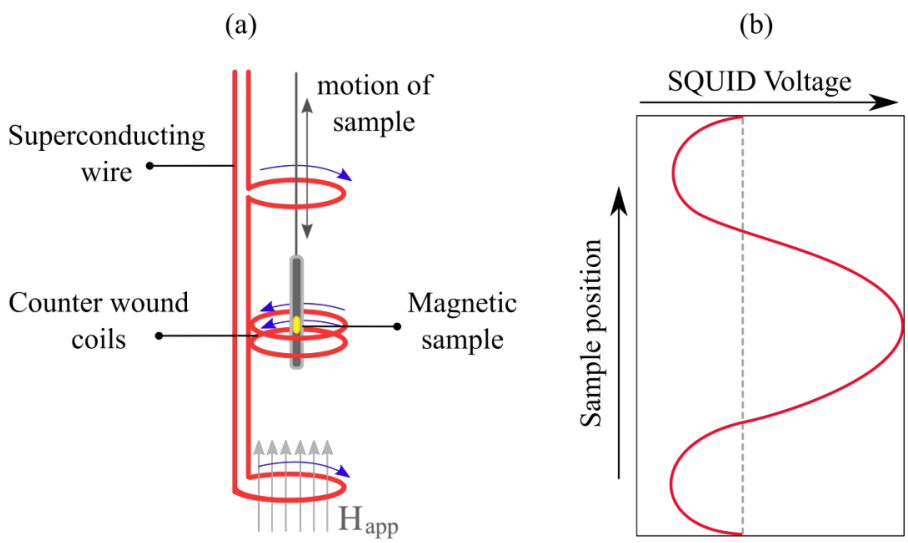

Figure 3.21 Schematic representation of SQUID magnetometer placed in a magnetic field. (b) The variation in SQUID voltage as a function of sample position

The SQUID technique is based on Josephson effect where SQUID magnetometer consists of 2 superconductors separated by thin insulting layers forming two parallel Josephson junctions in a superconducting loop operating at a constant DC supply Figure 3.21 (a). The sample travels longitudinally through the superconducting detection coils and there is a change in magnetic flux of the sample which induces an electric current in the detection coils following the Faraday's law of electromagnetic induction. As the sample is moved through the detection coils, there is a variation of SQUID voltage as shown in Figure 3.21(b).

3.6.2 Magneto-transport measurements – Hall effect

Hall effect is a transport measurement which is very sensitive to the perpendicular component of magnetization. It describes a phenomenon where transverse hall effect is generated on passing of electrical current *I*, through a magnetic conducting material. Hall Voltage for out of plane magnetized film is given by:

$$V_H = I\mu(R_0 H_z + R_E M_z) \qquad (3.6.1)$$

Where R_0 and R_E represent the ordinary and extraordinary hall coefficient. R_0 is related to the Lorentz force which acts on the moving charge carriers and R_E corresponds to the anomalous Hall voltage, that scales linearly with the out-of-plane component of the magnetization M_z. We can use anomalous hall voltage to measure out of plane magnetization M_z. For in depth view on this effect, refer [122]

3.7 Conclusion

In this chapter, we discussed the experimental set up that has been used in this thesis. We introduced synchrotron radiation which provide us the ability to tune the energy of the beam, change polarisation and at the same time provide high brilliance and flux enabling us to perform X ray scattering experiments. We understood briefly the set up at RESOXS and understood in depth how the data is collected at RESOXS including which scans we make for what reason. We also discussed how after the collection of data; we treat the data by refinement in which steps are followed to get a magnetisation profile at the end of the element we want to study. We also discussed magnetometry measurements which have also been used in this thesis. Following chapters will be related to the experiments conducted during thesis which will use all the concepts discussed in Chapter 3 as well as Chapter 2

4 DEPTH RESOLVED MAGNETIZATION PROFILE OF COFEB/MGO/COFEB/(W)TA PERPENDICULAR HALF MAGNETIC TUNNEL JUNCTIONS

4.1 Context

In the early studies of spintronic devices, magnetisation of ferromagnetic (FM) layer was made to be *in plane*(*ip*) of the film plane where a strong Tunnelling magnetoresistance (TMR) effect could be realised in the *ip* magnetised MTJs particularly with CoFe/MgO/CoFe structures [123]. However, it was realised that these devices suffer from problems such as low switching efficiency and limited scalability. Breakthrough of interfacial perpendicular magnetic anisotropy (*iPMA*) in CoFeB/MgO/CoFeB structures which showed higher TMR ratios, low magnetic damping and relatively small spin transfer torque (STT) switching current [124]. This *iPMA* was seen to exist at interface between magnetic transition metals and oxides [36], but was subsequently observed with a large variety of amorphous and crystalline oxides along with transition metals such as Co, CoFe and CoFeB alloys [125], [126], [127]. Since this discovery, plenty of endeavours have been put to **optimize the CoFeB/MgO interface so as to improve performance** [12]. Such phenomenon of *iPMA* at transition metal/oxide interfaces if of a great interest not only from research point of view but also applications such as magnetic memories. Spin-transfer torque magnetic random-access memory (STT- MRAM) is one of such mainstream memory due to its characteristics such as non-volatility, infinite endurance, low power, and high speed [128–130] with MTJ being the core component of a STT-MRM.

4.1.1 CoFeB/MgO/CoFeB systems

In 2010, a study by Nistor et al., [131] established a correlation between the amplitude of interfacial PMA existing at CoFe/MgO interface and the corresponding TMR in MTJ. Formation of CoFe-O bonds at the interface during oxidation was observed influencing both interfacial anisotropy and TMR. The origin of this lied at the magnetic transition metal/oxide interfaces due to hybridisation between O *p* and Fe (Co) d_z^2 orbitals. A similar experiment for the film containing CoFeB (Figure 2.1) showed that the magnetisation lies *ip* as compared to CoFe/MgO. This demonstrated occurrence of reduced *iPMA* in presence of B at CoFe(B)/MgO interface since presence of B hinders the hybridisation between Fe (Co) orbitals and oxygen *sp* orbitals. **Thus, this showed the importance of attracting B from the CoFeB/MgO interface.** This showed CoFeB/oxide systems with B show higher PMA.

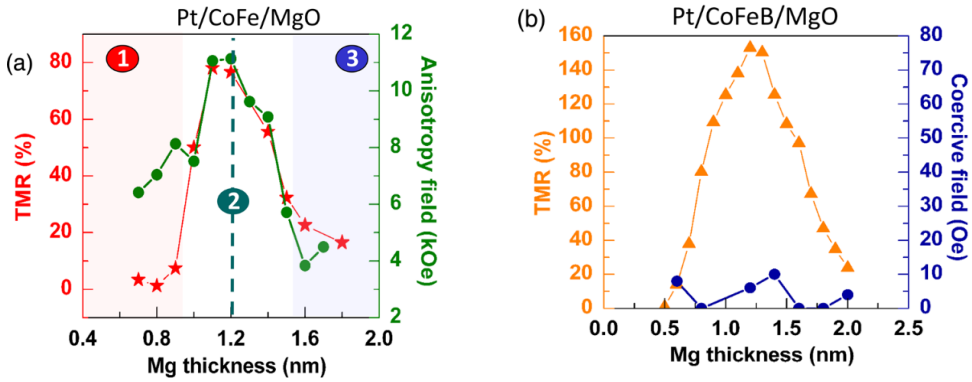

Figure 4.1 (a) Variation in the TMR ratio in CoFeB-based MTJ and in the perpendicular anisotropy of a Pt/CoFe/MgO bottom electrode as a function of the thickness of the naturally oxidized Mg barrier. (b) Comparison of TMR in *ip* magnetized CoFeB-based MTJ and of the anisotropy in Pt/CoFeB 1.1 nm MgO bottom electrode for various Mg thicknesses (figure taken from [131]).

4.1.2 First observations of PMA at Ta/CoFeB/MgO interfaces

In 2010, another study was published by Ikeda et al., [124] where Ta/CoFeB/MgO based MTJs were investigated for *iPMA*. The results proved to be a turning point since they showed large TMR and a large PMA could be obtained with relatively low STT switching current. They used Ta interfaced with CoFeB since Ta is known to be a good B getter. Thus, these studied showed that CoFeB/MgO MTJs with perpendicular magnetic easy axis arrive to fulfil three conditions for their high performance given as:

Thermal stability factor – given as $E = k_B T$, where E is the energy barrier that separates the two magnetization directions, k_B is the Boltzmann constant and T is the temperature should be more in amplitude than 40 [132] for non-volatility. $E = M_s H_K V/2$ where M_s is the saturation magnetisation, H_K is the anisotropy field. As the junction size is reduced, the volume is reduced, which means that anisotropy energy density $K = M_s H_k/2$ needs to be high enough to ensure high thermal stability.
Various materials such as FePt having perpendicular anisotropy have shown to satisfy this condition [133].

Efficient current switching - Intrinsic threshold current I_{C0} for current induced magnetization switching (CIMS) is proportional to E,

$$I_{C0} = \alpha \frac{\gamma e}{\mu_B g} M_S H_K V = 2\alpha \frac{\gamma e}{\mu_B g} E \qquad (4.1.1)$$

Where α is the damping constant, γ is the gyromagnetic ratio and g is a function of the spin polarisation of tunnel current as well as angle between the magnetisations of the free and reference layers [134], [135]. In case of *ip* anisotropy, equation (4.1.2) is replaced by E_{demag} called demagnetization energy results in E too large, which is also a reason why perpendicular anisotropy is required for reduction of switching current. Thus, this equation shows that low value of α is required for low switching current for a given E.

High tunnel magnetoresistance – bcc (001) CoFe(B)-MgO is a well-known system for high TMR. Crystal structures of PMA materials are usually different from bcc, on annealing CoFeB that was initially amorphous crystallises in structures apart from bcc as they are deposited in direct contact with materials with PMA [136].

Thus, CoFeB-MgO material system is able to meet all three conditions for high performance perpendicular MTJs [124].

4.1.3 PMA in HM/CoFeB/MgO structures

Experiments have suggested that apart from CoFeB/MgO interface, a heavy metal (HM) layer/ferromagnetic layer interface is also vital to achieve high PMA. Worledge et al., [137] showed that HM/CoFeB/MgO structures with Ta and Ru where Ta/CoFeB/MgO structures after annealing shows PMA although Ru/CoFeB/MgO structure remains *ip* magnetised. This revealed the fact that CoFeB/non-magnetic counter interface also to affects PMA highlighting that study at both interfaces is essential in order have better knowledge of such systems [138,139], [140], [141]. The cap layer on top of storage layer influences the magnetic as well as transport properties of the p-MTJ due to modification of interfacial, electronic and physiochemical properties [142], [118], [119], [120].

Annealing is an important parameter on magnetic anisotropy has also been explored by several groups where it has been seen that annealing temperature will significantly enhance the PMA. However, for practical applications it has been observed that thermally activated Ta ions have a tendency to diffuse toward CoFeB/MgO during annealing at temperatures which are greater than 300°C which causes PMA degradation [142,146].This limits the thermal budget that a PMA structure can tolerate [147,148] and hinders integration with CMOS circuits because thermal treatment at 400°C is normally necessary for back line processes. There has also been research on strong dependence of PMA on Ta thickness attributed to Ta oxidation or diffusion into CoFeB layer during annealing.

Due to this we are interested to explore other options that can be used as HM layer.

4.1.3.1 Introducing Tungsten(W) based systems

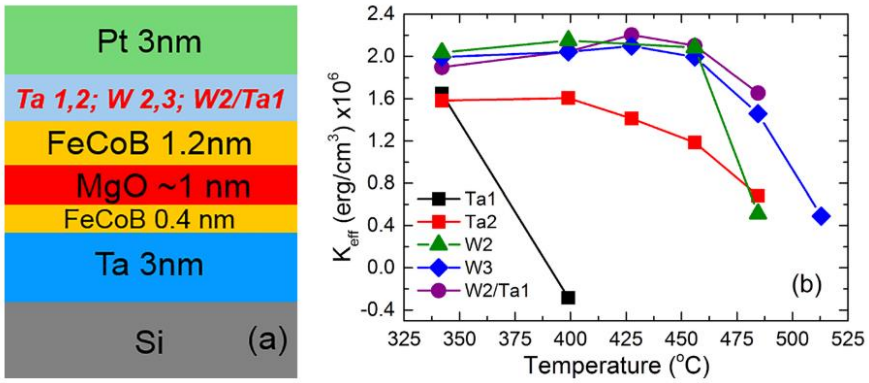

Figure 4.2 (a) Schematic drawing of top electrode half-MTJ stack and (b) Effective perpendicular anisotropy (K_{eff})as a function of annealing temperature(taken from [143]).

Recent years have seen numerous efforts made towards research on substitution materials to replace Ta with a material that can remain PMA even after annealing at high temperatures.
An et al., showed that with **W/CoFeB/MgO structure**, interfacial PMA of 1.98 mJm^{-2} is obtained when the sample is annealed at 350°C and even after annealing at 450°C, sample still exhibits interfacial PMA of 1.7 mJm^{-2} [149].

Thus, W has shown to improve PMA by 30% along with annealing stability as compared to Ta cap layer as shown in Figure 4.2 has been attributed to overall stiffness of the stacking caused by large mechanical hardness of W (melting temperature of 3422°C) [143], [150]. It also prohibits Fe diffusion from CoFeB layer to the cap layer, that remarkably improves thermal robustness and magneto transport properties of the stacks and corresponding patterned memory cells. W has other benefits such as reduced W interdiffusion due to the strong W-W chemical bonds as well as a reduced B diffusion towards the barrier layer.

These findings benefit the compatibility of p-MTJs with standard CMOS back-end-of- line processes and make W more attractive than Ta for practical applications. It has also been shown that W/CoFeB/MgO with metastable β-phase (amorphous) W which has high resistivity is a promising system for SOT-MRAM due its high spin hall conductivity [151–154].

4.1.4 Motivation to investigate HM/CoFeB/MgO structures with SXRMR

This far we have introduced p-MTJ systems where we understand that origin of PMA is linked to various factors such as role of oxidation state of **CoFeB/MgO interface which can be influenced by annealing temperature.** We have also seen that **capping layer can play a significant role in thermal stability of the system**. However, although in such heterostructures role of interface by itself hasn't been understood although we are working with ultrathin films with fine thicknesses. MTJs with crystalline MgO barrier and

Fe electrode such as Fe/MgO/Fe layers have showed discrepancies in the theoretical calculations and the experimental values where theoretical calculations [155], [156] showed high TMR up to 1000% whereas MTJs with Fe electrode have exhibited TMR ratios of 200% at RT [51], [157] and 604% for CoFeB used as a ferromagnetic electrode. Such discrepancy is associated with the interface properties of the heterostructures since spin dependent tunnelling is sensitive to the interface. For Fe/MgO interfaces, hybridization of Fe and O has been theoretically predicted to result in enhancement of interfacial Fe magnetic moment [158]. It has also been found that Fe magnetic moment at the interface may differ from the inner sublayers [39] which elucidated that PMA not only originates from the first interfacial layer but propagates to several monolayers.

There has been no experimental study to probe the depth dependence of Fe magnetic moment within HM/CoFeB/MgO heterostructure where Fe magnetic moment at the two separate interfaces may differ from the inner moment. Thickness dependent effects which sets limits on the useful magnetic thickness usually observed by measurements of magnetic moment versus thickness and specified by the offset value from the origin [159]. The calculated offset thickness indicates smaller magnetic thickness which is known to occur because of either formation of magnetically dead layer (MDL) inside the film or by lowering of Curie temperature near interfaces. Thickness of CoFeB becomes of prime importance due to the relationship between PMA energy density K_u and ferromagnetic layer thickness t.
Measurements by Worledge and co-workers [137] shows $K_u t$ rolls over as a function of CoFeB thickness below 9Å thus suggesting that $K_{interface}$ is not constant but it decreases for thinner CoFeB layers. In Ta/CoFeB cap layer systems, diffusion of Ta that is responsible for formation of dead layer, was suggested to be reason for dependence of $K_{interface}$ on thickness. However, origin of this phenomenon remains an open question. A better understanding of distribution of dead layer can enable a better understanding of magnetic profile hence this can aid in developing systems that maximize PMA.

Thus, we are motivated to systematically investigate Fe magnetic distribution a series of HM/CoFeB/MgO samples with counter interfaces with two kinds of cap layers – Ta and W for as deposited (before annealing) as well as after annealing (stackings are shown in Figure *4.3*)

4.2 Sample growth

The samples were deposited on Si wafers by magnetron sputtering under an Ar pressure of $2x10^{-2}$ mbar through a set up at Spintec, Grenoble [143]. MgO tunnel barrier was obtained by natural oxidation of a metallic Mg layer 0.8nm thick under an oxygen pressure of $3x10^{-2}$ mbar with a flow rate of 100 sccm for 240s. On the top of the oxidized layer, a 0.5 nm thick second Mg layer was deposited. The samples were annealed at different temperatures under high vacuum (5×10^{-2} mbar) for 10 minutes). The grown samples are shown in Figure 4.3 where the nominal thicknesses of each layer are given in the parenthesis in Å. It must be noted that all the experiments have been performed on the CoFeB layer of 15A. **The second layer CoFeB is magnetically dead. It must be noted here that it is also the reason why we call our system half MTJ.**

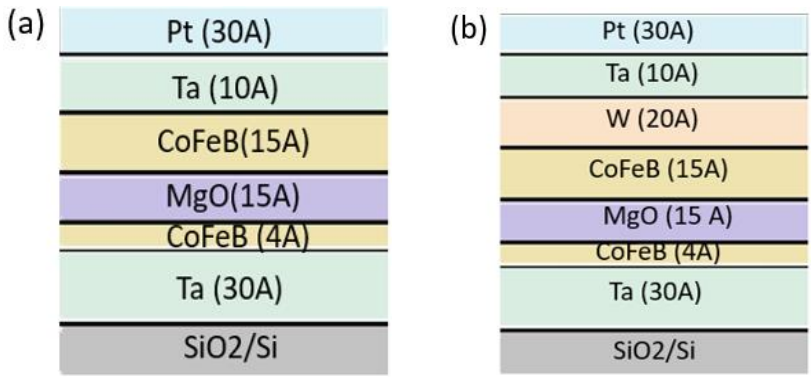

Figure 4.3 Schematic diagram of two stackings grown by magnetic sputtering studied in this thesis. (a) Ta cap layer (b) W/Ta cap layer

Throughout the thesis, we will refer to 5 samples – **S1, S2, S2', S3** and **S4** as shown below:

	Ta cap layer	W/Ta cap layer
As - deposited	S1	S3
Annealed at 340°C	S2	--
Annealed at 400°C	S2'	S4

4.3 Macroscopic magnetic properties

Hysteresis loops results have been obtained by Extraordinary Hall Effects (EHE, Neel Institute) for perpendicular (⊥) magnetic fields, and SQUID-SVSM (Neel Institute) for in-plane (**//**) magnetic ones. All measurements are performed at 300K and 1T as maximum magnetic field. Inside the inset of each hysteresis loop, we provide an inset to see the loop between ±1800 Oe since, this is the value of the applied **longitudinal** field at RESOXS. It must be that we do not present the values of remanence magnetization at 1700Oe here but along with the presentation of magnetization profile for each sample to aid in comparison.

4.3.1 Ta cap layer: Sample 1 and sample 2 and sample 2'

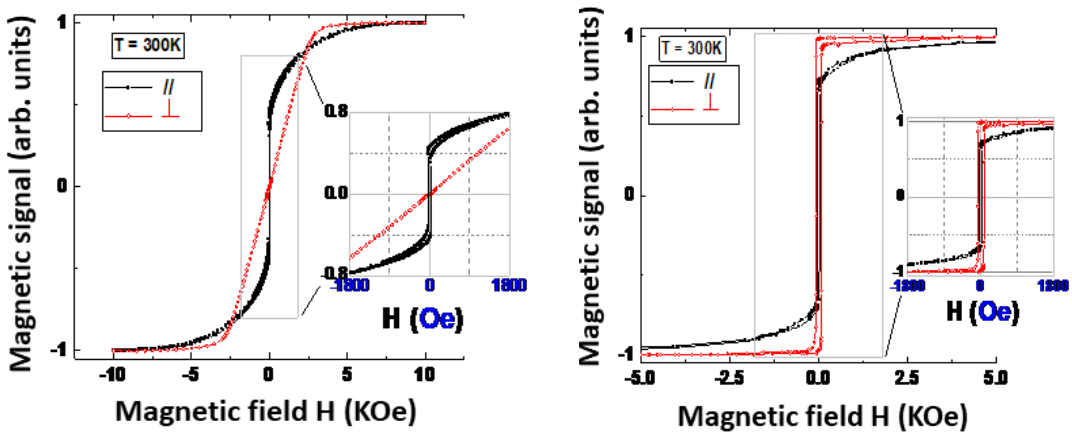

Figure 4.4 *Ip* and *oop* M(H) loops of as deposited half-MTJs with Ta cap layer for sample (a)as deposited and (b)annealed till 340°C

Figure *4.4*(a) and (b) shows the results for S1 and S2 containing insets within ±1800 Oe. For S1, we observe that the **magnetic anisotropy of the CoFeB layer is *ip***. It can also be clearly seen from the inset of Figure *4.4* where it should be noted that the magnetic saturation occurs only above 8 kOe which corresponds to an amplitude of magnetic field larger than the one available in the RESOXS experiments. **Remanence magnetization accounts for 47% of saturation magnetization from these results.** However, after annealing at 350°C we observe a transition in magnetic anisotropy of the CoFeB layer is now preferentially ***oop*** with close to 100% of the magnetization at saturation in remnant condition. Compare to S1, it can be noted that a larger magnetic field, in the range of 14 kOe (not shown), is required, to get the magnetization *ip*. However, the CoFeB layer retains more easily it's *ip* magnetization since the amplitude of the magnetization **at remanence is about 70%** of the value at saturation for S2 and only 47% in S1.

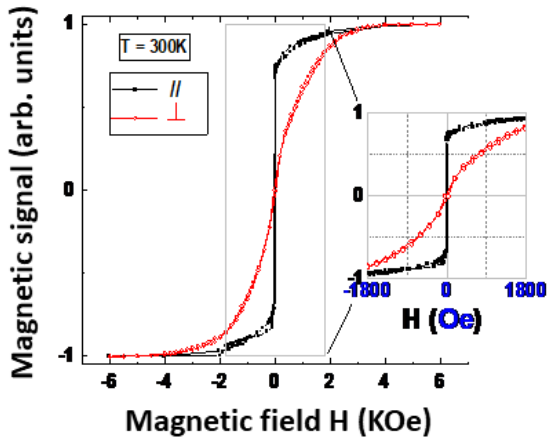

Figure 4.5 *Ip* M(H) loops of annealed half-MTJs with Ta cap layer (annealed till 400°C)

Figure 4.5 shows the results for **S2'** after annealing at a slightly higher temperature (400°C against 340°C), and we can see that **the magnetic anisotropy is again *ip***. Compare to S1, it can be noted that the saturation magnetization is reached at about 4kOe and the amplitude of magnetization **at remanence** is about **70%** close to the value for S2.

4.3.2 W cap layer: Sample 3 and sample 4

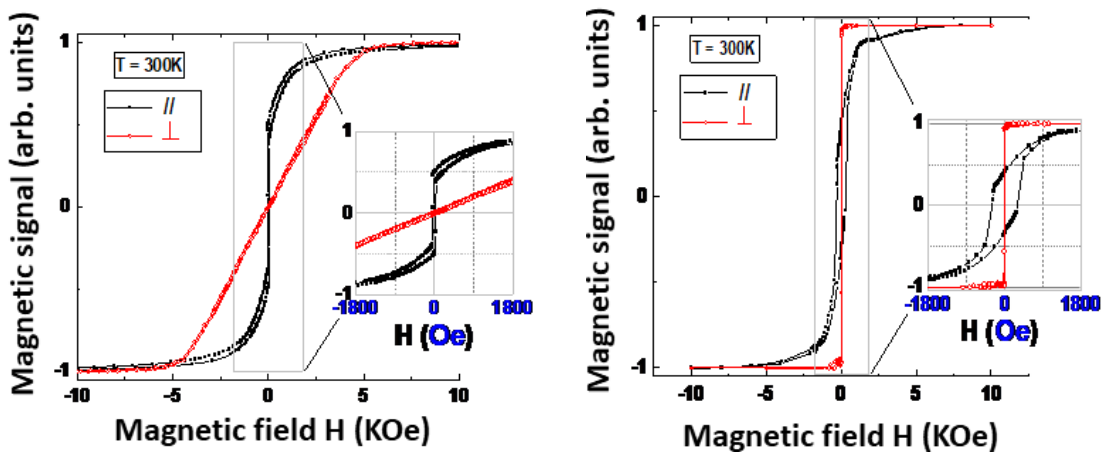

Figure 4.6 Ip and oop M(H) loops of as deposited half-MTJs with W cap layer for sample (a) as deposited and (b)annealed till 400°C

Figure 4.6 shows the results for **S3** and **S4**. **The magnetic anisotropy of the CoFeB layer is in plane** as for S1. Again, the magnetic saturation occurs above 8 kOe which corresponds to an amplitude of magnetic field larger than the one available in the RESOXS experiments. Remanence magnetization accounts for about 50 % of saturation magnetization

The magnetic anisotropy of the CoFeB layer is now preferentially **out-of-plane with close to 100% of the magnetization at saturation in remnant condition**. Compare to S3, it can be noted a similar amplitude of the applied magnetic field is required to saturate the magnetization in-plane. Additionally, a larger coercive field is observed, and the magnetization at remanence is reduced to 40%.

4.4 Investigation by Soft X Ray Resonant Magnetic Reflectivity

4.4.1 Qualitative analysis

In order to understand contributions of *ip* and *oop* components in our samples, we start by qualitative analysis of our samples S1, S2, S2', S3 and S4. Although all the measurements are made in the vicinity of Fe L3 edge, we were able to make some measurements in the vicinity of Co L3 edge for S4, which will be presented. It must be noted that the measurements were conducted at different periods of beamtimes thus, there may be some variations in experimental energies (within 1 eV) as well as in the intensity of the incoming beam.

4.4.1.1 Results for Ta cap layer

4.4.1.1.1 Sample 1

The comparison of SQUID and EHE data for S1 shows the magnetic anisotropy is *in plane* and thus we are prompt to use the **FlipHIon** acquisition mode.

Energy dependent reflectivity at specific angle

In Figure 4.7 we present the reflectivity scans at 3 different angular values – 5°, 14° and 26° together with their magnetic asymmetries. During the experiments on the SEXTANTS line, these energy dependent curves were used to choose photon energy in the vicinity of the L_3 edge to perform angular dependent scans. The refinement of these curves will allow us to determine the precise value *energy correction* to be taken into account for proper energy calibration.

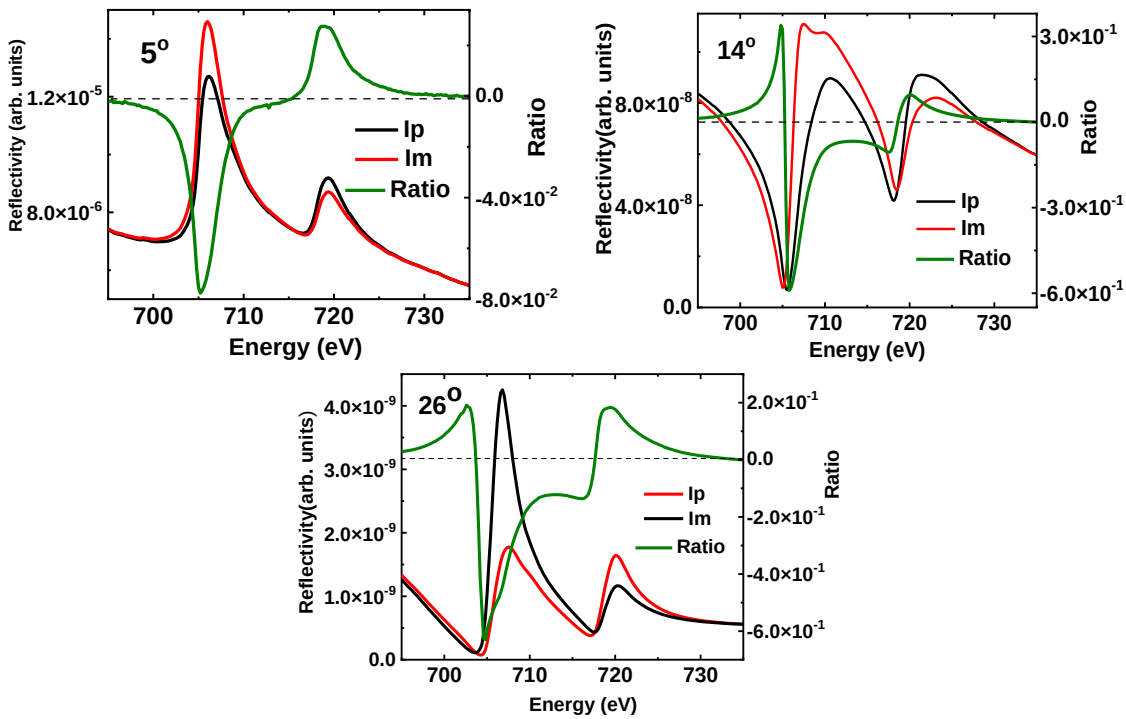

Figure 4.7 Experimental (red and black smooth lines) specular reflectivities at for 5°, 14° and 26° measured for S1 along with asymmetry ratios (blue smooth line)

Here, the smooth green line represents the strong magnetic asymmetry calculated from the intensities of left and right circular polarized light (*Ip*, *Im*) in the vicinity of the Fe L_3 and L_2 edges related to the nominally 1.4 nm thick CoFeB free layer as the 0.4 nm thick CoFeB layer below the MgO one is expected non-magnetic. Various shapes are related to the fact that the data have been collected different q value and hence a mixing of the real and imaginary part of the charge resonant parameters for the *Ip* and *Im* intensities as well as a mixing of the real and imaginary part of the magnetic resonant parameters magnetic asymmetry.

- For an incident angle of **5°**, both *Ip* and *Im* mimics quite well XAS data of Fe [120] and therefore the signal is dominated by the imaginary term.
- In contrast, the shape of the intensities and of the magnetic asymmetry collected at θ = **14°** are closer to the real part.
- The data collected at θ = **26°** looks like very much the one at 5°, except the crossing at 704 eV indicating a significant real part contribution as illustrated by the crossing at 704.5 eV in the data at 14°.

We expect at low angles to get a signal closer to absorption of Fe, since we are not sensitive to the structure at low angles as the beam goes into the sample without being scattered so absorption is high. On the other hand, as we go towards higher angles, we observe a larger intermixing of real and imaginary parts of ASF as the beam is scattered by interfaces giving us an interference pattern.

The position of the resonance appears to slightly shifted towards the low energies and this shift will have to be determined. At the time of these measurements the detection of the TEY signal was not working properly. Therefore, the photons energy for the measurements of the angular scans were selected with respect to these 3 curves and the adjustment of the energy values, that will be used for the fit of the angular scans, will be performed from a multi-angular fit of the energy dependence of the average intensity and discussed in the quantitative analysis.

Hysteresis loops at RESOXS

The maximum field available in RESOXS at the time of this experiment was 1700 Oe which was not strong enough to reach magnetic saturation, and probably not strong enough to ensure a single domain configuration as seen by SQUID. This question will be addressed in this section where we present hysteresis loops inside the RESOXS chamber.

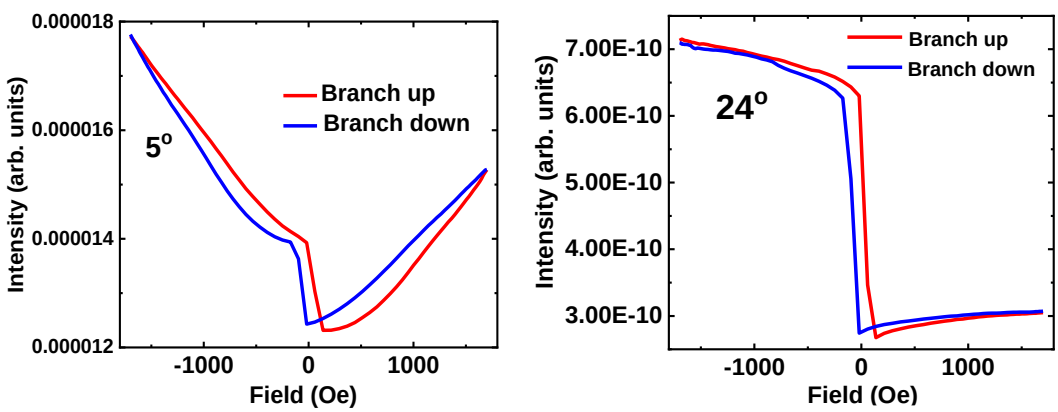

Figure 4.8 Hysteresis loops measured at RESOXS at 706.2 eV at 24° and 5°

We have used the ability of the RESOXS device to record the element-selective hysteresis curve (here only for Fe atom with the higher percentage in the composition).

Figure 4.8 shows hysteresis loops collected at θ = 24° and θ = 5° energy 706.2 eV with left circularly polarized light. This curve represents the variation of the specular reflected intensity at a specific angle

and for a defined incoming photon energy with respect to a magnetic field applied along the longitudinal direction.
At θ= 24° it shows mainly a square like reversal magnetic curve with a coercive field very close to the one observed by SQUID data in
Figure 4.4. At first glance, this hysteresis curve resembles that obtained from the SQUID data. However, there is a second contribution in the signal as illustrated by the slow decrease when going from negative to zero field and, after a cusp, a slow increase when going from zero to positive field. This second magnetic contribution is related to another net component of the magnetisation which appears to be larger on either side of zero. Its presence induces a different form of magnetic asymmetry at 24° than that produced by longitudinal magnetisation due to a very different angular dependence and combination of real and imaginary parts. The consequence is that the field-dependent intensity variation between *Ip* and *Im* is modified compared to that which would be due solely to a net longitudinal contribution. The signal at θ= 5° appears during the reversal of the magnetisation along the longitudinal direction, is preferentially attributed to a net in-plane transverse contribution of the magnetisation, as opposed to a net component perpendicular to the film. This attribution is supported by the following observation: if one seeks to isolate this additional signal by subtracting a step contribution for the longitudinal part, it appears that the reflected intensity at +1700 (A) to and -1700 Oe (B) is more or less identical, which is expected for a transverse component with a circular incident beam unlike a perpendicular component.

In the quantitative analysis section, we will try to determine the amplitude of the average magnetization by refining the magnetic asymmetries collected at low angles, which are less sensitive to an inhomogeneous distribution of the magnetization as to compare to magnetic asymmetries at large angles [160].

Angular dependent reflectivity scans

The next section presents the angle-dependent reflectivity curves and the derived magnetic asymmetries collected with H = 1700 Oe. Figure 4.9 shows the data recorded at 670 eV, 705.2 eV, 706.2 eV, 707.2 eV and 708.4 eV. Corresponding asymmetry ratio R (blue smooth line) has been plotted in the right column. They are values selected from the energy dependent reflectivity scans. As mentioned previously, more precise values have to be determined before trying to extract parameters from a refinement.
We also present average reflectivity at 670 eV which is sufficiently below the Fe L3 edge (-36.8 eV), useful for the determination of the structure specifically mass densities since we get rid of the uncertainties of the amplitude of resonant parameters. This is usually related to the various sources such as improper energy calibration since differences in the exact incident photon energy during the time of experiment in comparison with the one we use for calculations in DYNA.

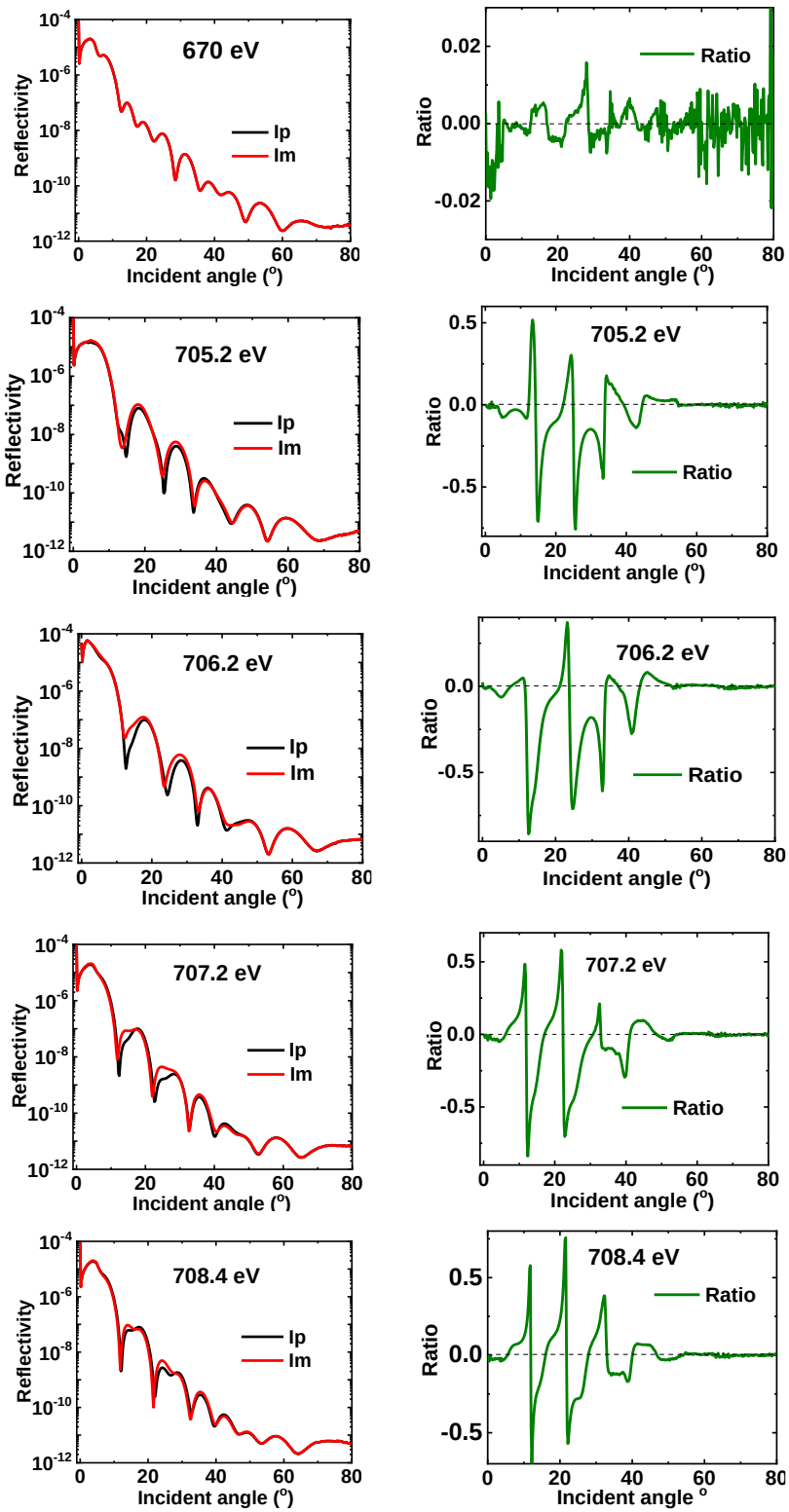

Figure 4.9 Experimental *Ip* and *Im* (red and black smooth lines) specular reflectivity at 670 eV, 705.2eV, 706.2eV, 707.2eV and 708.4 eV measured for S1 in the left column. Corresponding asymmetry ratio R (blue smooth line) has been plotted in the right column

A small signal (less than 1%) AT 670 eV in the magnetic asymmetry *R* indicates that the small real part of the resonant magnetic parameter *m'*(*m"* ≈ 0) is sufficient enough to play a sizeable role in separating I_p from I_m at least up to 50°. Additionally, the magnetic asymmetry at 670 eV is showing the level of noise in our experiment, especially at large angles, where the reflectivity is of the order of a few 10^{-12} amps.

The change in shape of the intensities as well as the asymmetry ratios can be observed as we go from 705.2 eV to 708.4 eV accounted to the different sets of parameters f_1, f_2, m_1 and m_2 at each energy value. The differences between intensities *Ip* and *Im* directly indicates the presence of magnetic ordering of Fe in the sample. The splitting starts to occur from 10° going up to almost 50° giving rise to an asymmetry ratio of large amplitude (right column) and reducing to 0 at higher angles. The reflectivity curves at all small angles for energies above 706.2 eV are significantly reduced. This can be attributed to the change in beam size which will be understood by the quantitative analysis. However, it must be noted that this effect, limited to values under the critical angle (or slightly above) will not affect the analysis of the magnetic asymmetry for a layer buried under two other layers whose nominal total thickness is 4 nm.
Referring to the equation we developed in chapter 2, we can say that it indicates an *ip* magnetization component in the magnetic layer, in agreement with the geometrical dependence of the atomic scattering factor corresponding to its relationship with $\cos^3\theta$. Thus, the magnetization is entirely in plane and longitudinal which can be said for all energies.
The very small asymmetry signal, ranging from -1% to +1% visible at baseline is showing the level of noise in our experiment, especially at large angles, where the reflectivity is of the order of a few 10^{-12} amps.
We will quantify these results to have a depth resolved picture on magnetization in the CoFeB layer in quantitative analysis section.

4.4.1.1.2 Sample 2

S2 was subsequently annealed at 340°C and the measurements performed by EHE shows square hysteresis loops with 100% remanence indicating *oop* magnetisation. We therefore start our experiment by using the RevPol mode in order to probe the magnetisation component. Although the EHE measurements show almost 100% remanence, in order to correct any demagnetization linked to the storage time and transport of the sample on the SEXTANTS beam line we decided to expose the sample to a permanent magnet.

Energy dependent reflectivity scans

Just as we described in the case for S1, we first present energy dependent *Ip* and *Im* reflectivity curves along with the asymmetry ratios shown in at 8 different θ angles (5°, 30°, 40°, 45°, 50°, 55°). We were able to measure ranging from 5° to 55° because of the signal expected from *oop* magnetization is expected to larger angles due to dependence on $\sin^3\theta$ as shown in details in section 2.4.1.3. This set of measurements was conducted in a different period of beam time, which means there can be some difference in the energy calibration as compared to S1.

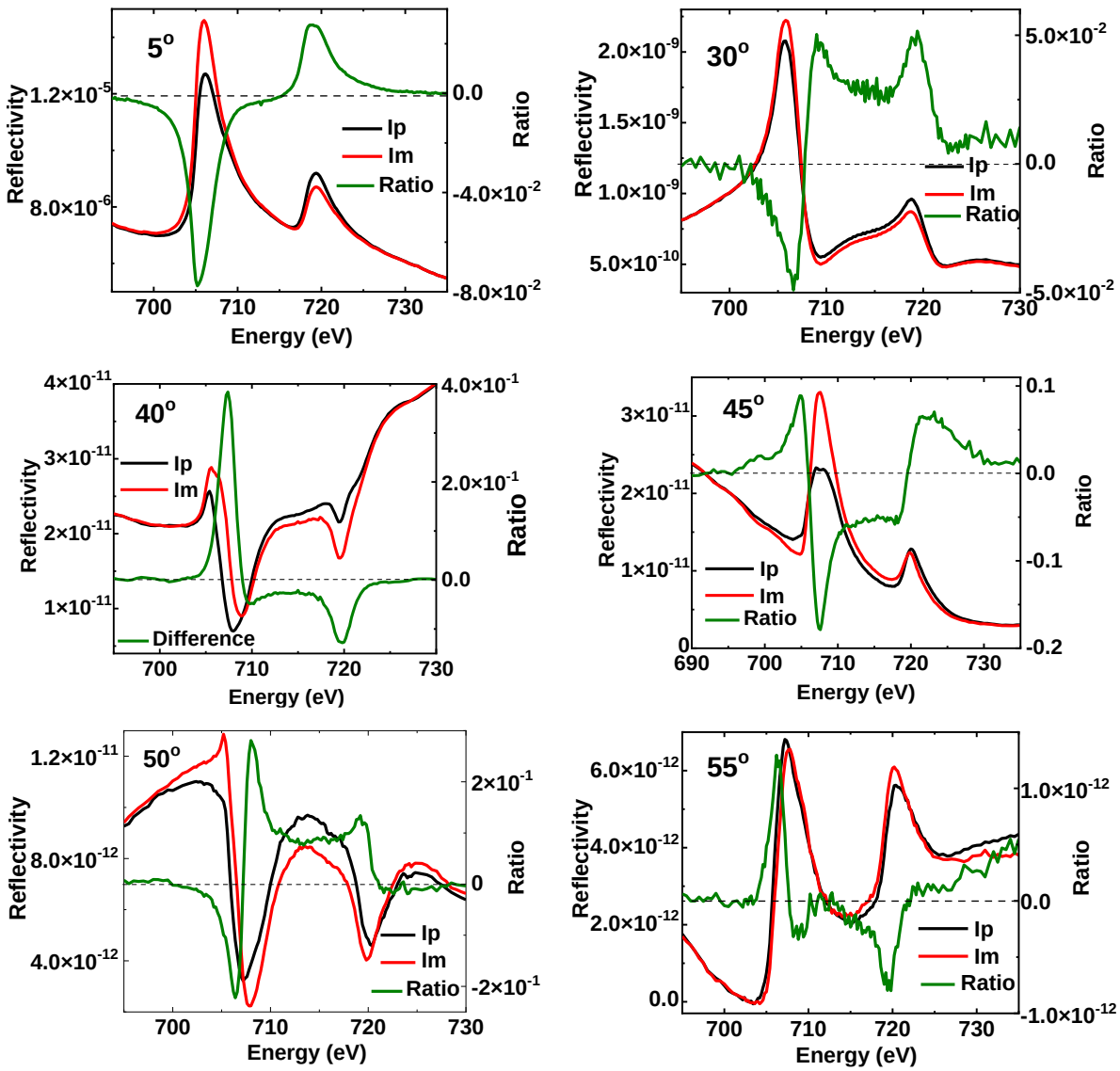

Figure 4.10 Experimental (red and black smooth lines) specular reflectivity at 5°, 30°, 40°, 45°, 50° and 55° measured for S2 along with asymmetry ratios (green smooth line) for each angle plotted on the right Y axis.

We can see that the *Ip* and *Im* at 5° mimics the *absorption of Fe* for metallic Fe [120] while at other angles we can see a mixing of real and imaginary part of *ASF*. As expected, the shape of the *Ip* and the *Im* intensities are very different at the different angular positions. The refinement of these measurements will allow us to determine the precise energy calibration to be considered in the quantitative analysis of the angular dependent reflectivity data.

The spectroscopic features of these curves, such as the position of the maxima in the magnetic asymmetries, will also help to optimise the choice of energies to be used for the angular scans.

Angle-dependent reflectivity

The angle-dependent reflectivity curves *Ip* and *Im* are collected at 670 eV and at three resonant energies 706.4 eV, 707.4 eV and 708 eV shown in left column of Figure 4.11 as well as the magnetic asymmetries derived from these curves (right column).

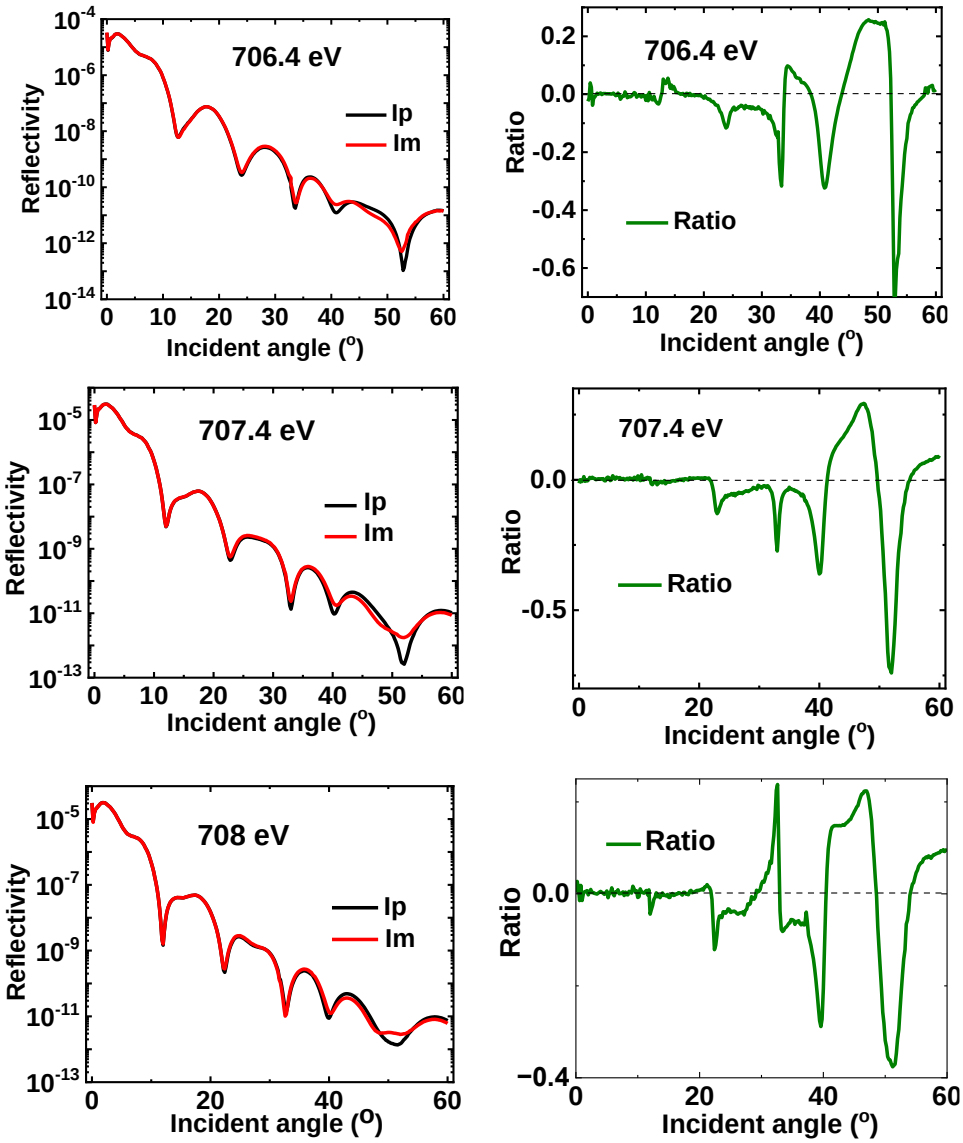

Figure 4.11 Experimental (red and black smooth lines) specular reflectivity at 706.4 eV ,707.4 eV and 708 eV measured for S2 in the left column. Corresponding asymmetry ratios (green smooth line) for each energy has been plotted in the right column.

Unlike S1, we notice that for S2 absence of splitting in lower angular range from 0° to 20° while splitting of *Ip* and *Im* occurs at larger angular range visible above 30° up to 60° at each energy. This corresponds to a magnetic asymmetry from an entirely *oop* magnetization as derived from the $\sin^3\theta$ dependence of the m_{pol} contribution in the analytical expression of *R* as discussed in Chapter 3. In agreement with the EHE

data, we are clearly sensitive to the easy *oop* magnetic axis of the sample at remanence and hence there is a clear transition of anisotropy from S1 to S2 after annealing through SXRMR as seen by the strong changes of the shape of the magnetic asymmetries. Quantitative analysis will tell us if the transition from in-plane to out-of-plane magnetization after annealing at 340°C is accompanied by a modification of the magnetization profile.

During the experiments on S2, we were also interested in the evolution of the magnetization profile when the sample is subjected to a longitudinal magnetic field of 1100 Oe. First the measurements were performed using the **RevPol mode** and we observed a strong magnetic contrast at small and wide angles revealing the simultaneous presence of *in-plane* and *out-of-plane* magnetisation components. This configuration may typically be due to a canting of the net magnetisation. To assess the stability of this configuration, we also measured the magnetic contrast using the **FlipHlon** mode (H=1100 Oe) for both CR and CL polarisations. Both data sets confirm the presence of two components. One of the motivations was to determine whether a change in the magnetisation amplitude distribution as a function of depth could possibly accompany the rotation of the magnetisation.

4.4.1.1.3 Sample 2'

We conducted measurements on another part of the MgO/CoFeB/Ta sample which was annealed at a higher temperature 400°C compared to S2 in order to observe any change in magnetic distribution or magnetic anisotropy after annealing higher temperature. From the SQUID results we have observed that there was a loss of PMA at this temperature resulting in *ip* anisotropy. The motivation was to probe changes in the magnetisation profile compared to S1 and S2 and possibly to gain additional information on the loss of PMA.

Energy dependent reflectivity at a specific angle

Figure 4.12 shows the energy dependent *Ip* and *Im* reflectivity curves collected at 4 different θ angles (5°, 13.8°,22° and 25°) together with the magnetic asymmetries at each energy plotted on the right-hand side Y axis. These curves were measured in RevPol mode at the remanence because at the time of the measurements, the magnetic anisotropy of this sample was expected to be *oop*. It was during the measurement that we realized that the magnetization of the sample was actually *ip*. As the magnetic contrast was strong enough, at least at small angles, we did not collect a new set of data in FlipHlon mode. New SQUID measurements on this piece of sample then showed that in remnant condition it exhibited a planar magnetization and 75% of the saturation magnetization.

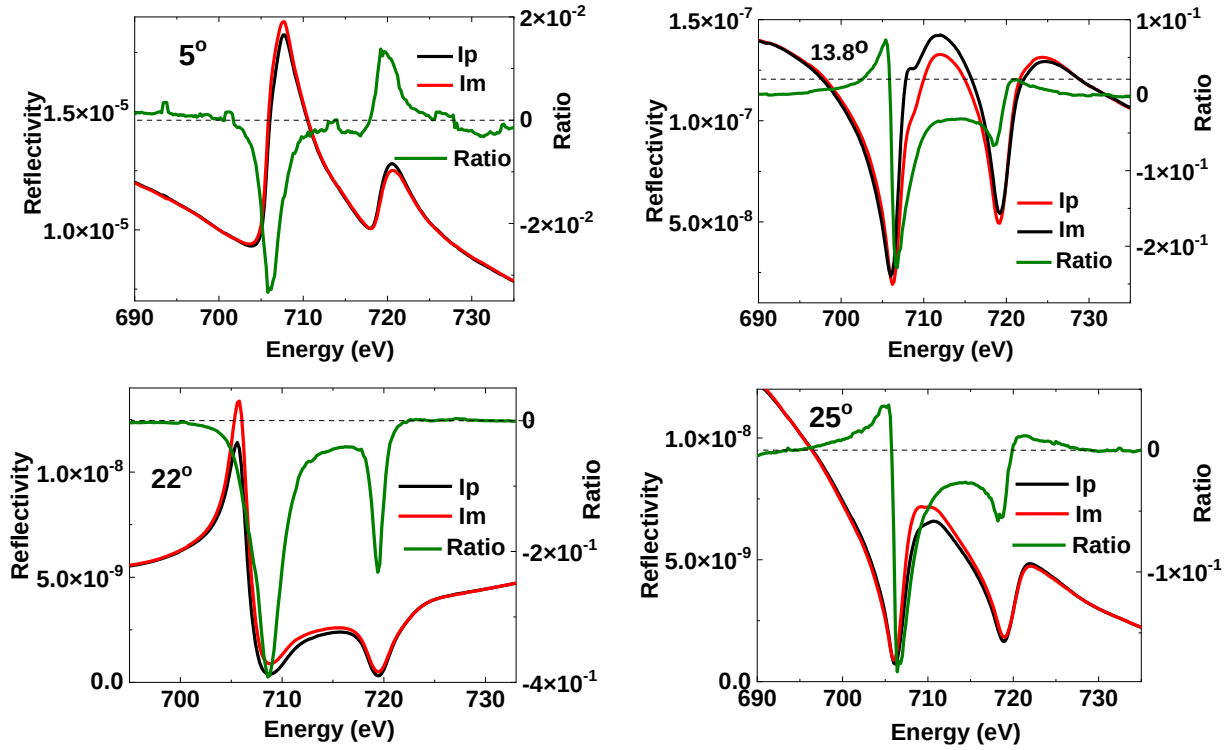

Figure 4.12 Experimental (red and black smooth lines) specular reflectivity at 5°, 13.8°, 22° and 25° measured for S2' along with asymmetry ratios (green smooth line) plotted on the right y axis.

The curves recorded at 5° and 13.8° exhibits general features similar that was seen for S1 in Figure 4.7. It is not possible to comment for the data collected at 25° for S2 and 26° for S1, because huge variations could occur with 1° difference. The fact that the data are similar at 5 and 13.8° indicates the effect of the annealing on the structure is not significant in this angular range.

If we compare the energy dependent reflectivity scan at 5° for S1 and S2' in *Figure 4.7* and Figure *4.12*, we can observe formation of a small shoulder around 706 eV in the reflectivity. If we refer to [161] the "shoulder" could rather be the increase of the intensity at the high-energy side of Fe L3-edge. In fact, although at 5°, the energy dependence reflectivity looks like the measurements of absorption by TEY, it is not a pure measurement of the absorption. It is therefore difficult to exclude that the difference observed at 5° is due to a small modification of the structure (linked to annealing at a higher temperature) rather than to an oxidation effect [162]. However, one would not expect to observe a change in reflectivity due to a change in stacking properties at an angle so close to the critical angle (about 3°). This will need to be verified with angle-dependent measurements but we believe that the 5° change is related to over-oxidation of Fe at the interface with MgO, which could at least partly explain the strong decrease in PMA.

Angle dependent reflectivity

Figure *4.13* presents the average intensity I_{av} and asymmetry ratio R. We wish to make a comparison between S1, S2 and S2' qualitatively, however the comparison is not very simple since the samples were measured at different times thus face variation of energy. The reflectivity curves of S2 are less relevant due to a shift of 0.2 eV of the incident photon energies, in particular near the Fe L_3 edge and a transition from in the plane to out of the plane for the magnetization which leads to intrinsically completely different magnetic asymmetries.

For S2', we can say by the shape of the magnetic asymmetries confirms the magnetization is entirely in the plane, meaning degradation of PMA occurs as soon as the annealing temperature rises over a certain threshold temperature. Such a phenomenon has been observed before for Ta cap layer on Ta/CoFeB interface [142]. We observe decrease of fringe amplitude of reflectivity in comparison with that of S1 not specifically at high scattering vector but for entire reflectivity curve. A strong change in reflectivity at 670 eV indicates that further annealing beyond 350°C strongly changes the structure of the thin film. The shape of asymmetry ratios again indicates that there has been a transition from *oop* back to *ip* as the signal is stronger at lower angles. It will be interesting to observe changes in structure and also how magnetisation profile changes from each sample.

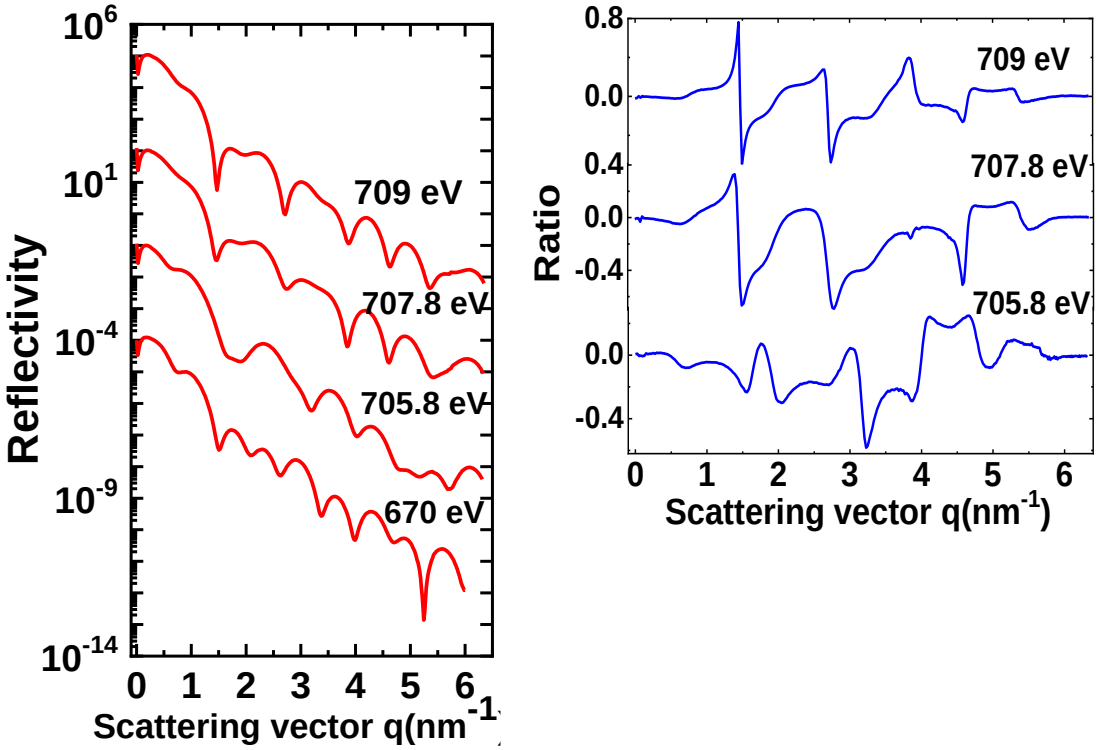

Figure 4.13 Experimental (red and black smooth lines) specular reflectivity and asymmetry ratio at 670 V,705.8 eV, 707.8 eV and 709 eV measured for S2' in the left column. Corresponding asymmetry ratios (blue smooth line) for each energy has been plotted on the right at column.

4.4.1.2 Insertion of W

In the following section, we will present the results on the series of sample with cap layer of W/Ta. We will follow the same steps as the three previous samples and highlight the main qualitative differences that can be observed by introduction W layer in the stacking.

4.4.1.2.1 Sample 3

This is the as-deposited MgO/CoFeB/W/Ta sample (S3) and as shown by SQUID results previously it indicates presence of *ip* magnetisation.

Energy dependent reflectivity at a specific angle

Figure 4.14 shows *Ip* and *Im* reflectivity curves collected at 4 angles - **8°**, **15.5°**, **21.5°** and **29.5°** together with calculated magnetic asymmetries (smooth green line). Except for the energy dependence of the reflectivity collected at 8°, that looks like absorption measured in transmission, the 4 others reflectivity curves represent is a mixture of both dispersive and absorptive parts of the atomic scattering factor.

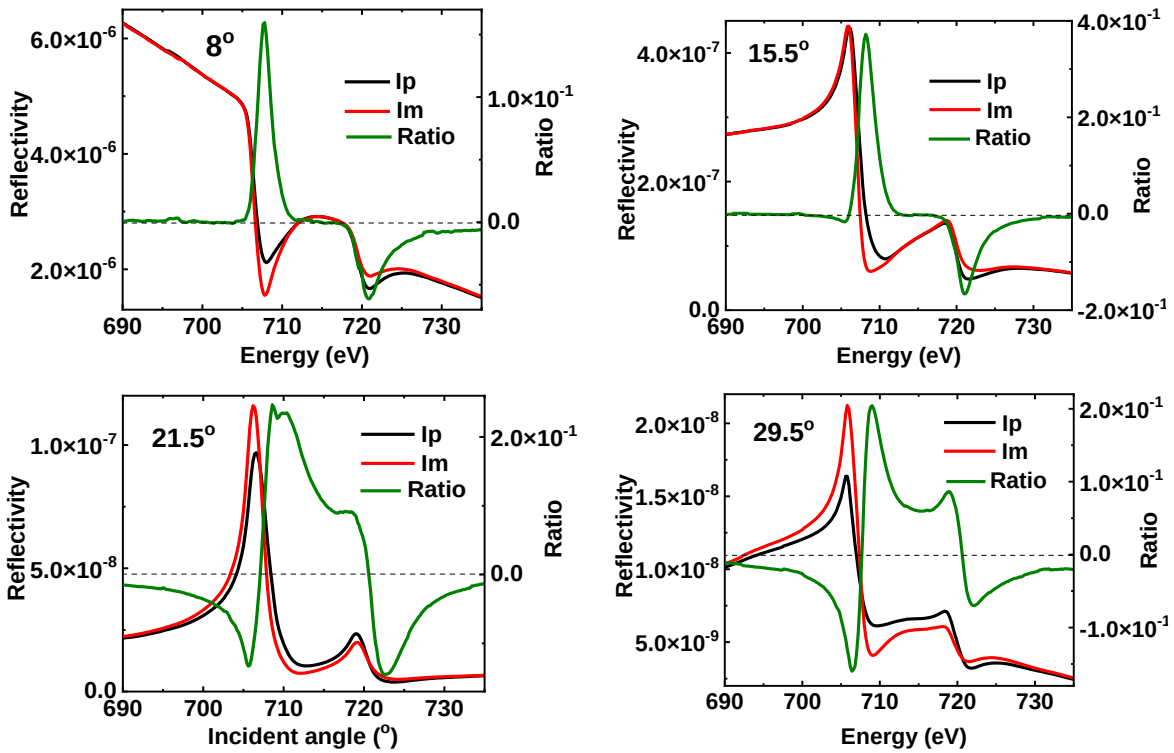

Figure 4.14 Energy dependent reflectivities *Ip* and *Im* (black and red smooth lines) at 8°, 15.5°, 21.5° and 29.5° with asymmetry ratios (blue smooth line) are presented in right y axis.

Hysteresis Loops

Figure *4.15*Figure *4.15* Hysteresis loops measured at RESOXS at 706.2 eV at 13.8° and 43.5° displays two hysteresis loops measured in RESOXS under specular reflectivity conditions at θ = 13.8°(a) and 43.5°(b) using an incident photon at nominally 707.8 eV.

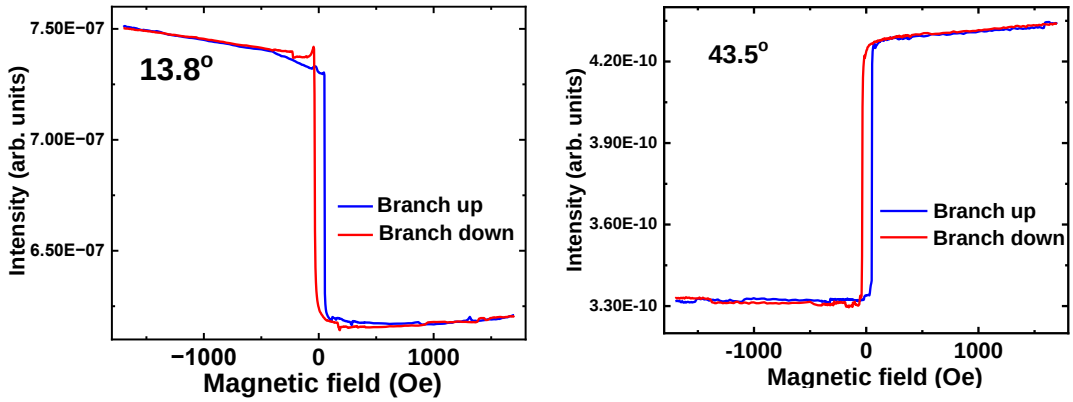

Figure 4.15 Hysteresis loops measured at RESOXS at 706.2 eV at 13.8° and 43.5°

They show the sharp reversal region observed in the SQUID data. Additionally, it appears that the loops are almost square and the two branches well superimposed above ±500 Oe. The opposite evolution of

the reflected intensity with the applied field is related to the change of sign of the angular dependence of the magnetic asymmetry at 707.8 eV for these values (see later). As for S1, the fact that the reflected intensities for the two branches overlap indicates that the net magnetization achievable at 1700 Oe and -1700 Oe correspond to a similar magnetic configuration, except for the orientation.

Angle dependent reflectivity

Figure 4.16 shows angle dependent reflectivity as red (*Im*) and black (*Ip*) smooth lines for applied field of -1700 and 1700 Oe respectively in the left column while the blue line represents the calculated asymmetry ratio, *R* in the right column. These measurements were performed for acquisition mode FlipHlon. We see that from 10° the splitting of *Ip* and *Im* becomes significant up to 45° giving rise to an asymmetry ratio which exhibits larger amplitude at lower angles and reduces to 0 as we proceed to higher angles (till 60°) showing existence of *ip*. However, compared to S1, the magnetic asymmetry starts to occur a larger angle (5° vs 10°). This is attributed to the position of the magnetic layer being deeper below the surface due to the insertion of the W.

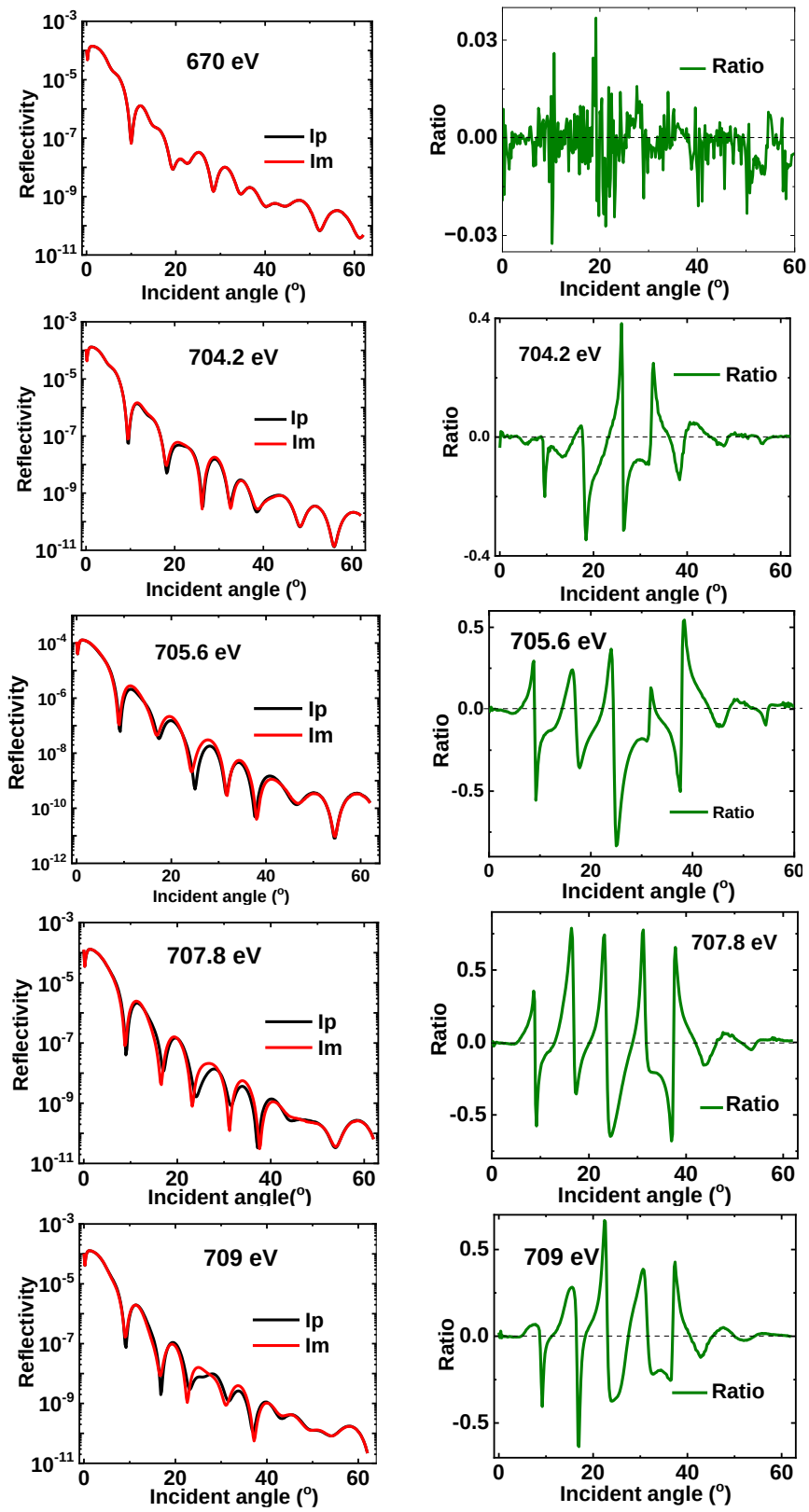

Figure 4.16 shows the experimental angle-dependent reflectivity collected at 670 eV and resonant energies 704.2, 705.6, 707.8, 709 eV in the left column. The corresponding asymmetry ratios for each energy are presented in the right column

4.4.1.2.2 Sample 4

Lastly in this section we will see the qualitative results for the sample S4 after subsequent annealing at 450°C similar to the case of S2. A similar pattern is followed where the results are presented from energy dependent reflectivity scans in order to help us choose the energies we worked on as well help in energy calibration to get quantitative results. The EHE measurement that showed a square hysteresis loop with 100% remanence as for S2, thus we have an idea of orientation of magnetisation vector.

Energy dependent reflectivity scans

We start discussion of our results at the RevPol mode where *Figure 4.17* shows the energy dependent *Ip* and *Im* reflectivity curves collected at **26.41°, 34°, 43.5° and 52.5°** together with the ratios which have been plotted in the right *y* axis. Since we are probing a sample with easy *oop* axis, we took measurements up to large angular value, where we expect higher sensitivity to this component.

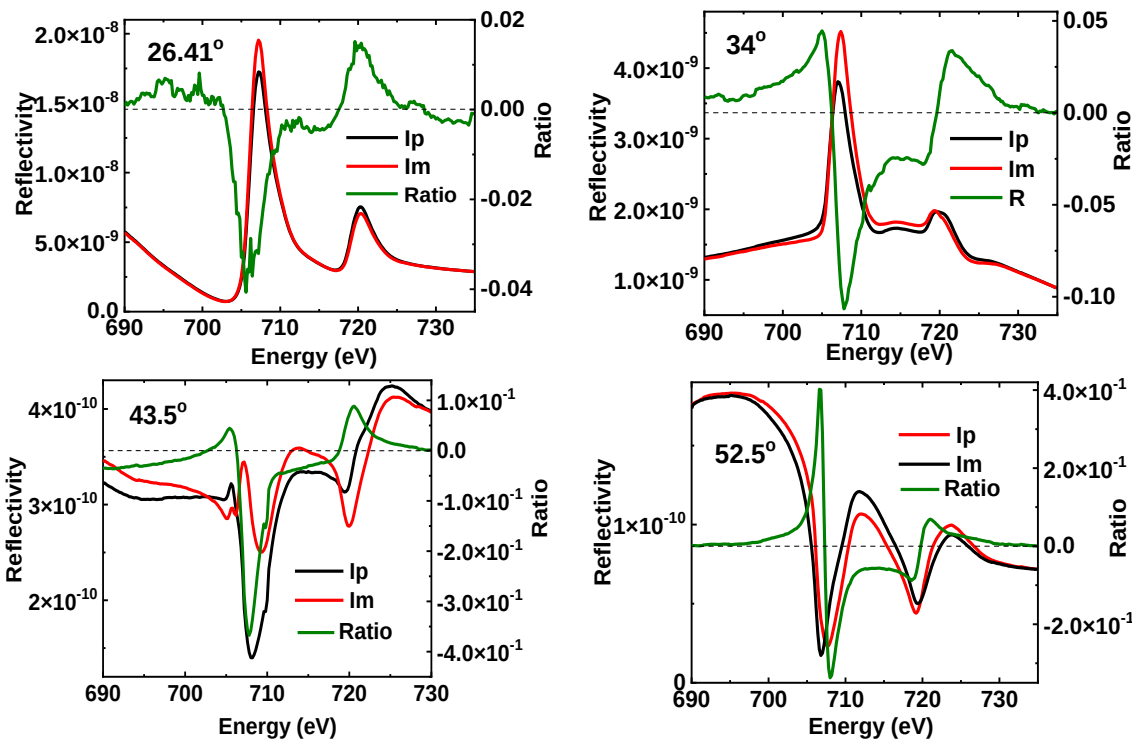

Figure 4.17 Experimental energy dependent reflectivity Ip and Im (black and red smooth lines) along with the asymmetry ratios plotted on the right y axis (green smooth line)

Again, such measurements show strong variations from one angle to another that are related to the interferences between the layers of the heterostructure. Unexpected details in the reflectivity curves can even be observed as in the case of the data collected at 43.5° below the L_3 edge. The quantitative analysis of these data, aiming at determining the energy calibration and at the same time obtaining additional information on the structure and the magnetization profile, will be presented in the following section.

Also, it is reminded that at the time of the investigation it was not possible to measure the out-of-plane hysteresis loops.

Angular dependent reflectivity scans till 60° and 80°

For this sample, we collected data for angular dependent reflectivity till angular range of 60° as well as 80° in order to get an improved knowledge on structure and specially the magnetization profile, since measuring till 80° means we are able to probe a larger **q** space for Fe. Thus, we can get improved depth resolution Figure *4.18* shows the angle-dependent reflectivity curves *Ip* and *Im* collected at 670 eV,704.2 eV, 707.8 eV, 709 eV as well as the corresponding magnetic asymmetries derived from these curves in the right column.

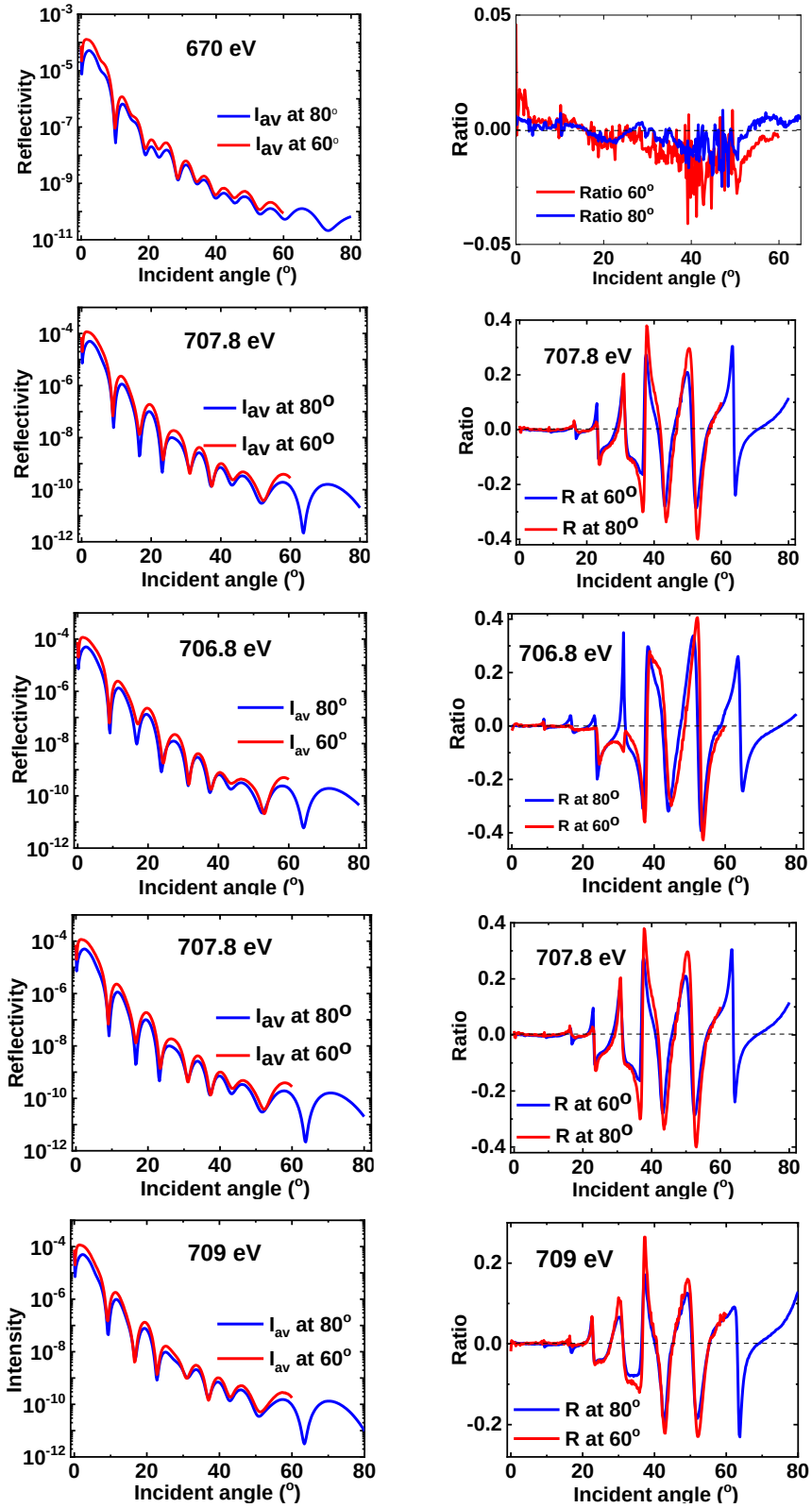

Figure 4.18 Experimental (red and blue smooth lines) specular reflectivity at 670 eV, 704.2 eV, 706.8 eV,707.8 eV and 709 eV measured for S4. Corresponding asymmetry ratio has been plotted on the right column for each energy.

Since this set of measurement took place at different periods of beamtimes, we can observe a slight difference in the intensity of the 2 reflectivities at 60° and 80° for all the energies shown. This is attributed to the different opening of the exit slits, 30 µm and 50 µm respectively at both time of measurements. However, both sets of reflectivities have the similar shape and are superimposable at each energy which is ideal. The corresponding asymmetry ratio retains almost similar shape for both sets of measurements with slight differences in amplitude of the asymmetries for both sets of measurements.

Moreover, the magnetic asymmetries show for 704.2, 706.8 and 709 eV a surprising high level of noise in particular compared to the data collected up to 80° where the magnetic contrast is relatively strong. The noise is due to the change of gain in the 2.10^{-10} range of the Keithley multimeter used for the measurements.

Co edge

Although all measurements were recorded mainly near the Fe L3 absorption edge due to the higher concentration of Fe, we also collect some data in the vicinity of Co L3 edge for S4. Since, there was not enough beam time to record several energy scans, we only performed 1 set of measurements at mode RevPol for energies 776.8 eV, 777.8 eV and 778.6 eV. The angle dependent reflectivity curves *Ip* and *Im* as well as the magnetic asymmetries derived from these curves are presented in Figure 4.19. The energy calibration of this set of data relies on the measurements of absorption through a thin foil of metallic Co. The edge was found at 777.8 eV for a tabulated value of 778.1 eV, therefore 0.3 eV will be added to the photon energies used during the measurements for the quantitative analysis based on simulation of this data.

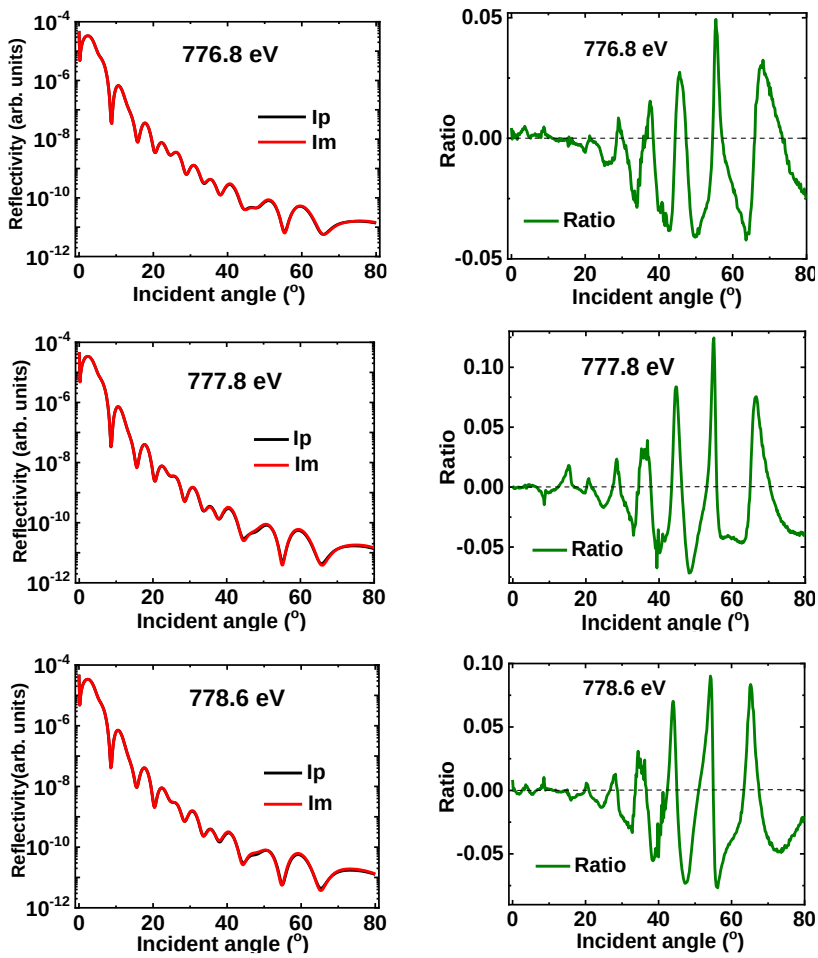

Figure 4.19 Experimental (red and black smooth lines) specular reflectivity at 776.8 eV, 777.8 eV and 778.6 eV measured for S4. Corresponding asymmetry ratio (green smooth line) has been plotted on the right column.

We can see that the reflectivity curves at all energies are quite similar which is attributed to the low amount of Co (8%) in the CoFeB layer of 1.6 nm nominal thickness. This quantity corresponds to a continuous layer of Co approximately 0.13 nm thick. The magnetic asymmetries are also very similar.

After annealing effect: S3 and S4

Annealing effect on a sample has been known to introduce structural changes such as changing of thickness or roughness at an interface of the sample or differences in composition grading. We are curious to see, what can superposition of average reflectivity and asymmetry ratio for S3 and S4 at different energies can show changes after annealing. This is shown in Figure *4.20*.

In the left panel we superimposed average reflectivity for S3 and S4 while on the right panel, we superimposed the asymmetry ratio.

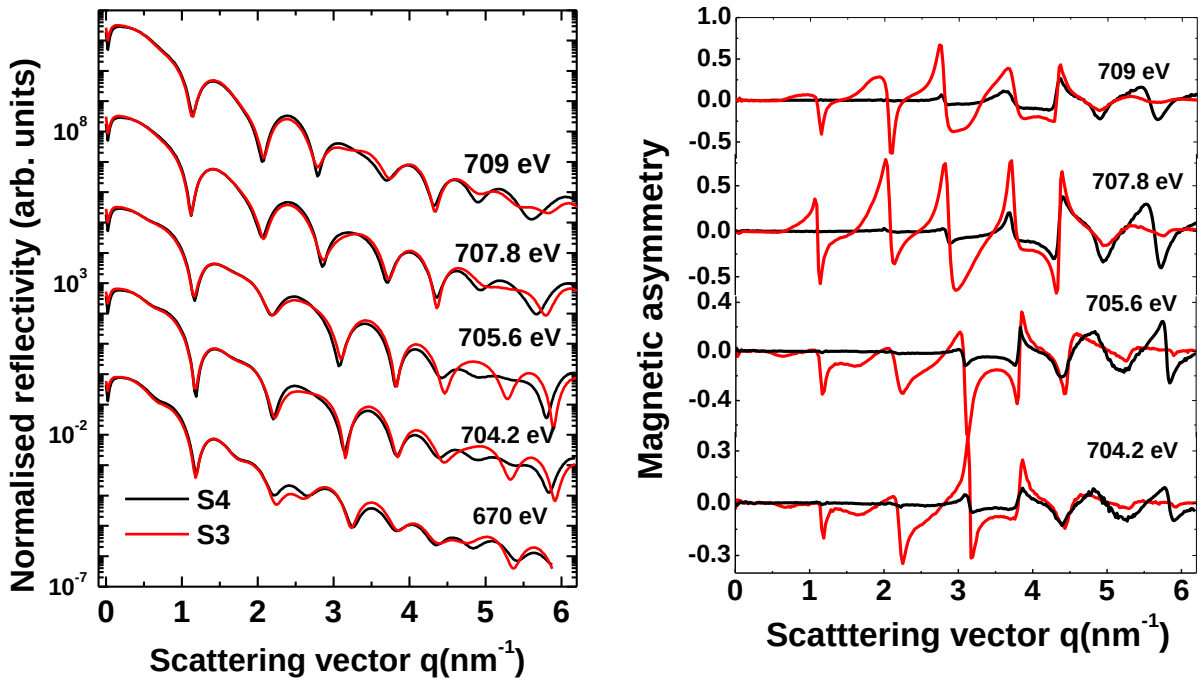

Figure 4.20 Average experimental reflectivities I_{av} (left column) and the corresponding asymmetry ratios (right column) superimposed for S3 and S4 at 670eV, and several energies in the vicinity of the Fe L3 edge

By looking at the comparison of *Iav*, we can see some changes directly in S3 and S4 differing from energy to energy, let us discuss these changes. For 670 eV, we observe that the oscillations are exactly superimposable till q = 2.2 nm^{-1} and shows changes (increase or decrease) in the amplitude of oscillations at some angular positions, however retaining the shape of reflectivity indicating a slight modification of the stacking after annealing. Changes for energies in the vicinity of the L3 edge of Fe become more significant such as amplitude of oscillations, shifts of the dip and formation of extra fringes. For 704.2 eV, 705.6 eV, 707.8 eV and 709 eV slight phase shift of reflectivity that is black curve for S4 has shifted more towards left than red curve for S3, is visible especially evident between q = 5.5 nm^{-1} and q = 6 nm^{-1}. This indicates change in thickness of particular a layer containing Fe atoms, since we only observe this change for energies close to L3 Fe edge. Another thing to note is formation of extra fringes particularly at 704.2 V and 705. 6 eV. Extensive simulations have revealed that changes in roughness and composition grading across interface generate additional interference fringes [163]. Also at large scattering vector from 4.5 nm^{-1} we see that intensity falls of faster for S4 than for S3 which may say that one of the interfaces has changed and thus roughness is maybe increased at some interface specially containing Fe atoms after annealing. Thus, all these observable changes in thicknesses and roughness's indicate that after undergoing annealing of sample 3 at 400°C, the structure is modified and quantitative analysis will reflect a better light on these changes.

Next, we observe changes in magnetic asymmetry after annealing for S3 and S4 for FlipHlon and RevPol respectively. Clearly a transition from *ip* to *oop* can be seen as soon as the sample is annealed as the oscillations at S4 are absent at low angles and oscillations for S3 die out at large angles.

4.4.2 Quantitative analysis

In this section, we are going to discuss the quantitative analysis by presenting the structural parameters as well as the magnetic profile for each sample S1, S2, S2', S3 and S4. This will be followed with a discussion on comparison of all magnetic profile obtained for each sample.

4.4.2.1 Ta cap layer

4.4.2.1.1Sample 1

Structure

Figure 4.21 shows the best fits obtained at RevPol and FlipHlon at 670 eV. We present both reflectivity curves at since they were measured at different periods of beamtime. The refinement of these two curves makes it possible to give an error bar on the structural parameters in particular on the densities we determined far from the absorption edge. The experimental data is in good agreement with fitted data. The derived parameters from the figure are given in Table *2* after the complementary analysis of the data measured in the vicinity of the Fe L3 absorption edge.

It must be pointed out here that the shape reflectivity at lower angles (up to 3°) can be seen as different. This is because, the measurements on the sample were not conducted at the same time, due to which beam size was slightly different.

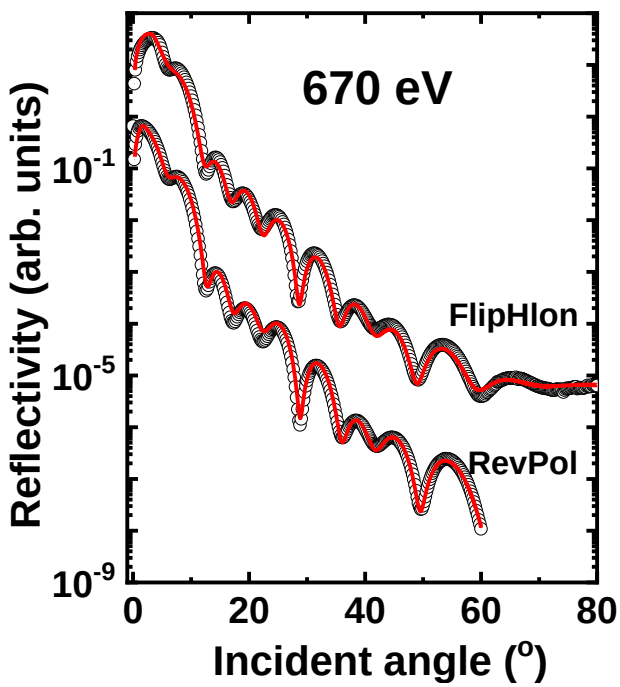

Figure 4.21 Experimental specular reflectivities (I_{av}) (black circles) along with their best fits at 670 eV for S1 at 2 acquisition modes FlipHlon and Revpol.

Before analysing the reflectivity curves collected at in resonant condition, we need to determine the amplitude of the energy shift to consider. By using the **structural parameters obtained at 670eV**, as an initial set of parameters, we perform a *multiA fit* and simultaneously refine the average energy dependent reflectivity curves at three different angular positions. We also perform *multiA fit* by considering a **gradient magnetization profile in the free CoFeB layer** to fit magnetic asymmetries. Figure *4.22* shows the experimental data at 3 angular positions and their best fit for average energy dependent reflectivity. Although we started to fit by considering a uniform profile for magnetisation, we had to consider a gradient profile in the end to have a good fit.

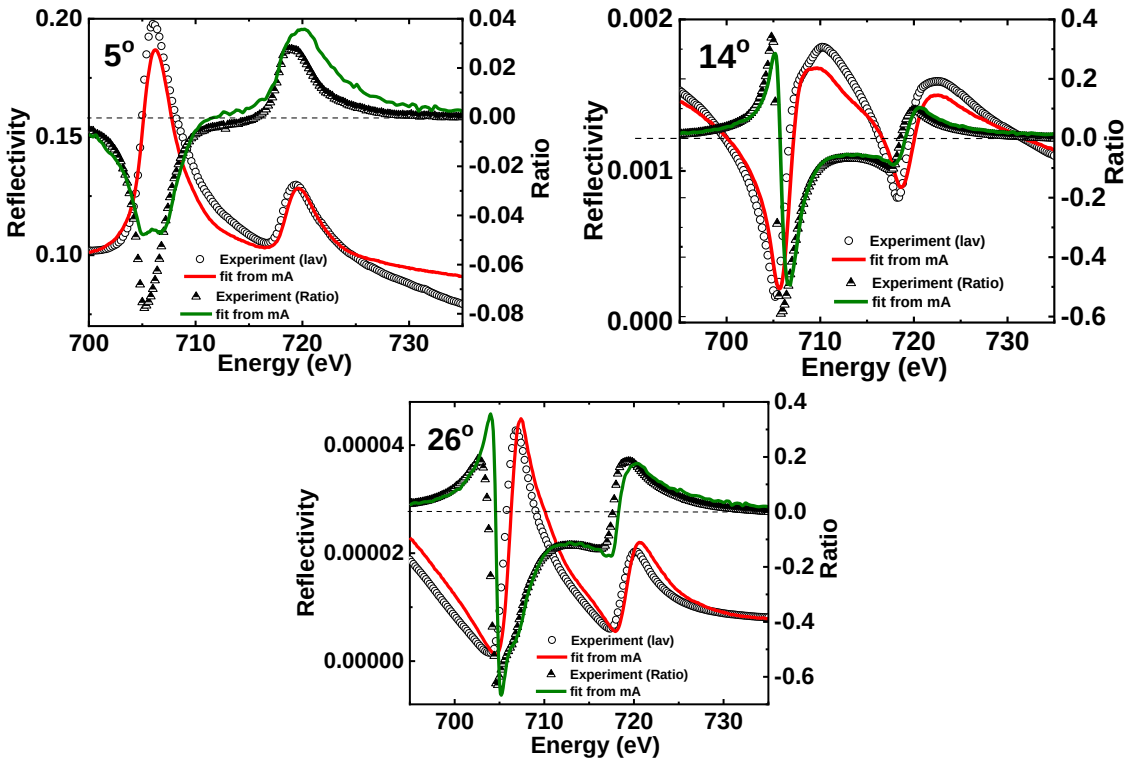

Figure 4.22 Experimental and fitted energy dependent average reflectivity(red line) as well as asymmetry ratio (green line) on the right *y* axis at 5°, 14° and 26°

The *multiA fit* carried out by using the same structural and magnetic model and same scaling factor at different angular positions. We are able to reproduce **reflectivity** nicely for all three angles.
The **fits of the magnetic asymmetry** also reproduced very nicely the shape of the experiments data except for the angle 5°. For all these angles the magnetic asymmetry was fitted with a gradient model with 4 sublayers. Although we tried to fit with only 1 sublayer with uniform magnetization, the small discrepancies as well as the small number of angular positions preclude from concluding about a homogeneous magnetization profile throughout the CoFeB layer [160]. For S3, we also show a fit of energy dependent magnetic asymmetry by considering uniform magnetic profile (1 sublayer).

It should be noted that we also made an attempt to consider a weak magnetization on the bottom CoFeB layer led to the absence of significant magnetization of Fe in this layer. For quantitative analysis of all the samples this led to the same conclusion.

Although we fit magnetic asymmetry here, we do not consider the amplitudes of *mms* very important. We will discuss *mms* in more detail for angle dependent reflectivity in the following paragraph. (It will be done the same way for all the samples)

The energy shift deduced from the fits is **δE = +0.45 ± 0.01 eV**. We will further look into what profile we obtain from refinement of the magnetic asymmetry of angular dependent reflectivity.
Following Figure 4.23 shows the experimental curves and their best fits taking into account the energy correction of **+0.45 ± 0.01 eV**. This is necessary to take into account due to difference in energy calibration of our measurement and the one of reference sample for which we calculated the resonant parameters in DYNA. We obtained fitted reflectivities in very good agreement with experiment for each energy. The derived parameters are shown in Table *2*.

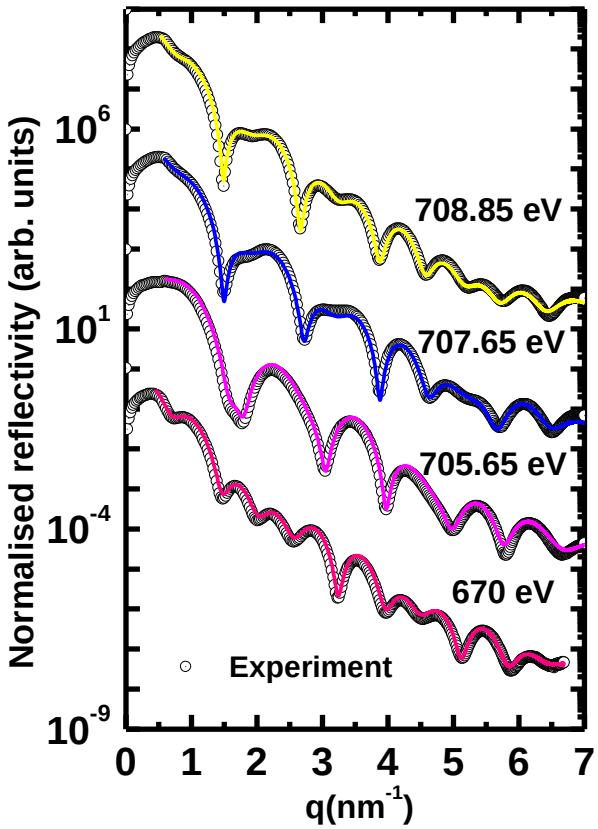

Figure 4.23 Experimental specular reflectivities (black circles) and their best fits at 670 eV at FlipHlon in the vicinity of the Fe L3 edge for S1

Table 2 Structural parameters *ρ, t and σ* for S1

	ρ(mol.cm^{-3})	t(Å)	σ(Å)
Pt	0.100 ± 0.05	30.4 ± 0.9	3.9 ± 0.1
Ta	**0.074 ± 0.009**	**7.8 ± 0.7**	**5.7 ± 2.1**
$Co_8Fe_{72}B_{20}$	**0.151 ± 0.009**	**13.5 ± 2**	**5.3 ± 1.6**
MgO	**0.152 ± 0.027**	**15.6 ± 2.2**	**5.7 ± 2**
$Co_8Fe_{72}B_{20}$	0.132 ± 0.021	3.2 ± 0.9	4.1 ± 0.9
Ta	0.074 ± 0.006	28.5 ± 0.9	4 ± 0.4

This table gives the average of over all the energies of thickness (t) and roughness (σ) after refinement of I_{av} along with error bars calculated by standard deviation. For ρ, we considered the values strictly from refinement at off resonant energy 670 eV, since we expect no influence of resonant affects that can occur due to difference in energy used during calculations. We observe almost no change in thickness of CoFeB and MgO as compared to the nominal values of 14Å and 15Å. We also note the roughness of CoFeB 5.3 ± 1.6 Å and 5.7 ± 2 Å for MgO. This roughness that may develop during deposition process due to mechanisms such as island formations at the interface. It must be said here that to make the structural profile given by SXRMR reliable, measurements are taken at several energies, which enables us to get an error bar which is presented along each parameter. Also, we take into account the structure at an energy far away from the edge, from which the data obtained is comparable to laboratory hard X ray reflectivity.

For Pt and Ta, we also observe a difference in their thicknesses with 2.2Å decrease in thickness for Ta in comparison with the nominal value of 10 Å. We must note here that during the refinement, between 2 Å to 4 Å thickness was interchangeable for Ta and Pt, therefore we fixed the thickness of Pt for refinement purposes. It would be interesting to see how the structure changes after the sample is annealed.

Magnetization profile

In order to arrive to the best fit, we performed various refinements by considering different models performed at more than one energy to confirm the accuracy of the best model. To constrain the determination of the magnetization profile, with the goal to avoid obtaining a very good experiment-simulation agreement with thicknesses of sub-layers whose sum would exceed the value of the thickness deduced from the fit of the reflectivity, I_{av} and R are then refined simultaneously. Figure *4.24* represents all the models at 2 energies 707.65 eV (right column) and 708.85 eV (left column). The first attempt is performed by just refining the amplitude mms for a single layer (constant profile) of Fe magnetisation throughout the layer, thus only fitting thickness of the CoFeB layer by setting ***mms*** = 1 for the whole layer. However, this value didn't stay at ***mms*** = 1, and as we can see, this did not result in the best fit to model asymmetry ratio for both energies. This led to considering a model by slicing the layer in half and define both slices with a specific value for ***mms*** and thickness. By considering 2 slices, we can see that we arrive closer to best fit, however at large angles, it can still be improved. In order to obtain the best fits, we considered a model with 4 slices of CoFeB layer which gave us a very good fits at all the energies proving

the correctness of this model as shown in Figure *4.25* (left panel). It must be noted that we kept the structure parameters constant at the time of refinement.

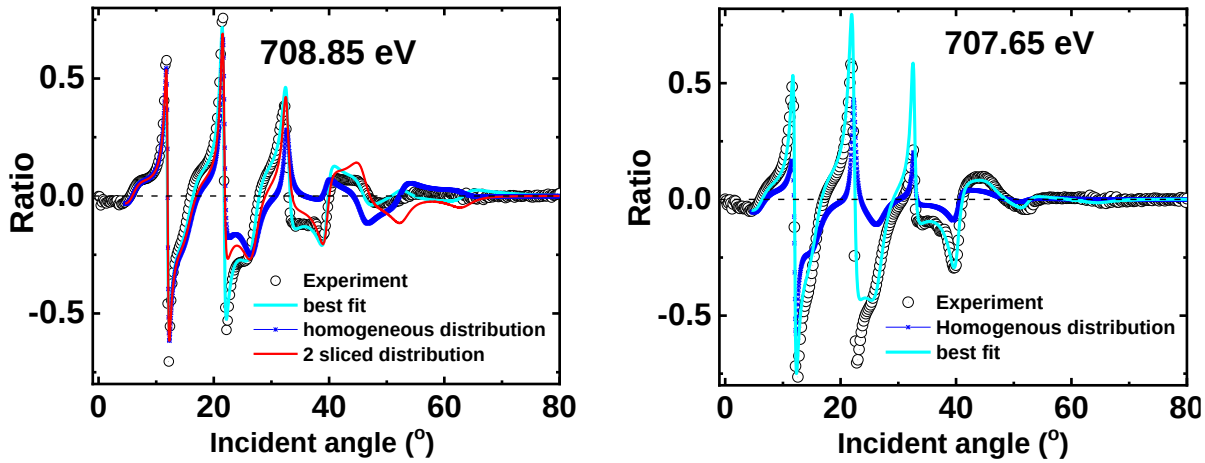

Figure 4.24 shows experimental and fitted asymmetry ratio at 708.85 eV and 707.65 eV for S1 at FlipHlon by considering several models to fit magnetic asymmetry.

Figure *4.25*(right column) shows magnetisation profile using derived values for mms and thickness over an average of all energies. On the *y* axis, we have the magnetic distribution represented by *mms* along with the error bars on the *mms* values as well as thickness of sublayers from the standard deviation of the values obtained for the different energies. Since, the profile does not consider the smoothing of the magnetisation between the sublayers, it was necessary to take into account the error bars for thickness.

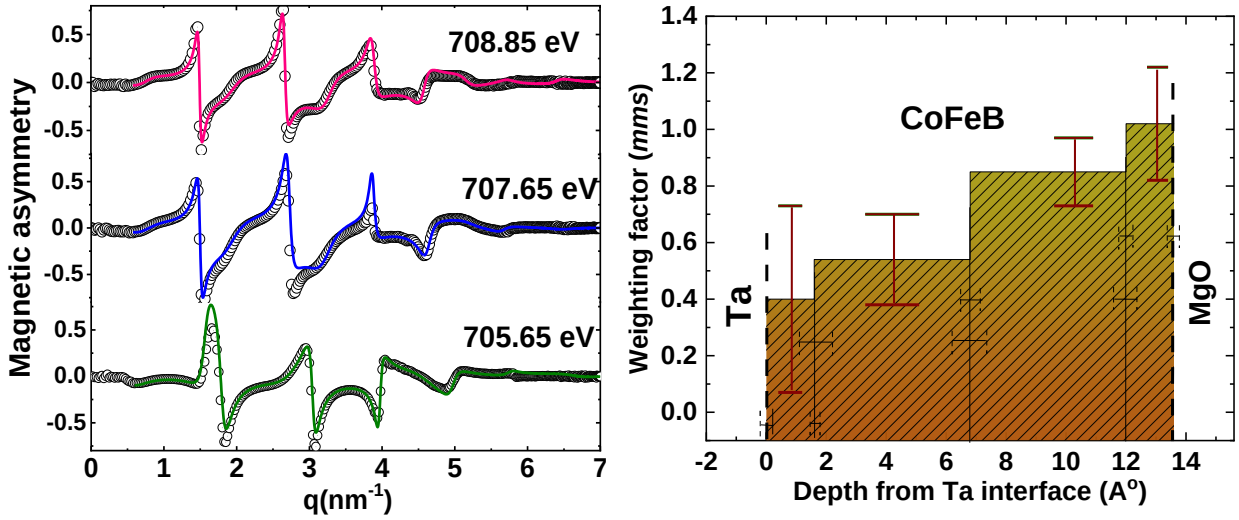

Figure 4.25 shows experimental and the best fits at energies 705.65 eV, 707.65 eV and 708.85 eV on the left column. Magnetic profile of Fe in CoFeB from Ta interface to MgO is shown on the right column. *(It must be kept in mind that the amplitude of mms should be read from 0 on the y axis.)*

From the profile, we can say that the magnetisation is non homogeneously distributed in form of a gradient. It increases from 40% at Ta/CoFeB up to full magnetisation of 100% at CoFeB/MgO. This type of profile can be confirmed by the various models that we considered to get the best fits at each energy. We

get the **average Fe magnetisation** in *mms* for this sample as 0.7 ± 0.17 giving us **1.47 ± 0.35 μ_B**[2] indicating that we reach **70% of full magnetisation for 1700 Oe**. To compare with moment from of Fe in CoFe, we observed it to be **2.34μ_B** [164]. Starting with **S1**, the first observation we make is that its magnetisation is non homogeneously distributed in form of a gradient with minimum magnetisation at the CoFeB/Ta interface with 40% of Fe magnetic moment of an atom (*mms* = 0.4 ± 0.33) increasing along CoFeB thickness up to CoFeB/MgO interface which is fully magnetised (*mms* = 1 ± 0.2).

Comparing with SQUID measurements from we understand that we reach saturation at very high fields that are unreachable in case of SXRMR measurements at RESOXS. Through SQUID we get M_s = 1.1 ± 0.08 µB at 8KOe (saturation) but **77% of the M_s at 1700 Oe** which corresponds to a moment of 0.85 μ_B**.** This has been shown in the *Table 3*. All these values are summarised below. Thus, on comparing moment at 1700Oe from SQUID and SXRMR, we don't reach at similar values. Through SXRMR, we are at low magnetization from SQUID. It will be important to see the behaviour for other samples before discussing the comparison in detail.

Table 3 shows comparison between moment calculated from SXRMR and SQUID

Avg. mms (SXRMR)	moment μ_B	% of saturation at 1700 Oe	Moment μ_B
0.7 ± 0.17	1.47 ± 0.35	77	0.85

4.4.2.1.2 Sample 2

Structure:

We followed the same procedure as we showed for S1, where we present *Figure 4.26* that shows best fits for all average reflectivities measured at 670 eV, energy far away from Fe L3 edge at 3 data sets. (FlipHlon 2 here represents a second data set at the same acquisition mode) We were able to obtain fitted data in very good agreement with the experimental data. The parameters that were derived has been summarised in *Table 4* along with the parameters derived from the analysis of the measured in the vicinity of the Fe L3 absorption edge.

[2] Here to get the magnetization in terms of µB, we used magnetic moment of 1 magnetic atom as 2.1 µB from [120]

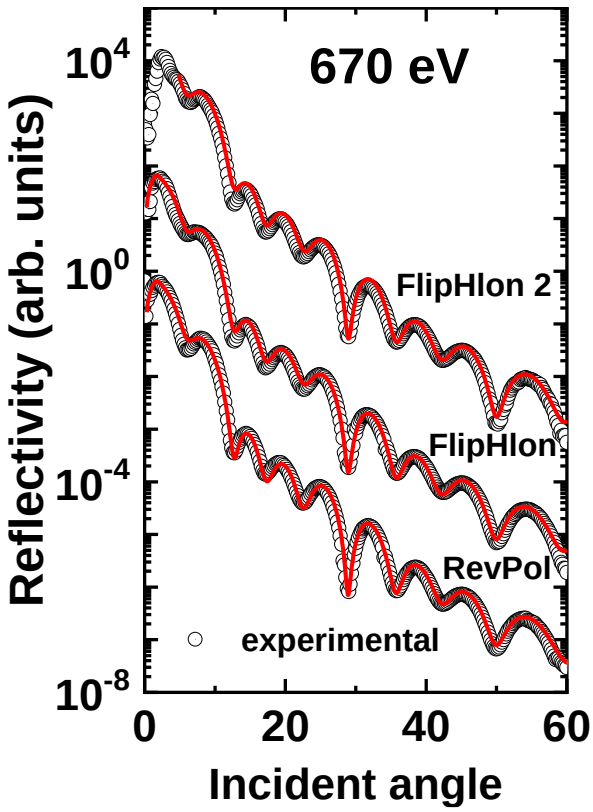

Figure 4.26 Experimental specular reflectivities I_{av} (black circles) and their best fits (red smooth lines) at 670 eV for S2 at three acquisition modes.

Although from qualitative analysis for S2, we observed no significant shift in energy scale (<0.1 eV), we performed similar *multiA fit* for S2 that was shown for S1. Figure *4.27* shows the experimental as well as refined energy dependent reflectivity through a *multiA fit* at angular positions of – 5°, 10°, 20°, 30°, 40°, 45° and 50° that were refined by using structural parameters given at 670 eV.

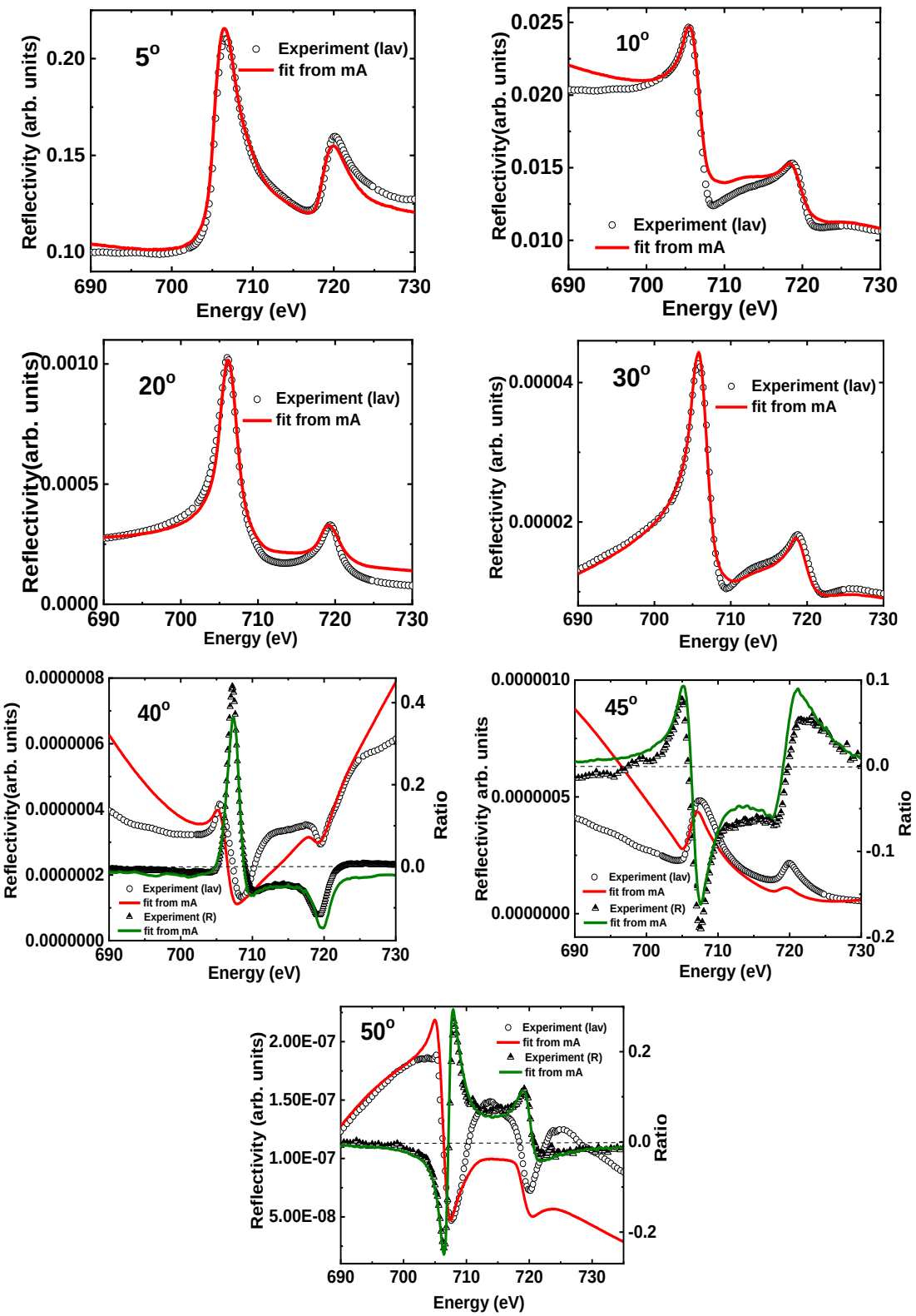

Figure 4.27 Experimental (black circles) and fitted energy dependent average reflectivity(red line) at 5°, 10°, 20°, 30°, 40°, 45° and 50°. For 40°, 45° and 50° asymmetry ratio is plotted on the right hand side y axis (green line).

We observe very good agreement with the same set of structural parameters from 5° to 30° (relatively lower angular range) however for, 40° to 55° although the evolution of the shape is fairly well understood, the agreement is not as good. For magnetic asymmetries on the other hand, agreement between the experimental and simulated is very good starting 30° (not shown) up to 55°.
We determined **δE** values derived as **0.0 ± 0.1 eV**. These results indicate that the resonance parameters used for the analysis, although measured on a thick Fe layer on another beamline, are relevant.

Figure *4.28* shows the experimental as well as best fits for energies in the vicinity of the Fe L3 edge with fitted data well reproduced. Since we determined δE as 0 for this set of measurements, no energy correction is added. Table *4* shows the structural parameters that we obtained from the refinement of average reflectivities for S2.

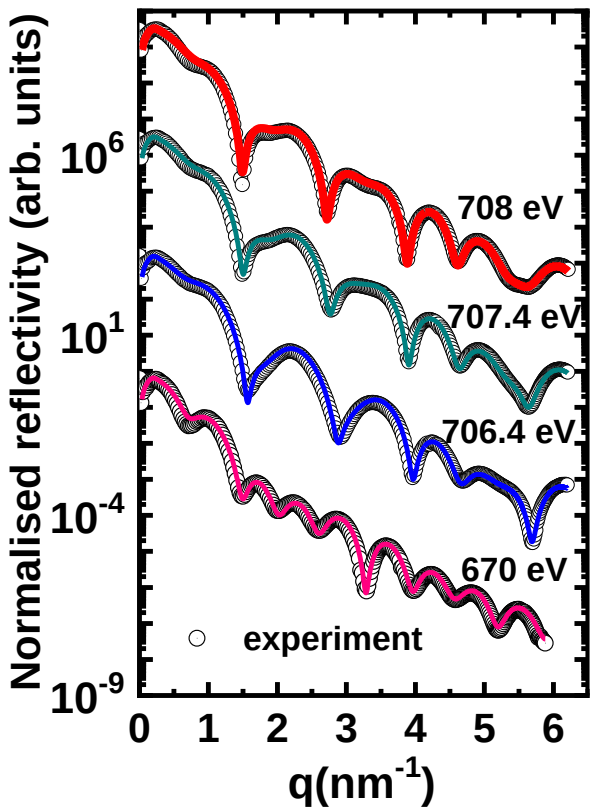

Figure 4.28 Experimental specular reflectivities (black circles) and their best fits at 670 eV, 706.4 eV, 707.4 eV and 708 eV in the vicinity of the Fe L3 edge measured for S2

In comparison to *Table 2* we can point out some changes that take place after annealing. Although thickness of CoFeB seems to remain unaffected, thickness of MgO can be observed is seen to decrease by 1Å. Such behaviour is known to occur to due crystallisation from annealing [165]. There is also an increase in roughness of CoFeB from 5.3 ± 2.1 to 7.1 ± 0.6 after annealing. Such an increase roughness maybe explained as an affect from annealing where Fe tends to intermix with Ta as we also observe a slight increase in roughness of Ta. Although, we see some increase in the thickness of Ta of about 2Å, we aren't sure if this is really due to an observation of interchange of thickness of Ta and Pt up to 2-4 Å. In the next section, we will see the structural parameters for S2'.

Table 4 Structural parameters ρ, t and σ derived from best fits for S2

	ρ(mol.cm^{-3})	t(Å)	σ(Å)
Pt	0.101 ± 0.007	28.3 ± 1.1	3.6 ± 0.3
Ta	**0.086 ± 0.004**	**9.6 ± 0.7**	**6.7 ± 2.1**
$Co_8Fe_{72}B_{20}$	**0.156 ± 0.003**	**13.3 ± 2.3**	**7.1 ± 0.6**
MgO	**0.161± 0.012**	**14.6 ± 4.2**	**4.2 ± 0.4**
$Co_8Fe_{72}B_{20}$	0.156 ± 0.014	2.5 ± 0.7	3.7 ± 0.6
Ta	0.077 ± 0.004	29.8 ± 0.5	4.2 ± 0.2

Magnetisation profile:

For this sample, we decided to see if the 4 sliced model like in the case of S1 could be used for refinement of data for S2. Using this model, we got a distribution that was more homogeneous instead of distributed in a gradient. To analyse the homogeneity, we considered a one-layer model at 708 eV as shown in Figure 4.29(left side top panel). We can see that the fit with one slice (red smooth line) gives us a shape as the experimental data however differs in the amplitude. This indicates that while homogeneous distribution is true, there is still small change in amplitude of *mms* over the layers which is why 4 slice model gives us the best fit. We used this model to refine data at all the 3 energies which resulted in very good fits, and we could obtain the best fit at each energy as shown in Figure 4.29(right side top panel).

Magnetisation profile as shown in Figure 4.29(bottom panel) for S2, shows a more homogeneous distribution compared to S1 as *mms* doesn't change between the interfaces (only by 10%).

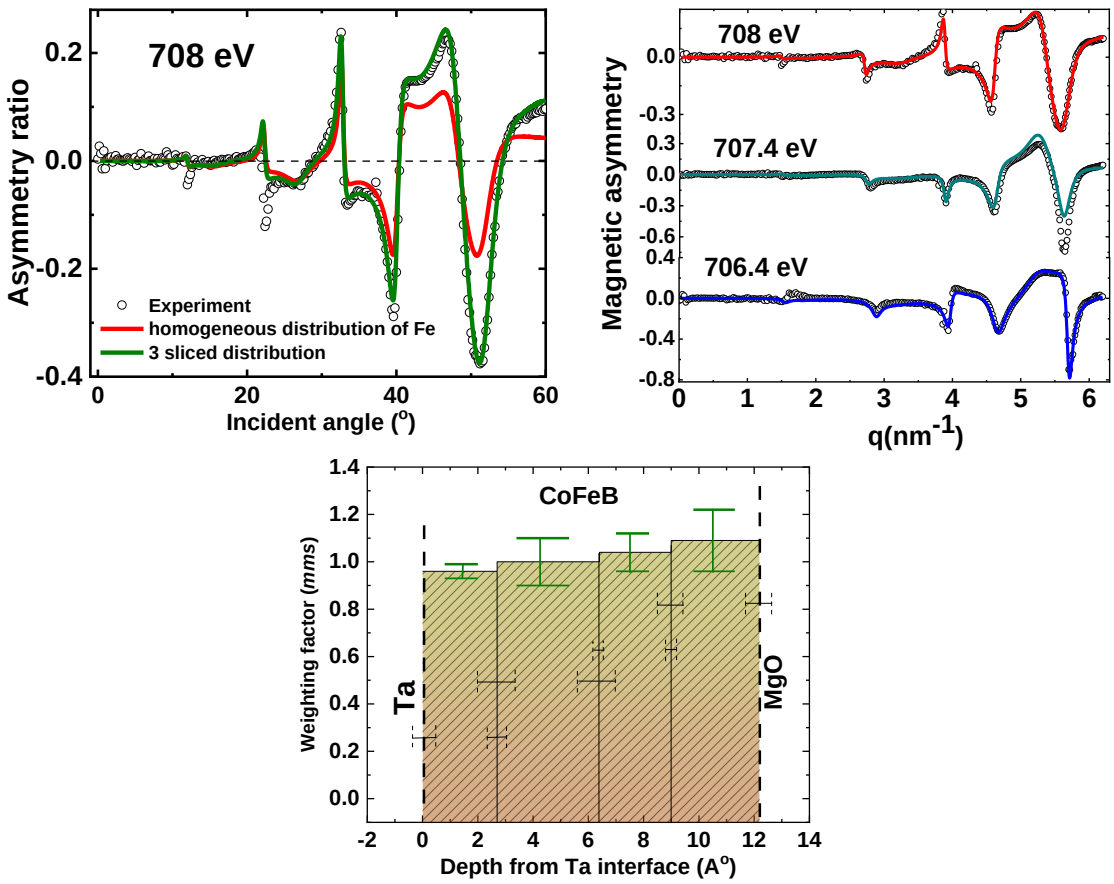

Figure 4.29 shows experimental asymmetry ratios for two models at 708eV (left side top panel). Best fit of asymmetry ratios at 708 eV, 707.4eV and 706.4eV in the vicinity of Fe L3 edge (right side top panel). Magnetisation profile from of Fe in CoFeB from Ta interface to MgO interface (bottom panel). *(It must be kept in mind that the amplitude of mms should be read from 0 on the y axis.)*

After annealing at 350°C, for **S2** we observe a **transition of easy axis from *ip* to *oop*** that the profile becomes homogeneous with only 10% change in mms of both interfaces. Thus, it becomes fully magnetised throughout the depth of the layer.

4.4.2.1.3 Sample 2'

Structure

For S2' we performed limited measurements of angular dependent reflectivity. The measurement at 670 eV has been shown along the measurements at energies (706.4 eV, 707.4 eV and 708.6 eV) in the vicinity of the resonant edge in Figure 4.30. The figure shows a good fit at each energy using an energy correction of -0.2 ± 0.1 eV. This value of energy correction was obtained from the *multiA* fit of experimental average reflectivity along with asymmetry ratios at several angular positions as shown in the Figure 4.31. The derived parameters are given in the Table 5.

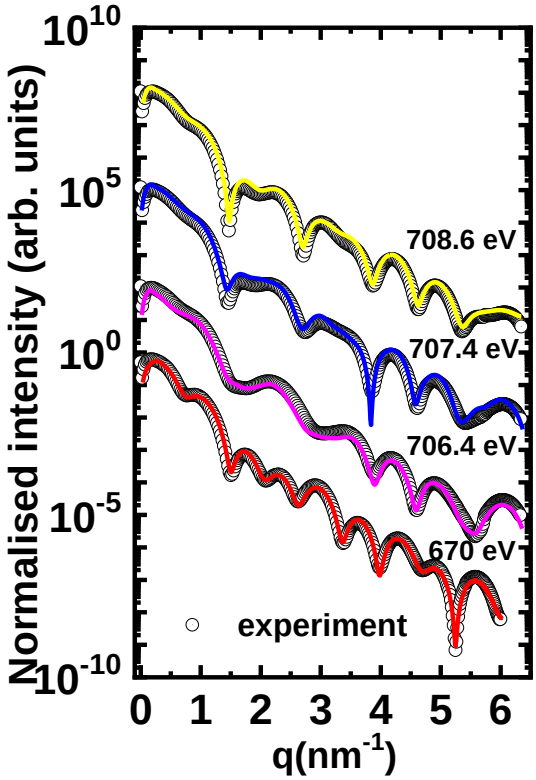

Figure 4.30 Experimental specular reflectivities (black circles) and their best fits at 670 eV in the vicinity of the Fe L3 edge at FlipHlon measured for S2'

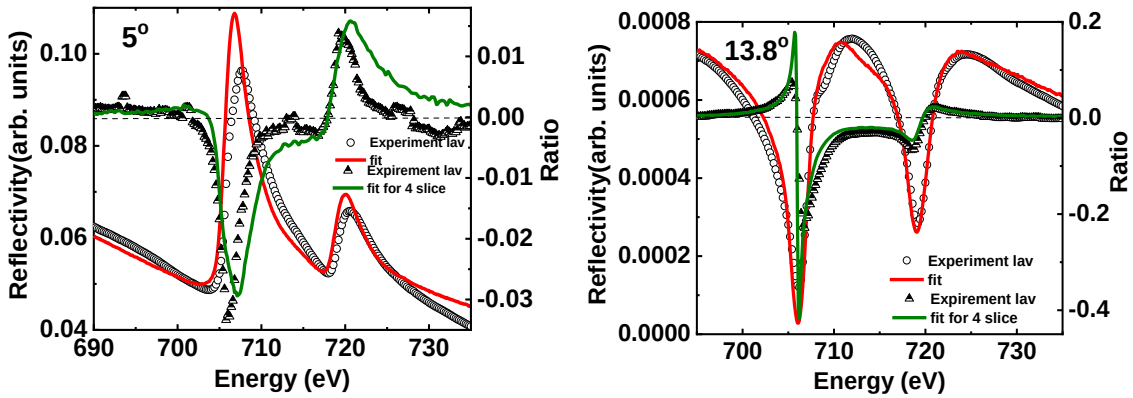

Figure 4.31 Experimental (black symbols) and fitted energy dependent average reflectivity (red line) as well as asymmetry ratio (green line) at 5° and 13.8°

As shown in the *Figure 4.31*, we were able to be a good agreement only for 5° and 13.8°. Although, the origin of this issue wasn't perfectly determined, an indication of oxide formation as observed in section 4.4.1.1.3, could be reasoned since our resonant parameters may not be good enough for data measured at high annealing temperatures. To fit the magnetic asymmetries, we again took into account a gradient profile with 4 sublayers.

Table 5 shows all the refined parameters for S2' from the reflectivity curves presented in *Figure 4.30*. On comparison to S1 and S2, for this sample we observe that the thicknesses of CoFeB and MgO have not changed significantly after annealing at 450°C. The roughness of Ta doesn't change a lot between the S1

and S2' but shows a higher value at S2. This evolution of Ta roughness is difficult to comment on since we understand Ta tends to move to CoFeB/MgO [142] as we increase annealing temperature indicating that roughness should also be high for S2'. CoFeB and MgO do not change significantly. The density of CoFeB can be seen to be decreased although we other densities don't change so much. It is surprising that we didn't see a significant change in Ta since it is known to diffuse into CoFeB/MgO interface due to annealing at higher temperatures [142]. Another thing to note is increase in roughness of CoFeB with increasing temperature, where such a change is known to occur due to some intermixing or uncorrelated roughing [166]. Rest of the parameters including densities, do not seem to be strongly affected.

Table 5 Structural parameters ρ, t and σ derived from best fits for S2'

	ρ(mol.cm^{-3})	t(Å)	σ(Å)
Pt	0.101 ± 0.007	25.1 ± 2.3	4.3 ± 0.6
Ta	**0.086 ± 0.004**	**10.9 ± 2.8**	**5.1 ± 2.5**
$Co_8Fe_{72}B_{20}$	**0.156 ± 0.003**	**13 ± 2.5**	**6.8 ± 1.1**
MgO	**0.161± 0.012**	**14 ± 0.7**	**3.8 ± 1.1**
$Co_8Fe_{72}B_{20}$	0.156 ± 0.014	3.9 ± 0.8	3.9 ± 0.6
Ta	0.077 ± 0.004	29 ± 2	5.6 ± 1.4

Magnetisation profile

Figure 4.32 shows the magnetisation profile comprising of error bars on the *mms* values and sublayers thicknesses using the 4-slice model similar to S1 and S2. However, the refinement of asymmetry ratios proved to be more difficult to get the best fits for this sample, however we managed to obtain relatively agreeable fits.

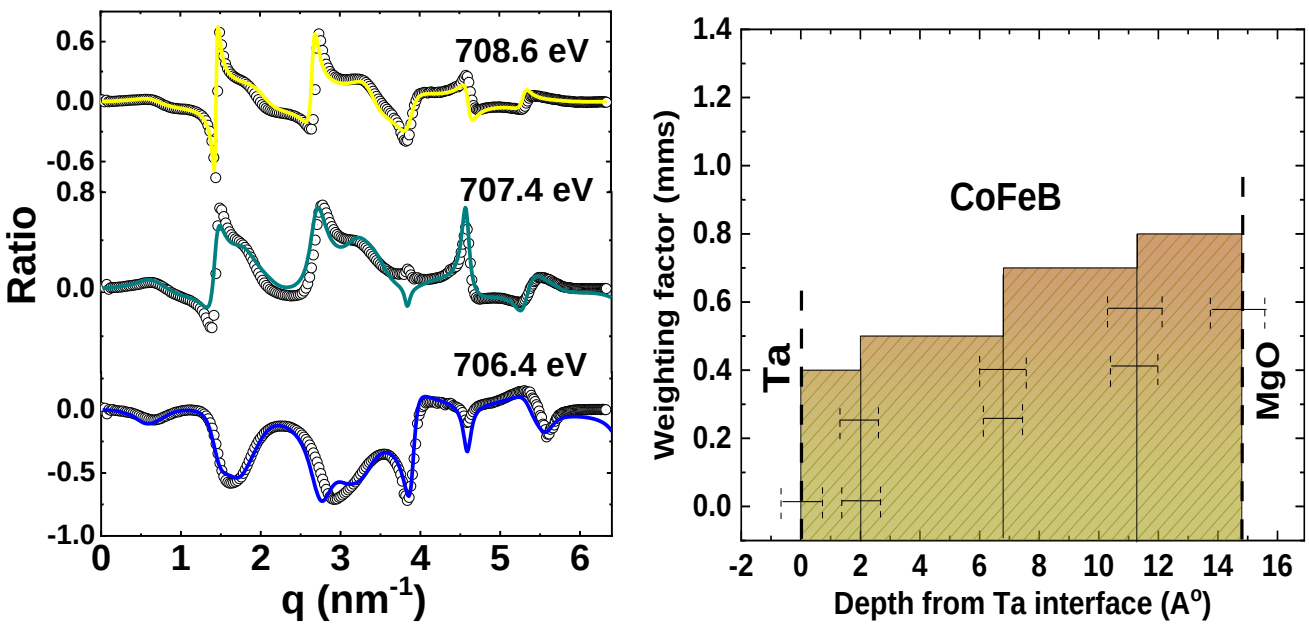

Figure 4.32 shows experimental and the best fits of magnetic asymmetry at energies 708.6 eV, 707.4 eV and 706.4 eV on the left-hand side. Magnetisation profile from Ta interface to MgO interface on the right-hand side. *(It must be kept in mind that the amplitude of mms should be read from 0 on the y axis.)*

From the magnetisation profile, we can see that after annealing at 400°C Fe magnetisation is redistributed in the layer resulting in the profile of **S2'** which is similar to the profile of S1 with same gradient distribution at each interface. It is interesting to note that the shape of the profile changes back to a more gradient form as observed in S1. Thus, we can say that after annealing at higher temperatures the magnetisation distribution in S2' changes in comparison to S2 with a decrease in overall magnetisation.

Through SXRMR, we got the average mms as 0.75 ± 0.09 giving us 1.57± 0.15 μ_B in comparison to SQUID at 1700 Oe, through which, we achieved 94% of the saturation corresponding to 1.08 μ_B. All these values are shown in Table *6*. In this case also we observe that we get higher value of moment from SXRMR in comparison to SQUID in par with previous results from S1 and S2.

Table 6 shows comparison between moment calculated from SXRMR and SQUID

mms (SXRMR)	Avg. moment μ_B	% of saturation at 1700 Oe (SQUID)	Moment μB
0.75 ± 0.09	1.57± 0.15	94	1.08

4.4.2.2 W/Ta

In this section, we will present the results on the structure profile after insertion of W, hence we will focus on sample 3 and sample 4. The presentation of results follows the similar pattern as it was for previous sections. We will start with results obtained at 670 eV, from where we will know about the structure of the sample, after which the obtained parameters were used to fit the reflectivity at energies close to the edge.

4.4.2.2.1 Sample 3

Structure

In *Figure 4.33*, we show the reflectivity measurements at 670 eV, at WoH, RevPol and FlipHlon. All the three curves are completely expectedly superimposable, and we obtain very good fits for all 3 measurements. The parameters that were obtained along with the fitted data at energies near resonance are presented in the Table *7*.

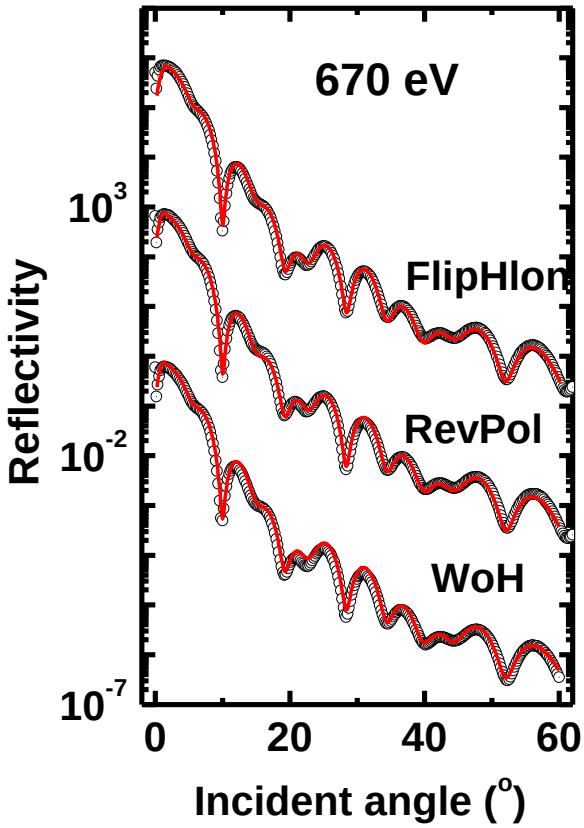

Figure 4.33 Experimental specular reflectivities (black circles) and their best fits (red line) at 670 eV at three acquisition modes

Now, we present the experimental energy dependent reflectivity and magnetic asymmetry ratio with their best fits at 8°, 15.5° and 29.5° that were obtained from multiA fit carried out by using the structure from 670 eV presented in *Figure 4.34*.

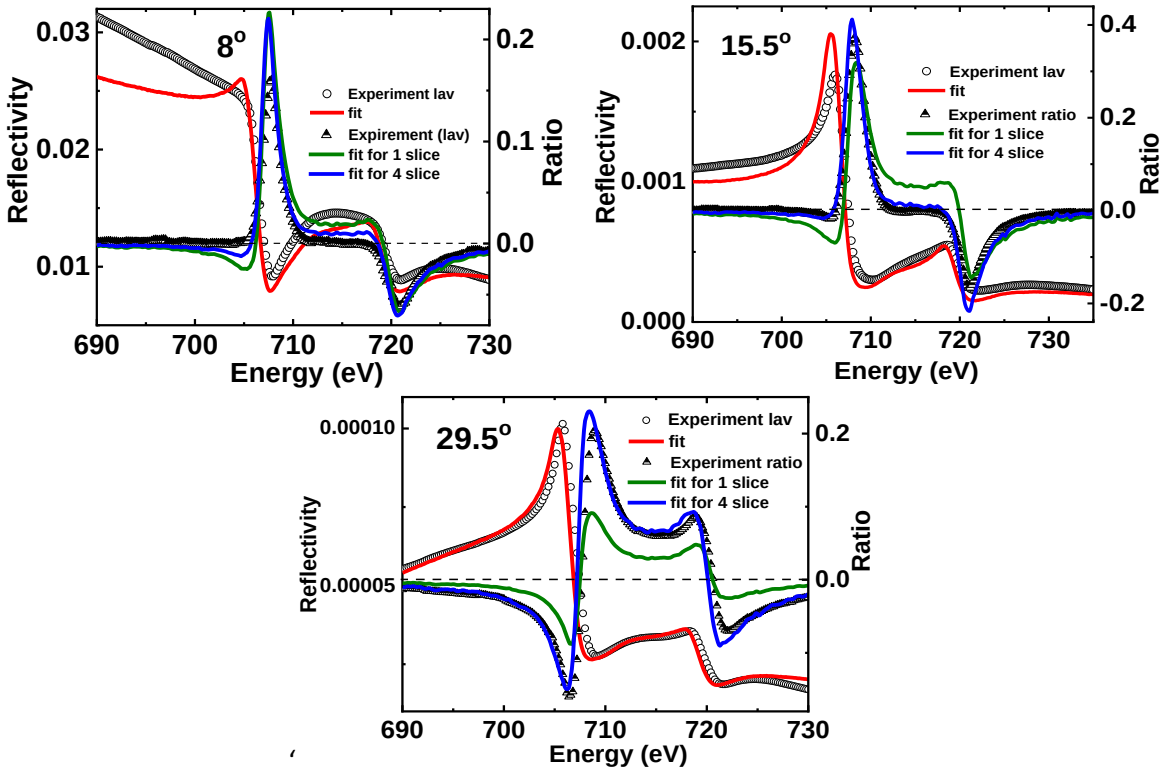

Figure 4.34 Experimental (black circles) and fitted energy dependent reflectivity(red line) as well as asymmetry ratio for two models (blue and green line) at 8°, 15.5° and 29.5°

We observe that the reflectivity at 8° and 15.5° which shows more of the spectroscopic features was reproduced fairly well (red smooth line) whereas at 29.5°, we get really good fit. We obtained a **δE = -0.45 eV.**

To fit the asymmetry ratio initially we considered a homogeneous profile (green curve) which reproduced evolutions of the shape however, we observe strong deviations with respect to the amplitude of asymmetry ratio. This indicates that the magnetization profile is in fact different from a homogeneous distribution. Thus, we tried to fit the data by slicing the layer and thus getting a very good fit at all 3 angles with 4 slice model (blue line). Since we applied refined asymmetry from angular reflectivity first, it gave us a non-uniform model with 4 slices. Thus, we observe that this same model is able to fit better all 5 energy-dependent magnetic asymmetries using the latter model allows to be reproduced more or less perfectly, providing an impressive confirmation of the graded magnetic profile. Although for 4 sublayers we got mms (from the top to the bottom of the layer) as: 0.00, 0.32, 0.50 and 0.65, here we do not care much about absolute amplitudes, but just the relative variations from one to the other.

Using the energy correction of -0.45 eV we present the best fits at energies close to the resonant edge in *Figure 4.35*. At each energy, we can see that we obtained a good agreement between experimental data and their best fits. All the parameters that have been derived are discussed in Table *7*.

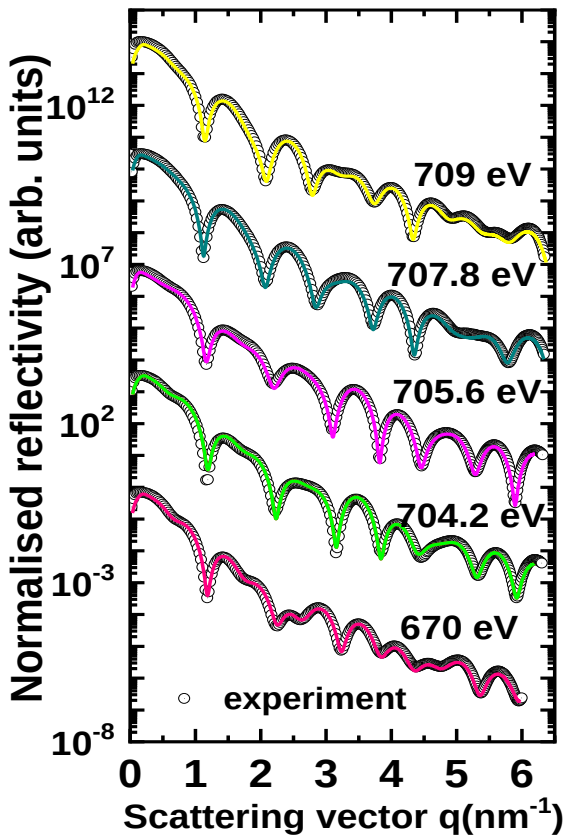

Figure 4.35 Experimental specular reflectivities (black circles) and their best fits at energies in the vicinity of the Fe L3 edge for S3

Table 7 Structural parameters ρ, t and σ derived from best fits for S3

	t(Å)	σ(Å)
Pt	27.9 ± 2.4	2.7 ± 0.3
Ta	**11.2 ± 0.8**	**3.9 ± 1.3**
W	**20.1 ± 0.9**	**3 ± 2.2**
$Co_8Fe_{72}B_{20}$	**14 ± 0.5**	**4.5 ± 0.4**
MgO	**13.3 ± 0.8**	**4 ± 0.5**
$Co_8Fe_{72}B_{20}$	2.1 ± 0.5	2.7 ± 0.1
Ta	29.5 ± 0.8	3.8 ± 0.5

The parameters of Ta, W, CoFeB and MgO are close to nominal values of the sample where given error bar for each parameter is calculated from standard deviation applied over all energies. The roughnesses

for all layers are relatively low except for CoFeB. It will be important to see its evolution. The thickness of W is very close to the nominal value of 20 Å which will be interesting to observe the change in after discussion of results after annealing.

Magnetisation profile

To derive the magnetisation profile, we will follow the same pattern as discussed for S1, S2 and S2'. We always obtained the best fit with 4 slices of CoFeB layer as shown in the *Figure 4.36*(left side top panel) with magnetisation distributed as a graded profile decreasing to CoFeB/W interface. To confirm this result, we show a model with a homogeneous profile at 708.55eV and 707.35eV (green colour) with uniform magnetisation, however it doesn't result in the best fit and is strongly deviated from experimental data. We also show a model where we started the fit with a profile with random values of *mms* at 708.55 eV (red colour), but it always converged to a graded profile. *Figure 4.36*(left side bottom panel shows good agreement between experiment and fitted data for all the energies.

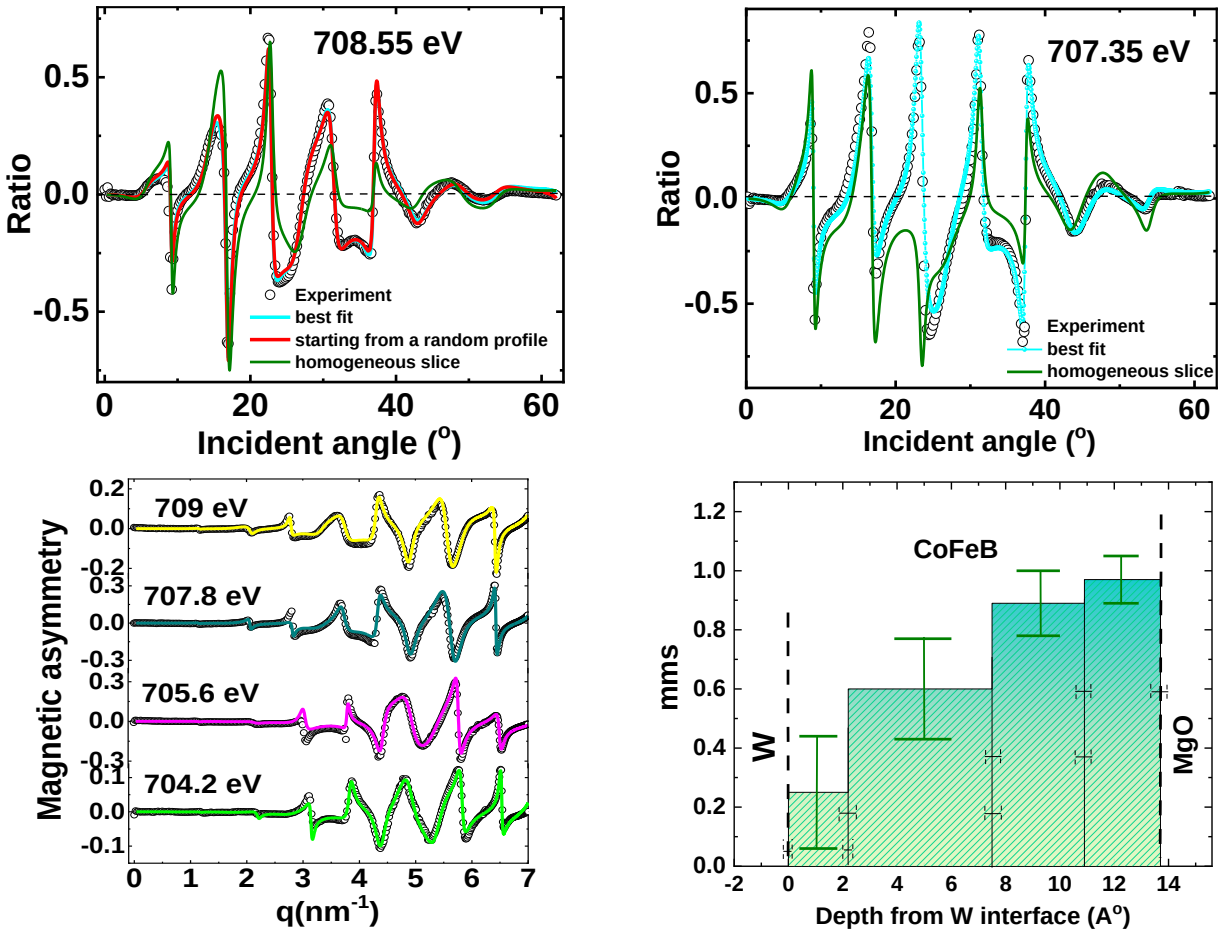

Figure 4.36 Experimental asymmetry ratios at 708.55eV and 707.35 eV with various models (top panel). Best fit of asymmetry ratios at 709 eV, 707.8eV, 705.6eV and 706.4eV in the vicinity of Fe L3 edge (right side top panel). Magnetisation profile from of Fe in CoFeB from W interface to MgO interface (bottom panel).

S3 therefore shows a gradient profile increasing from 0.25 ± 19 to almost full magnetisation 0.97 ± 0.08. All the values for this sample are derived from both SQUID and SXRMR are discussed in Table *8* for purpose of comparison. We observe that for this sample, we are in agreement with SQUID at 1700Oe.

Table 8 shows comparison between moment calculated from SXRMR and SQUID

Avg. *mms*	**Moment μ_B**	**% of saturation at 1700 Oe (SQUID)**	**Moment μ_B**
0.63 ± 0.14	1.32± 0.23	88	1.13

4.4.2.2.2 Sample 4

Structure

Figure 4.37 represents the experimental average specular reflectivity (black circles) along with their best fits (smooth red lines) at several energies for all measurements at RevPol and FlipHlon 670 eV where we were able to obtain very good fits good fits for all the data. Through refinement of these reflectivity curves, we were able to values for density with error bars given in Table *9* along with the parameters that are derived from energies in the vicinity of the edge.

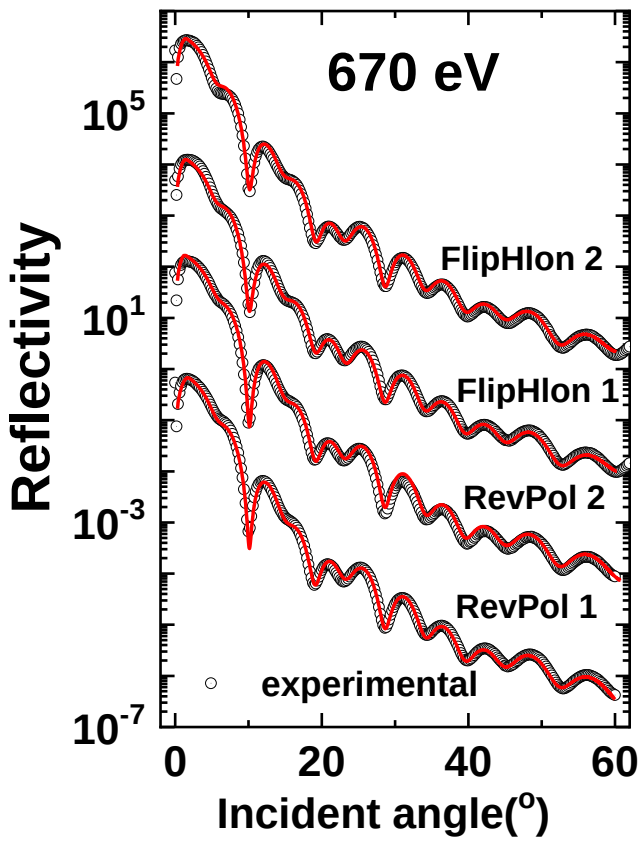

Figure 4.37 Experimental (black dotted line) and fitted (red smooth line) average specular reflectivity at energies at 670 eV for S4.

Figure 4.38 shows the ***multiA fit*** for the energy dependent reflectivity at 26.5°, 34°and 52.5°. For each angle we show refinement of energy dependent reflectivity (red line) and refinement of asymmetry with a model consisting of 4 slices.

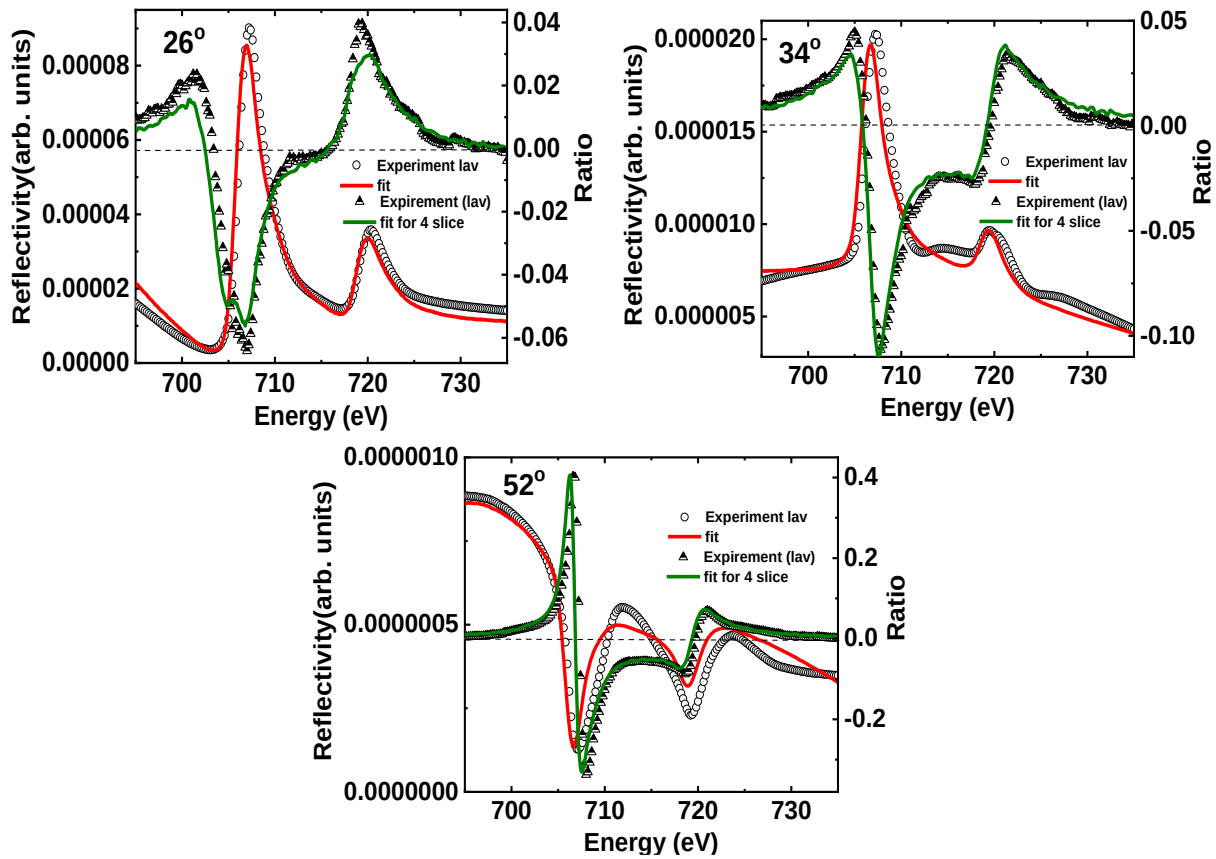

Figure 4.38 shows best fits of energy dependent reflectivity (red lines) and best fit of energy dependent magnetic asymmetry at 26°, 34° and 52°.

The refinement of reflectivity reproduced the experimental data quite well at 26.5° and 34°. For 52.5°, the shape of reflectivity is rather well reproduced with however strong discrepancies in the amplitude.

The magnetic asymmetry, except for the small magnetic asymmetry at 26.5°, the energy and angular dependence of the other are very well reproduced. From these refinements a δ**E = - 0.45 ± 0.1 eV** is optimized.

Now we come to the experimental angle dependent reflectivity. Figure 4.39(left hand side) shows all the experimental reflectivity curves measured at energies close to Fe L2,3 edge, where energies were corrected by adding **-0.45 eV** according to refinement of energy dependent reflectivity scans resulting in very good fits for all the energies at energies from top to bottom: 708.55 eV, 707.35 eV, 705.15 eV, 703.75eV and 670 eV.

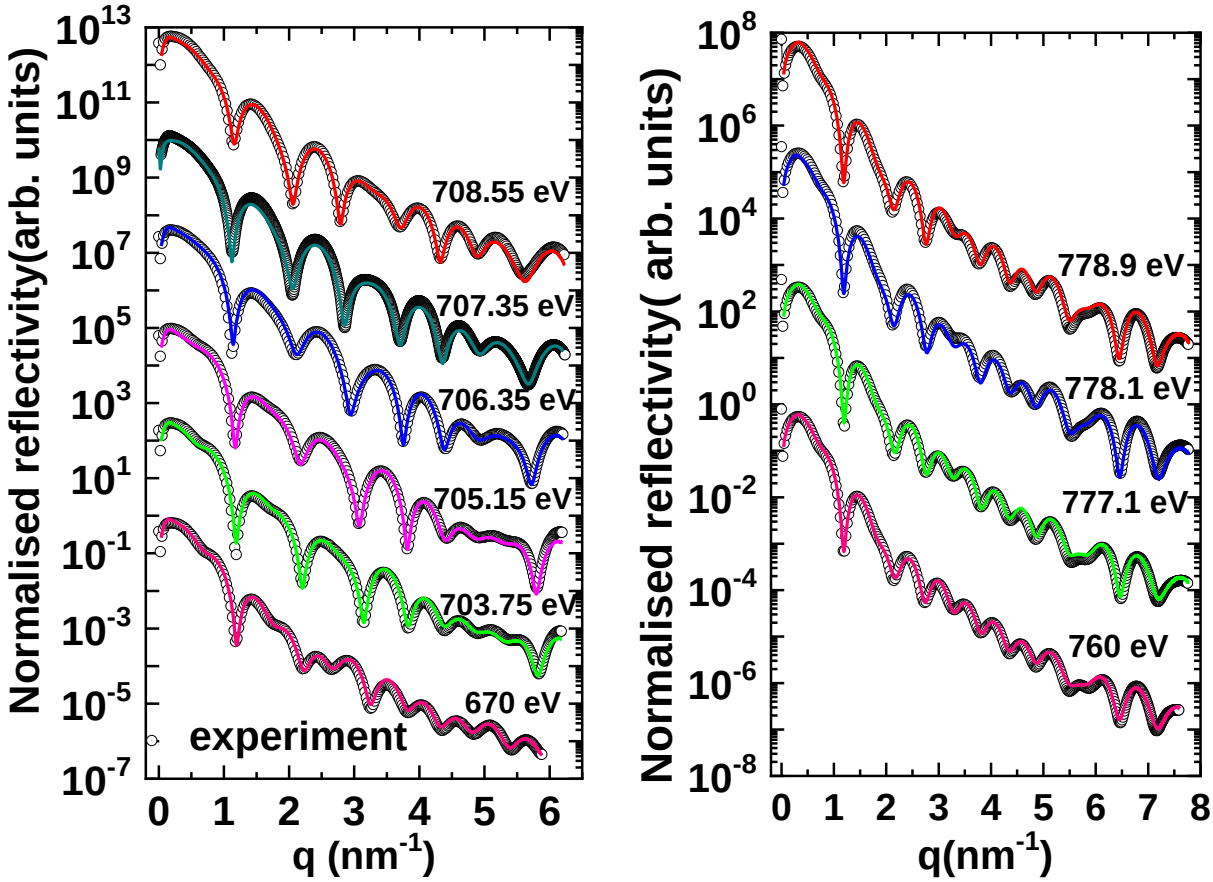

Figure 4.39 Experimental specular reflectivities (black circles) and their best fits at energies in the vicinity of the Fe L3 edge at several energies on the left-hand side and at Co L3 edge on the right-hand side.

Figure 4.39 on the right-hand side also represents the experimental reflectivities along with their fits for energies 760 eV (18.05 eV below the Co L3 edge) and 3 energies close the Co L3 edge. The measurements at Co edge were conducted to see if we can be sensitive to contribution from Co despite its small amount (8%) in the system. The analysis of structure and subsequently magnetism can help us in providing a better set of averaged parameters as well as the respective error bars. All the tabulated values of the structural parameters for both Co and Fe are given in Table *9*.

The values extracted at Fe and Co seem very close except slight reduction in thickness of CoFeB indicating that the interface MgO-CoFeB is poor in Co as thickness of CoFeB is reduced while thickness of MgO is increased and the layer above are very similar. On comparison with S3, we observe a decrease in thickness of W by 2A° however, this increase is not clear to explain. On significant change we observe is low roughness for W cap layer in comparison to Ta cap layer.

Table 9 Structural parameters *ρ*, *t* and *σ* derived from best fits for S4

	t **(80°) Å**	**σ (80°) Å**	***t*** **(Co)Å**	**σ (Co)Å**
Pt	27 ± 3.3	2.3 ± 0.1	28.8 ± 0.4	2.3 ± 0.0
Ta	**12.7 ± 3**	**6.6 ± 2.4**	**12.1 ± 1.0**	**9.7 ± 0.2**
W	**18.6 ± 1.4**	**2.9 ± 0.8**	**18.8 ± 1**	**3.5 ± 0.2**
$Co_8Fe_{72}B_{20}$	**13.8 ± 1**	**5.2 ± 0.2**	**12.5 ± 0.9**	**5.9 ± 0.3**
MgO	**13.3 ± 0.7**	**2.7 ± 1.1**	**14.2 ± 0.3**	**2.8 ± 0.1**
$Co_8Fe_{72}B_{20}$	1.4 ± 0.2	2 ± 0.1	2.6 ± 0.1	2.2 ± 0.1
Ta	30.2 ± 0.5	4 ± 0.3	29.3 ± 0.1	3.6 ± 0.2

Magnetisation profile:

In order to obtain the magnetic distribution of Fe in S4, at we started the refinement of magnetic asymmetry by initially considering a model with homogeneous *oop* magnetic distribution as shown by the blue line in *Figure 4.40* at 703.75eV, which if compared to the raw data (black circles) has differences in amplitude of asymmetry ratio. The homogeneous model shows smaller signal as well as shows a small phase shift at large scattering angle. Although, the shape of the fit along the scattering angles remains the same to the raw data, the deviations indicate that this model isn't the best one to consider. The apparent disagreement with the experimental asymmetry growing with incident angle implies that one or more magnetic sublayers have different magnetic properties. The model with 2/3 slices although improved the quality of the fit, did not give a fitting with high accuracy, however model with 4 slices gives a very good fit of the magnetic asymmetry. We were able to find that this model works for each energy as shown *Figure 4.41*(left hand side).

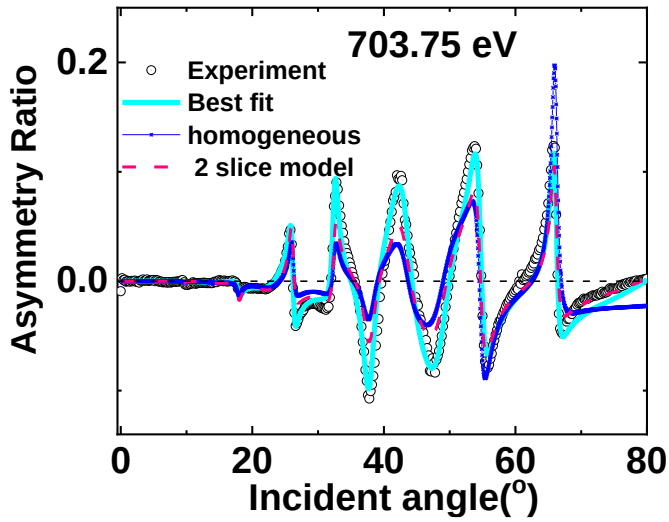

Figure 4.40 Experimental and fitted asymmetry ratio from various models at 703.75 eV

Figure 4.41(right hand side) shows the corresponding magnetic profile shows a non-homogeneous graded magnetization distribution from top to bottom along growth axis where CoFeB layer exhibits an *oop* magnetization gradient. We also observed a gradient distribution of magnetisation for Co close to that of Fe (not shown here).

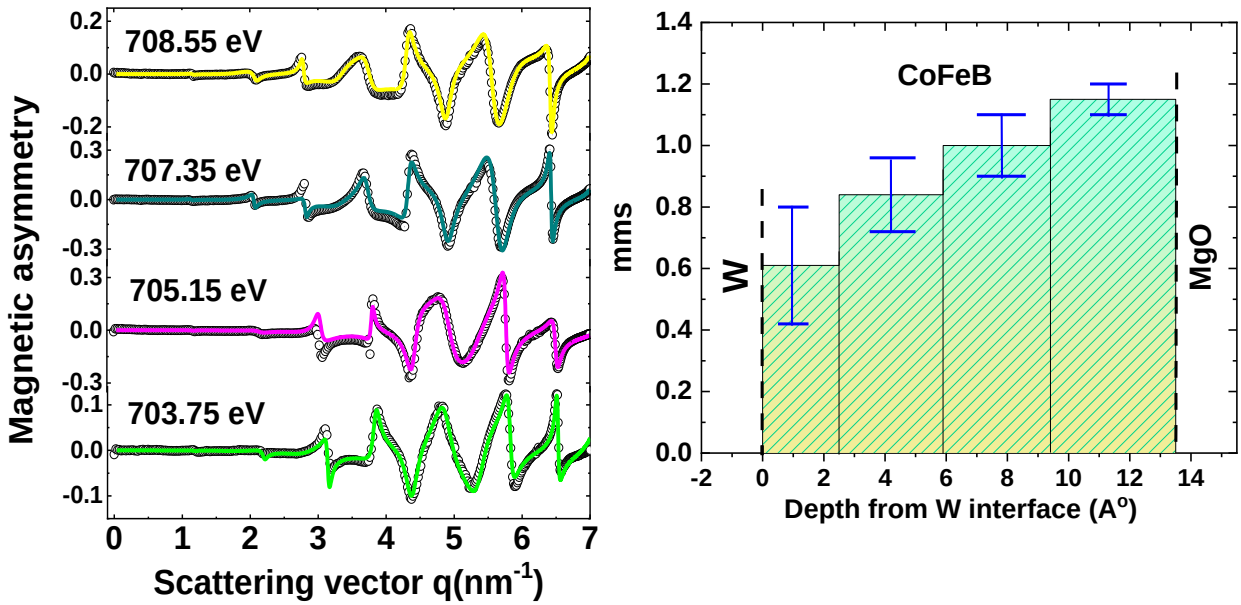

Figure 4.41 Best fits of magnetic asymmetry at 708.55eV, 707.35eV, 705.15eV and 703.75eV on the left-hand side. Magnetisation profile of Fe in CoFeB from W interface to MgO interface on the right-hand side.

4.5 Discussion

In order to see *annealing effect* in both Ta and W capped samples we have superimposed magnetic profiles for Fe moment of S1 and S2 including S2' on the left-hand column while superimposition of profiles of S3 and S4 are shown in the right-hand side of *Figure 4.42*. Also, to see *cap layer effect* between Ta and W before and after, we have superimposed profiles of S1 and S3 as well as S2 and this is shown in Figure *4.43*. To aid in discussion all values in terms of *mms* and magnetic moment are summarised in Table *10* to aid in discussion.

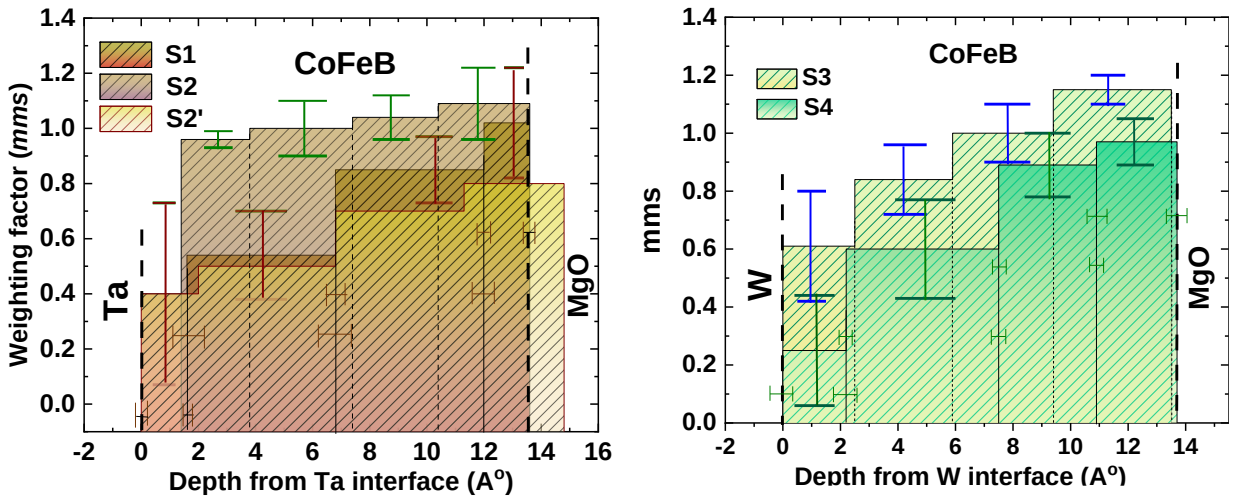

Figure 4.42 shows superimposition of magnetic profiles for (a) S1, S2 and S2' (b) S3 and S4 in along with calculated error bars along the depth of CoFeB from W/CoFeB interface till CoFeB/MgO interface

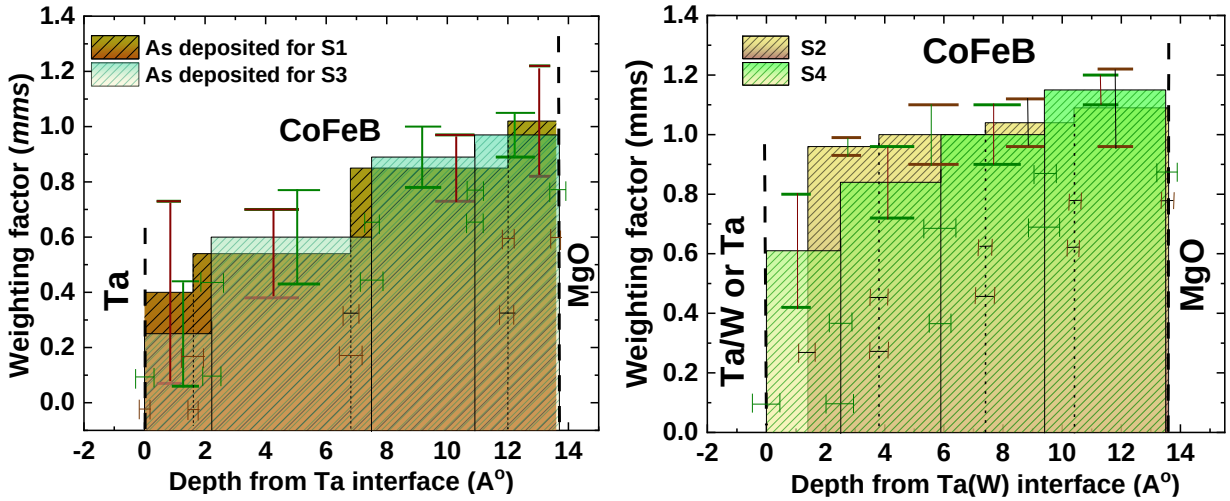

Figure 4.43 shows superimposition of magnetic profiles for (a) S1, S3 (b) S2 and S4 in along with calculated error bars along the depth of CoFeB from W/CoFeB interface till CoFeB/MgO interface

Table 10 *mms* and magnetic moment of Fe magnetization in S1, S2, S2', S3 and S4

Sample	*mms* at CoFeB/MgO interface	Moment at CoFeB/MgO interface (μ_B)	*mms* at Ta(W)/CoFeB interface	Moment at Ta(W)/CoFeB interface
S1	1 ± 0.2	2.1 ± 0.44	0.4 ± 0.33	0.88 ± 0.72
S2	1.09 ± 0.03	2.24 ± 0.11	0.96 ± 0.05	2.01± 0.11
S2'	0.8 ± 0.11	1.68 ± 0.24	0.4 ± 0.1	0.84 ± 0.22
S3	0.97 ± 0.08	2.03 ± 0.16	0.25 ± 0.19	0.52 ± 0.4
S4	1.15 ± 0.05	2.4 ± 0.1	0.61± 0.19	1.28 ± 0.39

- **Discussion** of the **gradient** profile in S1 and S3, **before annealing**

We observe that for S1 and S3, we get magnetic distribution in a gradient form, minimum value at the cap layer/CoFeB interface increasing till CoFeB/MgO. This observed distribution of magnetisation in form of a gradient signifies an occurrence of varying local moment along the thickness of CoFeB layer from Ta(W) interface to the CoFeB/MgO interface signifying differential interfacial magnetism. One possibility of this magnetization gradient could be related a gradient of composition The DSIMS depth profile on these samples [150] shows a change of composition since Ta and W do not attract Fe and Co the same way. DSIMS shows that the difference between Fe and Co is stronger for W as to Ta where Ta attracts a bit more the Fe. If a modification of magnetization amplitude has to be related, it is the change of the Fe/Co ratio that could lead to a small change of magnetization which may be able to provide an explanation for the difference of 0.88 µB (Ta) and 0.52µB (W) with large error bars. However, the explanation cannot be here only as the reduction is too strong. The change of composition, stronger in W cap compared to Ta cap, could be however at the origin of the smaller amplitude of Fe close to W (0.52) compare to Fe close to Ta (0.88).

Since a compositional gradient with different density is not easily detectable in the reflectivity, we cannot directly link to the gradient of Fe moment with its composition. But, from these results, we understand that there is some distribution of Fe at the time of depositing, 10% more in Ta than W.

To understand such a distribution in our profile we can link it with the change in local M_s and also T_c has been reported in [167], [168] were they observed higher M_s and T_c at CoFeB/MgO interface and decreasing up to the metallic cap layer (W,Ta) /CoFeB interface due to intermixing and diffusion between cap layer and magnetic layer as shown in the Figure *4.44*. A reduced M_s in the magnetic layer with a metal insertion in comparison to the free layer without insertion has been observed also before [169], [170].

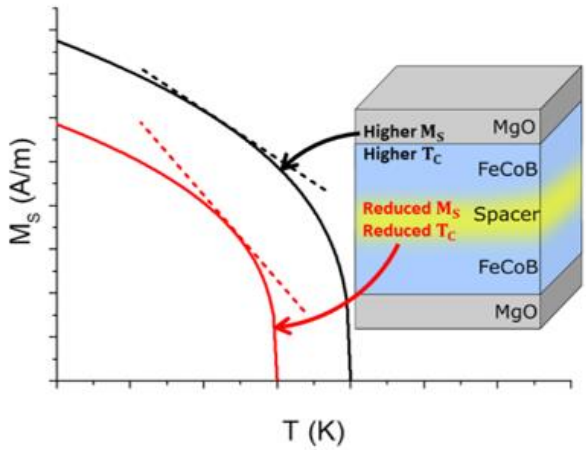

Figure 4.44 Sketch of local M(T) dependences (figure from [167])

We observe lower roughness for W cap layer in comparison to Ta for which we always observed higher roughness. It has been evidences in samples before annealing during deposition is known to occur readily during deposition as shown in Figure *4.46*. Even though the magnetisation of Ta at Ta/CoFeB interface seems to be higher than W by 20%.

<u>Possibility to consider a magnetic dead layer vs a gradient profile</u>

Since in magnetic calculations a MDL is usually considered, we tried to fit the profile by taking into account a MDL of specific thickness as shown in Figure *4.45*. We took into account another depth profile model for W cap layer, based on a dead layer 0.6 [150] nm thick at the upper interface with W and homogeneous magnetization over the rest of the layer as shown in the figure below (orange line) was tested and it can be seen that we weren't able to reproduce the data over the full angular range in comparison to the best fit that considered a gradient distribution.

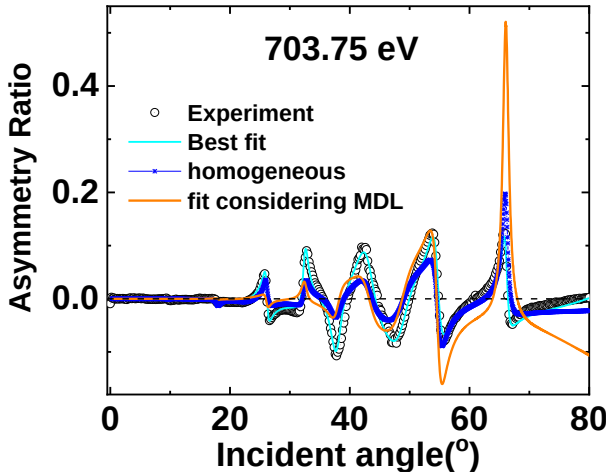

Figure 4.45 A model taking into account magnetic dead layer used to fit experimental magnetic asymmetry at 703.75 eV

This shows us that it may be more accurate to consider a gradual graded distribution of Fe magnetisation inside CoFeB instead of a region inside film which is completely magnetically dead.

- **Annealing effect in S1, S2 and S2'**

After annealing at 350°C, we observe a change in profile as it becomes more homogeneous with average *mms* = 1 for S2 only 10% change in amplitude. From the roughness values, we obtained an increase in roughness of CoFeB with annealing temperature. This can be expected since Ta tends to intermix with Fe easily due to the fact that FeTa has a negative large enthalpy of formation (-3468 meV/atom) [171], [172].

Transition of *ip* to *oop* easy axis after annealing and thus such occurrence of PMA after optimal annealing is known to occur due to the improved crystallinity of the CoFeB electrode into CoFe where B is absorbed by the Ta cap layer. **Enhancement of PMA basically arises from B affinity, which is an important factor for creation of PMA due to its tendency to diffuse out that leads to a formation of well aligned crystalline structures during annealing** [173].

After annealing at 350°C, we also observe an overall increase in magnetisation of about 30% for S1 and S2 has been identified as predominantly relevant to B atom out diffusion [144]. It has been known that annealing enables out diffusion of thermally activated B atoms from CoFeB interface toward Ta/CoFeB interface which leads to enhancement of CoFeB crystallization corresponding to the increased M_s. Diffusion of B out of CoFeB layers during annealing results in reduction of magnetic impurities (B atoms) and thus an increase in magnetic moment [159]. Since size of B atoms is much smaller than other transition metals (Fe or Co) atoms B diffusion may thus must be easier and faster compared to other atoms thus dominating the magnetization variation during annealing. In this case, it can be evidenced from study by Jyotirmoy *et al*., [143] which showed a decrease in B concentration at the CoFeB/MgO interface after annealing. This increase has also been seen in [174] where it also shows that the Fe dichroic signal has significantly increased after annealing thus indicating increased Fe magnetisation in the film.

After further annealing to a higher temperature till 400°C, we observe a deterioration of the *oop* component and the magnetisation again turns into *ip* accompanied by change of shape of profile to a more gradient distribution although, the amplitudes in case of S2' are not as high and the magnetisation at CoFeB/MgO is just 80%.

The transition of *ip* axis to *oop* axis has been observed in various studies for Ta/CoFeB samples before in [142], [175] and [176] where it has been indicated as a result of thermally activated diffusion of Ta into the CoFeB layer can occur in Ta/CoFeB may occur due to annealing. Ta is initially mixed with CoFeB but above 350°C its diffusion becomes prominent above a certain threshold temperature usually above 300 ◦C causing a significant PMA reduction as Ta migrates to CoFeB/MgO interface [142]. **This leads to decrease in M_s, and a decrease in K_s.** Although from our results, we don't see a significant change in Ta roughness, we observe an increase of roughness of CoFeB which can be due to alloying effect from Ta.

Such a decrease in K_s above 350°C is in agreement with previous work on a similar stack [138]. This can also be proven by Figure *4.46* shows Ta $4f_{7/2}$ and Ta $4f_{5/2}$ core level photo electron spectrum for 250°C annealed sample. For the middle component for alloyed Ta (green curve) it can be reasonable to consider that this component comes from an intermixture of Ta and CoFeB indicating that such an intermixing occurs readily on annealing. Also, we can see that the intensity of oxidized Ta is very less thus amount of

Ta diffused into MgO is negligible. However, on further annealing both alloyed and oxidized Ta components of the spectrum increases indicating migration of Ta into MgO.

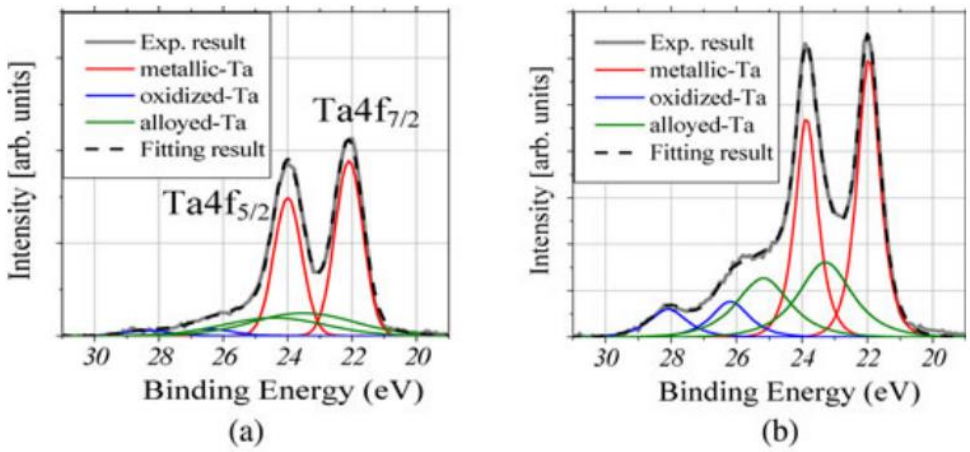

Figure 4.46 Ta 4f core-level XPS of Ta/CoFeB/MgO/Al2O3 stacks annealed at (a) 250◦C and (b) 400◦C [142]

Another notable characteristic of the Fe magnetization in the gradient profile is a **high 3*d* magnetization reaching up to *mms* = 1 before annealing and slightly increasing up to 10%** after annealing for all S1, S2 and S3, S4. Such an enhancement of the magnetization up to 2.7 ML Fe on MgO has been studied by XMCD [177] which is in accordance to our results. Another study using SXRMR showed enhancement of Fe magnetization in the 2–3 ML near both MgO interfaces in a MgO/Fe(12nm)/MgO (001) trilayer in comparison to the Fe magnetization in the center of the layer whose value was closer to the bulk value. Such an increase can be seen theoretically in [158]. Such an increase has been reported due t

- **Discussion of profile for W after annealing**

For W cap layer after annealing, we observe that even though the profile is maintained by a gradient form, there is an overall increase in magnetisation although there is an increase in amplitude of magnetisation in comparison to S2 by 30% at CoFeB/W interface to 10% at CoFeB/MgO interface. Like mentioned previously, this can occur due to B migration.

A key difference that we observe from our results is the different profiles for Ta and W after annealing. In case of Ta, we observe a more homogeneous profile for S2 with only 10% change in amplitude between 2 interfaces, where for W layer, it maintains a more gradient profile even after annealing similar to S3 for as deposited. This shows that after annealing, the interface magnetic effect is different in case of cap layers, W and Ta. W in general is known to be less prone to diffusion in comparison to Ta since FeTa has much negative larger enthalpy of formation (-3468 meV/atom) than of FeW (-554 MeV/atom) [171], [172]. Infact, we have more indication of changing roughness of CoFeB/Ta interface than CoFeB/W interface, CoFeB roughness increases more with Ta cap. If we look at the borides of each element Ta and W [178], we find that Ta-B has higher negative formation enthalpy in comparison to W-B, leading to increasing Ms for Ta-B. This may explain the higher magnetisation at CoFeB/Ta interface in comparison to CoFeB/W interface.

Another possibility of lower magnetization at W/CoFeB as compared to Ta/CoFeB can maybe considered due to possibility of DMI effect due to heavy metal and ferromagnetic effect [179]. At this interface, magnetism could appear to reorient like skyrmions resulting in locally reduced magnetism. This effect is different for Ta and W since W is heavier**.** Capability of skyrmions is more with W, thus we may create more non collinear in W. It just means that they are less aligned and thus reduction at certain z position.

4.6 Conclusions

Thus, in this study, we have investigated a depth resolved magnetization for a series of half magnetic tunnel junctions, with different cap layers and annealing temperatures. We observed that in case of Ta cap layer, the magnetization orientation changes from *ip* to *oop* after annealing at 350°C with a change in distribution of magnetization between 2 interfaces from gradient profile in case of as deposited to a more homogeneous distribution after annealing. After annealing to higher temperature, we see a transition back to *ip* and decrease in amplitudes of magnetization and the profile realigning again in a gradient.

In case of W cap layer, we observed that for before and after annealing, the shape of profile remains the same although as observed from SQUID, EHE and SXRMR results we observed a transition from *ip* to *oop* although there were some discrepancies in comparison of magnetization amplitude. Although we didn't understand the reason for this perfectly, it is worth mentioning that it is not easy to determine a magnetic moment absolute value from XRMS.

5 Depth resolved magnetization profile of Co and Gd in Ta/Pt/Co/Gd/AlOx

5.1 Context

5.1.1 Magnetic racetrack memories

In 2008, an alternative memory was proposed by Parkin, Hayashi and Thomas [180] called the magnetic domain wall racetrack memory (*Figure 5.1*). In contrast to the functioning of HDDs (where bits are displaced in relation to the recording head by a combination of rotating the recording disk and moving recording head), racetrack memory (RM) works through magnetic domains, specifically domain wall (DW) motion. These DWs are electrically shifted along racetrack memory with fixed read and writing positions, not having any moving parts. Thus, these devices propose higher efficiency of MRAMS and are able to overcome shortcomings of HDDs. High domain wall velocity is key to the performance of RM devices, promoting research in devising materials that can provide maximum DW velocities.

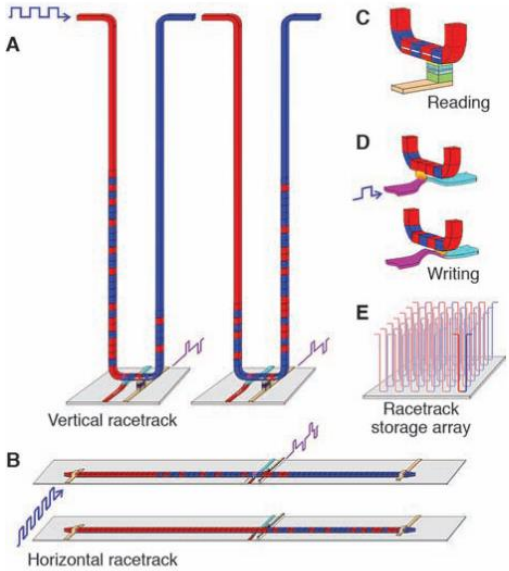

Figure 5.1 Sketch of a racetrack memory (A) A vertical-configuration racetrack in a U-shaped nanowire normal to the plane of the substrate. The two cartoons show the magnetic patterns in the racetrack before and after the DWs have moved down one branch of the U, past the read and write elements, and then up the other branch. (B) A horizontal configuration uses a nanowire parallel to the plane of the substrate. (C)Reading data from the stored pattern is done by measuring the tunnel magnetoresistance of a magnetic tunnel junction element connected to the racetrack. (D) Writing data is accomplished, for example, by the fringing fields of a DW moved in a second ferromagnetic nanowire oriented at right angles to the storage nanowire. (E) Arrays of racetracks are built on a chip (taken from [180]).

Initially magnetically soft permalloys were used to grow RTMs with in plane magnetization. Through application of spin – polarized current in the racetrack, there is an angular momentum exchange between electrons from the current and localized electrons in regions between opposite DWs. Such an angular momentum exchange exerts a torque called spin-transfer torque (STT) which moves the DWs in opposite direction to the current [181]. DW-velocities can be observed up to 100 m/s in these devices. However, the DW width in soft materials is influenced by shape anisotropy leading to rather large domain walls making the device unreliable [182].

More robust DWs were discovered in RMs with PMA with the magnetic preferential direction (easy axis) perpendicular to the racetrack surface. One of the ways to achieve PMA is through presence of heavy atoms like Pt at Co interface. This induces a strong hybridization of *5d* Pt orbitals with *3d* Co orbitals. Strong spin orbit coupling of Pt produces an increase of Co orbital momentum which makes it possible spin momentum perpendicular to the interface [183]. Miron *et al*., found in 2011, that Pt/Co layers give rise to a phenomenon called spin orbit torque which allows DWs to move with high speeds up to 350 m/s along the direction of the current [184].

In 2015, Parkin and Young introduced of a new version of RM using antiferromagnets [182]. One such example of a synthetic antiferromagnets is a bilayer of Co/Gd racetrack memory where Co is deposited on heavy metal Pt to benefit from the spin orbit coupling as shown in stacking in Figure 5.2. Magnetic properties of these ferrimagnet racetracks can be tuned by the composition of the metallic layers. For both Co and Gd, their magnetic properties behave differently with temperature due to a large difference in their curie temperatures T_C (for bulk Gd it is approximately 300K while for Co it is 1388K). Thus Co/Gd bilayers can be engineered in such a way that at a certain temperature T_M, often known as the compensation temperature there is no net magnetisation. This happens due to antiferromagnetic nature of such a bilayer. At such a compensation temperature, very high speed of domain walls has been observed [35]. Compensation of angular momentum at $T_{A,}$ has also been studied in such bilayers can also result in efficient DW motion [185].

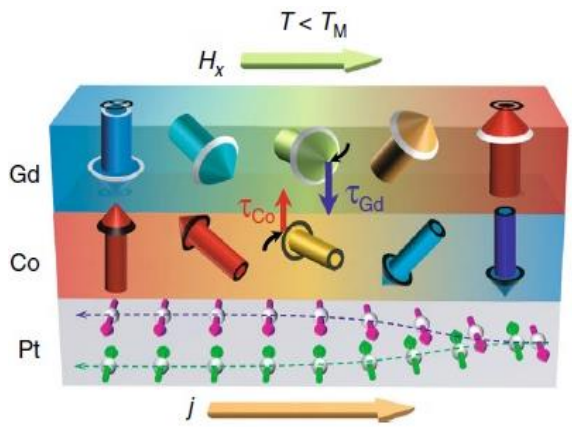

Figure 5.2 Schematic of a DW in ferrimagnetic Pt/Co/Gd in the presence of a current *j*. Arrows and colours in the Co/Gd layers represent the direction of the local magnetic moment, with the thickness of the arrows being the magnitude of the moment. The green and magenta arrows in the Pt layer represent the spin direction of the electrons in the current *j*. τ_{Gd} and τ_{Co} are the torques working on the magnetic moment of the Gd and Co layers. (Figure obtained from [186] with minor modifications)

5.2 Motivation

In recent years racetracks having (PMA) have gained considerable interest since they show very fast current and field induced domain wall motion [187], [35]. In non-centrosymmetric systems, presence of a layer with a strong spin orbit coupling such as Pt at one of the interfaces gives rise to an anti-symmetric exchange interaction, the so called *Dyzaloshinkii-Moriya interaction (DMI)* [25,188] which favors non-collinear spin alignment with a fixed chirality [189,190]. This leads to domain walls with a Néel internal structure whose stability and dynamics is influenced by the *DMI*, **but also by the spontaneous magnetization of the layer (M_S)** [191] and the effective magnetic anisotropy K_{eff}.
Very large domain wall velocities (>600 m/s) have been observed previously in rare earth-transition metal systems (which are known for their *large antiferromagnetic exchange coupling* between the RE and TM components [192] such **Pt/Co(1nm)/Gd/Pt multilayer driven by a magnetic field** [35] . This was said to be possible due to decrease of M_S with respect to metallic Co (the maximum domain wall velocity is proportional to D/M_S, with D the DMI energy), due to magnetic Gd coupled antiferromagnetically with the Co moments.

However, we have no direct information about the **extension of this interface coupling at the Gd/Co interface.** Is it just an **immediate interface** phenomenon or does the **coupling effect propagate** and modify the **magnetization distribution from the interface**?

To achieve full potential of RM with Pt/Co/Gd stacks, it is desired to tune T_A (temperature where angular momenta of Co and Gd are compensated) or T_M (temperature where magnetization of Co and Gd are compensated) closer to room temperature it is essential to study magnetism in across this bilayer as a function of thickness and temperature. By tuning magnetization of the magnetic layer or by having

accurate knowledge of magnetic thickness of the ferromagnetic Co layer along with Gd layer we can DW velocity can be optimize.

SXRMR can help us achieve this by depth resolved study at Co and Gd resonant edge along the growth axis by getting a direct determination of the distribution of the Co magnetization from the Pt/Co interface to the Co/cap one. Also, the magnetization profile in Gd layer to compare the thickness exhibiting antiferromagnetic coupling with respect to the roughness of the Co/Gd interface.

Thus, we are motivated to:

- To understand the magnetism at the interface Gd/Co
- To understand if there is propagation of this magnetism into the depth away from the interface and till which thickness and roughness.
- to understand the temperature evolution of the magnetization depth profile of Gd and Co layers in the sample by using X- ray resonant magnetic scattering (XRMS).

We will discuss magnetic properties in Pt/Co/Gd structures to have a better knowledge of these systems before we obtain a profile.

5.2.1 Magnetic properties of Pt/Co/Gd structures

In order to understand the magnetic properties of the Pt/Co/Gd, here we introduce the role of each material giving rise to magnetic effects at interfaces.

Pt is a heavy metal paramagnetic in nature with absence of spontaneous magnetization but presence of high magnetic susceptibility. This occurs due to the fact that Pt has an electronic band close to fulfil Stoner criterion for ferromagnetism [193]. On reduction of size, Pt atoms overcome the stoner criterion giving rise to ferromagnetivity whose effect if further observed in Pt/ferromagnets (Co etc.) interfaces. It is known to cause an enhancement of magnetization in FM materials through a phenomenon called *proximity effect*.

Co on the other hand is a ferromagnetic material known for creating spontaneous magnetic moment below Curie temperature (T_c, where T_c of bulk Co is 1388 K). M_s is dependent on temperature since thermal fluctuations due to localized spin that tend to distort parallel ordering. The material becomes paramagnetic above T_c due to thermal fluctuations distorting magnetic ordering.

Gd is a rare earth metal which is ferromagnetic in nature having a T_c close to room temperature (293K) for bulk Gd. The moment of a Gd atom consists of two components which are: (a) 4*f* electrons order indirectly via the conduction electrons which produces a moment of 7 μ_B (b) magnetization of 4*f* electrons polarizes electrons in 6*s* and 5*d* bands (combined conduction band) producing another 0.63 μ_B.

5.2.2 Magnetic properties at Co/Gd Interface

The magnetism at the interface of Gd and Co arises due to the indirect negative exchange coupling between Gd 4*f* magnetic moments and the Co 3*d* magnetic moments. Even though Gd 5*d* magnetic moments are parallel to Gd 4*f* moments through direct exchange, they are anti-parallel to Co *3d* magnetic moments via 5*d*-3*d* hybridization causing such an anti-parallel coupling [194]. Thus, the negative interlayer exchange coupling at the Co/Gd interface along with the positive intralayer exchange coupling (Co-Co and Gd-Gd) results in the creation of Co/Gd synthetic ferromagnetic bilayer where modification of the thicknesses of Gd and Co leads changes in magnetic properties (net magnetization of the bilayer) which can be tuned [195].

Thus, the Gd/Co/Pt stacking has been interesting in our study since the rare-Earth (RE) – transition metal (TM) interface forms a large antiferromagnetic coupling between the Gd and Co components.

5.3 Sample Growth

The sample under investigation Ta (4)/Pt (4)/Co(1)/Gd(wedge)/AlOx (6) where the numbers in parenthesis are the nominal thickness in nm and the system was grown on Si/SiO_2 substrate by magnetic sputtering at room temperature at Institut Neel as shown in Figure 5.3. The thickness of Ta, Pt and Co were kept constant while the Gd layer was deposited in form of a wedge with variable thickness and Gd layer was covered with 6 nm of Al to prevent its oxidation since after exposition to atmosphere the Al layer is expected to be oxidized. The sample was later divided into several pieces, out of which we investigated 2 sample pieces. The Co/Pt interface was deposited with < 2 nm thickness of Co to benefit from the perpendicular magnetic anisotropy and DMI for their use in motion in domain wall motion. Ta was used as a buffer layer between the substrate and the Pt layer to improve Pt adhesion.

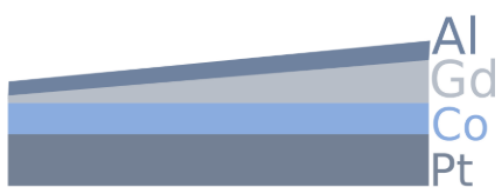

Figure 5.3 Stacks of non-centrosymmetric trilayer Pt/Co/Gd

It should be noted that the SXRMR data were in fact collected on two samples pieces of the original sample having in principle very same or similar characteristics. These samples will be labelled at A and B in the following.

5.4 Hard X ray reflectivity measurements

Hard X-ray reflectivity (HXRR) data was collected in the D8 reflectometer at Institut Néel with a Cu K_α x-ray source corresponding to a photon energy of at an energy of 8041 eV for both the samples A and B measured till ϑ_{max} = 3.5° (q =4.98 nm^{-1}). The experimental data (black circles) as well as their best fits (smooth red lines) are shown in Figure 5.4. From the refinements of the structure, we find that we were able to obtain a good agreement between experimental and fitted data. In fact, we can see that both the curves are superimposable and very close in shape indicating that the structure of both sample pieces should be similar. The structural parameters density (ρ), thickness (t) and roughness (σ) of each layer which were refined to obtain the best fits are shown in *Table 11* along with the error bars calculated over parameters over both the stackings.

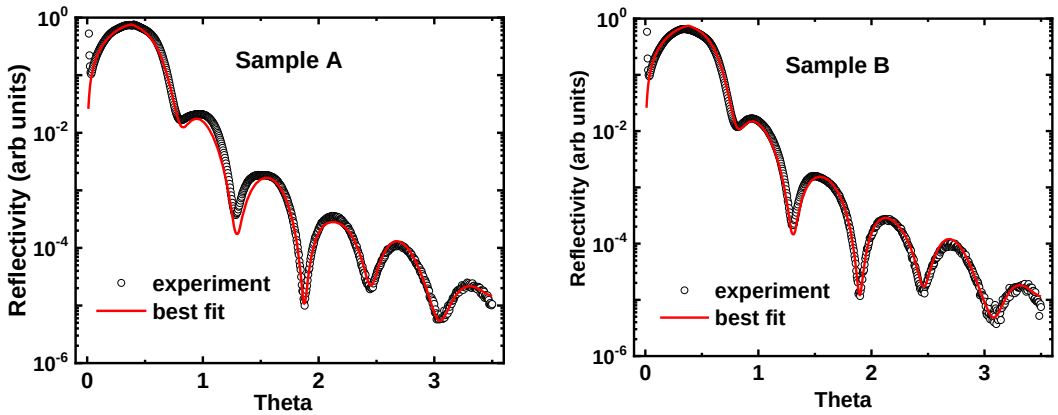

Figure 5.4 Experimental (black dotted line) and fitted (red smooth line) specular reflectivity collected by hard X ray reflectivity

Table 11 Structural parameters ρ, t and σ derived from best fits

	ρ_{bulk} (mol/cm^3)	(mol/cm^3)	t (Å)	σ(Å)
AlO_x	0.194	0.164 ± 0.019	40.7 ± 5.3	4.9 ± 2.3
Al	0.100	0.055 ± 0.007	16.7 ± 1.6	5.2 ± 0.1
Gd	0.050	0.029 ± 0.005	9.4 ± 0.2	2.8 ± 0.8
Co	0.108	0.095 ± 0.012	7.3 ± 0.1	1.4 ± 0.1
Pt	0.110	0.110 ± 0.000	37.3 ± 0.3	3.3 ± 0.1
Ta	0.092	0.092 ± 0.000	35.9 ± 0.5	3.1 ± 0.1
SiO_2	0.132	0.126 ± 0.000	1218.4 ± 5.9	1.5± 0.1
Si				3.0 ± 0.6

For refinement, we divided the Al layer into a pure Al metal layer and a layer of Al oxide with formula Al_2O_3. This was done since Al is well known for its tendency to get oxidised easily when exposed to the atmosphere. Due to the time gap between sample growth and SXRMR measurements, sample was exposed to the environment for a long time and thus to get better fits, we considered a separate layer of

Al oxide. In fact, since we were not completely sure of the composition of the oxide (perhaps a composition gradient related to the in-depth penetration of the oxygen atoms into the Al layer), the limits of the density parameter have been set between that of pure aluminium and that of Al_2O_3.
For both samples, we find total thickness of Al layer (thickness of Al + thickness of Al oxide) as 57.4 ± 6.9 Å in relatively good agreement with the nominal value. The refined thickness of the Ta and Pt layers are also found in good agreement with the nominal values. For Co thicknesses we get significantly different from nominal values Co = 10 Å. Unfortunately, the experimental data were recorded on a limited angular range up to 3.5° corresponding to a q_{max} value of 4.98 nm^{-1}. As a result, the precision of the parameters, extracted from the adjustment for the thinnest layers of Co and Gd, could also be limited. The very low amplitude error bars most often come from parameter values which for sample A and B have reached a high or low limits in the fits except for the roughness of the Pt and Ta layers. The interest of these two reflectivity curves measured in the hard X-ray range is essentially to show that samples A and B are very similar. However, the values of the structural parameters determined from measurements in a limited reciprocal space raise several questions as to their reliability. In order to increase precision of structure determination specially the thickness of Co and Gd, in the next section, we will look at the structural parameters derived from SXRMR measurements conducted at *off resonant energies (energy far away from resonant edges)* for both Co and Gd and compare the results with HXRR. We will also further compare these parameters with results obtained for energies in proximity to the Co L3 and Gd M5 edge where we can find increased sensitivity to Co and Gd respectively.

5.5 Soft X-ray magnetic reflectivity (SXRMR)

5.5.1 Determination of the optical constants:

The SXRMR experiments for these samples were conducted near the **Co L3 edge** and the **Gd M5 edge**. In this section we will present the resonant parameters that we used in order to obtain magnetic profile.

As in the previous chapter the $f_1(E)$, $f_2(E)$, $m_1(E)$, $m_2(E)$ for the **Co $L_{2,3}$ edge have been derived using CT Chen et al**, [120] data which was collected at room temperature. The data for the **Gd $M_{4,5}$ edge have been derived from the work of S. Mangin *et al.*** [196] at 100K. We have already indicated that the sum rules lead to m_{tot} = 1.7 μ_B/atom for Co. In the cases of Gd, the XAS/XMCD data came from total electron yield (TEY) measured on glass/$Gd_{40}Fe_{60}$ (100 nm)/$Tb_{45}Fe_{55}$ (3 nm)/Al (3 nm). The derived resonant parameters from these samples as shown in Figure *5.5*(a) and (b) for Gd and (c) and (d) for Co were used in DYNA program.

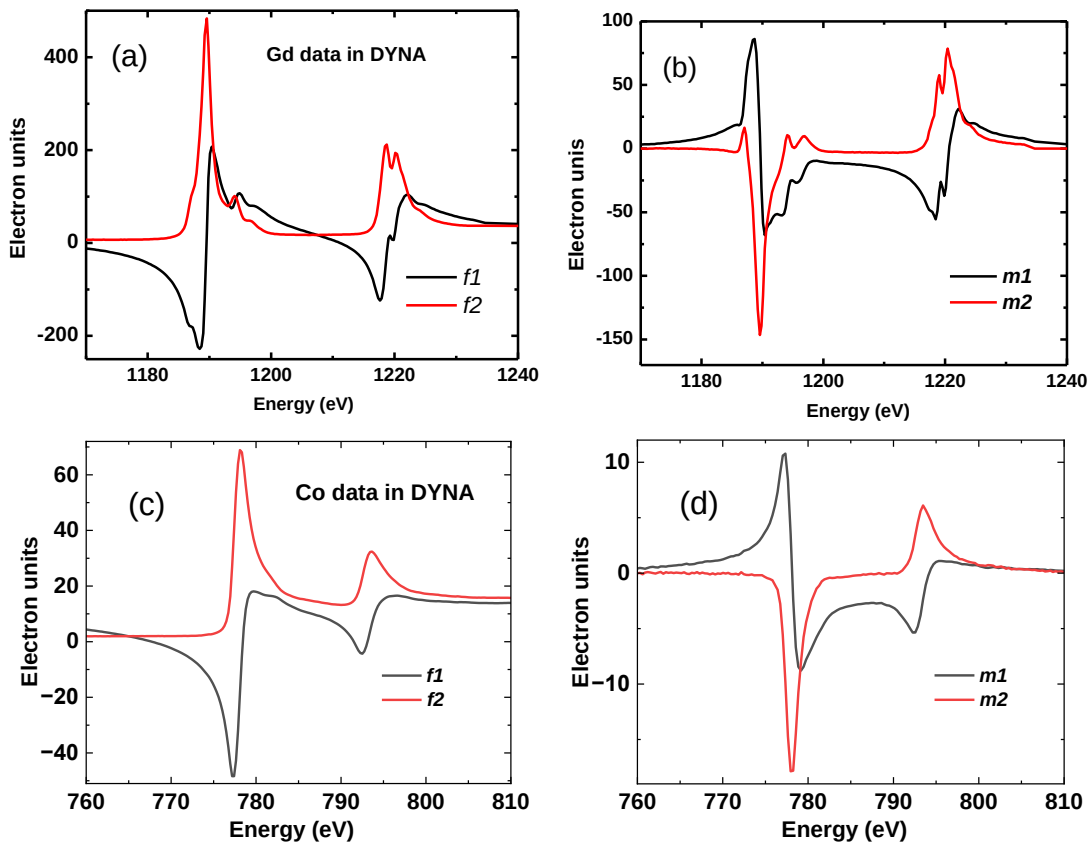

Figure 5.5 (a) and (b) shows resonant parameters at Gd M4,5 edge and (c) and (d) shows resonant parameters at Co L2,3 edge.

Later, we also took into account the XMCD and XAS data which was measured by J. Vogel and S. Pizzini at the DEIMOS beamline at SOLEIL to provide a basis for comparison and to assess the relevance of the resonant parameters used in DYNA from other references. Figure *5.6* (a) and (b) show the data XAS and XMCD data measured on the sample at 300K and 4K for Gd edge.

Figure *5.6* (c) displays superimposition of f_2 value of Gd in Dyna and the scaling of the XAS data measured on the sample at 4.2 K and (d) superimposition of scaled XMCD data and m_2 used in dyna scaled to chantlers.

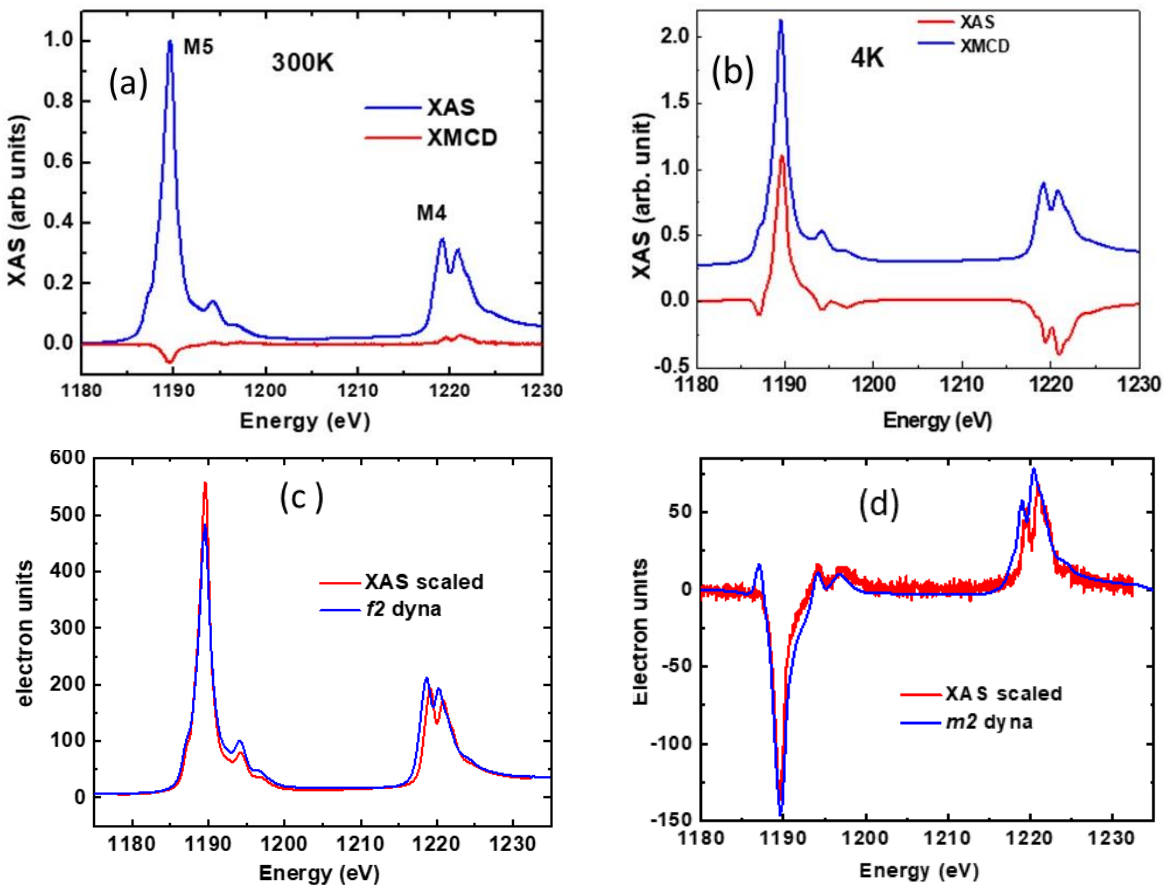

Figure 5.6 (a) and (b) are XAS and XMCD signals measured at Gd M4,5 edge at 300K and 4K measured at DEIMOS beamline (c) shows superimposition of XAS data scaled to Chantlers table of data from DEIMOS beamline along with data used in DYNA software. (d) shows superimposition of the XMCD data scaled and data used in DYNA

We observe that except for the difference in the energy scale between the measurements on ID12B and DEIMOS (not analyzed in detail), the data compares quite well. However, the data collected on DEIMOS seems to present a better energy resolution. As the energy resolution on SEXTANTS with 70µm exit slits, used during reflectivity measurements, is slightly worse than that of DEIMOS, the parameters available in Dyna were preferred. Moreover, the comparison of the XMCD signal shows changes in the amplitude of the spectroscopic characteristics below and above the resonance signal at 1188.2 eV. The origin of these modifications has not been studied and is tentatively attributed to a slightly different environment of the Gd atoms between the two multilayers. An analysis of the energy dependence of the reflectivity on SEXTANTS will be presented later to confirm the relevance of the parameters used.

Similar data has been presented for Co edge in Figure *5.7*. (a) displays XAS and XMCD data measured at DEIMOS. (b) show the superposition of XAS at 4K and 300K with data from CT Chen et al., scaled to Chantlers table.

Although there is a slight problem of resolution on the higher energy side of scaled XAS data, the peak seems to superimpose each other well.

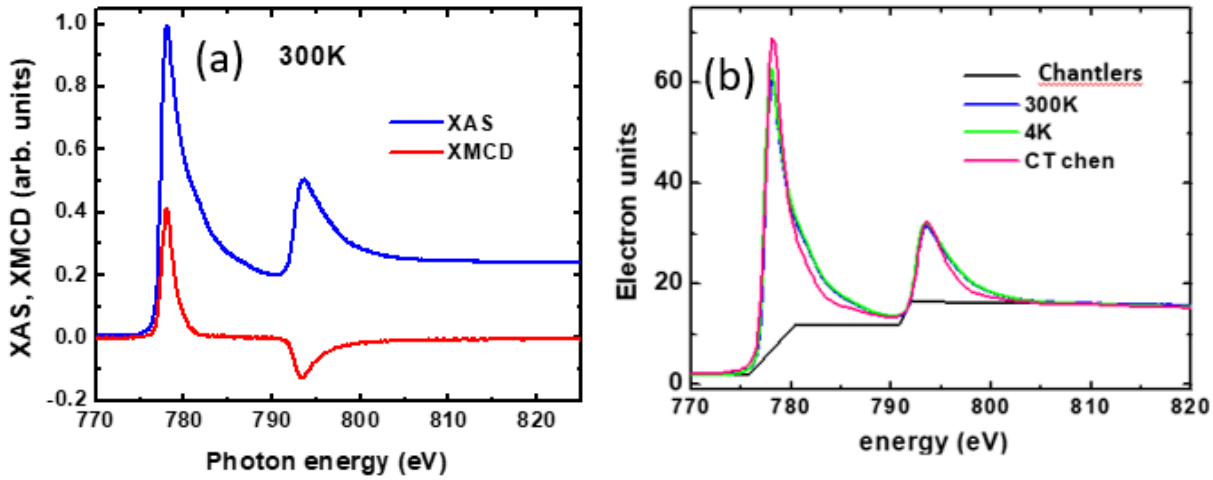

Figure 5.7 (a) shows XAS and XMCD signals measured at Co L2,3 edge at 300K and 4K. (b) shows superimposition of XAS data scaled to Chantlers table along with data used in DYNA software

We obtained the data for XMCD of Gd and Co on the sample measured J. Vogel and S. Pizzini much later after almost finishing analysis on the data using the resonant parameters of S. Mangin. That is why in order to see, if the data from both different samples are close enough, we have shown the superposition of the data. To see the SQUID results, for this sample we refer to the results on a similar sample since we weren't able to successfully perform VSM SQUID on this sample ourselves [197].

5.5.2 Determination of structure: off resonant analysis

Figure 5.8 shows the fits of average reflectivities at 760 eV (18.1 eV below Co L3 edge) and 1172.2 eV (17.4 eV below Gd M5 edge) which are energies far away from the L3 and M5 edge for Co and Gd respectively. From the Figure 5.4, we can say that we were able to obtain very good fits for both the energies with good agreement between experimental and fitted data. In all cases, these q_{max} values were higher than that reached with the incomplete hard X-ray measurements.

The average refined parameters are given in *Table 12* for both sample A and B at 760 eV and 1172.2 eV.

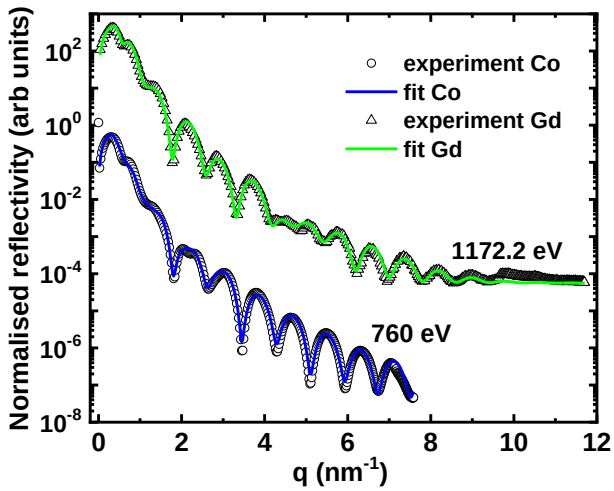

Figure 5.8 experimental and fitted average angular reflectivity at 1172.2 eV and 760 eV

Table 12 Structural parameters *t* and *σ* derived from best fits

	ρ_{bulk} (mol/cm^3)	(mol/cm^3)	*t* (Å)	*σ*(Å)
AlO_x	0.194	0.171 ± 0.016	34.7 ± 10.7	6.6 ± 2.4
Al	0.100	0.072 ± 0.019	16.9 ± 7.3	9.8 ± 5.3
Gd	0.050	0.040 ± 0.007	11.5 ± 0.8	7.3 ± 3.1
Co	0.151	0.095 ± 0.012	6.3 ± 1.1	2.8 ± 1.3
Pt	0.110	0.106 ± 0.006	38.9 ± 0.5	3.2 ± 0.4
Ta	0.092	0.092 ± 0.001	35.1 ± 0.5	3.7 ± 0.7
SiO_2	0.132	0.129 ± 0.003	1159.9 ± 132.4	2.3 ± 0.4
Si				2.4 ± 2.1

AlOx density appears to be slightly lower than Al_2O_3 density that is probably due to an incomplete oxidation process of Al or a density of the initial pure Al layer smaller than the bulk one. The 34.7 Å thickness of this layer indicates the depth to which the oxygen atoms have diffused inside the capping Al layer. The large error bar could have two origins on the one hand the inhomogeneous propagation of the oxygen atoms, as evidenced by the large roughness of the aluminum layer underneath, and on the other hand a *time evolution effect*, leading to a difference in the thickness of the AlOx layer, since the data at low temperatures were measured later than those at room temperature. The roughness of this capping layer is not so high. It should be noted here that for all the refinement an additional layer to simulate the surface contamination has been taken into account. The thickness and roughness of this layer are limited at RT to about 30 Å and 7.5 Å, respectively. To be able to satisfactorily reproduce the reflectivity curves recorded at much larger values must be considered. The thickness and the roughness also depend on the time spent at low T and the vacuum in the chamber before cooling the sample. The density of the Al layer assumed to be initially pure appears clearly lower than the bulk value. This could be due on the one hand to a poorly crystallized or amorphous Al layer, and on the other hand to an alloying effect with the Gd

atoms at the lower interface, as evidenced by the high roughness of the Gd layer. The sum of the thickness of the AlOx layer and that of Al appears slightly less than 60 Å as expected from the nominal values.

For Gd layer, the density is about 80% of that of the bulk, which seems reasonable for a layer thickness of the order of a nanometer. Although the refinements were performed over a larger range of **q**, the thickness of the Gd layer is again found to be around 1nm with a small standard deviation value. Since, we are working for Gd as a wedge, we maybe probing at a different part of the wedge where Gd is 1 nm. However, the Gd layer also exhibits large roughness at the Gd/Al interface as mentioned earlier. This high roughness could be associated *with a thick layer of intermixed GdAl* [198,199]. It would be interesting to compare the thickness obtained far from the edge and that obtained with incident photon energies close to resonance, which could enhance the contrast between the atoms of Gd and Al and give a greater thickness of Gd.

The density of the Co layer is reduced by 37% which a lot. This layer is also found smaller than the expected one with also a relatively small standard deviation. Again, the analysis of the reflectivity measurements at resonance could be sensitive to Co atoms intermixed with Pt at the bottom interfaces and Gd at the top interfaces and reveal a thickness closer to the nominal one.
The densities and the thicknesses of the Pt and Ta layers are much closer to the nominal ones. These layers show similar roughness values.

Finally, the roughness of the substrate is in agreement with a high-quality substrate. Moreover, due to the presence of high frequency but low amplitude oscillations in the large angle reflectivity, it was possible to refine the thickness of the SiO_2 layer. The value of the density is in agreement with the bulk one.

It must be noted that for good structure parameters, we will rely on the previous measurements discussed from HXRR and off reflectivity SXRMR. In the following sections, we will also study parameters derived from reflectivity at energies in the vicinity of the edge. We were not able to perform other experiments to determine the structure parameters during this thesis, for this sample.

5.5.3 Determination of magnetization profiles at room temperature

5.5.3.1 Energy dependent reflectivity

Figure 5.9 presents energy dependent reflectivity which was measured at 2 angular positions – 46° and 50° at Co L2,3 edge along with asymmetry ratio (green line). These high angular values were chosen to perform energy dependent scan to benefit from the strong signal due to *oop* magnetization in the system even though it is better to choose angular values close to the critical angle.

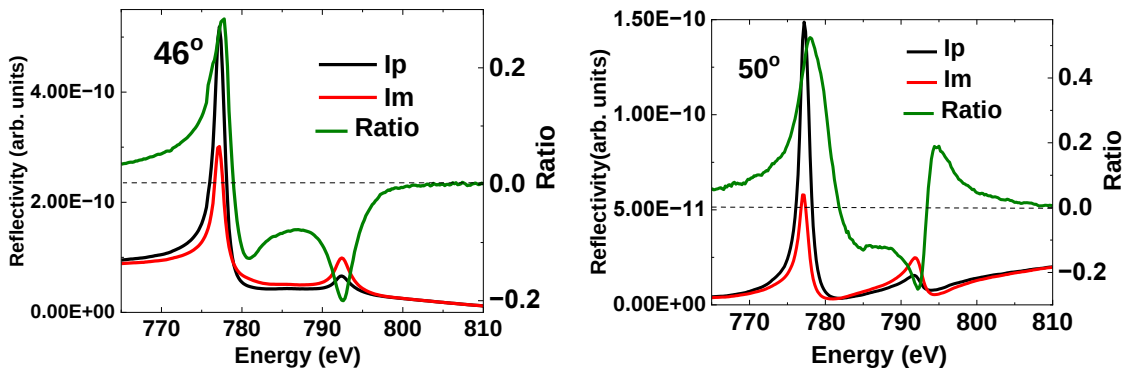

Figure 5.9 Experimental energy dependent reflectivity and asymmetry ratio at Co edge at 46° and 50°

The shapes of measured reflectivities *Ip* and *Im* for both angles strongly resemble the spectroscopy of metallic Co with both having maximum intensity resembling L3 edge. There is a finite asymmetry ratio up to 30% indicating presence of signal at remanence at 46° and reaching up to 60% presence of signal at 50°.

Since these curves are measured in reflectivity, they also present some weightage of the real and imaginary part of atomic scattering factor. Since the position of maxima of the L3 and L2 edge is shifted, determination of the difference in energy, to be taken into consideration as a correction to the calibration in energy, will be evaluated by refining the average reflectivity.

For Gd we don't present the qualitative energy dependent reflectivities however their best fit at 5° and 36.4° is discussed in the next section.

5.5.3.1.1 Determination of the energy correction

<u>Co edge</u>

Starting from the structural parameters determined from off-resonance angular reflectivity, the fit of the average intensity as well as the magnetic asymmetry led to very good agreement as seen on Figure *5.10*. The fit of the magnetic asymmetry was carried out by adding the data in the *multifit process* by considering the magnetism of the Co layer constant through the whole layer.

For two angular values separated by 4°, the *mms* value is the same and equal to 1.31. It indicates a magnetic moment 31% higher than 1.7μ_B. However, this value must first be put into perspective. We will discuss moment amplitude values after analyzing the angular dependence of magnetic asymmetries.

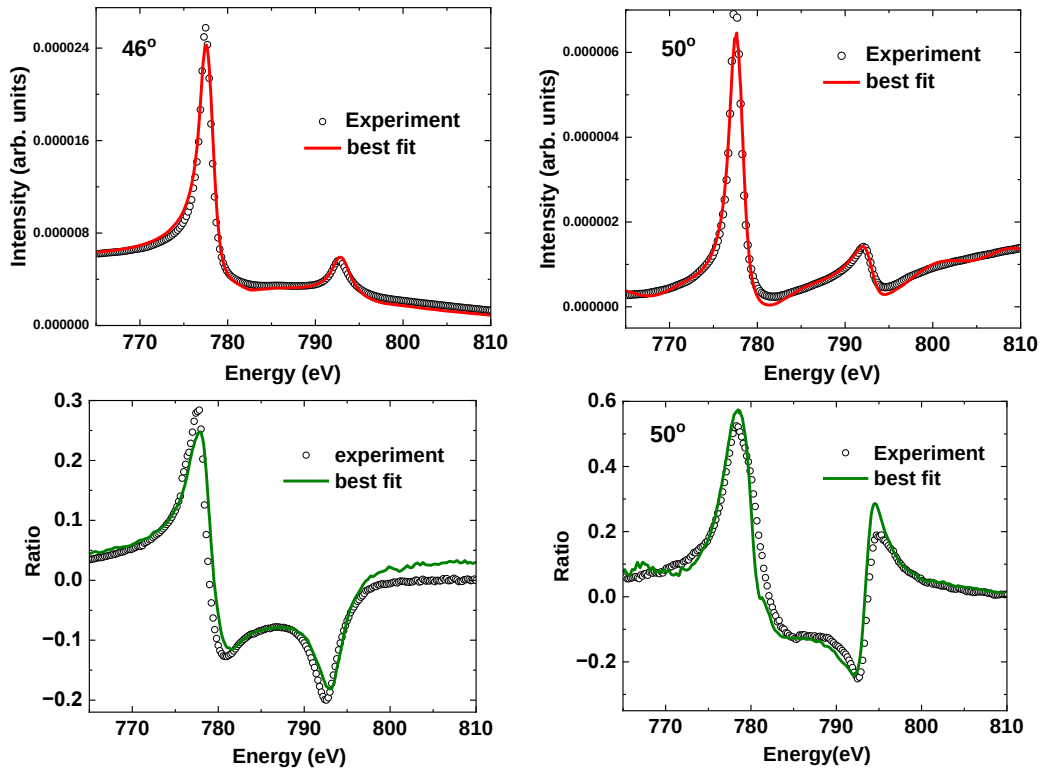

Figure 5.10 Experimental and best fit for energy dependent average reflectivity (upper panel) and magnetic asymmetry (lower panel) at 46° and 50° at Co edge

We calculated **δE = 0.35 eV to be added to experimental** values.

Gd edge

Figure *5.11* presents energy dependent reflectivity collected at 2 angular positions (5° and 10°) around the Gd M_5 edge together with the best fit. For Gd, we did not try to collect data at large angles because at room temperature as small magnetic asymmetries were expected. Moreover, we only recorded the energy dependence at the M_5 edge. At 5°, the shape of the scan is closer to the real part of resonant term, while the shape of scan at 36.4° indicates higher sensitivity to imaginary part of resonant term. Another point to take is the huge energy shift we observe through these curves compared to the M5 edge given in the data booklet [200] which is 1189.6 eV.

Similarly, in the case of Gd, spectral shapes of the absorption are essentially that of Gd as expected along with absorption spectra for pure Gd superimposed for comparison.

We obtained rather good fits leading to a correction of 12.75 eV to be subtracted to experimental values. Parameters f_1 and f_2 are good enough to reproduce the data except perhaps around 1187 eV (corrected value) where we late observed a difference in amplitude between the data tabulated in DYNA and the absorption data measured before.

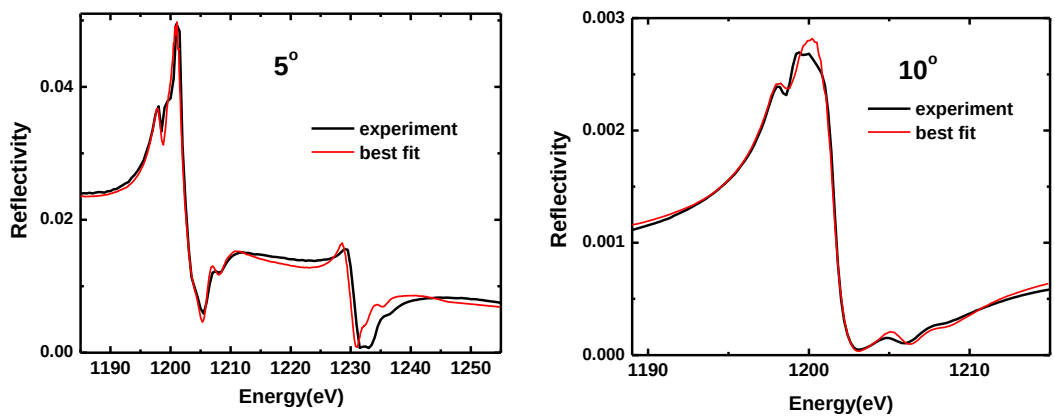

Figure 5.11 Experimental and best fit for energy dependent average reflectivity and magnetic asymmetry at 5° (left side) and 10° (right side) at Gd edge

5.5.3.2 Angular dependent reflectivity:

Figure *5.12* shows the angle dependent reflectivity for several energies in the vicinity of Co L3 edge (left hand side) and Gd M5 edge (right hand side) where we show experimental *Ip* and *Im* along with the asymmetry ratio for each energy. The energies are selected in a way that to benefit from the strong contrast in the real magnetic part of the ASF and the different signs of the resonant charge and magnetic terms.

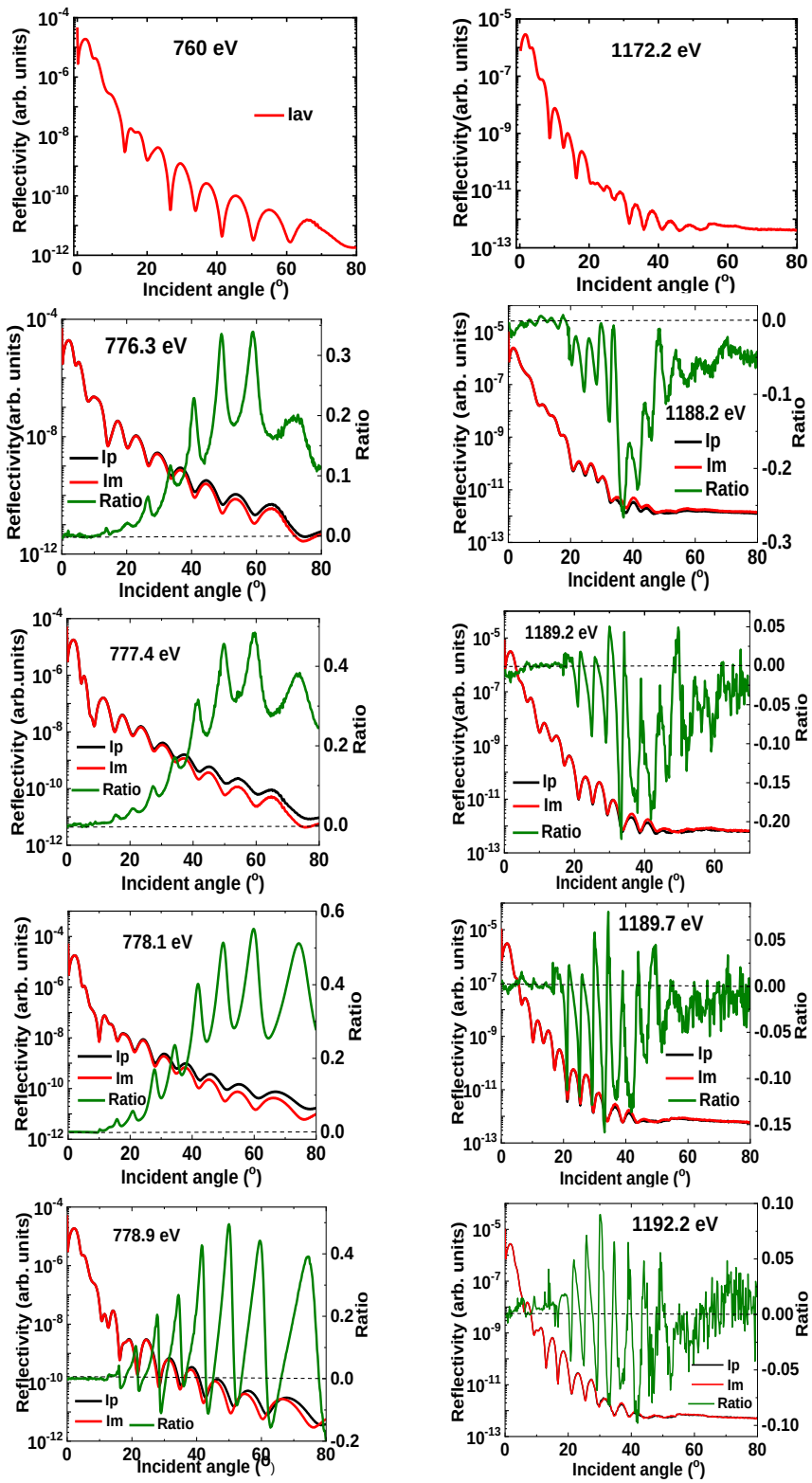

Figure 5.12 Experimental average specular reflectivities *Ip* and *Im* (red and black smooth lines respectively) and their corresponding asymmetry ratios (green smooth line) at energies in the vicinity of Co edge on the left-hand side panel. On the right-hand side shows the same in the vicinity of Gd edge.

For all the energies for both Co and Gd, we observe the similar behavior of splitting of *Ip* and *Im* at large angles, a typical characteristic of *oop* magnetizations with its absence at low angles.

In case of Co edge, *Ip* and *Im* start to split around 20° till 80° giving a large asymmetry ratio at large angle. From 776.3 eV to 778.1 eV (ascending side of the absorption edge), the shape of the magnetic asymmetries is similar, of positive sign and increasing to large angles. The oscillations are essentially related to the normalization by the average intensity. Above 60° the signal the reduction of the magnetic contrast is due to the background in the intensities I_p and I_m. At 778.4 eV the shape of the magnetic asymmetries changes as the oscillations of I_p and I_m begin to approach each other until they intersect, which leads to a decrease, first more marked at large angles, then to a beat between positive and negative amplitude whose envelope depends on the energy. The maximum amplitude of the asymmetry ratio continuously decreases from about 0.54 to 0.45. All these effects are related to the modifications of the quartet of values f_1, f_2, m_1, m_2.

In the case of Gd, the reflectivity curves are strongly affected by the background as soon as the amplitude of the intensities is either of the order than the dark current of the detector. However, it should be noted that it appears above 50° which correspond to a higher momentum transfer value than that reached at 80 degrees for Co (9.23 nm^{-1} vs 7.76 nm^{-1}) where the effect of roughness within the stack is also more penalizing. Here the data up to 80° although greatly reduced from 40 degrees, shows oscillations in the magnetic asymmetries that might be worth keeping. during data refinement. Some data are shown till 70° since they couldn't be measured till 80o at the beamline.

Evolution of the shape of the magnetic asymmetries during the transition from the rising side to the falling side of the absorption edge between 1189.2 eV and 1192.2 eV, shows a similar behavior to that of the Co with an opposite sign. This opposite sign is the signature of the antiparallel alignment of the net magnetization of the Co and Gd layers, linked to the antiferromagnetic coupling of Co and Gd. Although we expect a weak signal for Gd at room temperature [35] **the amplitude of the magnetic asymmetry is significant as it reaches about 27% at maximum. As for Co, the maximum amplitude of the magnetic signal increases when approaching the absorption edge energy.**

5.5.3.2.1 Determination of structure parameters

Figure *5.13* shows best fits refined at all the energies in the vicinity of Co L3 edge (left side) and Gd M5 edge (right side) as shown in from the very good fits of the experimental data. All intensities were first refined simultaneously for each edge and then individually.
We will discuss the table with structural parameters including the parameters calculated from analysis at different temperatures in Table *13*.

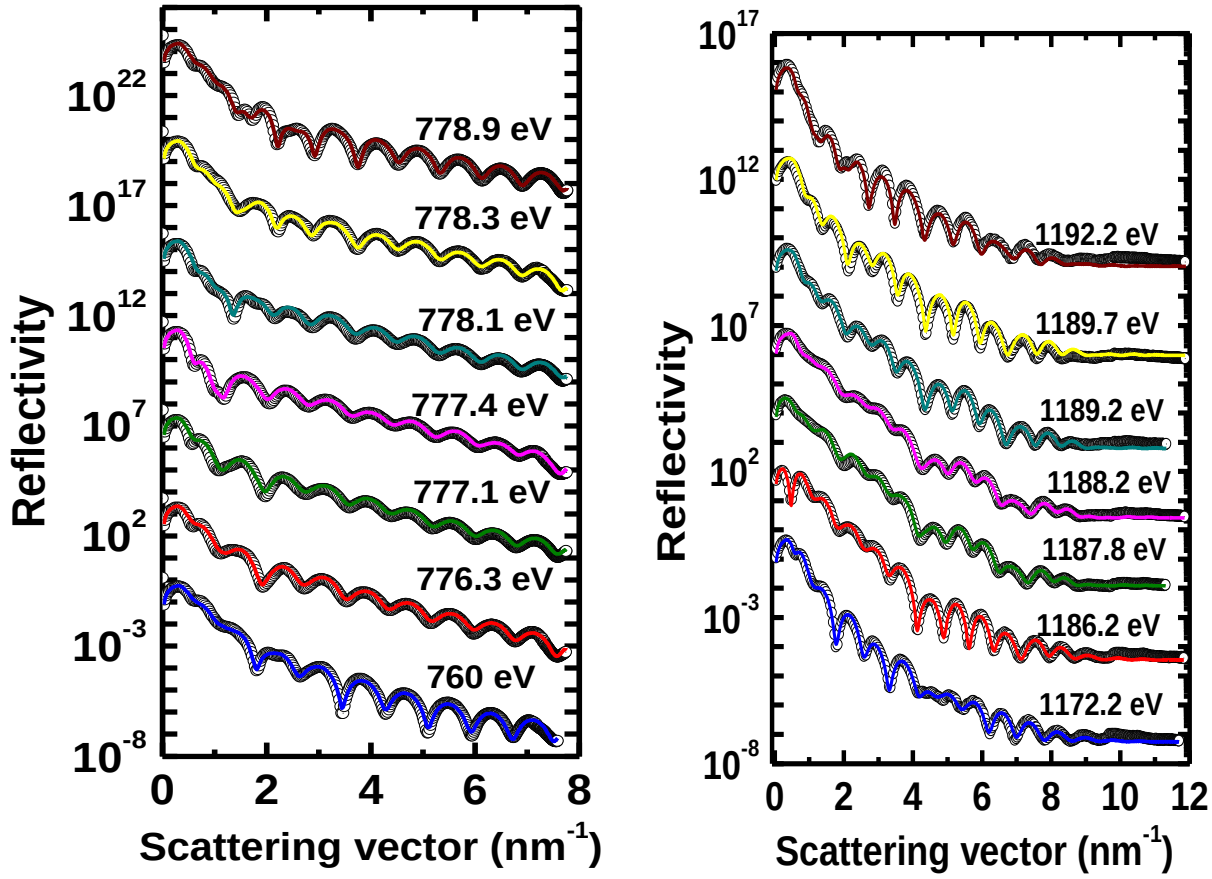

Figure 5.13 Experimental and best fit for all energies in the vicinity of Co edge (left hand side) and Gd edge (right hand side)

The tabulated values represent the mean value of the parameters obtained at each energy and the error bar is evaluated from the standard deviation of all the parameters.

Table 13 Structural parameters ρ, t and σ derived from best fits

	ρ (mol/cm^3)	t (Å)	σ (Å)
AlO_x	0.180 ± 0.022	40.1 ± 8.6	6.1 ± 2.4
Al	0.045 ± 0.036	12.5 ± 7.4	**2.8 ± 2.5**
Gd	0.038± 0.011	**14.1 ± 3.6**	**9.1 ± 4.8**
Co	0.128 ± 0.024	**7.6 ± 2.7**	2.8 ± 0.6
Pt	0.104 ± 0.007	36.2 ± 3.1	3.1 ± 0.8
Ta	0.083 ± 0.006	35.3 ± 1.7	4.7 ± 1.4
SiO_2	0.129 ± 0.003	1188 ± 50	2.3 ± 0.3
Si			1.0 ± 1.2

From the table, we can observe that the results are close to those derived from the analysis of the data measured *off-resonance*. The parameters for the SiO_2 layer are confirmed. For the Ta and Pt layer, considering the larger error bars, related to a much larger number of acquisitions, the values are quite

similar also. For Co, the numerous fits at resonant energy led to an increase of the density that could be related to small discrepancies between the f_1 and f_2 tabulated values with the actual ones. The thickness is larger than the 6.3 Å value derived off resonance. Although the total interfacial roughness with the Pt layer and with the Gd layer are found identical, this could be linked to a higher sensitivity to Co atoms intermixed with Pt and Gd at both interfaces, for measurements in the vicinity of the Co L_3 edge. This effect seems to be more pronounced on the Pt side since at the same time a slightly lower value of Pt thickness is noted. For Gd, the density value is the same at resonance and off resonance, indicating good agreement between the tabulated and actual resonance parameters. In contrast, the thickness and roughness values show more pronounced changes. The same applies to the thickness and roughness parameters for the Al and AlOx layers. On the one hand, these changes reflect a greater sensitivity to the Gd atoms dispersed in the Al layer due to measurements at the Gd M_5 edge, resulting in a larger effective Gd thickness and a smaller Al thickness. On the other hand, as the experiments were performed over several beam periods, it is also possible that the reduction in Al layer thickness is related to an increase in oxygen propagation in the Al layer, which is indicated by the increase in AlOx layer thickness. The reduction of the interface roughness between the Al layer and the AlOx layer could be related to an oxygen diffusion limit in the aluminum around 40 Å. The large roughness between the Gd and Al layer is confirmed and even strengthened in agreement with the ability of Gd and Al to form an alloy.

5.5.3.2.2 Co Magnetization profile

For the case of Co at 300K, we started the refinement procedure initially considering a model with homogeneous magnetization throughout Co layer since we do not expect strong changes in magnetization of Co at room temperature. The structural parameters obtained for each incident resonant photon energies were kept constant and the only fitting parameter was the weighting factor *mms* to depict uniform magnetization of Co layer. However, an equal distribution of magnetization from the Pt/Co interfaces up to the Co/Gd interface did not result in the best fit as illustrated in

Figure 5.14 (a) (green solid line). After, Co layer was divided into 3 sublayers where MMS of each sublayer was fitted along with the corresponding thickness to calculate the magnetization profile. We were able to get a very good fit for this model.

We made another fit by fixing the mms of sublayer at the interface Co/Pt, in order to see if we could have a complete homogeneous profile with no increase at Co/Pt interface as can be seen in Table *14*, however this did not result in a satisfying fit and was far from the best fit indicating that such an increase is necessary to consider.

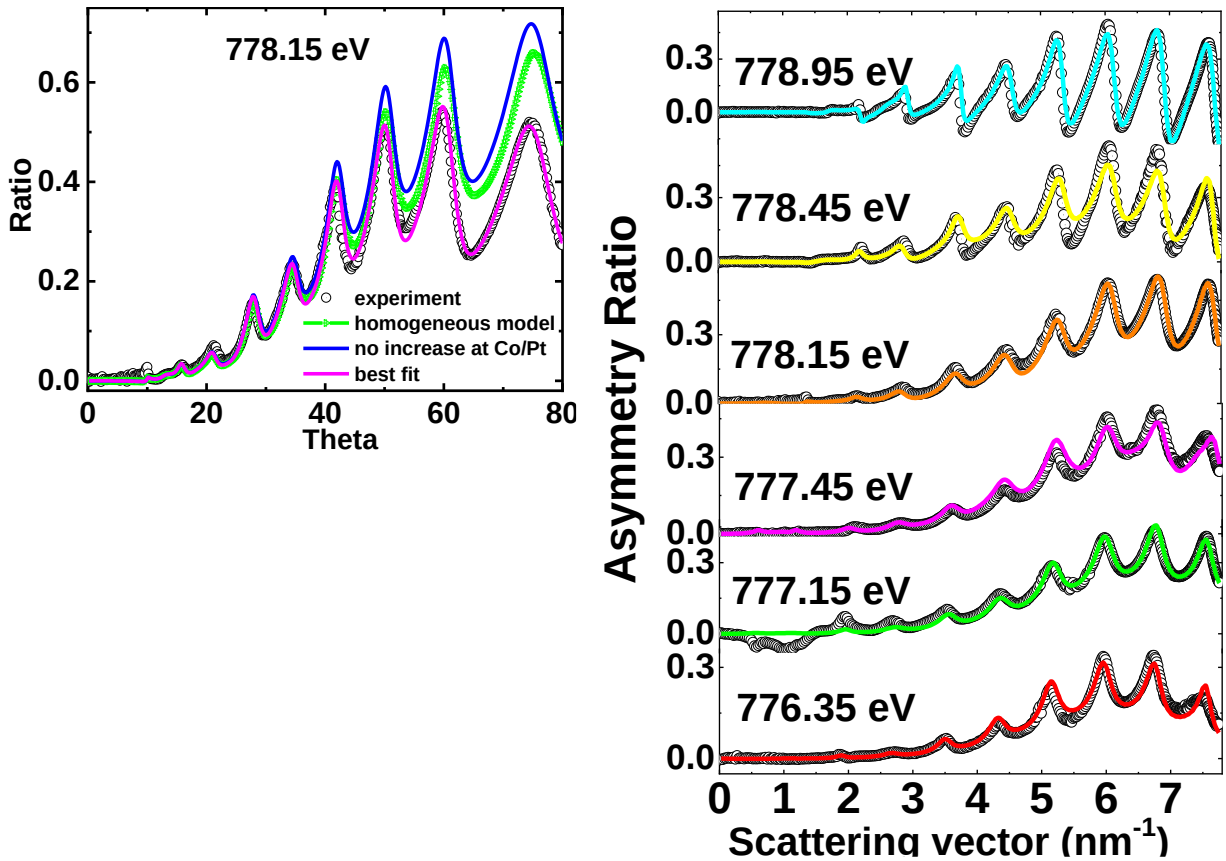

Figure 5.14 shows experimental and fitted asymmetry ratio at (a) 778.15 eV showing various models and (b) at various energies in the vicinity of Co edge after applying 3 slice model

The values describing the out-of-plane magnetization profile throughout the Co layer are given in Table *14* from the bottom Pt/Co interfaces to the Co/Gd interface

Table 14 Thickness and the mms values for each sub layer derived from refinement of asymmetry ratio at RT

Sublayers thickness	[Å]	*Magnetization amplitude*	Refined values	Corrected values
t_1	2.2 ± 0.4	mms_1	1.36 ± 0.16	0.89 ± 16
t_2	3.0 ± 0.8	mms_2	1.39 ± 0.19	0.92 ± 0.19
t_3	2.4 ± 0.3	mms_3	1.57 ± 0.24	1.04 ± 0.24

The average value of the magnetic amplitude calculated from the values of each sub-layer weighted by their respective thicknesses is equal to (1.44 ± 0.20) in good agreement with the value of 1.31 derived from the refinement of the energy-dependent asymmetry ratio as previously described. However, these *mms* values are larger than the ones assumed to correspond to a magnetic moment of $1.7\mu_B$ for Co. It is important to recall that SXRMR is not an appropriate technique to provide absolute amplitude for magnetic moment, as the parameter to be refine is not directly the *mms* values but in fact the product ρ

× *mms*. The Co layer is ultrathin and shows a strongly reduced mass density while the sample used to derive the reference resonant parameters f_2 and m_2 was a 7nm thicker film with probably a mass density closer to the bulk one. Therefore, to get more significant *mms* values, we proposed to consider a correction factor equal to 0.099/0.151= 0.66, **the value 0.099 being the average of the density parameters derived from the refinement of the off-resonance reflectivity measured in the soft X-ray range and the two reflectivity curves collected in the hard x-ray range.** These models of magnetization profile is within the errors bars more or less constant and shows an increase of the magnetization at the Pt/Co interface by 14.4%.

5.5.3.2.3 Gd Magnetization profile

Figure *5.15* (a) shows experimental Gd magnetic asymmetry at 1188.2 eV compared with various models. The blue curve corresponds to the asymmetry ratio obtained for a magnetization distribution model considering a homogeneous distribution of the out-of-plane magnetization of Gd (only one slice). Not only the shape of the magnetic asymmetry is not reproduced but the amplitude of the magnetization would correspond to 140% (mms=1.4) of the amplitude of the XMCD signal used as reference which would induce a magnetic moment unrealistic for Gd at room temperature of 8.7 µB/atom. The green curve presents the best result with a model where the Gd layer is divided into two slices and only the magnetization amplitude of the lower one, at the interface with the Co layer, as well as the thickness of the 2 slices are refined while the magnetization amplitude of the upper is set to zero.

Like for the magnetization profile within the Co layer, the best fit was obtained by dividing the Gd layer in 3 slices in order to refine the magnetic asymmetries. Figure *5.15* (b) shows the best fit obtained at several resonant energies to describe the magnetization profile.

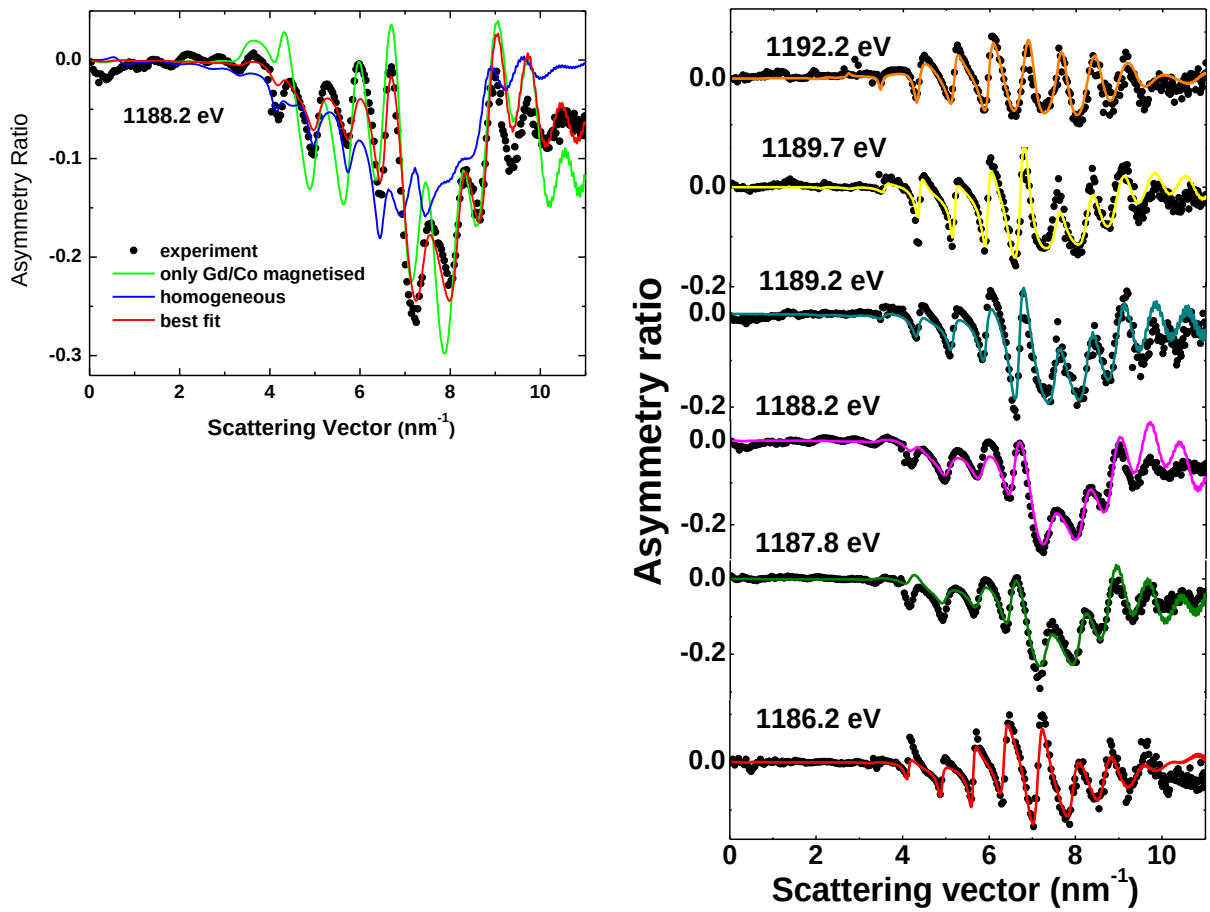

Figure 5.15 Experimental and fitted asymmetry ratio various energies in the vicinity of Gd edge obtained from a 3-slice model

The values describing the out-of-plane magnetization profile throughout the Gd layer are given in Table *15* from the bottom Co/Gd interfaces to the Gd/Al interface where t_3 is the bottom interface at Co/Gd and t_1 is the interface with Gd/Al.

Table 15 Thickness and the mms values for each sub layer derived from refinement of asymmetry ratio at RT. Here, t_1 is the Gd/Co interface and t_3 is the Gd/Al interface

Sublayers thickness	Å	*Magnetization amplitude*	Refined values	Corrected values
t_1	8.1 ± 1.4	mms_1	0.09 ± 0.04	0.06 ± 0.04
t_2	3.1 ± 0.9	mms_2	0.16 ± 0.05	0.12 ± 0.05
t_3	2.9 ± 0.6	mms_3	0.22 ± 0.09	0.16 ± 0.09

From this table, a first comment is that the magnetization is not limited in the immediate interface and extends up the to the Gd/Al interface. We observe a formation of magnetization gradient decreasing from the bottom Co interfaces to the Al top interfaces. Before discussing more about the amplitude of the magnetization, we propose to apply a *corrective factor* to the values of *mms* obtained similar to that used for Co i.e., 0.036/0.050= 0.72. Here, **the value 0.036 being the average of the density parameters derived**

from the refinement of the four off-resonance reflectivity measured in the soft X-ray range and the two reflectivity curves collected in the hard x-ray range. To find out the deduce the average value of the magnetic amplitude of the sublayer, we considered the reference [196] whose XMCD results at 100K. However, as will be discussed in the next section, from our measurements at 100K, we were able to deduce a proportionality factor to calculate results at 300K. From the corrected values of each sub-layer weighted by their respective thicknesses, we calculated average magnetization equal to (0.09 $\pm$ 0.05)

Thus, at RT, we estimated the average magnetization to be (0.56$\pm$ 0.31) μ_B/atom and about (0.99$\pm$ 0.55) μ_B/atom in the first 0.3nm at the Co interface.

Plots of the magnetization profile are provided in the next section along with those determined from the study of the evolution of the magnetization profiles of Gd at lower temperatures.

5.5.4 Temperature dependence of the Co and Gd magnetization profile

In this section, we present effect of temperature change on the magnetisation profile for both Co and Gd. In the case of Co, we understand that its curie temperature is relatively high, thus we do not expect to observe strong variation in magnetisation profile. We conducted measurements for Co at 3 specific temperatures – 43K, 130K and 200K. For Gd we measured in the range of 30K up to 300K considering the fact that its magnetisation is more temperature dependent. In addition, we were interested in detecting an eventual peculiar change in the static profile when crossing the compensation temperature T_m supposed to be around 100K [197].

The measurements at low temperatures were carried out during beam sessions 2 and 3 as follows:

i. The sample cannot be subjected to a perpendicular field and one relies on the strong perpendicular magnetic anisotropy of the system to maintain a perpendicular magnetization (it should be noted that the strength of this anisotropy can be reduced at lower temperatures when the magnetization of Gd becomes increasingly strong [197] the value of the temperature at which this phenomenon appears may depend on the thickness of the layer of Gd). Hysteresis loop measured by VSM SQUID measurements on similar sample is shown in thesis by Dayene [197].
ii. The settings for the reflectivity experiments are carried out at room temperature and a test for the presence of a significant dichroic effect at large angles is carried out.
iii. The sample is cooled to 30K and the measurements are made from low to high temperatures. During beam session 2, we performed measurements at 3 temperatures 43K, 130K and 200K and at each temperature we alternated measurements at the Co edge and at the Gd edge. We did not pay enough attention to the necessary readjustments when changing the grating to work at the Co edge and at the Gd edge. The analyzes at the Gd edge were not satisfactory and during beam session 3 we only collected data at the Gd edge between 33K and 160K for which greater variations were expected.

Therefore, our study focuses on the change of magnetization amplitude and distribution across the Co and Gd layers at low temperatures without applying a saturating perpendicular magnetic field.

1.1.1.1 Analysis of the magnetization profiles in the Co layer

Before fitting asymmetry ratio, the refinement of the average reflectivity curves lead to fits of the same quality as those obtained for the data presented in Figure 5.16 displays two examples of best fits obtained for magnetic asymmetry at 777.35 eV and 779.45 eV at three temperatures 43K, 130K and 200K in order to extract magnetic profiles and examine if we find evolution of magnetic distribution with temperature for Co.

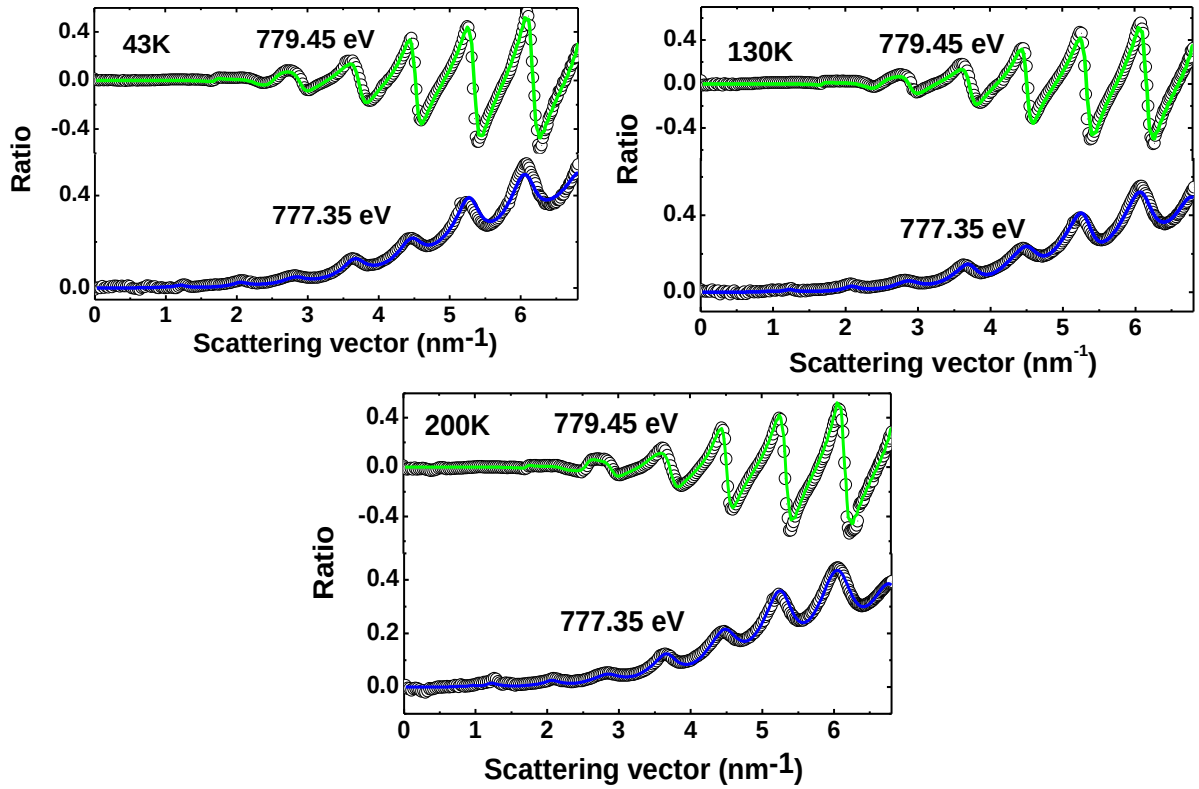

Figure 5.16 shows asymmetry ratio at 779.45 eV and 777.35 eV at (a) 43K, (b) 130K and (c) 200K

From these figures we can observe that the shape of reflectivity is indeed superimposable at all temperatures. The experimental data was refined using the same 3 slice model that was used to refine the ratios at 300K as discussed previously since any model considering a purely homogeneous distribution failed to provide a best fit. Considering a slightly graded distribution, we were able to get a good agreement between experimental and fitted asymmetry ratio at each energy.

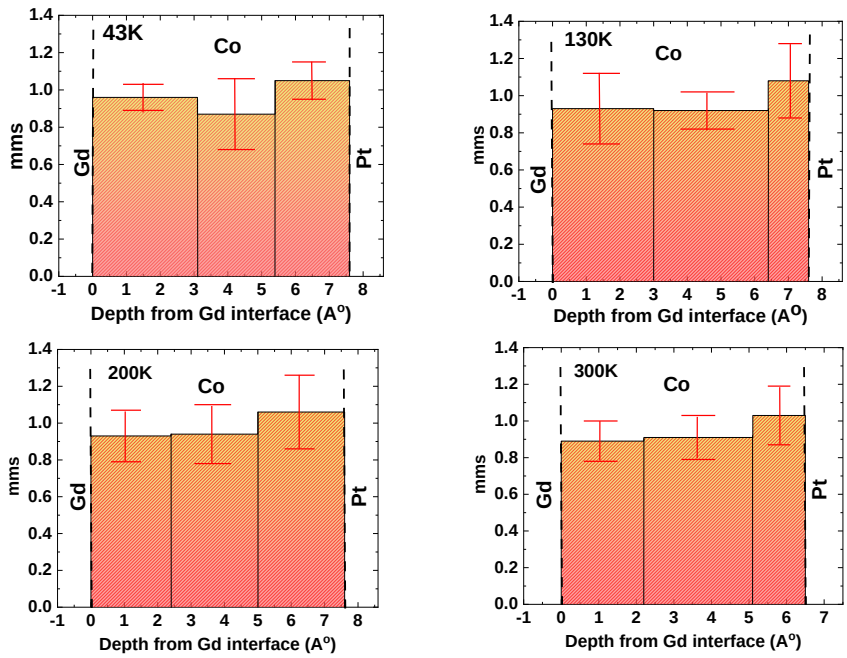

Figure 5.17 displays magnetic profiles for Co at 43K, 130K and 200K along with calculated error bars on each mms along the depth of CoFeB from Gd/Co interface till Co/Pt interface.

In agreement with very similar magnetic asymmetries, the magnetization profile exhibits the same features. We observe that across temperatures, Co is always fully magnetised out-of-plane in fact accompanied by a ~16% increase in amplitudes of magnetisation at Co/Pt interface.

Thus, magnetism at Co doesn't see a difference in profile and stays intact throughout the temperature evolution maintaining the same sign thus we observe a certain homogeneity throughout the temperatures. Since, we performed the measurements at remanence, without any external applied magnetic field

5.5.4.1 Analysis of the magnetization profiles in the Gd layer

The study of the temperature dependence of the magnetization profile of Gd is based on data collected at **10 different temperatures and for 3 different resonance energies**. The large
Figure *5.18* gathers the results for 5 temperatures from top to bottom, 50.3K, 65.4K, 73.3K,98.3K and 131.4K.

The reflectivity intensities show very similar behavior with temperature and slight changes between the 3 energies. The modification concerns only the reflectivity at low angles due to different thickness, density and roughness of the contamination layer. The magnetic asymmetries, on the other hand, reveal significant variations between the 3 energies and a strong decrease in amplitude, without a very marked variation in shape, when the temperature increases.

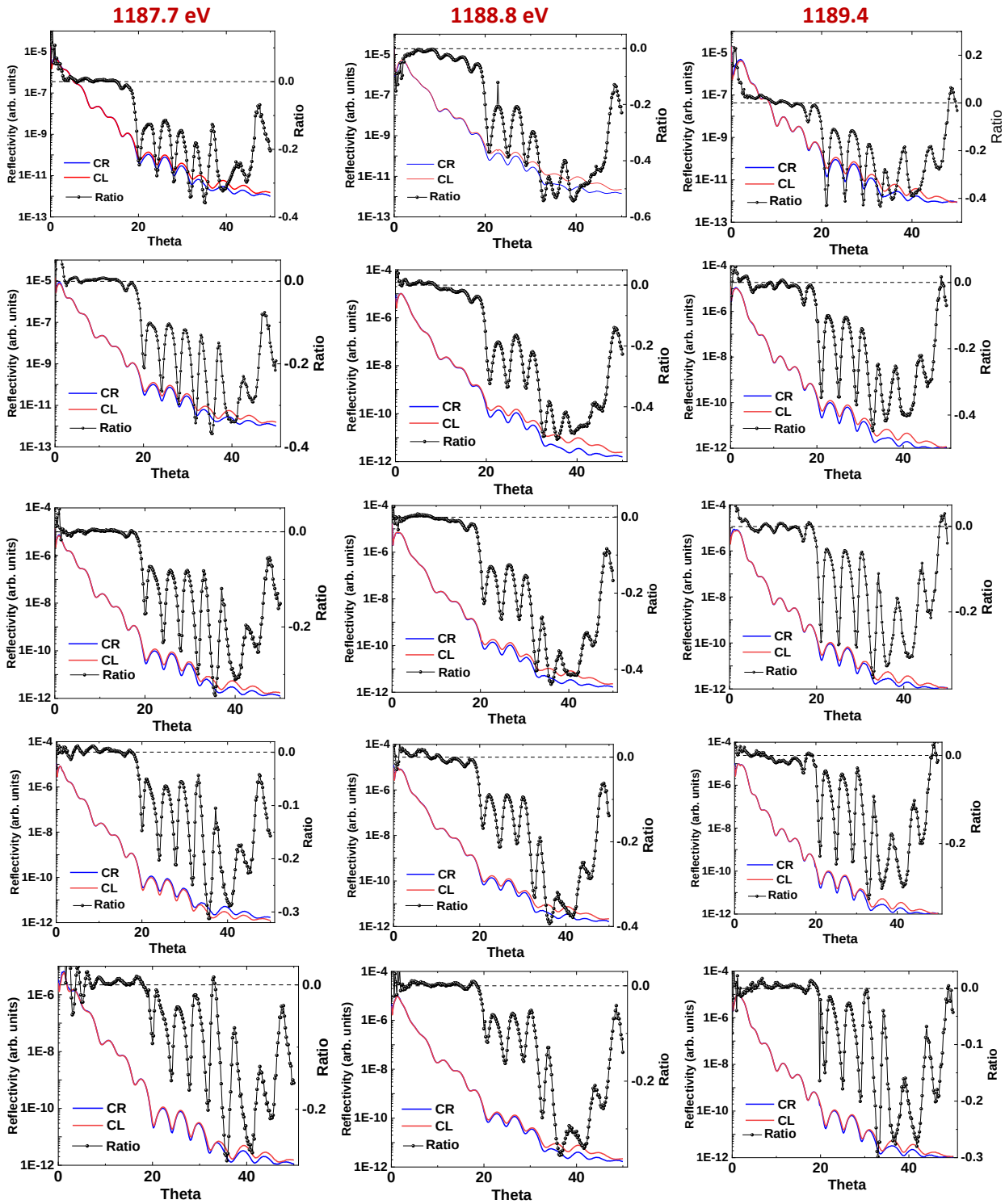

Figure 5.18 Experimental angle-dependent circular right and left reflectivity curves together with magnetic asymmetries at 1187.2 eV (left column), 1188.2 eV (central column), 1188.8 eV (right column) at, from top to bottom, 50.3K, 65.4K, 73.3K,98.3K and 131.4K

Figure *5.19* shows the experimental data at 1187.7 eV along with the best fits at each temperature. We were able to refine the parameters also at 2 other energies (not shown). The parameters that were derived from this refinement have been discussed in table along with the parameters calculated at Co edge. The derived structural parameters were used to build Table *13* (discussed previously in section 5.5.3.2.1).

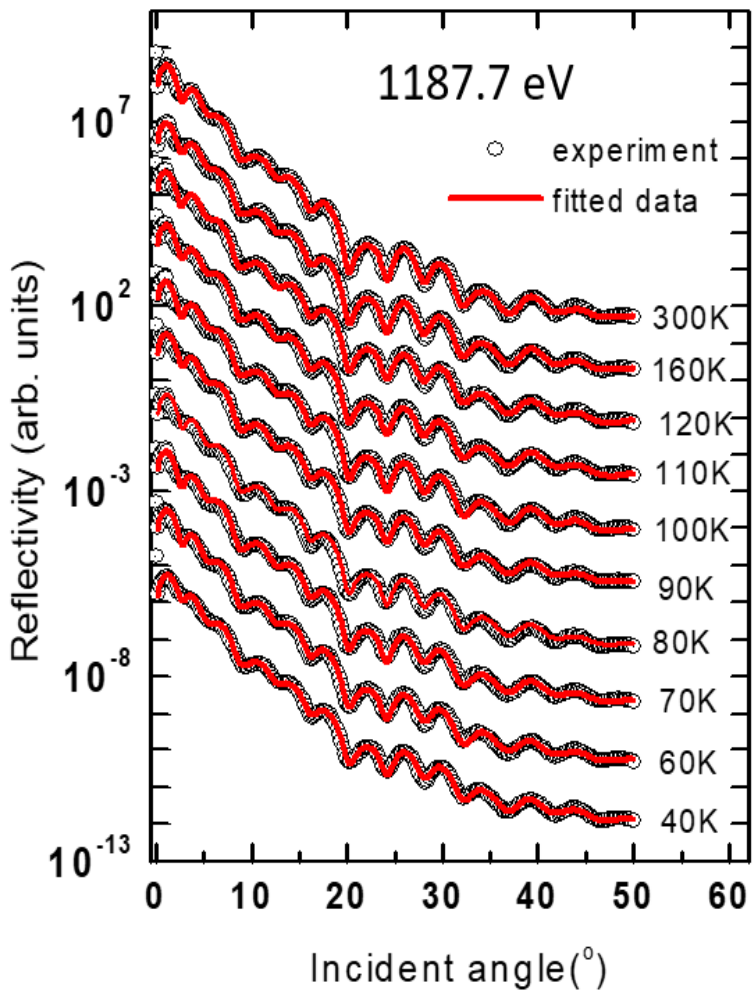

Figure 5.19 Experimental specular reflectivities (black circles) and their best fits (red lines) at 1187.7 eV in the vicinity of the Fe L3 edge for a range of temperatures

Figure *5.20* shows the experimental and fits of magnetic asymmetry at 3 energies for 2 models. The layer was subdivided in 3 slices, as for the profile at room temperature, and the refinement was carried out to determine their thickness and *mms* parameters. The best fits are shown in blue. They appear very satisfactory from 131.4K to 73.3K for magnetic asymmetries at 1188.8 eV. However, for magnetic asymmetries at 1187.2 eV, only the fit at 131.4 K is relatively good and none is satisfactory for magnetic asymmetries at 1188.2 eV. The lower the temperature the more the area between 20 and 30 degrees shows increasing discrepancies between the fit and the experiment. At 1187.2 eV the disagreement is also strong for the lowest temperatures. This indicates at that the simple assumption of a model with fully out-of-plane magnetisation does not hold in Gd. This result appears at first sight surprising because the

magnetization of the Co layer remains completely out of plane down to at least 43K. So, it prompts us to consider the possibility of an *in-plane* component of magnetization across the Gd layer.

It cannot be a longitudinal component because between 0° and 15° the magnetic asymmetries show a flat or very slowly decreasing contribution. We therefore considered the possibility of a planar component which could arise from the tilting of the out-of-plane magnetization along the in-plane transverse direction. Based on the analytical expression for the asymmetry ratio for a transverse magnetization, such a component will provide a contribution that changes sign around 45 degrees, is close to zero at small angles, and has a maximum either side of 45°. Therefore, a tilt in the magnetization somewhere in the Gd layer could produce an additional signal between 20 and 40°. Therefore, we added in the refinement procedure the φ angle for the 3 slices. It appeared very quickly that this contribution did not concern the magnetization of Gd at the Co interface. We therefore tried to refine all the data with the following parameters to be adjusted: thickness and *mms* for the slice at the Co interface, thickness, *mms* and φ for the central slice and the third one close to Al. In order to limit the number of parameters as much as possible, we constrained the two parameters φ to be identical. This model of two zones through the Gd layer, one with an out-of-plane magnetization close to the Co interface and the other with a tilted contribution with a transverse planar component allowed us to fit with very good agreement almost all data. For magnetic asymmetries measured at temperatures approaching room temperature, it was necessary to consider that the tilting direction could be distributed in a more random way by adding the γ parameter in the refinement. We finally use the γ parameter to further refine all the magnetic asymmetries.

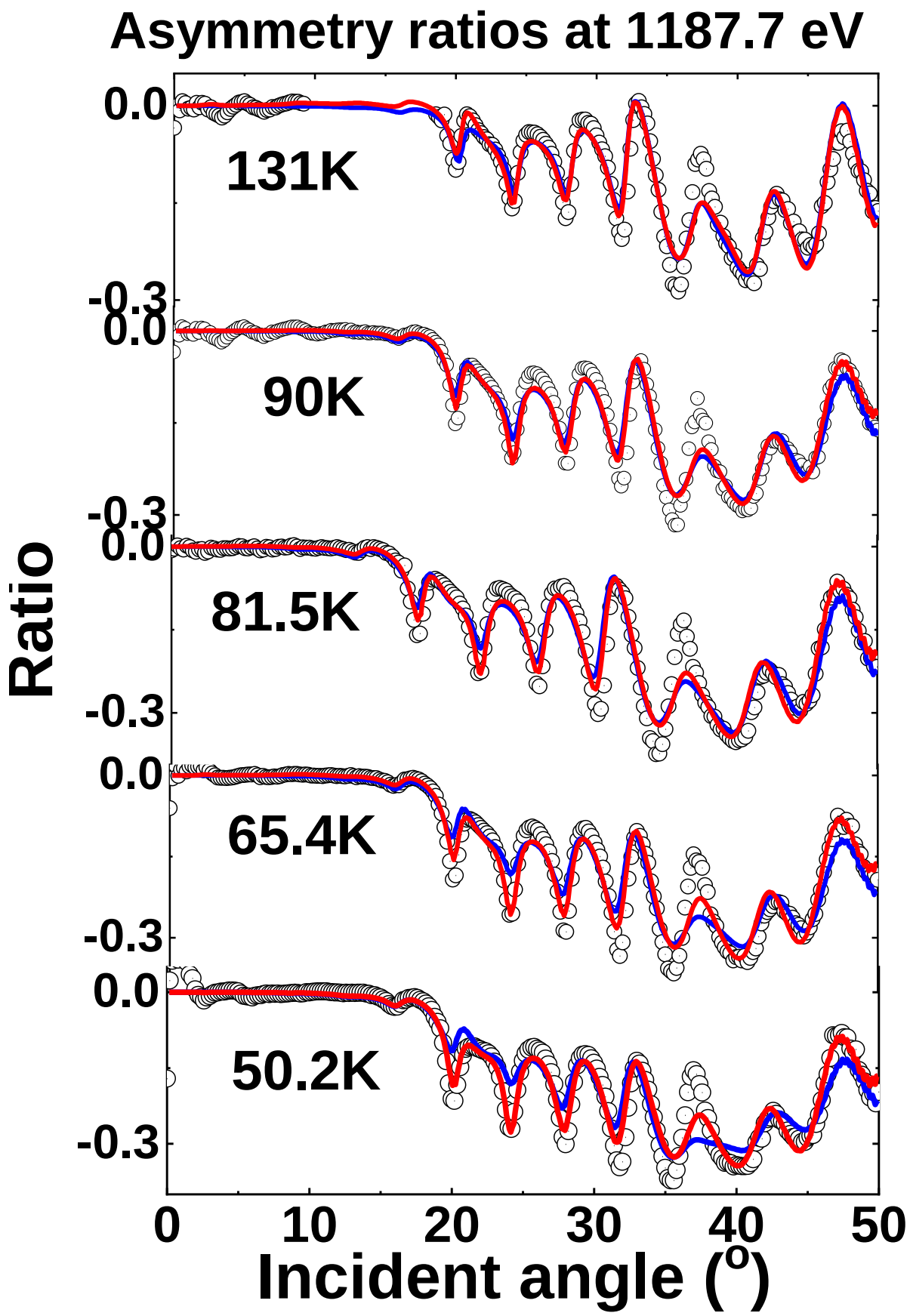
Asymmetry ratios at 1187.7 eV
131K
90K
81.5K
65.4K
50.2K
0.0
-0.3
Ratio
0
10
20
30
40
50
Incident angle (°)

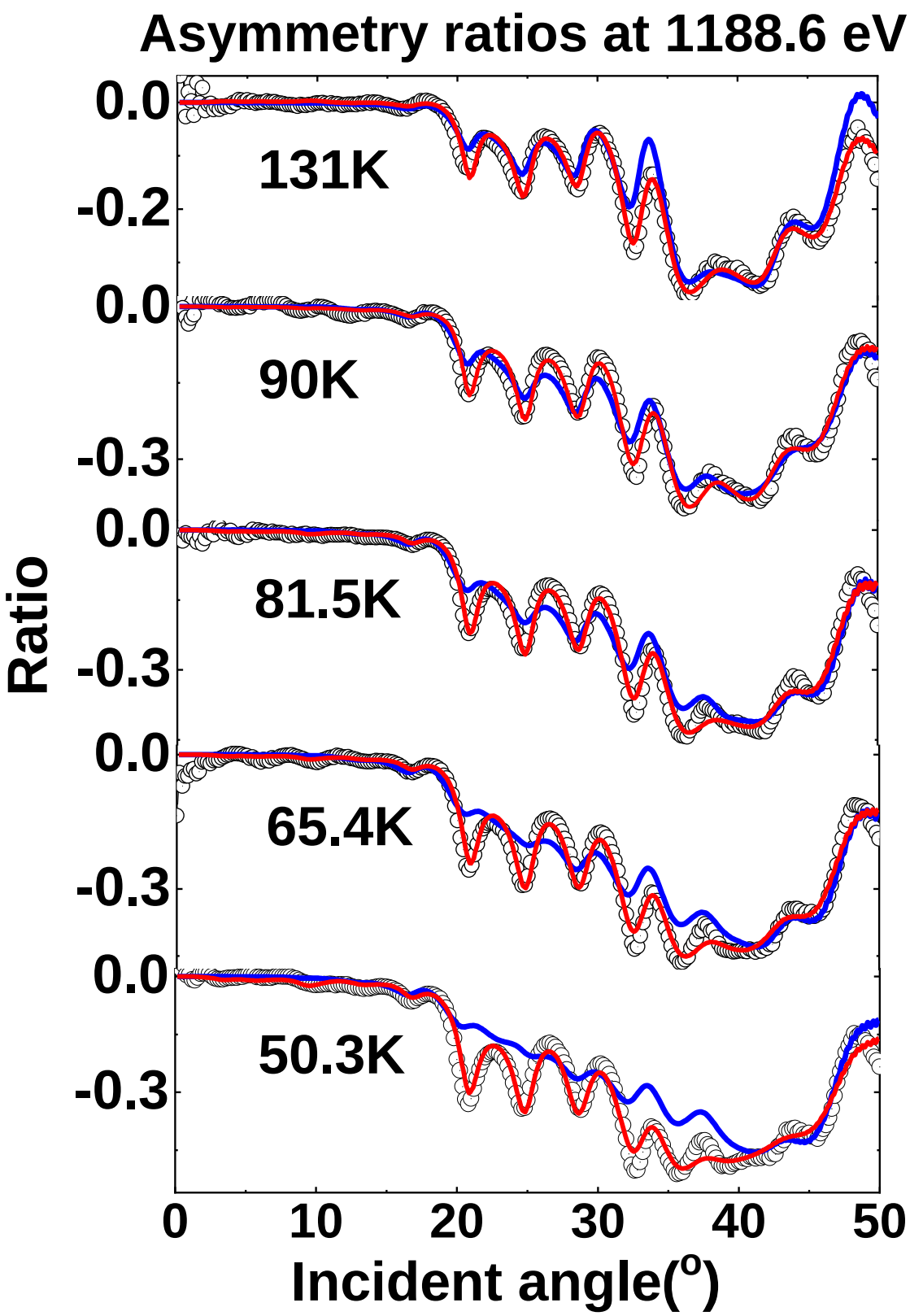
Asymmetry ratios at 1188.6 eV
131K
90K
81.5K
65.4K
50.3K
0.0
-0.2
0.0
-0.3
0.0
-0.3
0.0
-0.3
0.0
-0.3
Ratio
0
10
20
30
40
50
Incident angle(°)

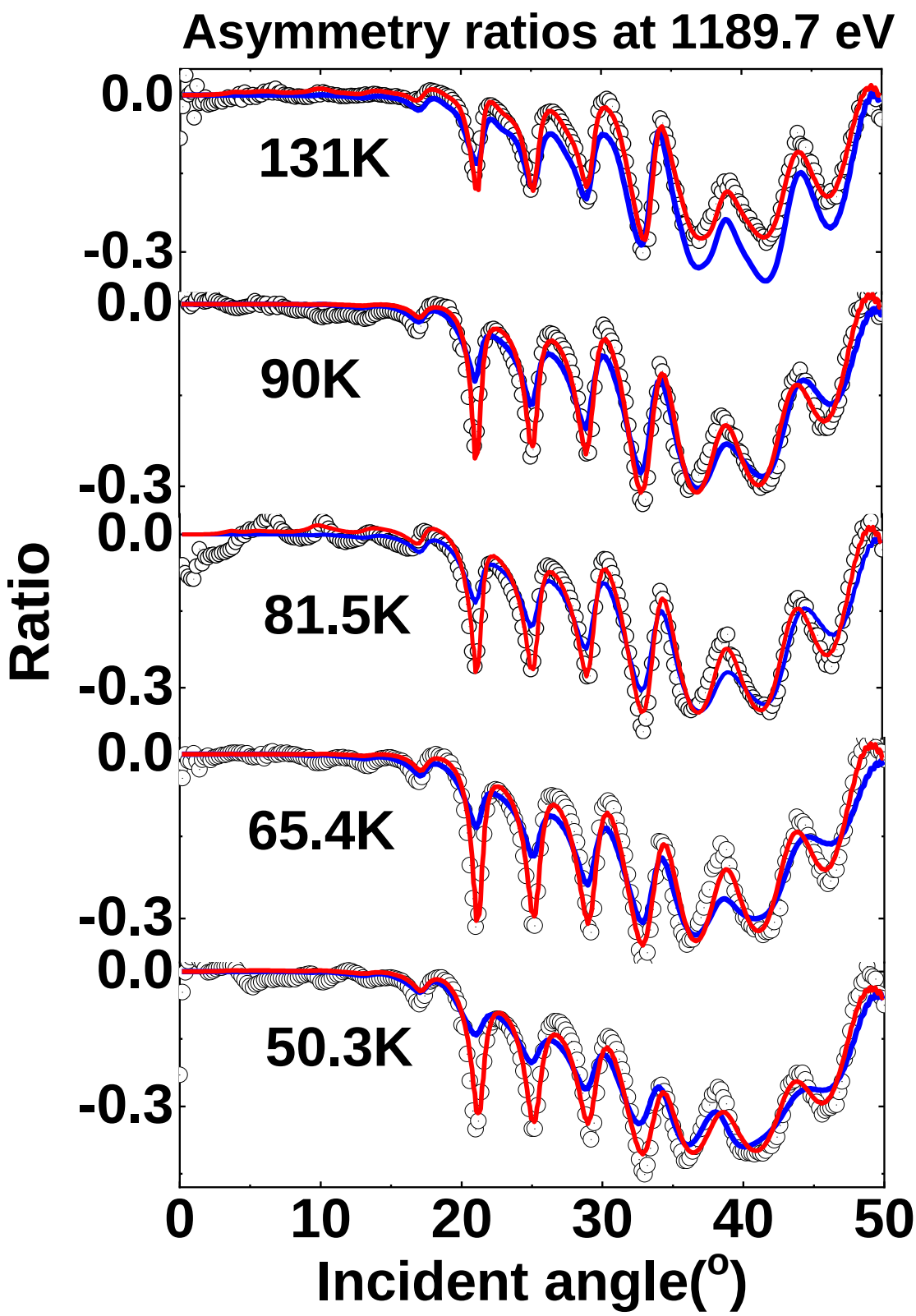

Figure 5.20 Experimental asymmetry ratios (black symbols) along with their fits - blue line for pure *oop* model and red line for a model consisting of *oop* as well as transverse components.

We constructed magnetization profiles in Figure *5.21* of Gd to be able to observe evolution of magnetic distribution through temperatures 32.9 k, 50.3K, 57.5K, 65.4K, 73.3K, 81.5K, 90K, 98K, 131K till 289K temperature including an error bar on the amplitude of weighting factor *mms*.

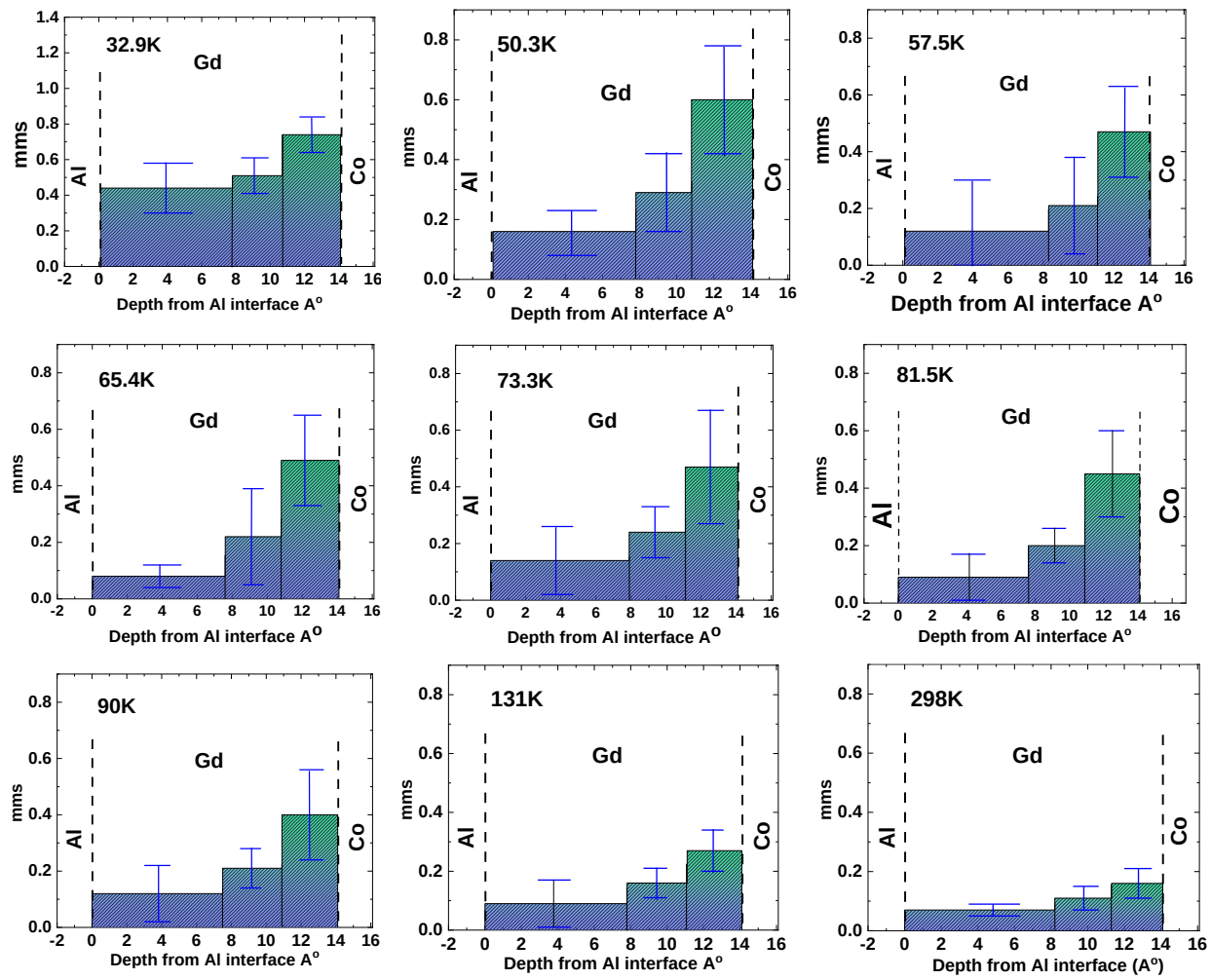

Figure 5.21 displays magnetic profiles for Gd at several temperatures along with calculated error bars on each mms from Gd/AlOx interface till Co/Pt interface.

From this display of profiles, the first key observation we make is the increase of average Gd magnetisation with decreasing temperature where distribution is always in the form of a gradient

The thickness of the two first sublayers at the interface with Co is (3.1 ± 0.8) Å which corresponds to about 1 monolayer (ML) of Gd, the thickness of the third one is (7.9 ± 2.0) Å and corresponds about 2-3 ML. It should also be noted that this representation for the profile does not take into account the large roughness of the Gd/Al interface (9.1 ± 4.8) Å and therefore takes into account neither the Gd atoms distributed in the Al layer nor the Al atoms at the top of the Gd layer. The fact that the net magnetization of Gd atoms does not increase much in the upper layer when the temperature is lowered, except at 32.9K, is probably related to the presence of a thick intermixed layer of GdAl.

The strong increase in magnetization, expected for Gd during the lowering of the temperature, is indeed located at the immediate interface with Co up to 50.3K. Within the first 1-2 MLs, the amount of Al atoms is negligible. The antiferromagnetic coupling of this more or less pure layer of Gd with that of Co is the dominant phenomenon and the net magnetization remains totally out-of-plane and increases from ***mms* = 0.16 (1μ_B) at 298 K** to ***mms* = 0.74 (4.6μ_B) at 32.9 K**. As the absolute value of the magnetization in μ_B is just indicative, it safer to mention a 460% increase from RT to 32.9K.

The evolution of φ is not well defined due to large error bars with an average value of (39$\pm$12) degrees. However, by removing the value at RT, due to lower total magnetization and more uncertain φ determination, since an *oop* model can also reproduce the data, it is possible to detect an increasing trend through a linear fit of the data.

We observe that except for 131.4K and 238 K the γ angle is fairly well oriented along the transverse direction γ = (0 $\pm$ 4) degrees. However, origin of such orientation for the canting of the magnetization in the upper layers of Gd is not well understood. We can just mention the fact that the Gd layer was grown in the form of a wedge. Therefore, the change in thickness along the length of the layer could lead to a rotation of the *oop* magnetisation in plane due to a possible increase in shape anisotropy induced by a somewhat thicker layer thickness. If at the time of the experiment the sample was positioned in such a way that the wedge is perpendicular to the diffraction plane, then the planar component of the magnetization could align along the transverse direction. This effect could be facilitated by the reinforcement of the in-plane magnetic anisotropy of Gd when the magnetic moment of Gd increases at low temperatures [197]. However, the tendency of the tilt angle to decrease at low temperatures reminds that the antiferromagnetic coupling with Co remains the main effect, even above the first 1-2 monolayers. The presence of these two zones at depth as well as the slower increase of the net magnetization in the upper part could have its origin in the reduction of the Gd-Gd exchange coupling interaction linked to the strong alloying effect with Al.

Figure 5.22 shows temperature dependent net magnetization of Co and Gd layers. The average weighting factor (*mms*) of data at all energies was multiplied by the magnetic moment derived from XMCD sum rules applied to our reference samples [Chen, Mangin] to give a value in μ_B and allow a comparison to attempt for example a determination of the compensation temperature in our sample. We have also plotted the temperature dependence of the net fully out of the plane magnetisation of the Gd sublayer at the interface with the Co layer as its magnetisation amplitude increases faster than the rest of the Gd layer. It is probably difficult to mention a compensation temperature from our curves due to the too large error bars on the magnetic amplitude. However, and as already mention in [201] , it is interesting to observe the possibility of two different compensation temperatures: one where the average magnetizations of the two layers compensate each other and the other where only the compensation with the perpendicular magnetization of the Gd layer is considered one of which might play the most important role for the speed of displacement of chiral domain walls in layers with perpendicular magnetization.

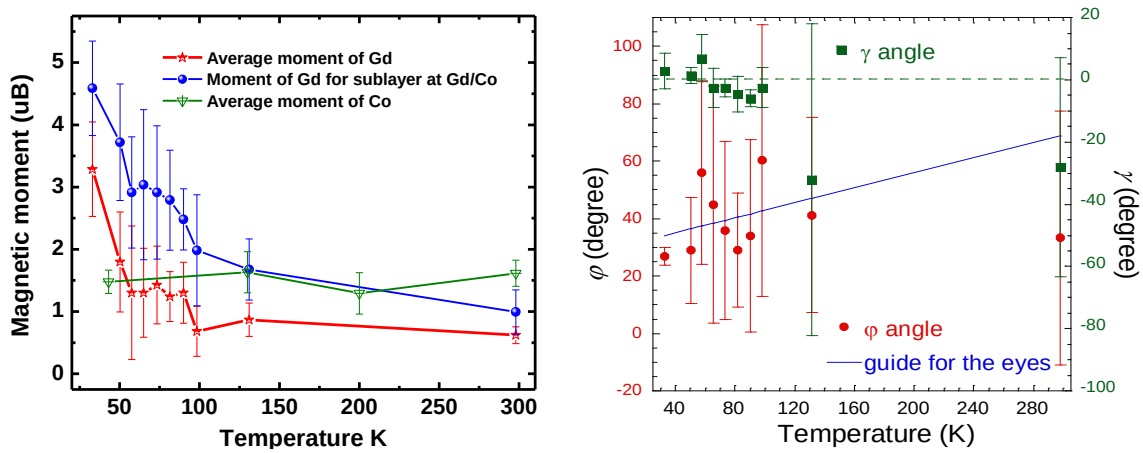

Figure 5.22 Displays magnetic moment vs temperature on the right-hand side for average moment of Gd (red line), average moment of Co (green line) and moment of Gd for sublayer at Gd/Co (blue line) on the left-hand side. On the right-hand side φ and γ are plotted against temperature.

5.6 Discussion and Conclusion

In this chapter, we investigated the system of Pt/Gd/Co stacking through soft X ray resonant reflectivity in order to probe the depth resolved magnetic distribution in the vicinity of both Co L2,3 and Gd M4,5 edge. We presented the data separately at both room and low temperature. Although we did not expect changes in the magnetic distribution for Co between interfaces, a homogeneous model did not fit the data, so we took into account a model with 3 sublayers with the total thickness of 7.6 ± 0.5Å. The magnetization profile at room as well as low temperature showed up to 90% of magnetization for the 2 sublayers at Co/Gd interface increasing up to 16% at Co/Pt interface at all temperatures. Such an increase in Co/Pt has been observed in [202,203] where they showed that the moment of Co in multilayers may increase due to enhancement of orbital moment. Thus, we can say that in case of Co, no significant change was observed through temperature dependence. However, same cannot be said for Gd edge.

Throughout all the measurements regarding structure of the stacking, we were always faced with an issue regarding the possibility of alloying of Gd and Al due to high roughness of Gd for all measurements and specifically higher value of thickness found from the data at the vicinity of Gd edge. The changes in both Gd and Al parameters reflected dispersion of Gd atoms in the Al layer. In fact, it is known that Gd and Al tend to alloy relatively easily due to low formation enthalpy of GdAl [199], [204].

For all measurements at Gd edge, both low and high temperature, we obtained a depth resolve magnetization profile in form of a gradient distribution increasing from Co/Gd interface lowering to Co/Al interface. To fit the asymmetry of this data, we had to take into account oop magnetization along with a tilted contribution with a transverse planar component whose origin in the upper layers is not understood. From our data, we tried to gain some idea about T_m in our system and establish a magnetic distribution but worked at remanence. This can be relevant in regards to the study by R. Blasing et al., [186] showed that by through current induced domain wall motion, varying the temperature in a single structure leads to compensation of the Co and Gd moments, but at T_A.

6 CONCLUSION AND PERSPECTIVE

In this thesis, we investigated of depth resolved along with chemical resolved magnetic profile for ultrathin film systems with *out of plane anisotropy (oop)* by Soft X ray resonant magnetic reflectivity (SXRMR). PMA is a key property utilized broadly in the field of spintronics specifically for magnetic storage and recording devices which can be found in different systems. It is observed variety of systems with distinct applications, such as perpendicular magnetic tunnel junctions of ferromagnet/oxide bi layers as well as rare-earth/3d transition metal ferrimagnetic films which are known for their applications in domain wall dynamics. It is an important magnetic anisotropy phenomenon which is strongly related to interface effects and thus its stability can be enhanced by modifying interface of systems.

It has been seen that the nature of magnetic interactions at interfaces play a fundamental role in determining properties of thin film magnetic device. Thus, studying magnetic inhomogeneities across a layer which can be introduced by interface "morphological" roughness, interfacial intermixing, extension of the intermixing away from the interface and concept of "dead layer" in these systems is essential. Thus, characterization of the magnetic profile is deeply beneficial since it provides us element specific, in-depth knowledge of magnetization distribution.

In chapter 4, we investigated a system MgO/CoFeB/(W)/Ta half tunnel junction with a cap layer of either W or Ta where we were motivated to observe changes in magnetic profile related to subsequent annealing as well as cap layer nature. SQUID and Extraordinary hall effect measurements showed the presence of *oop* signal magnetization for samples after annealing at 350°C as well as 400°C for Ta and W cap layer respectively in accordance to the previous study on the similar samples [143,150]. Infact, for the sample with Ta cap annealed till 400°C, the *oop* anisotropy transitioned back to *ip* anisotropy. This directly showed the higher thermal stability of W to be able to maintain its *oop* magnetization than Ta.

Turning on to the obtained depth resolved magnetic profile

- For samples before annealing,
    - In case of Ta, we observed that we obtained a gradient profile with minimum magnetization at Ta/CoFeB interface and maximum at CoFeB/MgO interface increasing from 40% magnetization to full 100% magnetization at CoFeB/MgO interface.
    - Although, there was a 20% difference in magnetization for Ta and W cap layer, for the latter, the profile as always gradient shaped. We also tested to a model using a magnetic dead layer however we always found that magnetization is distributed throughout the layer. Previously, investigation of PMA in such samples have considered a magnetic dead layer for simplication of analysis however, having an improved knowledge of such distribution can be useful to enhance the efficiency.

- However, after annealing, some interesting changes could be observed.

- The sample with Ta cap layer after annealing at 340°C, showed a more homogeneous distribution of magnetization with only 10% change in the amplitude at the two interfaces. This result has been interpreted as resulting from previously known phenomena of the migration of atoms from B to the layer of Ta. This was also caused due to rearrangement of Fe atoms inside after annealing inside the film although it is hard to clearly comment on since in our studies, we ourselves couldn't make measurements concerning compositional change. To have an idea of such a compositional change which can be simulated in DYNA, however it is complex but always possible to improve the program to consider (create) a change in the composition.
- Annealing at a higher temperature (400°C) for Ta cap layer, showed change in magnetic distribution again where it preferred to have the similar shape as that of sample before annealing, however accompanied by lower amplitudes of magnetization. The energy scans revealed apparition of FeO indicating that conditions for the existence of PMA is destroyed.
- In case of W cap layer after annealing, we observed that the profile maintains the similar shape as that from before annealing however, the amplitudes greatly enhanced along with the magnetization reaching above 100% at CoFeB/MgO interface.

For the system with Gd/Co/Pt in Chapter 5, we were interested

- The distribution of the *oop* magnetization distribution across the Co layer and the distribution of the weak Gd magnetization antiferromagnetic ally coupled to Co.
- To observe how the magnetization distribution can get affected through temperature dependence strongly dependent on Gd, since curie temperature of bulk Gd is known to be at room temperature.

These measurements were performed at remanence since at the moment, the ability to apply magnetic field perpendicular to the sample surface inside RESOXS chamber is not possible. Since compensation temperature as introduced before has been a significant part since it is the temperature where we observe high domain wall speeds, we tried to investigate where the compensation temperature may exist in our system (keeping in mind that we worked at remanence).

The off resonant and hard X ray reflectivity and resonant reflectivity, showed that Gd and Al interface showed a large dispersion of roughness which we mainly accounted due to the tendency of Gd to form an alloy with Al as well as some aging effect related to the fact that this specific roughness parameter increased with time. After defining the structure with all the data, the magnetization profile revealed for Co a fairly homogeneous distribution whereas for Gd a magnetization amplitude of Gd mainly localized at the interface with Co which was oriented antiparallel to the magnetization of Co. An extension of the magnetization towards the interface with Al although weaker in form of a gradient.

For the analysis that was conducted through temperature dependence, we did not observe any significant change for Co, however for Gd we observed a strong dependence expected due to the increase of the magnetic moment of Gd with decrease of temperature.

Infact, when we observed evidence of not only *oop* but also a transverse component, which was necessary to take into account to be able to refine asymmetry ratio, which we observed at all three energies at all temperatures however more evident at low temperatures. This study is in a great relevance with investigation of current induced domain wall motion, since they do not apply field similar to our case in order to obtain a point of compensation temperature. However, in our studies, since we didn't apply an *oop* field and also due to large error bars, a point of compensation temperature is not clearly understood and we can consider a possibility of two compensation temperatures: one where the average magnetizations of the two layers compensate each other and the other where only the compensation with the perpendicular magnetization of the Gd layer is considered one of which might play the most important role for the speed of displacement of chiral domain walls in layers with perpendicular magnetization.

Thus, considering the obtained experimental results, at a more general level, this study of the *in-plane* and *out-of-plane* magnetization profile in ultrathin film (in the range of 1-2nm) showed that a ***graded magnetic amplitude distribution*** is frequently observed. Such features correspond mainly to extrinsic magnetic properties related to structural defects like interfacial intermixing or change of composition in the case of an alloy layer. The technique of soft XRMR which provides sub nanometer resolution enables the description of magnetic distribution which is an important parameter in several emergent interfacial phenomena [41]. Such description could allow going beyond models that consider effective magnetic thickness often associated to the concept of dead layer and constant magnetization profile. This can be very useful to take into account in studies where in general they consider a single slab of magnetic layer, without considering the interplay of interfaces. PMA is also an interfacial property, thus to have an enhanced knowledge of interfacial magnetism is important to aid in improvement of magnetic devices.

It is worth noting that for application under magnetic field, the situation of a constant magnetization profile could be relevant. However, in the framework of field-free magnetization manipulation (by a spin current or *by a laser* it could be important to simulate the behavior of the heterostructures in a device with a more realistic magnetization distribution.

Throughout this thesis, we conducted measurements at remanence, since application of a variable magnetic field in perpendicular direction (normal to the sample surface is still not available). Thus, the next step will be to perform measurements and observe how we can get the magnetic distribution on application of the field.

Different applied field amplitudes could then be selected to keep the system in a specific macroscopic magnetic configuration (parallel vs antiparallel for example) as shown in Figure *6.1* for a particular stacking.

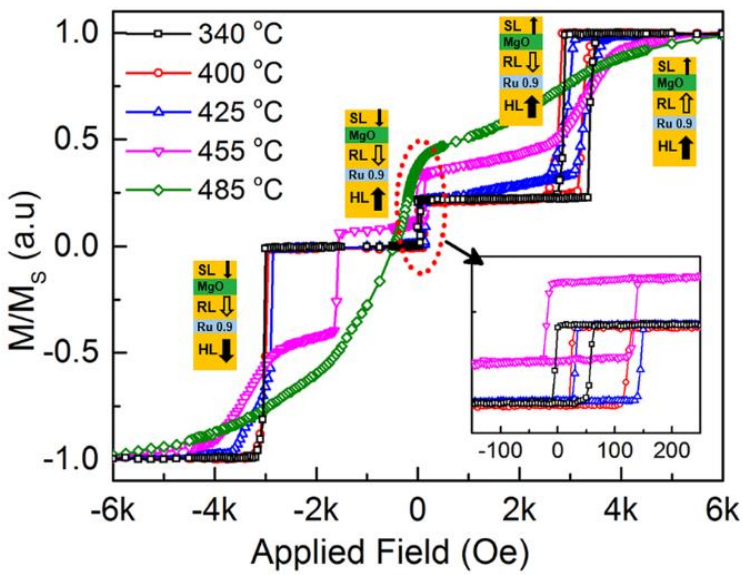

Figure 6.1 Shows hysteresis loops measured for a stacking with layers of stacking having variable PMA at different temperatures.

At the moment, a magnet which can generate a field in *oop* direction is under construction at SOLEIL and should be implemented in the RESOXS chamber next summer. Since, through such a magnet, we will be able to observe a depth resolved *oop* magnetic distribution not only at remanence but with the field. Thus, it will be important to study the systems again with the variable magnetic field. The magnet is shown in the Figure 6.2.

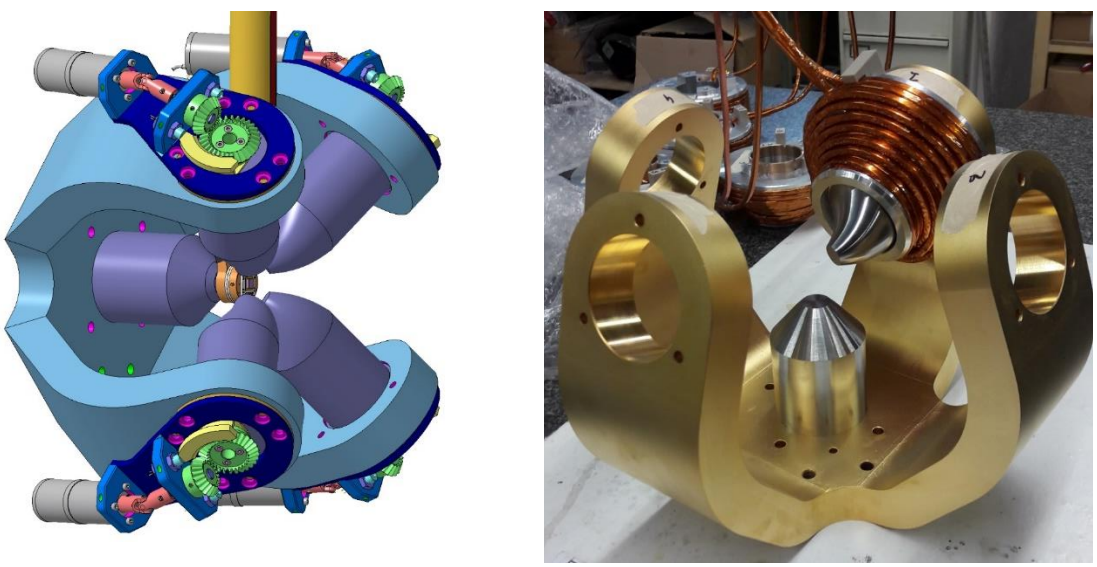

Figure 6.2 the new setup under construction at Soleil

It can also be interesting to study of the magnetization profile in a Gd/Co bilayer with a slightly thicker Gd layer, thus moving the aluminum-mixed under layer away from the interface with the Co and, therefore, offering the possibility of extending the zone corresponding to a thickness of perpendicular Gd, thus moving the compensation temperature to a higher value.

7 ANNEX

7.1 Comparison between RevPol and FlipHlon modes of measurement

We understand from the previously shown measurements, that we have in easy *ip* magnetic axis in S1. However, to investigate the robustness of *ip* orientation of magnetisation we also conducted measurements. We see that even at RevPol mode, there is evidence of 5% asymmetry. Clearly, there is a significant increase in amplitude of asymmetry ratio as soon as we apply a longitudinal magnetic field. Although there is a large enhancement of the *ip* magnetic signal, this a similarity in the features of the asymmetry ratio along angular range indicates that magnetic configuration inside the system remains the same and thus signifying the magnetisation of the system only prefers to stay in plane. This indicates that the sample always retains its *ip* magnetisation.

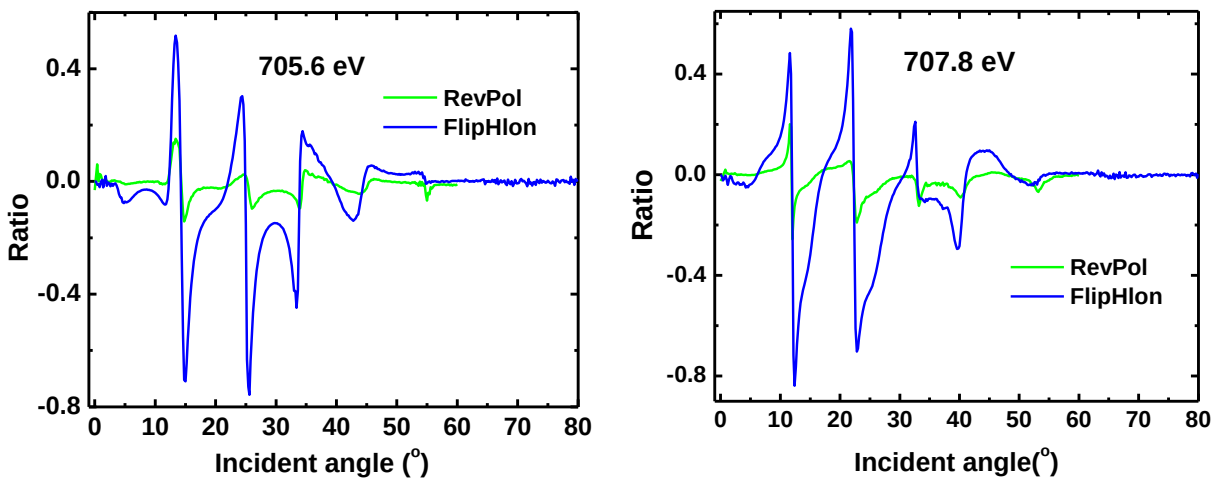

Figure 7.1 Comparison of experimental asymmetry ratio at 705.6 eV and 707.8 eV at for S1

For sample 3, we have presented the data at FlipHlon and we understand qualitatively that we have a clear *in plane* longitudinal signal. However, as discussed in the case of sample 1, we were also interested to observe results at RevPol. The motivation was to see robustness of sample's magnetic state, whether measuring for sample "as it is" or applying *oop* field affects its magnetic configuration. ***Figure 7.2*** compares the results for experimental angle dependent reflectivity as well as corresponding asymmetry ratios collected without applying any field, RevPol and FlipHlon.

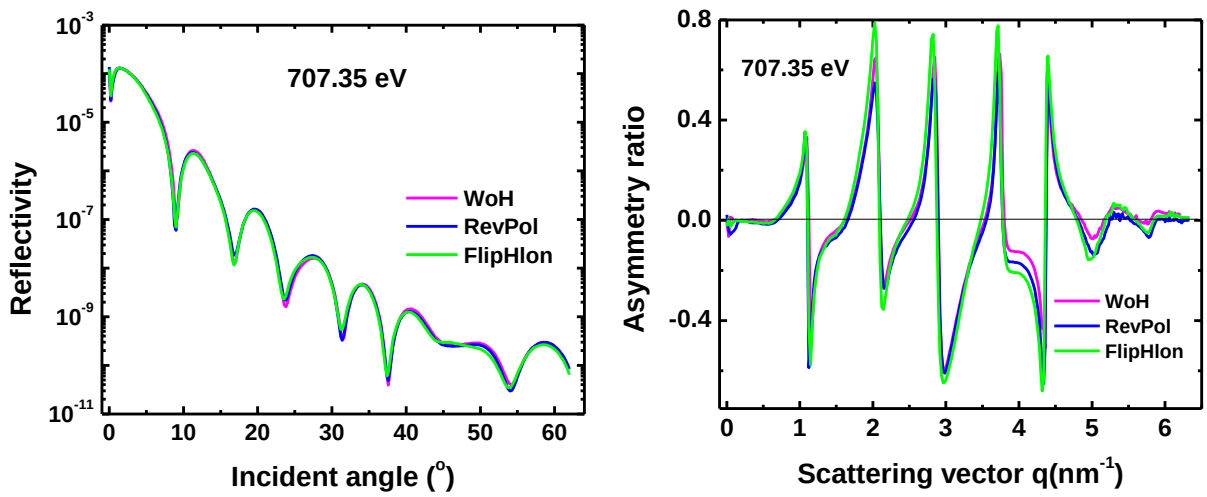

Figure 7.2 Experimental angle dependent reflectivity at 707.35 eV for **FlipHIon** mode in the left panel and the corresponding asymmetry ratio in the right panel

The I_{av} and R signals are fairly well superimposed for all the three modes of measurement indicating that the magnetic anisotropy was *in plane* before applying an external magnetic field and that the RevPol mode has not altered the planar magnetic configuration as mentioned above and in agreement with the SQUID data. This indicates to us that before annealing, the system likes to stay in *ip* configuration.

7.2 Effect of a small *in-plane* applied magnetic field

From the SQUID results as well as results from the as discussed previously, we are aware of the orientation of magnetisation inside the system, however, we ask ourselves, how easily can the system magnetisation change if we apply an *ip* field, parallel or anti-parallel to the diffraction plane. From the comparison at S1 and S3, we observe that they maintain *ip* anisotropy through measurements at different modes, thus in this section, we want to discuss results for S4 of measurement at **FlipHIon**. This can lead to an indication of how the magnetisation in the system aka, the change in orientation of magnetic moment along with the robustness of magnetization. However, it must be noted here that natural state of the magnetisation for the system is always *oop*, which has been observed from measurements at **RevPol** as discussed previously. Thus investigation of the robustness of the observed OOP distribution was conducted at **FlipHIon** under the effect of a 0.17T longitudinal magnetic field as shown in *Figure 7.3* for several energies.

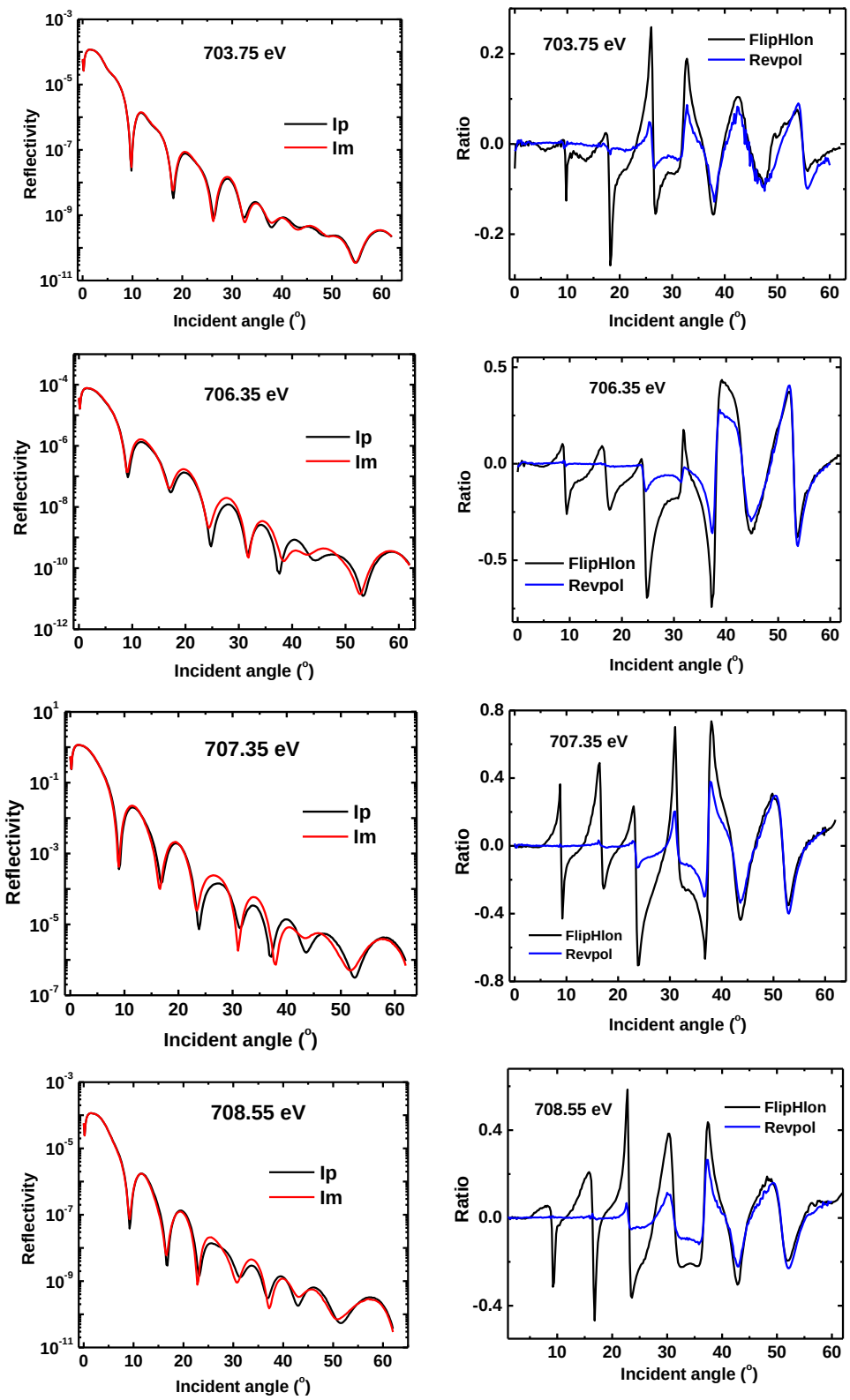

Figure 7.3 Experimental (red and black smooth lines) specular reflectivity at several energies measured at **FlipHlon** for S4. Corresponding asymmetry ratio (blue smooth line) has been plotted on the right column at two modes of acquisition FlipHlon (black curve) and RevPol (blue curve).

Here, we can observe a splitting between *Ip* and *Im* beginning around 8° and extending up to large 60° angles for all energies in the vicinity of Fe L3 edge. This corresponds to an asymmetry ratio exhibiting a signal at both low and large angles. Such a signal indicates presence of *ip* as well as *oop* component of magnetization where both components are reversed under the reversal of longitudinal magnetic field in contrary to the measurements at **RevPol** where we observed *oop* component. This can indicate either coexistence of domains that are purely *oop* and *ip* smaller than the finger print of the beam at the sample surface or a canted magnetisation configuration. Referring to the parallel hysteresis loop in Figure 7.4, this value of magnetic field (±1700 Oe) is insufficient to saturate the magnetization but appears sufficient to achieve a single domain configuration. Therefore, the magnetic asymmetry signal corresponds likely to the inversion of a tilted configuration due to insufficient field to rotate the magnetization fully *in plane*.

In order to discuss the measurements at **FlipHlon** more efficiently, we also recorded some hysteresis loops at different angular values 18°, 26.5°, 38° and 52.5° for Fe at 707.8 eV to analyze the field-dependent magnetic asymmetry as presented in Figure *7.4*.

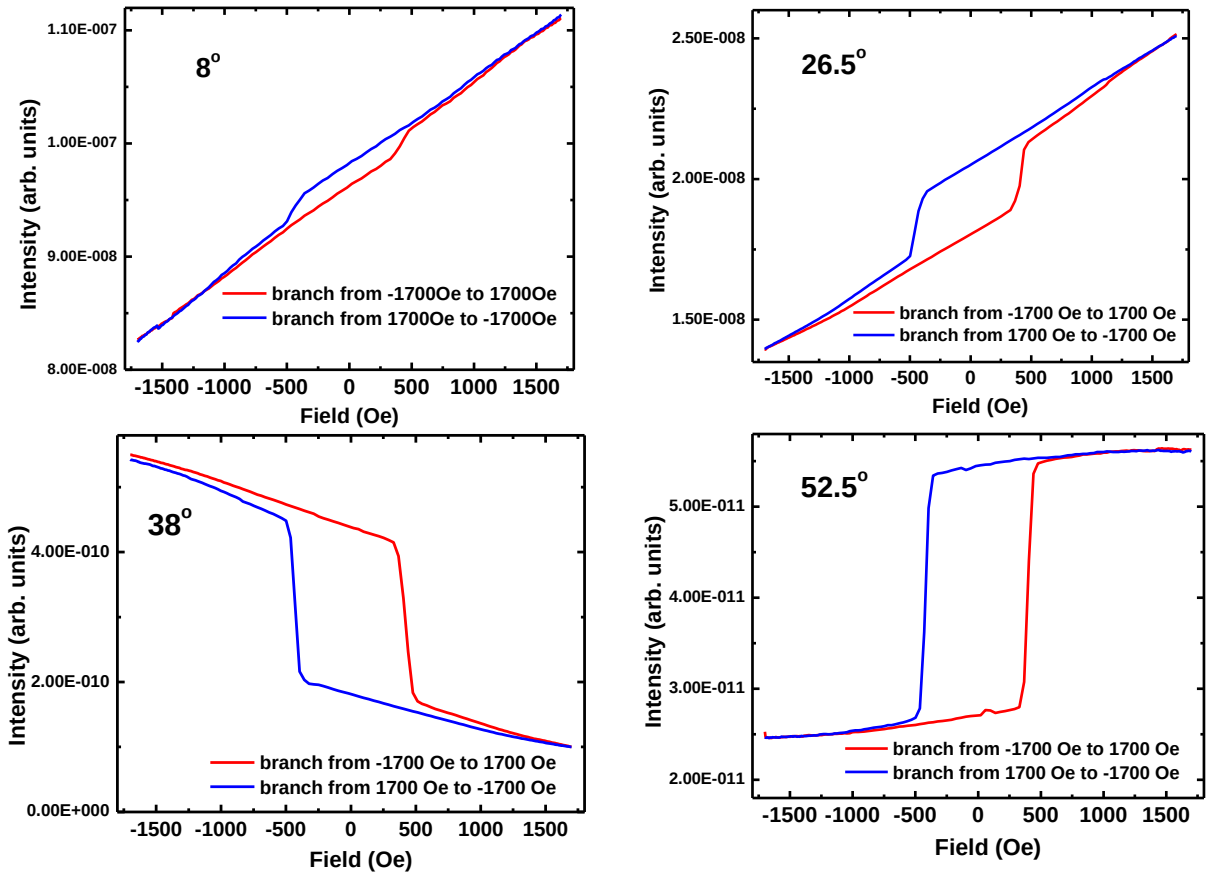

Figure 7.4 Hysteresis loops measured at different angular positions at RESOXS

At different angular positions, the shape of field dependent reflectivity changes in sign as well as amplitude. The magnetic asymmetry is close to zero at low angles, however the finite area of the hysteresis loop indicates the presence of an *ip* component. But as we go to higher angles, the area of hysteresis loop becomes larger and it reaches more towards saturation since, we are more sensitive to *oop* component at higher angles.

As we move to the larger angular value, the shape of the loops indicates that:

- first the magnetization coherently rotates continuously to downward oop magnetization
- around +0.04T, it abruptly reverses (*probably through domain quick evolution*) to point upward
- and then it rotates coherently to reach the angle defined, resulting *from the competition between the PMA energy and the Zeeman energy*, at the +0.17T
- The slope in the rotation regime decreases at large angles because the contribution of the *ip* component to the magnetic asymmetry signal is reduced compared to that due to the *oop* component as illustrated by the comparison of the asymmetry RevPol and FlipHlon.

7.3 Changing applied *ip* magnetic field

We are interested to study such tilted magnetization as it has shown improvement of magnetic devices by allowing lowering of energy costs. In PMA multilayers canted magnetization close to the surface allows understanding of various magnetic properties such as magnetization reversal. (it has to be developed … not clear as it is however keep in mind that here the tilted angle is not present at remanence). Depth resolved description on systems with tilted magnetizations is more challenging, look at Emmanuelle paper

It is known that magnetic configurations that exhibit a canted out of plane magnetisation gain considerable attention in the field of spintronics. Tilted magnetisations has shown to bring new opportunities for improvement of magnetic devices by lowering the energy costs.
Thus, introduce here more what we why is tilted magnetisation in our case is important.

To have a better understanding of the canted Fe magnetization in our thin film sample, we also performed a set of measurements where we changed the applied *ip* magnetic field from maximum 0.17T to 0T and measured *Ip* and *Im* for each value of magnetic field at the mode **RevPol_fliplon** for 707.8 eV

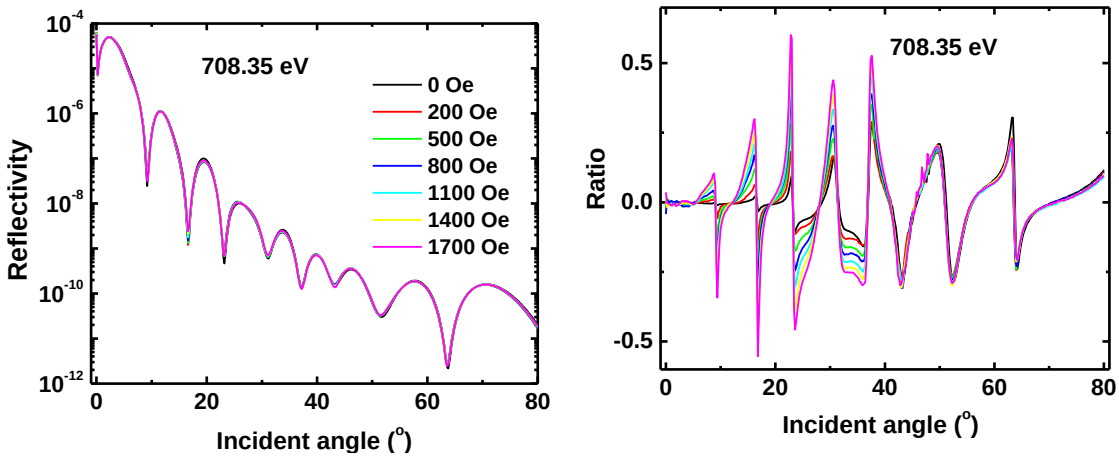

Figure 7.5 canting angle vs Hlon

Figure 7.5 shows all the I_{av} for measurement at each value of field where all the average reflectivities are almost perfectly superimposed indicating no change in structure, as expected. The superposition of R illustrates that while the charge reflectivity is the same whatever the applied field is, the in-plane magnetic contribution is significantly increased and the out-of-plane one is only slowly reduced when is Hlon reduced. These magnetic asymmetries behavior describes the rotation of the magnetization from oop to partially ip through a canting configuration.
However, in the right column of
Figure 7.5, asymmetry ratio at low scattering angles decreases as the applied field is reduced but no increase/decrease of signal is observed for signal after 40° indicating that only *ip* component changes with field whereas *oop* component doesn't.

Figure 7.6 shows the quantitative analysis of experimental data we obtained for S4 under the effect of a 0.17T *ip* magnetic field applied parallel to the diffraction plane. From the qualitative analysis we understand that this value of field is insufficient to saturate the *ip* component but appears sufficient to achieve a single domain configuration. Thus, in order to determine the magnetic profile, we decided to apply the same model as we applied for **RevPol** mode, where we divided the CoFeB layer into 4 slices to get very good fits of the magnetic asymmetry. From qualitative analysis, we observed through shape of asymmetry ratio that we are sensitive to both *in* plane and *out of plane* component, we decided to consider angle $\boldsymbol{\phi}$ for each of the 4 slices in order to take into account the tilting of the magnetization vector where $\boldsymbol{\phi}$ corresponds to the canting angle of magnetisation (rotation of magnetisation in the scattering plane). Thus, refinement was carried out by considering $\boldsymbol{\phi}$ along with *mms* for each slice however keeping the constant value of $\boldsymbol{\phi}$ for all slices with same tilt angle of **34±3** degree. Figure 7.6 shows magnetic asymmetry with their best fits.

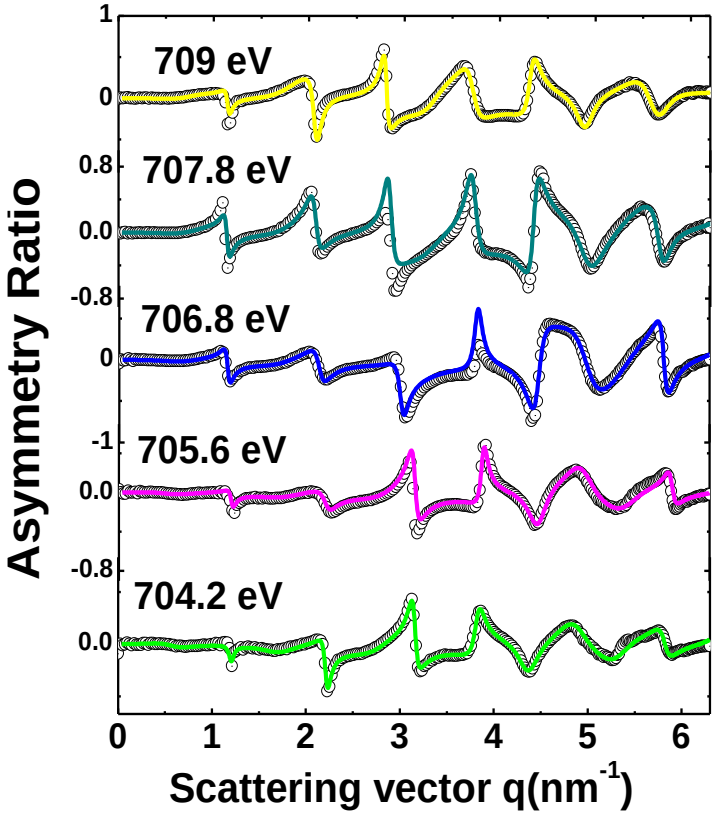

Figure 7.6 shows refined magnetic asymmetry at several energies for S4 at FlipHlon

7.4 Eliminating applied longitudinal field, Hlon = 0

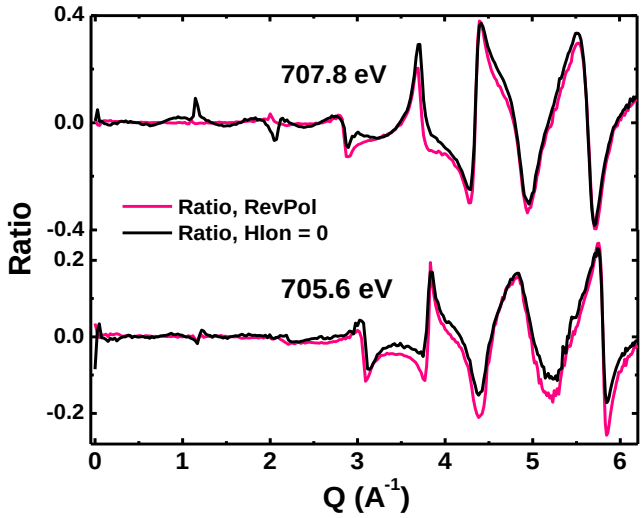

Figure 7.7 Comparison of experimental asymmetry ratios at 707.8 eV (below) measured at **RevPol** (pink smooth line) and field back to 0 (black smooth line) for S4.

These measurements show that the PMA is strong enough to bring the magnetization back in the out-of-plane configuration when Hlon is set to 0. Incidentally, from the mirror effect of the magnetic asymmetry signal, we note that the OOP magnetization is now pointing in the opposite direction (downwards). This may be related to the fact that we come from a negative value for Hlon. This is another indication that by flipping Hlon, we are reversing the OOP orientation.

We can see that the PMA is strong enough to bring the magnetization back in the *oop* configuration when applied longitudinal field is set to 0. In fact, here asymmetry ratio at mode D has actually been reversed in sign as it was originally pointing in the opposite direction to asymmetry at mode B representing a mirror effect.

.

8 BIBLIOGRAPHY

[1] L. Néel, *Anisotropie Magnétique Superficielle et Surstructures d'orientation*, J. Phys. Radium **15**, (1954).

[2] P. F. Carcia, A. D. Meinhaldt, and A. Suna, *Perpendicular Magnetic Anisotropy in Pd/Co Thin Film Layered Structures*, Appl. Phys. Lett. **47**, 178 (1985).

[3] F. J. A. den Broeder, W. Hoving, and P. J. H. Bloemen, *Magnetic Anisotropy of Multilayers*, J. Magn. Magn. Mater. **93**, 562 (1991).

[4] M. N. Baibich, J. M. Broto, A. Fert, F. N. Van Dau, F. Petroff, P. Etienne, G. Creuzet, A. Friederich, and J. Chazelas, *Giant Magnetoresistance of (001)Fe/(001)Cr Magnetic Superlattices*, Phys. Rev. Lett. **61**, 2472 (1988).

[5] G. Binasch, P. Grünberg, F. Saurenbach, and W. Zinn, *Enhanced Magnetoresistance in Layered Magnetic Structures with Antiferromagnetic Interlayer Exchange*, Phys. Rev. B **39**, 4828 (1989).

[6] T. Miyazaki and N. Tezuka, *Giant Magnetic Tunneling Effect in Fe/Al2O3/Fe Junction*, J. Magn. Magn. Mater. **139**, (1995).

[7] J. S. Moodera, L. R. Kinder, T. M. Wong, and R. Meservey, *Large Magnetoresistance at Room Temperature in Ferromagnetic Thin Film Tunnel Junctions*, Phys. Rev. Lett. **74**, 3273 (1995).

[8] S. S. P. Parkin, *Systematic Variation of the Strength and Oscillation Period of Indirect Magnetic Exchange Coupling through the 3d, 4d, and 5d Transition Metals*, Phys. Rev. Lett. **67**, 3598 (1991).

[9] I. Žutić, J. Fabian, and S. Das Sarma, *Spintronics: Fundamentals and Applications*, Rev. Mod. Phys. **76**, 323 (2004).

[10] B. Dieny, V. S. Speriosu, B. A. Gurney, S. S. P. Parkin, D. R. Wilhoit, K. P. Roche, S. Metin, D. T. Peterson, and S. Nadimi, *Spin-Valve Effect in Soft Ferromagnetic Sandwiches*, J. Magn. Magn. Mater. **93**, 101 (1991).

[11] V. Inamura, V. J. Toda, and V. T. Morita, *Ultra High Density Perpendicular Magnetic Recording Technologies*, Fujitsu Sci. Tech. J. **130**, 122 (2006).

[12] B. Dieny and M. Chshiev, *Perpendicular Magnetic Anisotropy at Transition Metal/Oxide Interfaces and Applications*, Rev. Mod. Phys. **89**, (2017).

[13] S. N. Piramanayagam, *Perpendicular Recording Media for Hard Disk Drives*, J. Appl. Phys. **102**, (2007).

[14] M. Julliere, *Tunneling between Ferromagnetic Films*, Phys. Lett. A **54**, 225 (1975).

[15] S. S. P. Parkin, K. P. Roche, M. G. Samant, P. M. Rice, R. B. Beyers, R. E. Scheuerlein, E. J. O'Sullivan, S. L. Brown, J. Bucchigano, D. W. Abraham, Y. Lu, M. Rooks, P. L. Trouilloud, R. A. Wanner, and W. J. Gallagher, *Exchange-Biased Magnetic Tunnel Junctions and Application to Nonvolatile Magnetic Random Access Memory (Invited)*, J. Appl. Phys. **85**, 5828 (1999).

[16] W. J. Gallagher and S. S. P. Parkin, *Development of the Magnetic Tunnel Junction MRAM at IBM: From First Junctions to a 16-Mb MRAM Demonstrator Chip*, IBM J. Res. Dev. **50**, 5 (2006).

[17] S. Ikegawa, F. B. Mancoff, and S. Aggarwal, *Commercialization of MRAM – Historical and Future Perspective*, in *2021 IEEE International Interconnect Technology Conference (IITC)* (2021), pp. 1–3.

[18] R. Bez, E. Camerlenghi, A. Modelli, and A. Visconti, *Introduction to Flash Memory*, **91**, (2003).

[19] A. Morisako and X. Liu, *Sm–Co and Nd–Fe–B Thin Films with Perpendicular Anisotropy for High-Density Magnetic Recording Media*, J. Magn. Magn. Mater. **304**, 46 (2006).

[20] B. Carvello, C. Ducruet, B. Rodmacq, S. Auffret, E. Gautier, G. Gaudin, and B. Dieny, *Sizable Room-Temperature Magnetoresistance in Cobalt Based Magnetic Tunnel Junctions with out-of-Plane Anisotropy*, Appl. Phys. Lett. **92**, 102508 (2008).

[21] I. Yoo, D. Kim, and Y. K. Kim, *Switching Characteristics of Submicrometer Magnetic Tunnel Junction Devices with Perpendicular Anisotropy*, J. Appl. Phys. **97**, 10C919 (2005).

[22] B. D. Cullity and C. D. Graham, *Introduction to Magnetic Materials* (2009).

[23] E. Rashba, *Spin -Orbit Coupling in Condensed Matter Physics*, Sov. Physics-Solid State **2**, 1109 (1960).

[24] I. Dzyaloshinsky, *A Thermodynamic Theory of "Weak" Ferromagnetism of Antiferromagnetics*, J. Phys. Chem. Solids **4**, 241 (1958).

[25] T. Moriya, *Anisotropic Superexchange Interaction and Weak Ferromagnetism*, Phys. Rev. **120**, 91 (1960).

[26] A. Soumyanarayanan, N. Reyren, A. Fert, and C. Panagopoulos, *Emergent Phenomena Induced by Spin–Orbit Coupling at Surfaces and Interfaces*, Nature **539**, 509 (2016).

[27] C. Kittel and D. F. Holcomb, *Introduction to Solid State Physics*, Am. J. Phys. **35**, 547 (1967).

[28] N. Spaldin, *Magnetic Materials: Fundamentals and Applications* (2010).

[29] A. J. P. Meyer and G. Asch, *Experimental G' and g Values of Fe, Co, Ni, and Their Alloys*, J. Appl. Phys. **32**, S330 (1961).

[30] P. Ferromagnétique and P. M. Pierre, *Langevin (2)*, 661 (1907).

[31] A. Hubert and R. Schäfer, *Magnetic Domains: The Analysis of Magnetic Microstructures* (Springer Science & Business Media, 2008).

[32] J. Stöhr, *Exploring the Microscopic Origin of Magnetic Anisotropies with X-Ray Magnetic Circular Dichroism (XMCD) Spectroscopy*, J. Magn. Magn. Mater. **200**, 470 (1999).

[33] B. Tudu and A. Tiwari, *Recent Developments in Perpendicular Magnetic Anisotropy Thin Films for Data Storage Applications*, Vacuum **146**, 329 (2017).

[34] M. T. Johnson, R. Jungblut, P. J. Kelly, and F. J. A. den Broeder, *Perpendicular Magnetic Anisotropy of Multilayers: Recent Insights*, J. Magn. Magn. Mater. **148**, 118 (1995).

[35] T. Pham, J. Vogel, J. Sampaio, M. Vanatka, J.-C. Rojas-Sanchez, M. Bonfim, D. D. S. Chaves, F. Choueikani, P. Ohresser, E. Otero, A. Thiaville, and S. Pizzini, *Very Large Domain Wall Velocities in Pt / Co / GdOx and Pt / Co / Gd Trilayers with Dzyaloshinskii-Moriya Interaction*, Europhys. Lett. **67001**, (2016).

[36] S. Monso, B. Rodmacq, S. Auffret, G. Casali, F. Fettar, B. Gilles, B. Dieny, and P. Boyer, *Crossover from In-Plane to Perpendicular Anisotropy in Pt/CoFe/AlO x Sandwiches as a Function of Al Oxidation: A Very Accurate Control of the Oxidation of Tunnel Barriers*, Appl. Phys. Lett. **80**, 4157 (2002).

[37] A. Manchon and S. Zhang, *Theory of Nonequilibrium Intrinsic Spin Torque in a Single Nanomagnet*, Phys. Rev. B **78**, 212405 (2008).

[38] B. Rodmacq, A. Manchon, C. Ducruet, S. Auffret, and B. Dieny, *Influence of Thermal Annealing on the Perpendicular Magnetic Anisotropy of Pt/Co/AlOx Trilayers*, Phys. Rev. B **79**, 24423 (2009).

[39] H. X. Yang, M. Chshiev, B. Dieny, J. H. Lee, A. Manchon, and K. H. Shin, *First-Principles Investigation of the Very Large Perpendicular Magnetic Anisotropy at Fe|MgO and Co|MgO Interfaces*, Phys. Rev. B - Condens. Matter Mater. Phys. **84**, 1 (2011).

[40] C.-H. Lambert, A. Rajanikanth, T. Hauet, S. Mangin, E. E. Fullerton, and S. Andrieu, *Quantifying Perpendicular Magnetic Anisotropy at the Fe-MgO(001) Interface*, Appl. Phys. Lett. **102**, 122410 (2013).

[41] F. Hellman, A. Hoffmann, Y. Tserkovnyak, G. S. D. Beach, E. E. Fullerton, C. Leighton, A. H. Macdonald, D. C. Ralph, D. A. Arena, H. A. Dürr, P. Fischer, J. Grollier, J. P. Heremans, T. Jungwirth, A. V. Kimel, B. Koopmans, I. N. Krivorotov, S. J. May, A. K. Petford-Long, J. M. Rondinelli, N. Samarth, I. K. Schuller, A. N. Slavin, M. D. Stiles, O. Tchernyshyov, A. Thiaville, and B. L. Zink, *Interface-Induced Phenomena in Magnetism*, Rev. Mod. Phys. **89**, 1 (2017).

[42] S. S. P. Parkin, *Origin of Enhanced Magnetoresistance of Magnetic Multilayers: Spin-Dependent Scattering from Magnetic Interface States*, Phys. Rev. Lett. **71**, 1641 (1993).

[43] J. Barnaś and G. Palasantzas, *Interface Roughness Effects in the Giant Magnetoresistance in Magnetic Multilayers*, J. Appl. Phys. **82**, 3950 (1997).

[44] P. Beliën, R. Schad, C. D. Potter, G. Verbanck, V. V Moshchalkov, and Y. Bruynseraede, *Relation between Interface Roughness and Giant Magnetoresistance in MBE-Grown Polycrystalline Fe/Cr Superlattices*, Phys. Rev. B **50**, 9957 (1994).

[45] P. Grünberg, D. E. Bürgler, R. Gareev, D. Olligs, M. Buchmeier, M. Breidbach, B. Kuanr, and R. Schreiber, *Experiments on the Relation between GMR and Interface Roughness and on the Interlayer Exchange Coupling across Semiconductors*, J. Phys. D. Appl. Phys. **35**, (2002).

[46] Y. Kamiguchi, Y. Hayakawa, and H. Fujimori, *Anomalous Field Dependence of Magnetoresistance in Fe/Gd Multilayered Ferrimagnets*, Appl. Phys. Lett. **55**, 1918 (1989).

[47] H. Fujimori, Y. Kamiguchi, and Y. Hayakawa, *New Phenomena of Magnetoresistance in Ferrimagnetic Fe/Gd Multilayers*, J. Appl. Phys. **67**, 5716 (1990).

[48] J. L. Prieto, B. B. van Aken, G. Burnell, C. Bell, J. E. Evetts, N. Mathur, and M. G. Blamire, *Transport Properties of Sharp Antiferromagnetic Boundaries in Gd/Fe Multilayers*, Phys. Rev. B **69**, 54436 (2004).

[49] J. Nogués and I. K. Schuller, *Exchange Bias*, J. Magn. Magn. Mater. **192**, 203 (1999).

[50] M. Grimsditch, A. Hoffmann, P. Vavassori, H. Shi, and D. Lederman, *Exchange-Induced Anisotropies at Ferromagnetic-Antiferromagnetic Interfaces above and below the Néel*

Temperature, Phys. Rev. Lett. **90**, 257201 (2003).

[51] S. Yuasa, T. Nagahama, A. Fukushima, Y. Suzuki, and K. Ando, *Giant Room-Temperature Magnetoresistance in Single-Crystal Fe/MgO/Fe Magnetic Tunnel Junctions*, Nat. Mater. **3**, 868 (2004).

[52] S. Zhang, P. M. Levy, A. C. Marley, and S. S. P. Parkin, *Quenching of Magnetoresistance by Hot Electrons in Magnetic Tunnel Junctions*, Phys. Rev. Lett. **79**, 3744 (1997).

[53] N. Tezuka and T. Miyazaki, *Temperature and Applied Voltage Dependence of Magnetoresistance Ratio in Fe/Al Oxide/Fe Junctions*, Jpn. J. Appl. Phys. **37**, L218 (1998).

[54] S. Yuasa, A. Fukushima, H. Kubota, Y. Suzuki, and K. Ando, *Giant Tunneling Magnetoresistance up to 410% at Room Temperature in Fully Epitaxial Co/MgO/Co Magnetic Tunnel Junctions with Bcc Co(001) Electrodes*, Appl. Phys. Lett. **89**, 42505 (2006).

[55] S. Tsunegi, Y. Sakuraba, K. Amemiya, M. Sakamaki, E. Ozawa, A. Sakuma, K. Takanashi, and Y. Ando, *Observation of Magnetic Moments at the Interface Region in Magnetic Tunnel Junctions Using Depth-Resolved x-Ray Magnetic Circular Dichroism*, Phys. Rev. B - Condens. Matter Mater. Phys. **85**, 1 (2012).

[56] D. L. Mills, *Surface Effects in Magnetic Crystals near the Ordering Temperature*, Phys. Rev. B **3**, 3887 (1971).

[57] K. Binder and P. C. Hohenberg, *Surface Effects on Magnetic Phase Transitions*, Phys. Rev. B **9**, 2194 (1974).

[58] K. Binder and D. P. Landau, *Critical Phenomena at Surfaces*, Phys. A Stat. Mech. Its Appl. **163**, 17 (1990).

[59] M. Farle, K. Baberschke, U. Stetter, A. Aspelmeier, and F. Gerhardter, *Thickness-Dependent Curie Temperature of Gd(0001)/W(110) and Its Dependence on the Growth Conditions*, Phys. Rev. B **47**, 11571 (1993).

[60] F. Huang, M. T. Kief, G. J. Mankey, and R. F. Willis, *Magnetism in the Few-Monolayers Limit: A Surface Magneto-Optic Kerr-Effect Study of the Magnetic Behavior of Ultrathin Films of Co, Ni, and Co-Ni Alloys on Cu(100) and Cu(111)*, Phys. Rev. B **49**, 3962 (1994).

[61] E. N. Abarra, K. Takano, F. Hellman, and A. E. Berkowitz, *Thermodynamic Measurements of Magnetic Ordering in Antiferromagnetic Superlattices*, Phys. Rev. Lett. **77**, 3451 (1996).

[62] M. Marynowski, W. Franzen, M. El-Batanouny, and V. Staemmler, *Observation of an Extraordinary Antiferromagnetic Transition on the NiO(100) Surface by Metastable Helium Atom Diffraction*, Phys. Rev. B **60**, 6053 (1999).

[63] F. Essenberger, S. Sharma, J. K. Dewhurst, C. Bersier, F. Cricchio, L. Nordström, and E. K. U. Gross, *Magnon Spectrum of Transition-Metal Oxides: Calculations Including Long-Range Magnetic Interactions Using the LSDA+U Method*, Phys. Rev. B **84**, 174425 (2011).

[64] M. Charilaou and F. Hellman, *Anomalous Magnetic Thermodynamics in Uncompensated Collinear Antiferromagnets*, Europhys. Lett. **107**, 27002 (2014).

[65] M. Charilaou and F. Hellman, *Roughness Effects in Uncompensated Antiferromagnets*, J. Appl. Phys. **117**, 83907 (2015).

[66] M. Charilaou and F. Hellman, *Surface-Induced Phenomena in Uncompensated Collinear Antiferromagnets*, J. Phys. Condens. Matter **27**, 86001 (2015).

[67] P. J. Grundy, *Thin Film Magnetic Recording Media*, J. Phys. D. Appl. Phys. **31**, (1998).

[68] A. Hoffmann and S. D. Bader, *Opportunities at the Frontiers of Spintronics*, Phys. Rev. Appl. **4**, 47001 (2015).

[69] A. Guinier, *X-Ray Diffraction: In Crystals, Imperfect Crystals, and Amorphous Bodies* (Dover Publications, 2013).

[70] G. van der Laan, B. T. Thole, G. A. Sawatzky, J. B. Goedkoop, J. C. Fuggle, J.-M. Esteva, R. Karnatak, J. P. Remeika, and H. A. Dabkowska, *Experimental Proof of Magnetic X-Ray Dichroism*, Phys. Rev. B **34**, 6529 (1986).

[71] G. Schütz, W. Wagner, W. Wilhelm, P. Kienle, R. Zeller, R. Frahm, and G. Materlik, *Absorption of Circularly Polarized x Rays in Iron*, Phys. Rev. Lett. **58**, 737 (1987).

[72] J. B. Goedkoop, B. T. Thole, G. van der Laan, G. A. Sawatzky, F. M. F. de Groot, and J. C. Fuggle, *Calculations of Magnetic X-Ray Dichroism in the 3d Absorption Spectra of Rare-Earth Compounds*, Phys. Rev. B **37**, 2086 (1988).

[73] C. T. Chen, F. Sette, Y. Ma, and S. Modesti, *Soft-x-Ray Magnetic Circular Dichroism at the L2,3 Edges of Nickel*, Phys. Rev. B **42**, 7262 (1990).

[74] J. B. Goedkoop, J. C. Fuggle, B. T. Thole, G. van der Laan, and G. A. Sawatzky, *Magnetic X-ray Dichroism of Rare-earth Materials*, J. Appl. Phys. **64**, 5595 (1988).

[75] J. Geissler, E. Goering, M. Justen, F. Weigand, G. Schütz, J. Langer, D. Schmitz, H. Maletta, and R. Mattheis, *Pt Magnetization Profile in a Pt/Co Bilayer Studied by Resonant Magnetic x-Ray Reflectometry*, Phys. Rev. B **65**, 20405 (2001).

[76] J. M. Tonnerre, L. Sève, D. Raoux, G. Soullié, B. Rodmacq, and P. Wolfers, *Soft X-Ray Resonant Magnetic Scattering from a Magnetically Coupled Ag/Ni Multilayer*, Phys. Rev. Lett. **75**, 740 (1995).

[77] D. R. Lee, S. K. Sinha, D. Haskel, Y. Choi, J. C. Lang, S. A. Stepanov, and G. Srajer, *X-Ray Resonant Magnetic Scattering from Structurally and Magnetically Rough Interfaces in Multilayered Systems. I. Specular Reflectivity*, Phys. Rev. B **68**, 224409 (2003).

[78] C. Kao, J. B. Hastings, E. D. Johnson, D. P. Siddons, G. C. Smith, and G. A. Prinz, *Magnetic-Resonance Exchange Scattering at the Iron L2 and L3 Edges*, Phys. Rev. Lett. **65**, 373 (1990).

[79] C.-C. Kao, C. T. Chen, E. D. Johnson, J. B. Hastings, H. J. Lin, G. H. Ho, G. Meigs, J.-M. Brot, S. L. Hulbert, Y. U. Idzerda, and C. Vettier, *Dichroic Interference Effects in Circularly Polarized Soft-x-Ray Resonant Magnetic Scattering*, Phys. Rev. B **50**, 9599 (1994).

[80] F. W. Lytle, D. E. Sayers, and E. A. Stern, *Extended X-Ray-Absorption Fine-Structure Technique. II. Experimental Practice and Selected Results*, Phys. Rev. B **11**, 4825 (1975).

[81] G. S. Henderson, F. M. F. de Groot, and B. J. A. Moulton, *X-Ray Absorption Near-Edge Structure (XANES) Spectroscopy*, Rev. Mineral. Geochemistry **78**, 75 (2014).

[82] A. Guinier, *X-Ray Diffraction in Crystals, Imperfect Crystals, and Amorphous Bodies* (Courier

Corporation, 1994).

[83] J. Zak, E. R. Moog, C. Liu, and S. D. Bader, *Universal Approach to Magneto-Optics*, J. Magn. Magn. Mater. **89**, 107 (1990).

[84] Z. Q. Qiu and S. D. Bader, *Surface Magneto-Optic Kerr Effect*, Rev. Sci. Instrum. **71**, 1243 (2000).

[85] B. T. Thole, G. van der Laan, and G. A. Sawatzky, *Strong Magnetic Dichroism Predicted in the M4,5 X-Ray Absorption Spectra of Magnetic Rare-Earth Materials*, Phys. Rev. Lett. **55**, 2086 (1985).

[86] S. Macke and E. Goering, *Magnetic Reflectometry of Heterostructures*, **26**, 15 (2014).

[87] B. T. Thole, P. Carra, F. Sette, and G. van der Laan, *X-Ray Circular Dichroism as a Probe of Orbital Magnetization*, Phys. Rev. Lett. **68**, 1943 (1992).

[88] P. Carra, B. T. Thole, M. Altarelli, and X. Wang, *X-Ray Circular Dichroism and Local Magnetic Fields*, Phys. Rev. Lett. **70**, 694 (1993).

[89] M. Blume, *Magnetic Scattering of x Rays (Invited)*, J. Appl. Phys. **57**, 3615 (1985).

[90] D. Fleisch, *A Student's Guide to Maxwell's Equations* (Cambridge University Press, 2008).

[91] M. Blume, *Magnetic Scattering of x Rays (Invited)*, J. Appl. Phys. **57**, 3615 (1985).

[92] G. Materlik, *Resonant Anomalous X-Ray Scattering*, Theory Appl. (1994).

[93] J. P. Hannon, G. T. Trammell, M. Blume, and D. Gibbs, *X-Ray Resonance Exchange Scattering*, Phys. Rev. Lett. **50**, 477 (1989).

[94] J. P. Hannon, G. T. Trammell, M. Blume, and D. Gibbs, *X-Ray Resonance Exchange Scattering*, Phys. Rev. Lett. **61**, 1245 (1988).

[95] S. Brück, *Magnetic Resonant Reflectometry on Exchange Bias Systems*, (2009).

[96] F. de Bergevin, M. Brunel, R. M. Galera, and C. Vettier, *X-Ray Resonant Scattering in the Ferromagnet CoPt*, Phys. Rev. B **46**, 772 (1992).

[97] J. P. Hill and D. F. Mcmorrow, *X-Ray Resonant Exchange Scattering: Polarization Dependence and Correlation Functions*, Acta Crystallogr. Sect. A Found. Crystallogr. **52**, 236 (1996).

[98] L. Sève, N. Jaouen, J. M. Tonnerre, D. Raoux, F. Bartolomé, M. Arend, W. Felsch, A. Rogalev, J. Goulon, C. Gautier, and J. F. Bérar, *Profile of the Induced 5d Magnetic Moments in Ce/Fe and La/Fe Multilayers Probed by X-Ray Magnetic-Resonant Scattering*, Phys. Rev. B **60**, 9662 (1999).

[99] A. Verna, B. A. Davidson, Y. Szeto, A. Y. Petrov, A. Mirone, A. Giglia, N. Mahne, and S. Nannarone, *Measuring Magnetic Profiles at Manganite Surfaces with Monolayer Resolution*, J. Magn. Magn. Mater. **322**, 1212 (2010).

[100] J. Als-Nielson and D. F. Mcmorrow, *Elements of Modern Physics* (2011).

[101] J. K. LL.D., *On Rotation of the Plane of Polarization by Reflection from the Pole of a Magnet*, London, Edinburgh, Dublin Philos. Mag. J. Sci. **3**, 321 (1877).

[102] M. Mansuripur, *Analysis of Multilayer Thin-film Structures Containing Magneto-optic and Anisotropic Media at Oblique Incidence Using 2×2 Matrices*, J. Appl. Phys. **67**, 6466 (1990).

[103] J. Zak, E. R. Moog, C. Liu, and S. D. Bader, *Magneto-Optics of Multilayers with Arbitrary Magnetization Directions*, Phys. Rev. Appl. **43**, 1991 (1991).

[104] M. Elzo, E. Jal, O. Bunau, S. Grenier, Y. Joly, A. Y. Ramos, H. C. N. Tolentino, J. M. Tonnerre, and N. Jaouen, *X-Ray Resonant Magnetic Reflectivity of Stratified Magnetic Structures: Eigenwave Formalism and Application to a W/Fe/W Trilayer*, J. Magn. Magn. Mater. **324**, 105 (2012).

[105] M. Elzo, Diffraction Résonnante Des Rayons X Dans Des Systèmes Multiferroiques, 2013.

[106] E. Jal, *Reflectivite Resonante de Rayons X Mous : Une Sonde de La Distribution d'aimantation Complexe Au Sein de Films Minces*, (2013).

[107] K. Amemiya, S. Kitagawa, D. Matsumura, H. Abe, T. Ohta, and T. Yokoyama, *Direct Observation of Magnetic Depth Profiles of Thin Fe Films on Cu(100) and Ni/Cu(100) with the Depth-Resolved x-Ray Magnetic Circular Dichroism*, Appl. Phys. Lett. **84**, 936 (2004).

[108] H. Zabel, *X-Ray and Neutron Reflectivity Analysis of Thin Films and Superlattices*, Appl. Phys. A **58**, 159 (1994).

[109] G. Sharma, A. Gupta, M. Gupta, K. Schlage, and H.-C. Wille, *In Situ Small-Angle x-Ray and Nuclear Resonant Scattering Study of the Evolution of Structural and Magnetic Properties of an Fe Thin Film on MgO (001)*, Phys. Rev. B **92**, 224403 (2015).

[110] S. Balerna, A., & Mobilio, *Synchrotron Radiations: Basics, Methods and Applications*, Springer (2015).

[111] H. A. Durr, T. Eimuller, H.-J. Elmers, S. Eisebitt, M. Farle, W. Kuch, F. Matthes, M. Martins, H.-C. Mertins, P. M. Oppeneer, and others, *A Closer Look into Magnetism: Opportunities with Synchrotron Radiation*, IEEE Trans. Magn. **45**, 15 (2009).

[112] M. Sacchi, N. Jaouen, H. Popescu, R. Gaudemer, J. M. Tonnerre, S. G. Chiuzbaian, C. F. Hague, A. Delmotte, J. M. Dubuisson, G. Cauchon, B. Lagarde, and F. Polack, *The SEXTANTS Beamline at SOLEIL: A New Facility for Elastic, Inelastic and Coherent Scattering of Soft X-Rays*, J. Phys. Conf. Ser. **425**, 6 (2013).

[113] W. Jark and J. Stöhr, *A High-Vacuum Triple-Axis-Diffractometer for Soft x-Ray Scattering Experiments*, Nucl. Instruments Methods Phys. Res. Sect. A Accel. Spectrometers, Detect. Assoc. Equip. **266**, 654 (1988).

[114] N. Jaouen, J. Tonnerre, G. Kapoujian, P. Taunier, and J. Roux, *An Apparatus for Temperature-Dependent Soft X-Ray Resonant Magnetic Scattering Research Papers*, J. Synchrotron Rad. 353 (2004).

[115] B. L. Henke, E. M. Gullikson, and J. C. Davis, *X-Ray Interactions: Photoabsorption, Scattering, Transmission, and Reflection at E = 50-30,000 EV, Z = 1-92*, At. Data Nucl. Data Tables **54**, 181 (1993).

[116] C. T. Chantler, K. Olsen, R. A. Dragoset, J. Chang, A. R. Kishore, S. A. Kotochigova, D. S. Zucker, and X. F. Factor, *Attenuation and Scattering Tables*, Detail. Tabul. At. Form Factors, Photoelectr. Absorpt. Scatt. Cross Sect. Mass Attenuation Coefficients 1 (2005).

[117] V. Lucarini, J. J. Saarinen, K.-E. Peiponen, and E. M. Vartiainen, *Kramers-Kronig Relations in Optical Materials Research*, Vol. 110 (Springer Science & Business Media, 2005).

[118] M. Yasaka and others, *X-Ray Thin-Film Measurement Techniques*, Rigaku J. **26**, 1 (2010).

[119] J. Tonnerre, E. Jal, E. Bontempi, N. Jaouen, M. Elzo, and S. Grenier, *Depth-Resolved Magnetization Distribution in Ultra Thin Films by Soft X-Ray Resonant Magnetic Reflectivity*, **187**, 177 (2012).

[120] C. T. Chen, Y. U. Idzerda, H.-J. Lin, N. V Smith, G. Meigs, E. Chaban, G. H. Ho, E. Pellegrin, and F. Sette, *Experimental Confirmation of the X-Ray Magnetic Circular Dichroism Sum Rules for Iron and Cobalt*, Phys. Rev. Lett. **75**, 152 (1995).

[121] H. L. Meyerheim, J. Tonnerre, L. Sandratskii, H. C. N. Tolentino, M. Przybylski, Y. Gabi, F. Yildiz, X. L. Fu, E. Bontempi, S. Grenier, and J. Kirschner, *New Model for Magnetism in Ultrathin Fcc Fe on Cu (001)*, **267202**, 4 (2009).

[122] N. Nagaosa, J. Sinova, S. Onoda, A. H. MacDonald, and N. P. Ong, *Anomalous Hall Effect*, Rev. Mod. Phys. **82**, 1539 (2010).

[123] S. S. P. Parkin, C. Kaiser, A. Panchula, P. M. Rice, B. Hughes, M. Samant, and S.-H. Yang, *Giant Tunnelling Magnetoresistance at Room Temperature with MgO (100) Tunnel Barriers*, Nat. Mater. **3**, 862 (2004).

[124] S. Ikeda, K. Miura, H. Yamamoto, K. Mizunuma, H. D. Gan, M. Endo, S. Kanai, J. Hayakawa, F. Matsukura, and H. Ohno, *A Perpendicular-Anisotropy CoFeB-MgO Magnetic Tunnel Junction*, Nat. Mater. **9**, 721 (2010).

[125] B. Rodmacq, S. Auffret, B. Dieny, S. Monso, and P. Boyer, *Crossovers from In-Plane to Perpendicular Anisotropy in Magnetic Tunnel Junctions as a Function of the Barrier Degree of Oxidation*, J. Appl. Phys. **93**, 7513 (2003).

[126] A. Manchon, C. Ducruet, L. Lombard, S. Auffret, B. Rodmacq, B. Dieny, S. Pizzini, J. Vogel, V. Uhlíř, M. Hochstrasser, and G. Panaccione, *Analysis of Oxygen Induced Anisotropy Crossover in Pt/Co/MOx Trilayers*, J. Appl. Phys. **104**, 43914 (2008).

[127] L. E. Nistor, B. Rodmacq, S. Auffret, and B. Dieny, *Pt/Co/Oxide and Oxide/Co/Pt Electrodes for Perpendicular Magnetic Tunnel Junctions*, Appl. Phys. Lett. **94**, 12512 (2009).

[128] J.-M. Hu, Z. Li, L.-Q. Chen, and C.-W. Nan, *High-Density Magnetoresistive Random Access Memory Operating at Ultralow Voltage at Room Temperature*, Nat. Commun. **2**, 553 (2011).

[129] K. L. Wang, J. G. Alzate, and P. K. Amiri, *Low-Power Non-Volatile Spintronic Memory: STT-RAM and Beyond*, J. Phys. D. Appl. Phys. **46**, 74003 (2013).

[130] A. D. Kent and D. C. Worledge, *A New Spin on Magnetic Memories*, Nat. Nanotechnol. **10**, 187 (2015).

[131] L. E. Nistor, B. Rodmacq, C. Ducruet, C. Portemont, I. L. Prejbeanu, and B. Dieny, *Correlation Between Perpendicular Anisotropy and Magnetoresistance in Magnetic Tunnel Junctions*, IEEE Trans. Magn. **46**, 1412 (2010).

[132] S. Ikeda, J. Hayakawa, Y. M. Lee, F. Matsukura, Y. Ohno, T. Hanyu, and H. Ohno, *Magnetic Tunnel Junctions for Spintronic Memories and Beyond*, IEEE Trans. Electron Devices **54**, 991 (2007).

[133] A. Barman, S. Wang, O. Hellwig, A. Berger, E. E. Fullerton, and H. Schmidt, *Ultrafast Magnetization Dynamics in High Perpendicular Anisotropy [Co/ Pt] n Multilayers*, J. Appl. Phys. **101**, 09D102 (2007).

[134] J. C. Slonczewski, *Current-Driven Excitation of Magnetic Multilayers*, J. Magn. Magn. Mater. **159**, L1 (1996).

[135] L. Berger, *Emission of Spin Waves by a Magnetic Multilayer Traversed by a Current*, Phys. Rev. B **54**, 9353 (1996).

[136] K. Mizunuma, S. Ikeda, J. H. Park, H. Yamamoto, H. Gan, K. Miura, H. Hasegawa, J. Hayakawa, F. Matsukura, and H. Ohno, *MgO Barrier-Perpendicular Magnetic Tunnel Junctions with CoFe/Pd Multilayers and Ferromagnetic Insertion Layers*, Appl. Phys. Lett. **95**, 232516 (2009).

[137] D. C. Worledge, G. Hu, D. W. Abraham, J. Z. Sun, P. L. Trouilloud, J. Nowak, S. Brown, M. C. Gaidis, E. J. O'Sullivan, and R. P. Robertazzi, *Spin Torque Switching of Perpendicular Ta/CoFeB/MgO-Based Magnetic Tunnel Junctions*, Appl. Phys. Lett. **98**, 22501 (2011).

[138] M. Yamanouchi, R. Koizumi, S. Ikeda, H. Sato, K. Mizunuma, K. Miura, H. D. Gan, F. Matsukura, and H. Ohno, *Dependence of Magnetic Anisotropy on MgO Thickness and Buffer Layer in Co20Fe60B20-MgO Structure*, J. Appl. Phys. **109**, 1 (2011).

[139] T. Liu, J. W. Cai, and L. Sun, *Large Enhanced Perpendicular Magnetic Anisotropy in CoFeB/MgO System with the Typical Ta Buffer Replaced by an Hf Layer*, AIP Adv. **2**, (2012).

[140] T. Liu, Y. Zhang, J. W. Cai, and H. Y. Pan, *Thermally Robust Mo/CoFeB/MgO Trilayers with Strong Perpendicular Magnetic Anisotropy*, Sci. Rep. **4**, 1 (2014).

[141] C. F. Pai, M. H. Nguyen, C. Belvin, L. H. Vilela-Leão, D. C. Ralph, and R. A. Buhrman, *Enhancement of Perpendicular Magnetic Anisotropy and Transmission of Spin-Hall-Effect-Induced Spin Currents by a Hf Spacer Layer in W/Hf/CoFeB/MgO Layer Structures*, Appl. Phys. Lett. **104**, (2014).

[142] N. Miyakawa, D. C. Worledge, and K. Kita, *Impact of TA Diffusion on the Perpendicular Magnetic Anisotropy of Ta/CoFeB/MgO*, IEEE Magn. Lett. **4**, 2 (2013).

[143] J. Chatterjee, R. C. Sousa, N. Perrissin, S. Auffret, C. Ducruet, and B. Dieny, *Enhanced Annealing Stability and Perpendicular Magnetic Anisotropy in Perpendicular Magnetic Tunnel Junctions Using W Layer*, Appl. Phys. Lett. **110**, (2017).

[144] S. Mukherjee, R. Knut, S. M. Mohseni, T. N. Anh Nguyen, S. Chung, Q. Tuan Le, J. Åkerman, J. Persson, A. Sahoo, A. Hazarika, B. Pal, S. Thiess, M. Gorgoi, P. S. Anil Kumar, W. Drube, O. Karis, and D. D. Sarma, *Role of Boron Diffusion in CoFeB/MgO Magnetic Tunnel Junctions*, Phys. Rev. B - Condens. Matter Mater. Phys. **91**, 1 (2015).

[145] S. Peng, M. Wang, H. Yang, L. Zeng, J. Nan, J. Zhou, Y. Zhang, A. Hallal, M. Chshiev, K. L. Wang, Q. Zhang, and W. Zhao, *Origin of Interfacial Perpendicular Magnetic Anisotropy in MgO/CoFe/Metallic Capping Layer Structures*, Sci. Rep. **5**, 3 (2015).

[146] Y. Yang, W. X. Wang, Y. Yao, H. F. Liu, H. Naganuma, T. S. Sakul, X. F. Han, and R. C. Yu, *Chemical Diffusion: Another Factor Affecting the Magnetoresistance Ratio in Ta/CoFeB/MgO/CoFeB/Ta Magnetic Tunnel Junction*, Appl. Phys. Lett. **101**, 12406 (2012).

[147] S. Ikeda, J. Hayakawa, Y. Ashizawa, Y. M. Lee, K. Miura, H. Hasegawa, M. Tsunoda, F. Matsukura, and H. Ohno, *Tunnel Magnetoresistance of 604% at 300K by Suppression of Ta Diffusion in CoFeB/MgO/CoFeB Pseudo-Spin-Valves Annealed at High Temperature*, Appl. Phys. Lett. **93**, 82508 (2008).

[148] M. Yamanouchi, R. Koizumi, S. Ikeda, H. Sato, K. Mizunuma, K. Miura, H. D. Gan, F. Matsukura, and H. Ohno, *Dependence of Magnetic Anisotropy on MgO Thickness and Buffer Layer in Co20Fe60B20-MgO Structure*, J. Appl. Phys. **109**, 07C712 (2011).

[149] G. An, J. Lee, S. Yang, J. Kim, and W. Chung, *Highly Stable Perpendicular Magnetic Anisotropies of CoFeB / MgO Frames Employing W Buffer and Capping Layers*, Acta Mater. **87**, 259 (2015).

[150] J. Chatterjee, E. Gautier, M. Veillerot, R. C. Sousa, S. Auffret, and B. Dieny, *Physicochemical Origin of Improvement of Magnetic and Transport Properties of STT-MRAM Cells Using Tungsten on FeCoB Storage Layer Physicochemical Origin of Improvement of Magnetic and Transport Properties of STT-MRAM Cells Using Tungsten on FeCoB Storage*, Appl. Phys. Lett. **092407**, (2019).

[151] C.-F. Pai, L. Liu, Y. Li, H. W. Tseng, D. C. Ralph, and R. A. Buhrman, *Spin Transfer Torque Devices Utilizing the Giant Spin Hall Effect of Tungsten*, Appl. Phys. Lett. **101**, 122404 (2012).

[152] Q. Hao and G. Xiao, *Giant Spin Hall Effect and Switching Induced by Spin-Transfer Torque in a W/Co40Fe40/B20/MgO Structure with Perpendicular Magnetic Anisotropy*, Phys. Rev. Appl. **3**, 34009 (2015).

[153] J. Kim, P. Sheng, S. Takahashi, S. Mitani, and M. Hayashi, *Spin Hall Magnetoresistance in Metallic Bilayers*, **097201**, 1 (2016).

[154] C. Zhang, S. Fukami, K. Watanabe, A. Ohkawara, S. DuttaGupta, H. Sato, F. Matsukura, and H. Ohno, *Critical Role of W Deposition Condition on Spin-Orbit Torque Induced Magnetization Switching in Nanoscale W / CoFeB / MgO*, **192405**, (2016).

[155] J. Mathon and A. Umerski, *Theory of Tunneling Magnetoresistance of an Epitaxial Fe/MgO/Fe(001) Junction*, Phys. Rev. B **63**, 220403 (2001).

[156] W. H. Butler, X.-G. Zhang, T. C. Schulthess, and J. M. MacLaren, *Spin-Dependent Tunneling Conductance of Fe/MgO/Fe Sandwiches*, Phys. Rev. B **63**, 54416 (2001).

[157] S. Ikeda, J. Hayakawa, Y. Ashizawa, Y. M. Lee, K. Miura, H. Hasegawa, M. Tsunoda, F. Matsukura, and H. Ohno, *Tunnel Magnetoresistance of 604% at 300 K by Suppression of Ta Diffusion in CoFeBMgOCoFeB Pseudo-Spin-Valves Annealed at High Temperature*, Appl. Phys. Lett. **93**, 67 (2008).

[158] J. I. Beltrán, L. Balcells, and C. Martinez-Boubeta, *Interfacial Geometry Dependence of the Iron Magnetic Moment: The Case of MgO/Fe/MgO*, Phys. Rev. B **85**, 64417 (2012).

[159] Y. H. Wang, W. C. Chen, S. Y. Yang, K. H. Shen, C. Park, M. J. Kao, and M. J. Tsai, *Interfacial and Annealing Effects on Magnetic Properties of CoFeB Thin Films*, J. Appl. Phys. **99**, 97 (2006).

[160] A. Déchelette, M. C. Saint-Lager, J. M. Tonnerre, G. Patrat, D. Raoux, H. Fischer, S. Andrieu, and M. Piecuch, *Fe(x)Mn(1−x)Alloy Phases Strained in Thin Films: Depth-Dependent Investigation of Fe(x)Mn(1−x)/Ir(001) Multilayers by x-Ray Diffraction*, Phys. Rev. B **60**, 6623 (1999).

[161] W. C. Tsai, S. C. Liao, H. C. Hou, C. T. Yen, Y. H. Wang, H. M. Tsai, F. H. Chang, H. J. Lin, and C. H. Lai, *Investigation of Perpendicular Magnetic Anisotropy of CoFeB by X-Ray Magnetic Circular Dichroism*, Appl. Phys. Lett. **100**, 1 (2012).

[162] Y. Iida, J. Okabayashi, and S. Mitani, *Perpendicular Magnetic Anisotropy in Sputter-Deposited Fe/MgO Interfaces Tuned by W Buffer and Tb Capping Layers*, Appl. Phys. Lett. **113**, (2018).

[163] M. Raju, S. Chaudhary, D. K. Pandya, M. Raju, S. Chaudhary, and D. K. Pandya, *X-Ray Reflectance Studies of Interface in Ion Beam Sputtered CoFeB / MgO Bilayers X-Ray Reflectance Studies of Interface in Ion Beam Sputtered CoFeB / MgO Bilayers*, **212506**, 2012 (2014).

[164] J. Lalo, *Atomic-Scale Interface Magnetism for Spintronics*, (2007).

[165] A. You, M. A. Y. Be, and I. In, *Interface Sharpening in Tunnel Junctions Magnetic*, **162505**, 1 (2011).

[166] G. I. R. Anderson, H. X. Wei, N. A. Porter, V. Harnchana, A. P. Brown, R. M. D. Brydson, D. A. Arena, J. Dvorak, X. F. Han, and C. H. Marrows, *Changes in the Layer Roughness and Crystallography during the Annealing of CoFeB/MgO/CoFeB Magnetic Tunnel Junctions*, J. Appl. Phys. **105**, (2009).

[167] B. M. S. Teixeira, A. A. Timopheev, N. Caçoilo, S. Auffret, R. C. Sousa, B. Dieny, and N. A. Sobolev, *Stabilization of the Easy-Cone Magnetic State in Free Layers of Magnetic Tunnel Junctions*, Phys. Rev. B **100**, 184405 (2019).

[168] T. Koyama, A. Obinata, Y. Hibino, A. Hirohata, B. Kuerbanjiang, V. K. Lazarov, and D. Chiba, *Dependence of Curie Temperature on Pt Layer Thickness in Co/Pt System*, Appl. Phys. Lett. **106**, 36 (2015).

[169] M. P. R. Sabino, S. Ter Lim, and M. Tran, *Influence of Ta Insertions on the Magnetic Properties of MgO/CoFeB/MgO Films Probed by Ferromagnetic Resonance*, Appl. Phys. Express **7**, 93002 (2014).

[170] J. M. Iwata-harms, G. Jan, H. Liu, S. Serrano-guisan, J. Zhu, L. Thomas, R. Tong, V. Sundar, and P. Wang, *High-Temperature Thermal Stability Driven by Magnetization Dilution in CoFeB Free Layers for Spin-Transfer- Torque Magnetic Random Access Memory*, Sci. Rep. 1 (2018).

[171] M. C. Troparevsky, J. R. Morris, P. R. C. Kent, A. R. Lupini, and G. M. Stocks, *Criteria for Predicting the Formation of Single-Phase High-Entropy Alloys*, **011041**, 1 (2015).

[172] F. R. De Boer, R. Boom, W. C. M. Mattens, A. R. Miedema, and A. K. Niessen, *Cohesion in Metals North-Holland*.

[173] A. T. Hindmarch, V. Harnchana, A. S. Walton, A. P. Brown, R. M. D. Brydson, and C. H. Marrows, *Zirconium as a Boron Sink in Crystalline CoFeB/MgO/CoFeB Magnetic Tunnel Junctions*, Appl. Phys. Express **4**, 13002 (2010).

[174] A. T. Hindmarch, K. J. Dempsey, D. Ciudad, E. Negusse, D. A. Arena, and C. H. Marrows, *Fe Diffusion, Oxidation, and Reduction at the CoFeB/MgO Interface Studied by Soft x-Ray Absorption Spectroscopy and Magnetic Circular Dichroism*, Appl. Phys. Lett. **96**, 2 (2010).

[175] H. Shi, M. Li, S. Fang, W. Zhou, C. Yang, Y. Jiang, D. Wang, and G. Yu, *Characterization of the Interfacial Structure and Perpendicular Magnetic Anisotropy in CoFeB-MgO Structures with Different Buffer Layers*, Surf. Interface Anal. **50**, 59 (2018).

[176] Y. Yang, W. X. Wang, Y. Yao, H. F. Liu, H. Naganuma, T. S. Sakul, X. F. Han, and R. C. Yu, *Chemical Diffusion: Another Factor Affecting the Magnetoresistance Ratio in Ta/CoFeB/MgO/CoFeB/Ta Magnetic Tunnel Junction*, Appl. Phys. Lett. **101**, (2012).

[177] T. Saito, K. Miyokawa, S. Saito, T. Kamino, K. Hanashima, T. Katayama, Y. Suzuki, K. Mamiya, T.

Koide, and S. Yuasa, *Magnetic and Electronic States of a Monatomic Fe (001) Layer Facing an Epitaxial MgO (001) Tunnel Barrier Studied by Using XAS and XMCD Measurements*, **54416**, 54416 (2005).

[178] F. R. de Boer, W. C. M. Mattens, R. Boom, A. R. Miedema, and A. K. Niessen, *Cohesion in Metals* (North-Holland, Netherlands, 1988).

[179] J. Torrejon, J. Kim, J. Sinha, S. Mitani, M. Hayashi, M. Yamanouchi, and H. Ohno, *Interface Control of the Magnetic Chirality in CoFeB/MgO Heterostructures with Heavy-Metal Underlayers*, Nat. Commun. **5**, 4 (2014).

[180] S. S. P. Parkin, M. Hayashi, and L. Thomas, *Magnetic Domain-Wall Racetrack Memory*, Science (80-.). **320**, 190 (2008).

[181] M. Hayashi, L. Thomas, C. Rettner, R. Moriya, Y. B. Bazaliy, and S. S. P. Parkin, *Current Driven Domain Wall Velocities Exceeding the Spin Angular Momentum Transfer Rate in Permalloy Nanowires*, Phys. Rev. Lett. **98**, 37204 (2007).

[182] S. Parkin and S. H. Yang, *Memory on the Racetrack*, Nat. Nanotechnol. **10**, 195 (2015).

[183] N. Nakajima, T. Koide, T. Shidara, H. Miyauchi, H. Fukutani, A. Fujimori, K. Iio, T. Katayama, M. Nývlt, and Y. Suzuki, *Perpendicular Magnetic Anisotropy Caused by Interfacial Hybridization via Enhanced Orbital Moment in Co/Pt Multilayers: Magnetic Circular X-Ray Dichroism Study*, Phys. Rev. Lett. **81**, 5229 (1998).

[184] I. M. Miron, T. Moore, H. Szambolics, L. D. Buda-Prejbeanu, S. Auffret, B. Rodmacq, S. Pizzini, J. Vogel, M. Bonfim, A. Schuhl, and G. Gaudin, *Fast Current-Induced Domain-Wall Motion Controlled by the Rashba Effect*, Nat. Mater. **10**, 419 (2011).

[185] K.-J. Kim, S. K. Kim, Y. Hirata, S.-H. Oh, T. Tono, D.-H. Kim, T. Okuno, W. S. Ham, S. Kim, G. Go, Y. Tserkovnyak, A. Tsukamoto, T. Moriyama, K.-J. Lee, and T. Ono, *Fast Domain Wall Motion in the Vicinity of the Angular Momentum Compensation Temperature of Ferrimagnets*, Nat. Mater. **16**, 1187 (2017).

[186] R. Bläsing, T. Ma, S. H. Yang, C. Garg, F. K. Dejene, A. T. N'Diaye, G. Chen, K. Liu, and S. S. P. Parkin, *Exchange Coupling Torque in Ferrimagnetic Co/Gd Bilayer Maximized near Angular Momentum Compensation Temperature*, Nat. Commun. **9**, (2018).

[187] T. A. Moore, I. M. Miron, G. Gaudin, G. Serret, S. Auffret, B. Rodmacq, A. Schuhl, S. Pizzini, J. Vogel, and M. Bonfim, *High Domain Wall Velocities Induced by Current in Ultrathin Pt/Co/AlOx Wires with Perpendicular Magnetic Anisotropy*, Appl. Phys. Lett. **93**, 262504 (2008).

[188] I. Dzyaloshinskii, *Ie Dzyaloshinskii*, Sov. Phys. JETP **5**, 1259 (1957).

[189] S. Pizzini, J. Vogel, S. Rohart, L. D. Buda-Prejbeanu, E. Jué, O. Boulle, I. M. Miron, C. K. Safeer, S. Auffret, G. Gaudin, and A. Thiaville, *Chirality-Induced Asymmetric Magnetic Nucleation in Pt/Co/AlOx Ultrathin Microstructures*, Phys. Rev. Lett. **113**, 47203 (2014).

[190] M. Belmeguenai, J.-P. Adam, Y. Roussigné, S. Eimer, T. Devolder, J.-V. Kim, S. M. Cherif, A. Stashkevich, and A. Thiaville, *Interfacial Dzyaloshinskii-Moriya Interaction in Perpendicularly Magnetized Pt/Co/AlO x Ultrathin Films Measured by Brillouin Light Spectroscopy*, Phys. Rev. B **91**, 180405 (2015).

[191] A. Thiaville, S. Rohart, É. Jué, V. Cros, and A. Fert, *Dynamics of Dzyaloshinskii Domain Walls in Ultrathin Magnetic Films*, Europhys. Lett. **100**, 57002 (2012).

[192] I. A. Campbell, *Indirect Exchange for Rare Earths in Metals*, J. Phys. F Met. Phys. **2**, L47 (1972).

[193] J. M. D. Coey, *Magnetism and Magnetic Materials* (20189).

[194] J. Kim, D. Lee, K.-J. Lee, B.-K. Ju, H. C. Koo, B.-C. Min, and O. Lee, *Spin-Orbit Torques Associated with Ferrimagnetic Order in Pt/GdFeCo/MgO Layers*, Sci. Rep. **8**, 1 (2018).

[195] M. A. Basha, C. L. Prajapat, S. Singh, and S. Basu, *Optimization and Characterization of Cobalt & Gadolinium Films Using X-Ray Scattering*, in *AIP Conference Proceedings*, Vol. 1832 (2017), p. 80051.

[196] S. Mangin, C. Bellouard, S. Andrieu, F. Montaigne, P. Ohresser, N. B. Brookes, and B. Barbara, *Magnetization Reversal in Exchange-Coupled GdFe/TbFe Studied by x-Ray Magnetic Circular Dichroism*, Phys. Rev. B - Condens. Matter Mater. Phys. **70**, 1 (2004).

[197] D. D. S. Chaves, *Pour Obtenir Le Grade de Dans l ' École Doctorale de Physique de Grenoble Dynamique de Parois Chirales Dans Les Multicouches Magnétiques Avec Anisotropie Perpendiculaire The Dynamics of Chiral Domain Walls in Multilayer Films with Perpendicular Magnetic A*, (2018).

[198] C. W. Bale and E. Bélisle, *Fact-Web Suite of Interactive Programs*, www. factsage. com.

[199] L. T. Baczewski, P. Pankowski, A. Wawro, K. Mergia, S. Messoloras, and F. Ott, *Induced Magnetism at Interfaces in Ultra-Thin Epitaxial V Gd Bilayers*, Phys. Rev. B - Condens. Matter Mater. Phys. **74**, 1 (2006).

[200] A. C. Thompson, D. T. Attwood, E. M. Gullikson, M. R. Howells, J. B. Kortright, A. L. Robinson, and J. H. Underwood, *X-Ray Data Booklet* (Lawrence Berkeley National Laboratory, 2001).

[201] N. Bergeard, A. Mougin, M. Izquierdo, E. Fonda, and F. Sirotti, *Correlation between Structure, Electronic Properties, and Magnetism in CoxGd(1-x)Thin Amorphous Films*, Phys. Rev. B **96**, 64418 (2017).

[202] G. Y. Guo, H. Ebert, W. M. Temmerman, and P. J. Durham, *First-Principles Calculation Ofmagnetic x-Ray Dichroism in Fe and Co Multilayers*, Phys. Rev. B **50**, (1994).

[203] Y. Wu, J. Stöhr, B. D. Hermsmeier, M. G. Samant, and D. Weller, *Enhanced Orbital Magnetic Moment on Co Atoms in Co/Pd Multilayers: A Magnetic Circular x-Ray Dichroism Study*, Phys. Rev. Lett. **69**, 2307 (1992).

[204] J. Gröbner, D. Kevorkov, and R. Schmid-Fetzer, *Thermodynamic Calculation of Al-Gd and Al-Gd-Mg Phase Equilibria Checked by Key Experiments*, Int. J. Mater. Res. **92**, 22 (2001).